Free Volume Manipulation Techniques of Polymer Membranes for Gas Separations

by

Sharon Lin

B.S., University at Buffalo, State University of New York (2016)

M.S., Massachusetts Institute of Technology (2018)

Submitted to the Department of Chemical Engineering in Partial Fulfillment of the Requirements

for the Degree of

Doctor of Philosophy

at the

MASSACHUSETTS INSTITUTE OF TECHNOLOGY

September 2021

Signature of Author_____
Department of Chemical Engineering
September 2021

Certified by_____
Zachary P. Smith
Assistant Professor of Chemical Engineering
Thesis Supervisor

Accepted by_____
Patrick S. Doyle
Robert T Haslam (1911) Professor
Chairman, Committee for Graduate Students

Free Volume Manipulation Techniques of Polymer Membranes for Gas Separations

Sharon Lin

Abstract

Gas separations are ubiquitous in today's industries and society, playing a role in many key applications such as oxygen generation for medical procedures and natural gas separations for power generation and petrochemicals. In the United States, separation processes consume about 16 quadrillion BTU of energy per year, with nearly half of that energy consumption coming from energy-intensive and thermally-driven processes such as distillation. Using non-thermally-driven processes, such as polymer membranes, for gas separations could reduce energy costs by up to 90% and save the United States over 4 billion USD per year.

Recently, polymers of intrinsic microporosity (PIMs) have shown promise as a platform for energy-efficient gas separations due to their rigid and contorted chemical structures, which increase the amount of free volume and gas throughput. The combination of high permeability and good selectivity exhibited by many PIMs have placed them near or above the Robeson upper bound, a standard metric used to compare polymer membrane performance. However, free volume that is generated from PIMs is done in a "bottom-up" manner where the rigid and contorted chains cause free volume formation. The size and distribution of free volume elements, therefore, are not selectively controlled.

In this thesis, alternative methods to free volume generation are explored. The first method involves a "top-down" approach, where thermally labile functional groups are attached to a polymer backbone. After film formation, the functional groups are thermally removed well below the glass transition temperature to systematically template free volume elements of a desired size and distribution within the polymer matrix. The effect of various thermal treatments on both the

packing structure and gas transport properties was analyzed, and the results suggest that polymer chain mobility occurring below glass transition temperatures can disrupt the templated free volumes. Therefore, more robust polymer systems that can preserve the free volume architecture after thermal treatment from this approach are needed.

The second method is a “bottom-up” approach similar to that used by PIMs, but with a new chemical structure consisting of a flexible polymer backbone and rigid side chains that form a “bottlebrush”-like structure. The polymers were generated via ring-opening metathesis polymerization (ROMP), and their gas transport properties were examined in ideal and realistic industrial conditions. These polymers, referred to as ROMP polymers, showed excellent gas transport properties, as well as unprecedented plasticization and physical aging resistance. The excellent stability exhibited by ROMP polymers was attributed to the rigid side chains. The effect of side-chain length on the gas transport properties of a methoxy-functionalized ROMP (OMe-ROMP) was also studied. In this case, increasing side-chain length led to increased free volume and plasticization resistance. Lastly, to further probe their plasticization resistance, sorption measurements and mixed-gas tests using realistic industrial conditions were conducted on OMe-ROMP samples with different side-chain lengths. Overall, this thesis focuses on alternative methods to free volume generation in polymer membranes that can be used for energy-efficient gas separations.

Thesis Supervisor: Zachary P. Smith, Assistant Professor of Chemical Engineering

Acknowledgements

As I put together the dissertation that represents what I have been up to for the past 5 years, I am reminded of all of the support and guidance I have received during my time at MIT. I would like to give a personal shout-out to all of the people that I am indebted to for bringing me to this point in my life.

First and foremost, to my advisor, Professor Zach Smith: thank you for your mentorship, support, and patience throughout this journey. Your passion for the fields of polymer membranes and gas separations have provided me with invaluable knowledge and skills, and your dedication to the research group continues to amaze and inspire me. Even when I felt lost and was struggling to collect and understand data, you have continuously believed in me and uplifted me. I feel truly honored that I can proudly call myself one of your first graduate students. I could not have asked for a better advisor to start up an entire lab with from scratch.

To my thesis committee members, Professor Pat Doyle and Professor Tim Swager: thank you for your constant support and guidance throughout my time here. Your insightful questions and suggestions have been instrumental to my research, and I am so fortunate to have such a wonderful committee.

To my year-mates, Dr. Qihui Qian and Dr. Albert Wu: I can call myself Ph.D #3 now! Thank you so much for being the best people to start a lab with, and thank you for your tenacity as we overcame various challenges together. I'm so excited to see the future of the lab, and I am proud of us for what we have accomplished during our time here.

To my wonderful labmates: I am so lucky that the best people have joined the Smith lab. Katherine Mizrahi Rodriguez, thank you for being an amazing collaborator and friend, and for your unwavering support and encouragement even when I was struggling with my research.

Taigyu Joo, thank you for being an awesome person to mentor and work with – I am so excited to see you bring more of my ideas to life. Dr. Francesco Benedetti, thank you for making me laugh during the most stressful times and for your library of knowledge on everything related to polymer membranes. And to everyone else, past and present: Dr. Won-seok (Lucas) Chi, Dr. Gang (Andy) Han, Dr. Shaofei Wang, Dr. Stephen DeWitt, Dr. Fatimah Edhaim, Dr. Moonjoo Lee, Dr. Justin Teesdale, Patrick Asinger, Pablo Dean, Aristotle Grosz, Eric Hahnert, Hyunhee Lee, Kayla Storme, Wan-ni Wu, Jing Ying Yeo, Dr. Holden Lai, Robin Studer, and Shiqi Zhao: thank you for being amazing labmates. You are all incredible researchers and people, and I'll miss all of our times going out to eat, running along the Charles, making impromptu coffee runs, indoor rock-climbing, playing board games, and making silly inside jokes and lasting memories. I'll truly miss being in such a wonderful and supportive lab group, full of collaborative, innovative, and highly accomplished scholars. To the undergraduate students I had the honor to mentor, Laura Chen and Evan Gwozdz: thank you for your dedication and passion for research and learning. The quality of work both of you have produced during your time in the Smith lab is unparalleled, and I am so proud of both of you.

I am also grateful for the chances I had to foster interesting and fruitful collaborations. To the members of the Swager lab, Dr. Yuan (Frank) He and Dr. You-Chi (Mason) Wu: your wealth of knowledge on chemistry has been incredibly helpful and inspiring. To everyone at the Deshpande Center, thank you for all of the guidance and support you have provided to help industrialize some unique polymers for separations. I also had the incredible opportunity to travel to CSIRO in Melbourne, Australia for a month, where I was able to work with Dr. Cara Doherty and the members of Professor Matt Hill's group. Cara, thank you so much for mentoring me and sharing your knowledge of positron annihilation lifetime spectroscopy to me, and for being

instrumental in bringing this technology to MIT. I also found myself back at my undergraduate institute, SUNY Buffalo, for a week to work with Professor Haiqing Lin and Dr. Liang Huang on mixed-gas permeation, who I thank immensely for their guidance and knowledge.

During my time at MIT, I also was able to partake in the School of Chemical Engineering Practice (Practice School), where I had the once-in-a-lifetime opportunity to travel to two international stations (MSD in Carlow and Brinny, Ireland, and Woodside Energy Inc. in Perth, Australia). I'd like to thank my station directors, Dr. Tom Blacklock and Dr. Brian Stutts, for their support and vast knowledge that allowed me to gain insight into industry.

To the lifelong friends I have made at MIT, thank you so much for uplifting me during my biggest periods of stress. I'll cherish all the wonderful memories we have made together. To all of the friends I have made back home in Guilderland, but also in Buffalo and Los Angeles, and wherever else I've been to, thank you for always being there for me.

Lastly, I'd like to give my heartfelt thanks to my loving parents, Hung-yun and Heng-yuan, and my sister, Cassie. Thank you so much for being my personal cheerleaders and encouraging me to keep going even through the toughest times. You have inspired me greatly during my lifetime and I hope I continue making you proud. And to my partner, Aristotle Grosz: your love and support have carried me through my Ph.D., and I can't thank you enough. Your kindness and infectious humor kept me smiling, and you were (and still are) a beacon of light during my darkest periods of self-doubt. I couldn't have done it without you.

Table of Contents

List of Figures

List of Tables

Chapter 1. Introduction

Gas separations are ubiquitous in today's industries and society, playing a key role in a wide variety of applications.[1,2] For example, gas separations can involve nitrogen separation for inerting and food packaging, oxygen generation for medical applications, and natural gas purification for power generation and petrochemicals.[3] However, in the United States, the separations industry alone accounts for approximately 50% of all industrial energy consumption, and nearly half of that is due to thermally-driven separation technologies such as distillation.[4,5] Since distillation processes rely on liquid–vapor phase changes, the energy required to overcome heats of vaporization leads these processes to be incredibly energy-intensive.[4] Cryogenic distillation, a technique similar to conventional distillation that is run at low temperatures to separate mixtures based on boiling point, is often used for air separations.[6] In this process, nitrogen (boiling point = 77.4 K) is removed as the distillate while argon (boiling point = 87.3 K) and oxygen (boiling point = 90.2 K) are removed as the bottoms and further purified by a second column.[6] While cryogenic distillation can produce outlet streams of more than 99% purity,[7] there are large operating costs associated with cooling and pressurizing the column for condensing gases.[3,8]

Other techniques employed in industry today include pressure swing adsorption (PSA), temperature swing adsorption (TSA), and chemical absorption. In PSA and TSA, gas mixtures are fed through an adsorbent bed, where the strongly-adsorbing gases will remain in the column while the less adsorbing gases will pass through.[9] Adsorbents are often solid-state materials such as zeolites and activated carbons that contain extremely high internal surface areas.[10] While PSA relies on changes in pressure to regenerate the column (by inducing desorption),[11] TSA uses elevated temperatures for regeneration.[12] While the efficacy of PSA and TSA highly depend on the gas mixture composition and adsorbent used, purities of around 98% can often be reached for

applications such as CO_2-based separations, nitrogen enrichment, and oxygen purification.[13,14] However, there are energy costs associated with desorption of gas from the adsorbent after every cycle. Because gas throughput generally scales linearly with the amount of adsorbent required, both PSA and TSA are often used for smaller-scale applications with lower purity requirements.[15]

Chemical absorption is another technology that is often used for separations, especially CO_2-based separations.[1,16] Here, an amine-based chemical absorbent reacts with CO_2 to generate a carbamic acid.[17,18] The carbamic acid will then decompose at elevated temperatures, releasing the captured CO_2 and regenerating the amine for further purification steps. Some examples of liquid amines that are used in chemical absorption include monoethanolamine (MEA), diethanolamine (DEA), and methyldiethanolamine (MDEA).[19] While chemical amine absorption can produce streams that are up to 99% pure,[20] drawbacks include the need to use elevated temperatures (> 100 °C) that require large energy inputs for amine regeneration, the risk of amines degrading under the presence of oxygen and heat that results in corrosive mixtures, and the possibility of amines forming nonreversible salts when exposed to trace amounts of SO_2 or NO_x.[3,16,21,22] Given the high energy costs and complications of current methods implemented today in industry, utilizing energy-efficient and simple alternatives for separations is highly desired.

Polymer membranes are one such promising alternative. Unlike distillation, polymer membranes do not rely on phase changes for separations, and thus the energy costs associated with overcoming heats of vaporization are significantly mitigated.[2,3] The implementation of polymer membranes, which are oftentimes more mechanically simple in terms of operation, can also reduce spatial requirements that are typically needed for conventional separation processes.[1,3,23] By using polymer membranes in place of conventional separation processes like distillation, energy costs

can be reduced by up to 90%, eliminating 100 million tons of CO_2 and saving $4 billion in energy costs per year in the United States.[4]

In this chapter, the current market for gas separation membranes will be discussed in more detail. Then, the mechanisms of gas transport in polymer membranes will be discussed, as well as the metrics to determine polymer membrane efficacy for separations. Next, common issues with polymer membranes that preclude their widespread use in industry will be discussed. Then, the concept of free volume in polymer membranes will be introduced, along with emerging materials and techniques for free volume manipulation (FVM). Lastly, the outline of this thesis will be presented.

1.1. Current Market for Gas Separations

In 1963, Loeb and Sourirajan introduced a phase inversion process for fabricating membranes,[24] in which a polymer is dissolved in an organic solvent and then submerged in a non-solvent to form a selective and dense polymer film on a porous and asymmetric support. During this process, the solvent rapidly evaporates, causing the polymer to vitrify.[25,26] Because this method enables the formation of thin films (e.g., ~100 nm thickness), which allows for high gas flux, virtually all polymer membranes for gas separations have been formed in this manner.[25] In addition, different geometries such as hollow fibers or spiral wound membranes that can be formed from this phase inversion approach, maximizing membrane surface area in a given cylindrical volume.[2] This feature is particularly beneficial because a high surface-area-to-volume ratio will reduce the size of pressure vessels needed to treat a given flowrate of gas.[2,27]

Currently, four major commercial applications for gas separations exist that represent 80–90% of the gas separation membrane industry.[1] These four applications are hydrogen recovery,

natural gas treatment, nitrogen production, and vapor recovery, and their relevant gas pairs and approximate market sizes (in millions USD) are presented in **Table 1.1**. Given the nine-fold increase in the market size from 2002 to 2018, as well as the projected increase in 2022, the market for gas separation membranes is expected to continue its strong growth.

Table 1.1. Four major commercial applications for gas separation membranes, relevant gas pairs involved, and approximate market size for 2002, 2018, and 2022 (projected).[1,2,28]

Application	**Relevant gas pairs**	**Approximate Market Size (millions USD)**		
		2002	**2018**	**2022 (projected)**
Hydrogen recovery	H_2/N_2, H_2/CH_4, H_2/CO	25	200	-
Natural gas treatment	CO_2/CH_4, H_2S/CH_4, He/CH_4	30	300	-
Nitrogen production	O_2/N_2	75	800	-
Vapor recovery	C_3H_6/N_2, C_2H_4/N_2, C_2H_4/Ar, C_{3+}/CH_4, CH_4/N_2, gasoline/air	20	100	-
Total	-	150	1400	2610

In 1979, Monsanto was the first company to provide a membrane system for hydrogen recovery from purge gas (nitrogen, argon, and methane).[27,29] This system, consisting of polysulfone hollow fibers named Prism® membranes, can achieve up to 95% recovery of hydrogen (H_2).[30] Today, hydrogen separation membranes are used not only for hydrogen recovery from purge gas, but are also used for adjusting molar compositions of syngas feeds in oxo-chemical synthesis (H_2/CO) and refinery off-gas purification (H_2/CH_4).[3,25,28,31]

Natural gas usually consists of methane (CH_4) and carbon dioxide (CO_2), but also many other compounds such as ethane and larger hydrocarbons, hydrogen sulfide (H_2S), inert gases such as helium and argon, and trace components of many others including BTEX aromatics (benzene, toluene, ethylbenzene, and xylenes).[16] To deliver this complex mixture to U.S. pipelines requires that the mixture is treated such that it contains less than 2% CO_2, 120 ppm water, and 4 ppm H_2S.[16] The first membranes for natural gas purification were developed in the 1980s, with W.R. Grace and Separex (now both part of UOP) developing spiral-wound membranes and Cynara (now part of Schlumberger) developing hollow fiber cellulose acetate-based membranes.[16] Currently, membranes occupy only 10% of the natural gas purification market due to low selectivity, while chemical amine absorption occupies the rest of the market.[2,16] However, due to the complications involved with chemical amine absorption, including energy and maintenance costs, there is potential for more selective membranes to be developed. In the past 15–20 years, polyimide membranes (by Air Liquide) and perfluoropolymer membranes (by ABB/MTR) have also been developed.[32–34]

Nitrogen purification via air separations is typically performed using cryogenic distillation and PSA, though membranes have also been developed for this application.[11,15,25,28,35] In the 1980s, Generon developed a poly(4-methyl-1-pentene) (TPX) membrane for air separations.[28] Since then, new hollow fiber membranes such as polyimides by Praxair, polyimide and polyaramide membranes by Medal, and tetrahalogenated bisphenol-based polycarbonates by Generon, were developed and commercialized.[28,36]

For vapor recovery, which typically involves the removal of light hydrocarbons from petrochemical process streams (consisting of about 20–30% of various hydrocarbons in nitrogen), silicone rubber is the most widely used membrane for separations.[29] The first commercial vapor

separation plants were installed in 1988 by MTR, GKSS, and Nitto Denko.[28] Since then, silicone rubber continues to be the dominant material.

While there have been successes with current commercial membranes, there is still room for improvement within current applications mentioned above as well as in emerging applications. As stated earlier, membranes currently only occupy about 10% of the natural gas purification market.[16] This is largely due to the current membranes in use having low gas permeability (production) and selectivity (purity) capabilities. Therefore, membranes with better performance will be beneficial in increasing their use in this market. In addition, there is potential for membrane technology to be used in other separations, mainly olefin/paraffin separation, carbon capture from flue gas or syngas streams, and vapor/vapor separations.[1–3]

In terms of olefin/paraffin separations, ethylene and propylene are the two largest hydrocarbon feedstocks in the chemical industry due to their use in the synthesis of several vinyl monomers and polymers such as ethylene oxide and polyethylene from ethylene and acrylonitrile and polypropylene from propylene.[37] In order to obtain compounds such as ethylene and propylene for further syntheses, separations from paraffins (such as ethane and propane, respectively) is necessary.[38] In 2017, the global production capacity of ethylene and propylene was 169 and 116 MMt (metric million tons) per year, respectively,[39] indicating the high demand for such compounds. Currently, the technology used to separate olefin/paraffin mixtures is cryogenic distillation, which often require 100–150 stages since the components' boiling points only differ by 4–5 °C.[1,8,38] While this is an area of interest for membranes, the purity and throughput requirements necessary to replace distillation are far higher than what today's membrane materials can provide.[1]

Another area of interest for membranes is that of carbon capture, which can be accomplished through various enabling separation processes, such as purification of gas effluent from steam methane reforming and subsequent water gas shift reaction (CO_2/H_2), oxycombustion processes (O_2/N_2), and CO_2 capture for sequestration from postcombustion flue gas (CO_2/N_2).[2] Production of H_2 streams from the water–gas shift reaction in the first application can be used as fuel or as a hydrogen source in a refinery, while in the last application, CO_2 can be captured in order to reduce CO_2 emissions to the atmosphere.[1] The leading method for post-combustion carbon capture that has been demonstrated in industry is amine absorption, but due to high operating/capital costs, large footprint, and toxicity of amines used, membranes have potential to replace amine absorption as the dominant technology.[1] For other carbon capture processes, the largest hurdle that precludes membranes from being used for pre-combustion carbon capture is the high operating temperature needed for economical separation. For steam reforming reactions, operating temperatures of 700 °C are needed, while for water–gas shift reactions, temperatures between 300 and 500 °C are preferred, and commercial membranes are unstable under these conditions.[40]

The last application that will be discussed is the separation of organic mixtures. The use of membranes has been considered for the separation of water from solvents such as ethanol, isopropanol, and acetone since these solvents form azeotropes with water at purities less than what is required, which means that distillation is no longer a simple option.[1,3] In 1982, GFT built the first membrane ethanol dehydration system using crosslinked poly(vinyl alcohol) membranes.[1] While most plants were pervaporation-based, there has been an increase towards using vapor permeation systems with zeolite membranes.[1] While it is considerably easier to perform

water/solvent separations since water is significantly smaller than the nonpermeating organic solvent, it is currently unclear whether polymer or zeolite membranes will dominate the industry.[1]

1.2. Transport in Polymer Membranes

Gas transport in polymer membranes is governed by the sorption–diffusion model.[41] A detailed discussion and derivation of the sorption–diffusion model can be found elsewhere,[41] but a general summary is given as follows. In this model, it is assumed that permanent pores in the membrane do not exist, so molecules travel by means of both diffusion and sorption.[41] Gas molecules will sorb into the high-pressure side of the membrane, diffuse through the membrane via a concentration (or chemical potential) gradient, then desorb on the low-pressure side of the membrane.[41] During the diffusion step, stochastic molecular chain fluctuations of the polymer backbone result in the opening and closing of transient gaps in the polymer matrix that are otherwise known as free volume elements, through which gas molecules will diffuse.[41]

The permeability of a penetrant, P_i, through the membrane is defined as:

$$P_i = \frac{J_i l}{p_{i,u} - p_{i,d}} \tag{1.1}$$

Where J_i is the penetrant flux, l is the membrane thickness, and $p_{i,u}$ and $p_{i,d}$ are the upstream and downstream pressures, respectively.[2,3] Permeability is often expressed in units of barrer (10^{-10} cm^3 (STP) cm/(cm^2 s cmHg)).[2,3] In non-ideal cases, the upstream and downstream pressures are replaced by their respective fugacities.[3] The penetrant flux can also be described using the following equation:

$$J_i = D_i S_i \frac{p_{i,u} - p_{i,d}}{l} \tag{1.2}$$

Where D_i is the diffusion coefficient, and S_i is the sorption coefficient. By combining Equations 1.1 and 1.2, the following relationship can be established:

$$P_i = D_i S_i \tag{1.3}$$

Therefore, permeability is a function of both diffusion and sorption coefficient.[41]

The ideal separation ability (ideal selectivity) of a membrane is expressed through the following equation:

$$\alpha_{i/j} = \frac{P_i}{P_j} = \frac{D_i}{D_j}\frac{S_i}{S_j} \tag{1.4}$$

Where species i is generally the more permeable of the two such that $\alpha_{i/j}$ is greater than 1. As shown above, the ideal selectivity can be decoupled into diffusivity selectivity and sorption selectivity. Mixed-gas selectivities can also be determined by assessing gas-phase composition of the permeate using gas chromatography, mass spectrometry, among other techniques.[42]

The sorption coefficient can be determined using direct sorption experiments which involve measuring the concentration of gas sorbed in the membrane as a function of equilibrium pressure.[42] There are various models to describe the sorption behavior of a polymer membrane,[43,44] but one of the most common models used is the dual-mode sorption model.[45] The dual-mode sorption model describes sorption as an addition of Henry and Langmuir sorption, shown below:

$$C = k_D p + \frac{C'_H b p}{1 + bp} \tag{1.5}$$

Where C is the concentration of gas sorbed into the polymer membrane, k_D is Henry's constant, p is the equilibrium pressure, C'_H is the Langmuir sorption capacity, and b is the Langmuir affinity coefficient.[45] In terms of the sorption coefficient, the above equation can be rewritten as follows:

$$S = \frac{C}{p} = k_D + \frac{C'_H b}{1 + bp} \tag{1.6}$$

The sorption coefficient at infinite dilution (S^{∞}), which physically represents the affinity of the first gas molecule to sorb into the polymer, can be obtained by taking the limit of the above equation as pressure approaches zero:[42]

$$S^{\infty} = \lim_{p \to 0} S = k_D + C'_H b \tag{1.7}$$

1.3. Current Issues in Polymer Membranes

Ideally, a membrane will have both high permeability and selectivity in order to maximize purity while cutting back on material costs. However, a trade-off relationship exists between the two parameters, such that materials that exhibit high permeability generally have low selectivity, and vice versa. This experimental trade-off was first identified by Robeson,[46,47] who collected a large database of membrane permeabilities and selectivities for a number of common gas pairs in plots that are known as Robeson upper bound plots. Since then, Freeman established a theoretical basis for this trade-off,[48] and a number of other upper bounds have been developed to account for new data.[49–52]

Figure 1.1 shows an example of a Robeson upper bound for the CO_2/CH_4 gas pair. In such plots, the gas pair selectivity is plotted as a function of gas permeability for all polymers available in literature, and an upper bound line is established beyond which no data will appear. The performance of new materials developed is often compared against Robeson upper bound plots. However, data points plotted on the upper bound are pure-gas data obtained with a narrow range of testing conditions (usually 1 atm and 35 °C). In industrial settings, feed pressures and temperatures are often higher than what is tested in the laboratory scale. Separation performance in mixtures can also differ significantly from that for pure gases, especially when the gases involved are condensable. For example, in a CO_2/CH_4 mixture, competitive sorption between CO_2

and CH_4 and swelling effects from high pressures of CO_2 can drastically alter the separation performance.[29,53] Therefore, while upper bound performance is an indication of viability in industrial applications, other considerations must be taken into account, such as membrane stability and separation performance in mixtures.

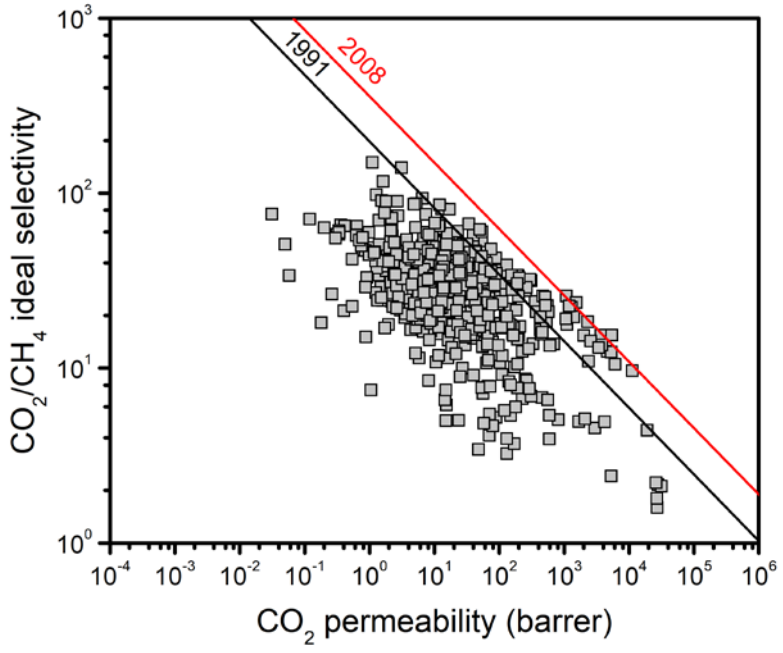

Figure 1.1. CO_2/CH_4 Robeson upper bound plot. Each gray square represents a homogeneous, solution-processable polymer material. The black line represents the 1991 upper bound,[46] while the red line represents the 2008 upper bound.[47]

Membrane stability is another issue that precludes membranes from being the dominant method for gas separations in industry. In polymer-based membranes, plasticization is a phenomenon that occurs when the presence of a highly condensable gas (e.g., CO_2, C_3H_6, C_3H_8, H_2S, etc.) results in increased polymer translational motion.[54,55] Condensability of a gas is related to its critical temperature, where more condensable gases will have higher critical temperatures, and vice versa. While polymer swelling leads to an increase in gas permeability, selectivity is often

compromised as a result. In a laboratory setting, a membrane's susceptibility to plasticization is often measured using high pressure pure-gas tests, in which the feed pressure of condensable gas is increased while monitoring permeability. During these tests, the permeability will initially decrease at lower pressures. The pressure at which the permeability reaches a minimum and subsequently begins to increase with increasing pressure is commonly known as the "plasticization pressure".[56] Since permeability is a function of both diffusivity and sorption, the plasticization pressure is an indication of when the increase in diffusion coefficient overtakes the decrease in sorption coefficient as pressure increases (**Figure 1.2**).[57–59]

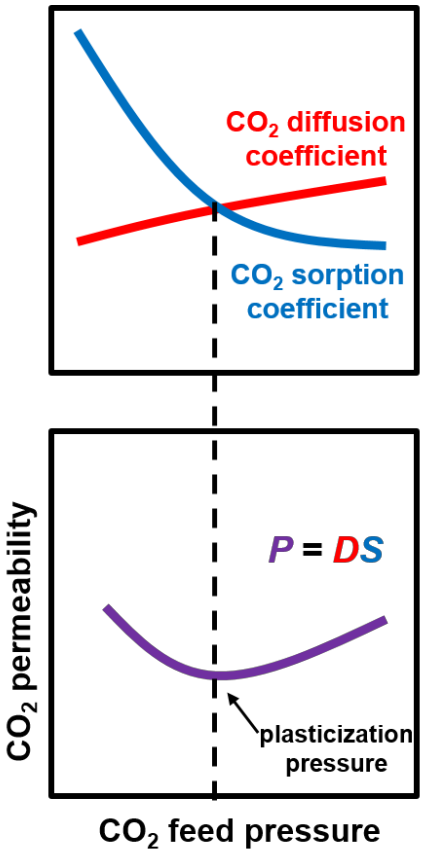

Figure 1.2. Graphical representation of CO_2 diffusion coefficient, sorption coefficient, and permeability as functions of CO_2 feed pressure. The feed pressure at which the CO_2 permeability begins to increase is known as the "plasticization pressure".

Some polymers have not shown a plasticization pressure within the pressure range tested, suggesting plasticization resistance.[60–65] However, plasticization pressure alone is not a sufficient measure of plasticization resistance since it does not take into account the changes in gas selectivity (which will decrease if plasticization is occurring), as well as changes in permeability of the non-plasticizing gas in a mixed-gas test. Therefore, mixed-gas tests have also been employed to determine the plasticization behavior of a material. For example, when running a CO_2/CH_4 mixed-gas test, polymer chain translation due to the presence of CO_2 can cause CH_4 permeability to increase, also known as "CH_4-creep," and can more directly identify plasticization effects, even when CO_2 permeability does not show a plasticization pressure.[60] In contrast to CO_2, permeability of CH_4 in pure-gas tests rarely reveals plasticization effects since CH_4 dissolution in polymers is significantly lower than that of CO_2, as correlated with metrics of condensability, such as critical temperature ($T_{c,\,CH_4}$ = 190.55 K and $T_{c,\,CO_2}$ = 304.19 K). Thus, CH_4 provides a better probe for assessing plasticization when co-permeating with CO_2, whereas pure-gas CH_4 permeation would not typically reveal information about plasticization phenomena.

Physical aging is another phenomenon that preclude glassy polymer membranes from being used in industry. A polymer is in its "glassy" state when it is at a temperature below its glass transition temperature (T_g), and a polymer is in its "rubbery" state when it is at a temperature above its T_g. While polymers in their glassy state are more viscous and "solid-like", rubbery polymers are elastic and "liquid-like". When polymers are cooled from their rubbery to glassy state, the polymer chains access a meta-stable packing state that is out of equilibrium.[66] However, over time, the polymer chains will rearrange slowly toward their equilibrium packing state, which will result in a decrease in overall free volume as shown in **Figure 1.3**.[67] This phenomenon results in an increase in permselectivity, but a decrease in permeability.[67–70]

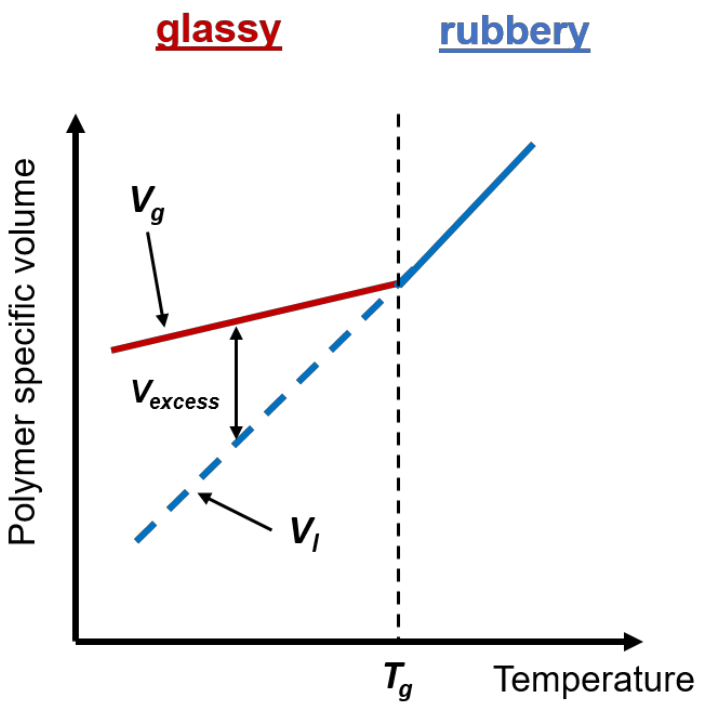

Figure 1.3. Graphical representation of change in volume as a function of temperature. V_g represents observed specific volume of the glassy state, V_l represents specific volume of the hypothetical rubbery state (equilibrium), and V_{excess} is the non-equilibrium excess volume.

1.4. Concept of Free Volume

As discussed earlier, the sorption–diffusion model assumes that no permanent pores exist in the membrane.[41] However, transient gaps, known as free volume elements, exist in the membrane which allow molecules to pass through. These free volume elements refer to the void space not occupied by the polymer chains.

Fractional free volume (FFV) is a common metric to describe the amount of free volume present in a polymer membrane.[23] To calculate the FFV, the following equation is used:

$$FFV = \frac{V_{sp} - V_0}{V_{sp}} \tag{1.8}$$

Where V_{sp} is the specific volume (the inverse of polymer density) and V_0 is the van der Waals volume. V_0 is most often estimated using a group contribution method.[71–74] Correlations between free volume and permeability have been established as such:

$$P = Aexp\left(-\frac{B}{FFV}\right) \tag{1.9}$$

Where A and B are adjustable parameters. Therefore, as FFV increases, it is expected that permeability will increase as well.

While FFV measurements can give an indication of how much free volume is within a polymer membrane, such measurements do not provide any information on free volume size or distribution. A number of techniques have been developed to interpret the amount of free volume in a polymer matrix, such as X-ray diffraction, ^{129}Xe nuclear magnetic resonance (NMR) spectroscopy, and molecular dynamic (MD) simulations.[23]

One technique that can provide information on the free volume size and distribution of polymer membranes is known as positron annihilation lifetime spectroscopy (PALS). In a typical PALS experiment, positrons emitting from a source (such as ^{22}Na) may either annihilate as a "free" particle or interact with the electrons present in the material to form a positronium, which is a bound state of an electron and a positron.[75,76] Whether the spin orientation of the positron and electron are antiparallel or parallel, either a para-positronium (pPs) or an ortho-positronium (oPs) will form, respectively.[76,77] While the lifetime of the pPs is around 125 ps, the lifetime of the oPs is significantly longer.[76] Under vacuum, the oPs will have a lifetime of about 142.1 ns.[76] However, "pick-off" annihilation during collision with electrons in the polymer matrix will significantly shorten the lifetime.[76] The average free volume element size can be correlated to the lifetime of

the oPs, as oPs trapped in larger free volume elements will have longer lifetimes due to the reduced electron density that will delay annihilation. By assuming that the free volume elements inside polymers are spherical and that there exists a homogeneous electron layer with a thickness of $\Delta R = R_0 - R$ (in which R is the radius of the free volume element and ΔR is an empirical parameter determined to be 1.66 Å),[75,76] the Tao-Eldrup equation, below, can be used to correlate the oPs lifetime (τ_{oPs}) to the average free volume element radius:[78,79]

$$\tau_{oPs} = \frac{1}{2}\left[1 - \frac{R}{R_0} + \frac{1}{2\pi} sin\left(\frac{2\pi R}{R_0}\right)\right]^{-1} \quad (1.10)$$

Besides the oPs lifetime, the oPs pick-off annihilation intensity, I_{oPs}, can also be determined from PALS experiments. I_{oPs} is proportional to the probability of oPs formation in a polymer,[80] and thus can be assumed to be correlated to the amount of free volume elements. By observing hundreds of thousands to millions of oPs lifetime events, free volume size distributions can be generated via various computer programs such as PATFIT,[81] PAScual,[82] and MELT.[83]

PALS has been regarded as an effective way to measure the average free volume element size in polymers due to the small size of the positronium probe (1.59 Å).[76] However, several considerations must be taken into account when analyzing PALS data. As mentioned earlier, the Tao-Eldrup equation is valid when assuming free volume elements are spherical. In addition, the oPs may not be able to access every free volume element with equal probability.[75] The inhibition of Ps formation, which would lead to lower intensities, may also occur when the positron is exposed to polar groups such as –OH or –C=O.[80] In these cases, the positron may be trapped in the negatively charged portion of the dipole existing in the polar group.[80] Ps quenching can also occur in the presence of oxygen, which would shorten τ_{oPs} in porous polymers such as PTMSP.[84,85]

1.5.Emerging Materials for Gas Separations

Since the development of PIM-1 by Budd and McKeown,[86,87] polymers of intrinsic microporosity (PIMs) have garnered much interest in the gas separations field due to their ultrahigh gas permeability with minimal losses in selectivity compared to commercial polymers. **Figure 1.4** below shows a CO_2/CH_4 Robeson plot with some high-performing emerging polymers indicated in color, which have all been discovered within the past twenty years. The high-performing polymers (PIM-1, PIM-TMN-SBI, and PIM-TMN-Trip) all possess high permeability with minimal loss in selectivity, compared to the commercial polymers listed in the Robeson plot (cellulose triacetate, polysulfone, and Matrimid®). In particular, both PIM-1 and PIM-TMN-Trip exceeded the 2008 Robeson upper bound limit for CO_2/CH_4.[88,89]

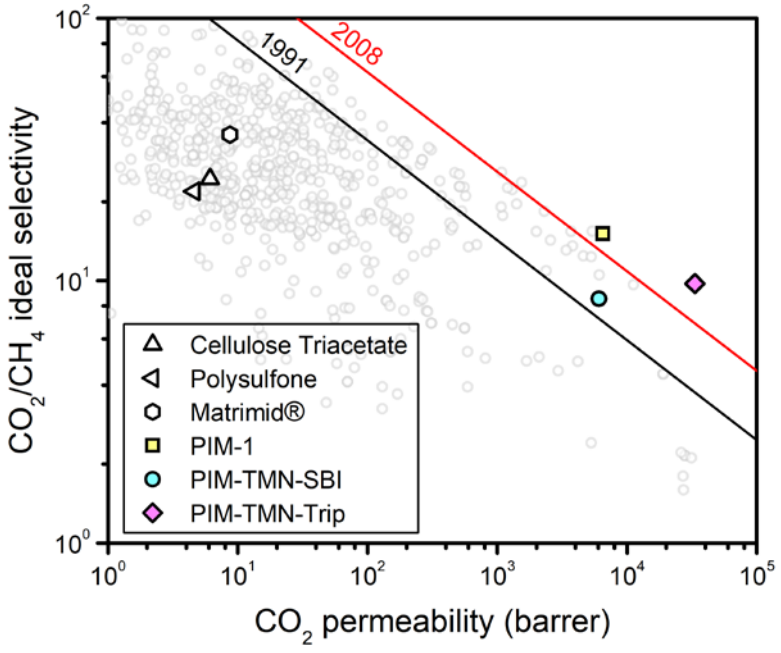

Figure 1.4. CO_2/CH_4 Robeson plot containing some commercial polymers and some high-performing polymers tested recently. Light gray dots indicate other polymer data.

As shown in Equation 1.9, increases in FFV often lead to increases in permeability. The ultrahigh permeabilities of the emerging polymers can therefore be attributed to high FFV. For

instance, the FFV value of PIM-1 ranges from 0.24 to 0.26.[89] PIM-TMN-SBI has been reported to have an FFV value of 0.276 ± 0.004, while PIM-TMN-Trip has an FFV of 0.309 ± 0.005.[88] In contrast, the FFV values of cellulose triacetate, polysulfone, and Matrimid® are 0.157,[90] 0.158,[91] and 0.11,[92] respectively.

The high FFV values of the aforementioned materials can be attributed to their rigid and contorted structures, which hinder polymer chain packing and allow for larger free volume elements to be formed. The structures of PIM-1, PIM-TMN-SBI, and PIM-TMN-Trip are shown in **Figure 1.5**. Compared to commercial membranes such as cellulose triacetate, polysulfone, and Matrimid® (**Figure 1.5**), the structures of PIM-type polymers are considerably bulkier, with ladder-type bonds between each repeat unit. However, the free volume elements in PIM-type polymers are generated in a "bottom up" fashion, in which the rigidity and contortion of PIM polymers form free volume elements as the polymers vitrify through solvent casting. As such, the size and distribution of free volume elements cannot be selectivity controlled, and alternative methods are currently being studied to freely manipulate both the size and distribution of free volume elements in polymer membranes for gas separation applications.

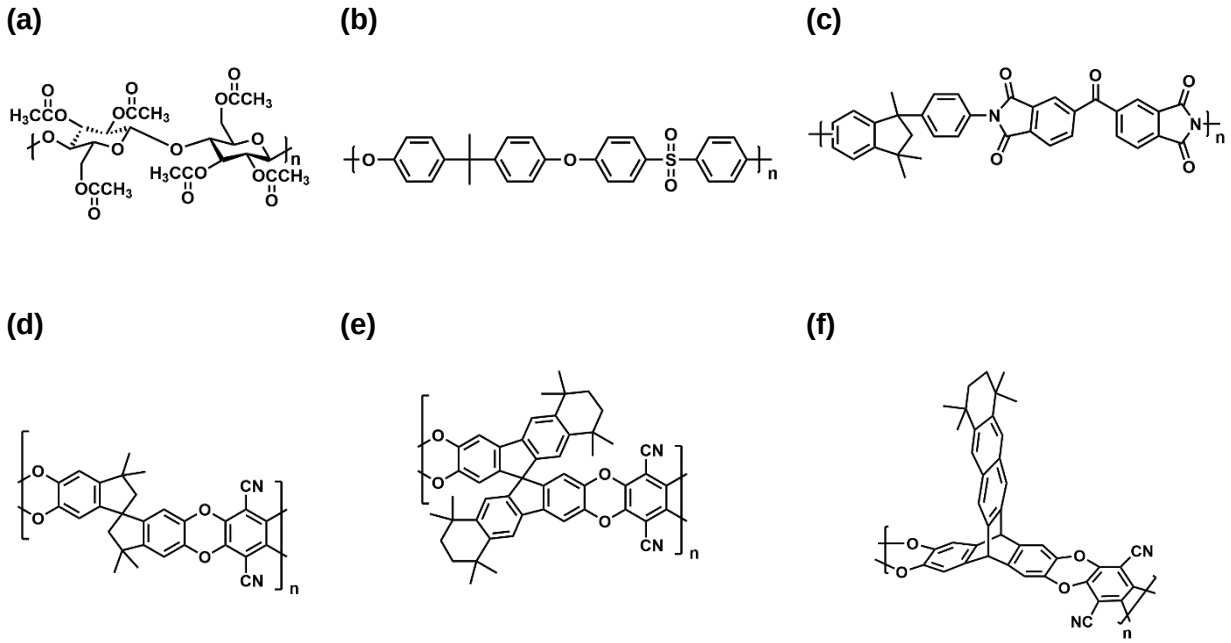

Figure 1.5. Chemical structures of (a) cellulose triacetate, (b) polysulfone, (c) Matrimid®, (d) PIM-1, (e) PIM-TMN-SBI, and (f) PIM-TMN-Trip.

1.6.Dissertation Outline

In this dissertation, alternative strategies to generate free volume elements in polymer membranes and their effects on gas transport will be discussed. Future directions and outlook for such alternative strategies are also discussed. In Chapter 2, a simple thermal treatment to generate porogens in a 6FDA-HAB polyimide functionalized with t-BOC was introduced. Characterization techniques including thermal gravimetric analysis (TGA), dynamic scanning calorimetry (DSC), nuclear magnetic resonance (NMR) spectroscopy, FFV, PALS, and pure-gas permeation tests were used to determine the effects of thermal deprotection on polymer free volume and gas transport properties.

Chapter 3 presents a new design strategy for polymers in gas separations, namely polymers synthesized via ring-opening metathesis polymerization (ROMP). Unlike in rigid PIMs, pore

generation in ROMP polymers occurs due to rigid side chains on a flexible poly(norbornene) backbone. The gas transport properties of two ROMP polymers, CF_3-ROMP and OMe-ROMP, named for their chemical functionality, are compared to those of PIM-1, which is a current state-of-the-art polymer in gas separations. The resistance of CF_3-ROMP and OMe-ROMP to two common issues found in polymer-based membranes, CO_2-induced plasticization and physical aging, are also analyzed in detail.

Chapter 4 extends on the work presented in Chapter 3 by introducing the concept of uniform side-chain length. Previously, both CF_3-ROMP and OMe-ROMP were synthesized from oligomers with varying side-chain lengths. In this work, OMe-ROMP with uniform side chains of lengths ranging from $n = 2$ to $n = 5$ repeat units were synthesized and characterized. Brunauer–Emmett–Teller (BET) surface areas and pure-gas permeation tests were used to determine the effect of both side-chain length and dispersity on chain packing and gas transport properties, and the findings are discussed in this chapter. The effect of side-chain length on CO_2 plasticization resistance is also investigated.

Chapter 5 expands on the idea of side chain uniformity with additional studies that further probe free volume and plasticization resistance. Specifically, FFV and pure-gas CO_2 and CH_4 sorption measurements were conducted to determine the effect of side-chain length on chain packing. In addition, CO_2/CH_4 mixed-gas tests at varying compositions and pressures are also discussed in detail to further elucidate the unprecedented CO_2 plasticization resistance of ROMP polymers.

Lastly, Chapter 6 presents conclusions and recommendations for further studies on the various methods of free volume manipulation (FVM) discussed in this dissertation.

Chapter 2. Free volume manipulation of a 6FDA-HAB polyimide using a solid-state thermal protection/deprotection strategy

Reprinted with permission from **Lin, S.**; Joo, T.; Benedetti, F. M.; Chen, L. C.; Wu, A. X.; Mizrahi Rodriguez, K.; Qian, Q.; Doherty, C. M.; Smith, Z. P. Free Volume Manipulation of a 6FDA-HAB Polyimide Using a Solid-State Protection/Deprotection Strategy. *Polymer* **2021**, *212*, 123121.

Tert-butoxycarbonyl (t-BOC) is a thermally labile moiety that can be used to protect hydroxyl groups on polymers. In this study, t-BOC was appended onto a polyimide consisting of 2,2'-bis-(3,4-dicarboxyphenyl) hexafluoropropane dianhydride (6FDA) and 3,3'-dihydroxy-4,4'-diamino-biphenyl (HAB), after which the polymer was formed into self-standing films. Solid-state thermal treatments were performed to systematically remove t-BOC moieties to alter the physical packing structure and concomitant gas transport properties of the polymer. Despite performing deprotection reactions well below the glass transition temperature of 6FDA-HAB (~300 °C), this free volume manipulation (FVM) approach produced only subtle differences in polymer density, fractional free volume, average free volume element size, and gas transport properties relative to the unprotected polymer. While these findings suggest that thermally removing covalently bound functional groups from polymer films can be used to manipulate free volume and gas transport performance for glassy polymers, more robust polymer systems than linear polyimides are required to preserve the nascent free volume architecture generated from this approach.

2.1. Introduction

Polymer membranes have shown great promise for applications in energy-efficient gas separations, such as nitrogen enrichment, oxygen generation, and natural gas sweetening.[1,3,28] In order to be suitable for gas separations, membrane materials should be solution-processable, highly permeable, and selective.[3] A general strategy to improve permeability is to generate high free volume materials, and along these lines, "bottom up" approaches such as synthesizing rigid and contorted backbones have resulted in impressive advancements in materials performance.[23] Most notably, polymers of intrinsic microporosity (PIMs) have continued to surpass upper bound performance limits by incorporating bulky groups into the polymer backbone such as Tröger's base and triptycene.[23,49,88,93–96] Thermally rearranged (TR) polymers have also been used to tune free volume size and distribution.[97–99] An alternative strategy, however, is to use a "top down" approach to modify free volume from thermal decomposition of functional groups in the solid state.

In the 1980s and 1990s, researchers in the field of lithography began to investigate high glass transition temperature materials such as polyimides.[100] Of note, Omote et al. demonstrated that a polyimide (6FDA-AHHFP) that contained hydroxyl functional groups could be functionalized with tert-butoxycarbonyl (t-BOC), cast into a film, and then thermally- or UV-treated in the presence of an acid to remove t-BOC.[101] A more recent study by Fukumaru et al. demonstrated that thermally removing t-BOC groups from functionalized films of poly(p-phenylene benzobisoxazole) (PPBO) could generate porosity.[102] Merlet et al. also showed that the thermal removal of t-BOC from a poly(phenylquinoxaline) (PPQ) backbone could lead to the generation of free volume elements in the polymer matrix.[103,104] In the field of gas separations, Chung and coworkers have used this approach to generate free volume elements by thermally treating polyimide films to remove labile functional groups such as cyclodextrine[105–107] or various

saccharides.[108] Zhou et al. and Islam et al. both reported increases in permeability after thermally removing sulfonic acid groups from a polyimide at temperatures above the glass transition temperature of the polymer.[109,110] Maya et al. investigated in situ pyrolysis and thermal crosslinking of carboxylic acid functionality on a polyimide that led to changes in free volume distribution.[111] In addition, Martínez-Mercado et al. reported that short thermal treatments (i.e. < 3.5 h) at moderate temperatures (160–180 °C) of a poly(oxindole biphenylylene) film with a $–CH_2OH$ group led to higher gas permeabilities.[112] There are also indications of applying this "top down" approach in the patent literature.[113]

While the aforementioned studies indicate some success in post-synthetically generating free volume using thermal treatments, other studies report a decrease in free volume. In a study by Sánchez-García et al., it was found that thermally removing t-BOC from poly(oxindole biphenylylene) resulted in decreases in fractional free volume (FFV) and permeability, but an increase in selectivity.[114] Similar results were reported by Hernández-Martínez et al.[115] Notably, thermal treatment can accelerate densification of glassy polymer films, which leads to decreased FFV and permeability.[116–121] Therefore, a systematic study is needed to evaluate the role of deprotection in the glassy state and concomitant changes in morphology and transport without competing effects such as cross-linking, which are common features of other studies.[105–109,111,113,115]

In this study, we seek to extend the "top down" approach of free volume manipulation (FVM) to further understand the effects of thermal treatment on gas transport properties of glassy polymers with thermally labile functional groups. The model polymer selected for this study is a 6FDA (2,2'-bis-(3,4-dicarboxyphenyl) hexafluoropropane dianhydride)-based polyimide because these polymers have been studied as promising membrane materials for many years.[122–125] More

specifically, we investigated 6FDA-HAB,[126–129] which combines 6FDA with a diamine, HAB (3,3'-dihydroxy-4,4'-diamino-biphenyl), that contains hydroxyl groups that can react with di-tert-butyl-dicarbonate to generate a BOC-protected polyimide. BOC protection of 6FDA-HAB, as shown in **Scheme 2.1**, results in a polyimide that will henceforth be referred to as "6FDA-HAB-t-BOC".

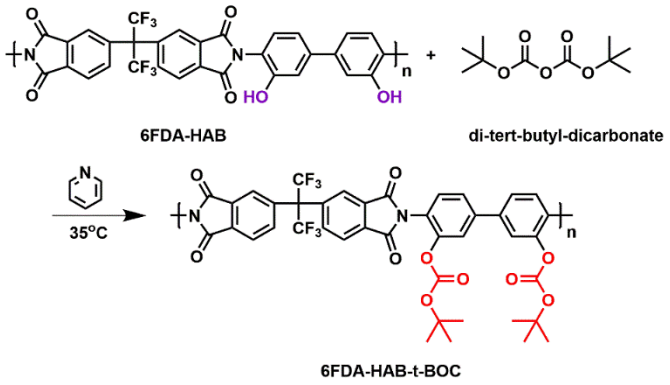

Scheme 2.1. BOC protection of 6FDA-HAB. The ortho-positioned functional groups are shown in purple for 6FDA-HAB and in red for 6FDA-HAB-t-BOC.

After being cast into a film, 6FDA-HAB-t-BOC can be thermally treated to deprotect the t-BOC group, as presented in **Scheme 2.2**. The thermal decomposition of t-BOC results in two gaseous products, CO_2 and isobutylene.[101,114] In this way, the original 6FDA-HAB chemical structure is recovered, but what remains is a polymer in an altered morphological state. By deprotecting 6FDA-HAB-t-BOC films using different treatment temperatures and times, this study seeks to systematically investigate the effects of treatment conditions on the free volume architecture of a linear polyimide.

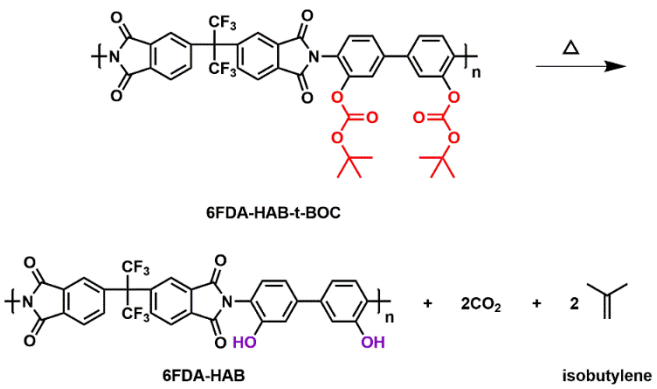

Scheme 2.2. BOC deprotection of 6FDA-HAB-t-BOC.

2.2. Experimental

2.2.1. Materials

The aromatic dianhydride, 2,2'-bis-(3,4-dicarboxyphenyl) hexafluoropropane dianhydride (6FDA, 99.86%), was purchased from *Chem-Impex International, Inc.* and underwent vacuum sublimation at 235 °C for approximately 1 h before use. The diamine, 3,3'-dihydroxy-4,4'-diamino-biphenyl (HAB, >99.0%), was purchased from *TCI Chemicals* and dried under vacuum at 60 °C overnight before use. Di-tert-butyl-dicarbonate (≥ 99%) was purchased from *Sigma-Aldrich* and used as received. Anhydrous 1-methyl-2-pyrrolidinone (NMP, 99.5%), anhydrous o-dichlorobenzene (o-DCB, 99%), methanol (≥ 99.9%), pyridine (99.9%), dimethylacetamide (DMAc, ≥ 99.5%), N,N-dimethylformamide (≥ 99.9%), and n-heptane (≥ 96%) were obtained from *Sigma-Aldrich* and used as received. Chloroform (≥ 99.8%) was purchased from *Macron Fine Chemicals* and used as received. Deuterated dimethyl sulfoxide (DMSO-d_6, 99.9%) was purchased from *Cambridge Isotope Laboratories, Inc.* and used as received.

2.2.2. Synthesis of 6FDA-HAB polyimide and BOC protection

A three-neck flask fitted with an overhead mechanical stirrer was purged with nitrogen (*Airgas,* 99.999%) for 30 min to remove water vapor. HAB (8.008 mmol) and 30 mL of anhydrous NMP were added to the flask and stirred to dissolution. An equimolar amount of 6FDA (8.008 mmol) and an additional 20 mL of anhydrous NMP were added to the flask to generate a ~10.6 w/v% solution. The solution was then left stirring overnight, forming a viscous poly(amic acid).

Thermal imidization in solution was used to form a polyimide from the poly(amic acid). In this procedure, 12.5 mL of o-DCB was added to the reaction flask to form an ~8.5 w/v% solution. A reverse Dean-Stark trap with an overhead air condenser was then used to assist in the removal of water vapor with o-DCB acting as an azeotropic agent. The solution was heated to 180 °C for 24 h to convert the poly(amic acid) to a polyimide.

After imidization, the polymer was precipitated from the reaction solution using methanol that was stirring in a blender to produce a light brown and fibrous precipitate. In order to extract solvent, the precipitated 6FDA-HAB polyimide was filtered and rinsed with methanol before stirring in fresh methanol for an additional 24 h. The polyimide was filtered again, rinsed with fresh methanol for a second time, and stirred in fresh methanol for another 24 h. This solvent extraction procedure was performed one additional time. The polyimide was then placed on a glass dish and dried under full vacuum at 200 °C and 225 °C for 24 h and 48 h, respectively.

To generate 6FDA-HAB-t-BOC, an equimolar amount of pyridine (which acted as a catalyst for BOC protection) and di-tert-butyl-dicarbonate (24.025 mmol) was added directly to the reaction solution after imidization. The reaction was allowed to proceed for 24 h at 35 °C. The polymer was then precipitated (as a light tan precipitate) and washed in an identical fashion to that

of 6FDA-HAB. After the last methanol wash, 6FDA-HAB-t-BOC was placed on a glass dish and left to dry at room temperature in a chemical fumehood for 48 h.

2.2.3. Film fabrication and thermal treatment of 6FDA-HAB-t-BOC films

6FDA-HAB was dissolved in DMAc (1 w/v%) for 24 h at 90 °C, similar to a previously reported procedure.[98] The solution was then filtered through a 5 μm Whatman PTFE syringe filter (*GE Healthcare Life Sciences*) onto a 5 cm diameter flat-bottomed glass dish and heated at 60 °C for 48 h under –10 inHg (–34 kPa) vacuum, following a similarly reported procedure.[98] During this process, vaporized solvent from the headspace of the vacuum oven was occasionally removed by pulling vacuum while opening the vacuum pump vent to maintain an oven pressure of –10 inHg (–34 kPa). Solvent was collected using a solvent trap submerged in liquid nitrogen. The formed films were then exposed to full vacuum for 1 h and then heated at 200 °C and 225 °C for 24 h and 48 h, respectively, to remove residual solvent. The 6FDA-HAB films, which were 10–15 μm in thickness, were removed from the glass dish by submersion in deionized water for 10 min.

Since the boiling point of DMAc is 165 °C, which is above the reported BOC deprotection temperature of 150 °C, a solvent with a lower boiling point of 61 °C, chloroform (3 w/v%), was required to cast 6FDA-HAB-t-BOC so that the solvent could subsequently be removed without BOC deprotection. It should be noted that 6FDA-HAB was found to be insoluble in solvents with boiling points lower than that of DMAc. The 6FDA-HAB-t-BOC solution was filtered through a 0.45 μm PTFE syringe filter (*VWR, 28145-497*) onto a 5 cm diameter flat-bottomed glass dish. The glass dish was covered with aluminum foil and another glass dish as a cover, thereby enabling film formation via slow solvent evaporation inside a chemical fumehood for 72 h. The films, which

were 10–35 μm in thickness, were removed from the glass dish by submersion in deionized water for 10 min, and the film was heated at 90 °C under full vacuum for 16 h to remove residual solvent.

Three treatment temperatures were selected to study the effects of temperature on BOC deprotection and the resulting polymer properties. 6FDA-HAB-t-BOC films were held at 130 °C, 140 °C, or 160 °C using a forced air convection oven with a temperature accuracy of ±1 °C (*Lab Safety Supply*, #32EZ25). Since 130 °C and 140 °C are both below the prominent deprotection temperature of t-BOC, these experiments allowed for slower deprotection. The hold times considered at both of these temperatures were identical. However, because 160 °C is above the prominent deprotection temperature of t-BOC, hold times considered for this temperature were shorter. The oven was pre-heated to the designated temperature before placing a 6FDA-HAB-t-BOC film onto a flat glass dish inside the oven. Thermal treatment protocols are shown in **Table 2.1**, and samples are thus named according to their treatment protocol (i.e., samples treated at 130 °C for 1 h are labeled as "t-BOC-130-1h").

Table 2.1. Thermal treatment protocols for 6FDA-HAB-t-BOC films.

Temperature (°C)	Hold times
130	1 h, 2 h, 16 h
140	1 h, 2 h, 16 h
160	5 min, 15 min, 16 h

2.2.4. Characterization

^{1}H nuclear magnetic resonance (NMR) spectroscopy was performed using a *Bruker Avance Neo402* spectrometer to confirm the chemical structures of all samples in this study. 6FDA-HAB and 6FDA-HAB-t-BOC, in their powder form, as well as 6FDA-HAB-t-BOC and thermally-

treated 6FDA-HAB-t-BOC films, were dissolved in DMSO-d_6 (10 w/v%). Percent conversion (%) for each sample undergoing thermal treatment was determined by comparing relative peak integrations of BOC to hydroxyl functional groups. Percent conversion and the corresponding uncertainty are reported as the average and standard deviation, respectively, of at least 3 measurements. Heteronuclear single quantum correlation (HSQC) was run on a *Bruker Avance Neo500* spectrometer for t-BOC-130-1h dissolved in DMSO-d_6 (10 w/v%) to confirm the presence of isobutylene. A ^{1}H NMR spectrum of a solution of DMSO-d_6 and dosed-in isobutylene gas (*Airgas*, ≥ 99%) was also collected to further confirm isobutylene presence.

The molecular weight of 6FDA-HAB was determined using a *Waters* gel permeation chromatograph with a polystyrene (PS) reference and a mobile phase of DMF with 0.01 M lithium bromide. Chloroform GPC was performed on 6FDA-HAB-t-BOC using a *Tosoh EcoSEC HLC-8320* gel permeation chromatograph with *Dual TSKgel SuperH3000* columns, a PS reference, and a mobile phase of chloroform with 0.75% ethanol preservative.

Thermogravimetric analysis (TGA) was performed on all samples using a *TA Instruments TGA550*. Samples were heated from room temperature at a rate of 10 °C/min up to 800 °C in a nitrogen atmosphere. Nitrogen gas was flushed at a flow rate of 20 mL/min over the TGA balance and 40 mL/min in the sample chamber. TGA scans for 6FDA-HAB and thermally treated samples were normalized by their weight percent at 100 °C to eliminate the mass loss of atmospheric moisture that can strongly associate with polar groups in the polyimides.

The glass transition temperature (T_g) of 6FDA-HAB and 6FDA-HAB-t-BOC films was measured using a *TA Instruments DSC250* differential scanning calorimeter (DSC). Samples were heated at 10 °C/min from 25 °C to 350 °C under a nitrogen atmosphere with a flowrate of 50

mL/min. Three scans were taken for each sample, and the T_g was taken as the midpoint in the step change in heat capacity of the third scan.

Fourier transform infrared spectroscopy (FTIR) in attenuated total reflection (ATR) mode was performed using a *Bruker ALPHA FT-IR Spectrometer*. The spectra have a resolution of 4 cm^{-1}, and 256 scans per sample were performed in the range of 400–4000 cm^{-1}.

Density was measured using a *Mettler Toledo* density measurement kit (*ME-DNY-4*). Because of its slow uptake in polyimide samples, n-heptane was used as the buoyant liquid [43]. The density and corresponding uncertainty for each sample were taken as the average and standard deviation, respectively, of at least 3 measurements.

Positron annihilation lifetime spectroscopy (PALS) was performed on an automated *EG&G ORTEC* fast-fast coincidence system under vacuum at room temperature. During a PALS experiment, positrons from a radioisotope source enter the material and will either annihilate in the presence of free electrons or form a positronium (Ps) atom.[75] The Ps atom can exist either as a parapositronium (pPs) or an orthopositronium (oPs) atom.[75] Since Ps atoms can only form in areas of low electron density such as within the free volume elements of amorphous polymers,[106,130–132] PALS can be used to determine the average free volume element size from correlations with the oPs lifetime. To conduct a PALS experiment, a Mylar envelope containing a ^{22}Na radioisotope source was placed in between two stacks of polymer films, and the envelope-film stack was wrapped in aluminum foil. At least 5 files of 4.5×10^6 integrated counts per file were collected for each sample, and data was analyzed with a three-component model using LT9.[133] The three components consisted of the pPs atom, the free positron, and the oPs atom.[75] The lifetime of the pPs atom was fixed at τ_1 = 0.125 ns,[78] while the lifetimes of the free positron (τ_2 ~ 0.4 ns) and oPs atom (τ_3), as well as the intensities (I) of all three components, were fit using least squares

optimization by the LT9 program. The error for τ_3 for each sample was taken as the standard deviation of the τ_3 values calculated from each file. The average size of free volume elements was calculated using a spherical assumption for free volume shape and the Tao-Eldrup equation:[78,79]

$$\tau_3 = \frac{1}{2}\left[1 - \frac{R}{R_0} + \frac{1}{2\pi} sin\left(\frac{2\pi R}{R_0}\right)\right]^{-1} \quad (2.1)$$

in which R is the radius of the free volume element, ΔR is an empirical parameter determined to be 1.66 Å, and $R_0 = R + \Delta R$.[75,76] Since low intensities were found for some samples, which may indicate oPs inhibition from the polar hydroxyl functionality,[78,80] we do not report calculated free volume size distributions.

2.2.5. Pure-gas permeability measurements

Pure-gas permeabilities were evaluated at ~1 bar (100 kPa) for He, H_2, CH_4, N_2, O_2, and CO_2 at 35 °C for each sample using an automated constant-volume, variable-pressure system from *Maxwell Robotics*. All gases were ultra-high purity and purchased from *Airgas*. Cut films of approximately 1 cm^2 were placed on top of a hole in the center of a circular brass disk and secured using epoxy (*Devcon 5 min Epoxy*), which was left to cure for at least 30 min. The samples were then sealed in a stainless steel permeation cell (*Millipore*), which was immersed in a water bath that was temperature controlled by an immersion circulator (*ThermoFisher SC150L*). Before testing permeation, the testing chamber was dosed with ~2 bar (200 kPa) of helium gas to remove dissolved atmospheric gases. The sample was then held under vacuum at 35 °C for 8 h. Before switching to a new permeating gas, samples were again dosed with ~2 bar of helium and held under vacuum for at least six time lag-equivalents. Each sample was tested at least twice to confirm reproducibility.

Pure-gas permeability (P) was calculated using the following equation:

$$P = \frac{V_d l}{p_2 ART}\left[\left(\frac{dp}{dt}\right)_{ss} - \left(\frac{dp}{dt}\right)_{leak}\right] \quad (2.2)$$

where V_d is the downstream volume, l is the film thickness, p_2 is the upstream pressure, A is the area of film exposed to the gas, R is the ideal gas constant, T is the absolute experimental temperature, $\left(\frac{dp}{dt}\right)_{ss}$ is the rate of pressure rise in the permeate at steady state, and $\left(\frac{dp}{dt}\right)_{leak}$ is the leak rate.[42] The ideal gas selectivity ($\alpha_{i,j}$) was taken to be the ratio of the pure-gas permeabilities of the more permeable gas, i, to that of the less permeable gas, j (i.e., $\frac{P_i}{P_j}$). Diffusion coefficients for each gas were determined using the time-lag method, $D = \frac{l^2}{6\theta}$, in which θ is the time lag.[134] Sorption coefficients were calculated using the sorption–diffusion model ($S = \frac{P}{D}$).[41] Error bars for permeability, diffusion coefficients, and sorption coefficients were determined by error propagation.[135] Time-lag values obtained for He and H_2 were within the resolution of acquisition time (i.e., 1–2 s) of the permeation systems, and thus could not be accurately determined. We therefore only include diffusion and sorption coefficients calculated from the time-lag method for N_2, O_2, CH_4, and CO_2, which all yielded time-lags greater than 6.2 s, which is significantly longer than the acquisition time of the permeation system.

2.3. Results and Discussion

2.3.1. Characterization of 6FDA-HAB polyimide and BOC-protection

Fully assigned ^{1}H NMR spectra of both 6FDA-HAB and 6FDA-HAB-t-BOC powder samples are reported in **Section A.1**. In the ^{1}H NMR spectrum of 6FDA-HAB-t-BOC, there is a singlet at 1.25 ppm, which corresponds to the protons in the t-BOC functional group. The presence of this singlet

and the absence of a hydroxyl proton singlet at 10.08 ppm indicate successful BOC protection. GPC analysis indicated that BOC protection had a minimal impact on molecular weight (**Section A.1**).

TGA scans of 6FDA-HAB and 6FDA-HAB-t-BOC powder are shown in **Figure 2.1**. In the TGA scan of 6FDA-HAB, two distinct regions of mass loss are clearly observed. The first region, which begins at approximately 400 °C, is attributed to thermal rearrangement of the polyimide (labeled as "TR" in **Figure 2.1**), while the second region, which begins at approximately 500 °C, is attributed to thermal degradation.[97,98] The process of thermal rearrangement, a decarboxylation process, leads to structural changes in polyimides that contain ortho-positioned functional groups, such as 6FDA-HAB.[97] In the TGA scan of 6FDA-HAB-t-BOC, a third distinct region of mass loss is clearly observed starting at approximately 150 °C. This mass loss, which was determined to be 25.9 wt%, is associated with the removal of t-BOC from the polymer backbone.[101,114,115] This finding correlates well with the theoretical weight percent of t-BOC on the polymer backbone, which is 24.8 wt%. The stable sample weight across a broad temperature range between BOC deprotection and the TR region of the polyimide indicates that these two processes occur independently, which makes this system ideal for exclusively studying the effects of t-BOC removal without competing chemical reactions.

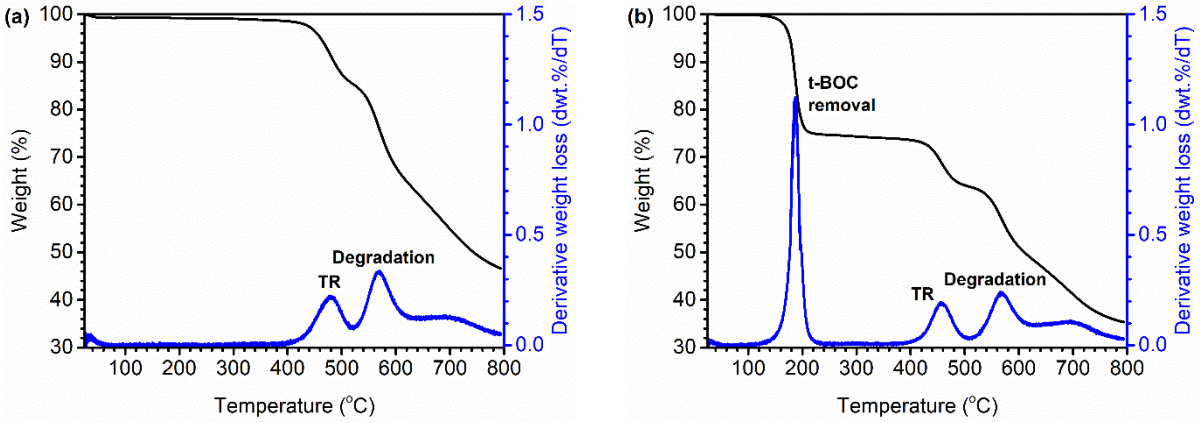

Figure 2.1. TGA scans of (a) 6FDA-HAB and (b) 6FDA-HAB-t-BOC powder. Distinct regions of mass loss are labeled accordingly.

From DSC, the T_g of 6FDA-HAB was found to be approximately 300 °C, while the T_g of the deprotected 6FDA-HAB-t-BOC sample was approximately 306 °C (**Section A.1**). Given the rather broad temperature range for these transitions, the T_g values between the two samples are roughly equivalent. Guo et al. previously reported differences in T_g for acetate-functionalized variants 6FDA-HAB,[128] but acetate moieties are more thermally stable than t-BOC, and hence, are not removed below the polymer T_g. Thus, for our work, similar values of T_g for 6FDA-HAB and the deprotected 6FDA-HAB-t-BOC are expected because both samples have an identical chemical structure.

2.3.2. Thermal treatment of 6FDA-HAB-t-BOC films

Optically transparent films of 6FDA-HAB, 6FDA-HAB-t-BOC, and thermally treated 6FDA-HAB-t-BOC are presented in **Section A.1**. Upon heating, the optically clear 6FDA-HAB-t-BOC turns slightly yellow, indicating a shift in color that more closely matches that of 6FDA-HAB. FTIR measurements also indicated that thermal treatments resulted in the conversion of 6FDA-HAB-t-BOC to 6FDA-HAB (**Section A.1**).

^{1}H NMR was used to track the extent of deprotection for each thermal treatment condition, as shown in **Figure 2.2**. Spectra for 6FDA-HAB and 6FDA-HAB-t-BOC are included for reference. It is important to note that the 6FDA-HAB-t-BOC spectrum was obtained from films that had previously been heated at 90 °C under full vacuum to remove solvent. All ^{1}H NMR spectra shown in **Figure 2.2** were normalized by the proton in the polymer backbone labeled "B" in **Figure A.1**. The ratios of peak integrations were used to determine the percent conversion of 6FDA-HAB-t-BOC to 6FDA-HAB, and these results are tabulated in **Table 2.2**. From this analysis, we can confirm that film formation and solvent removal for 6FDA-HAB-t-BOC resulted in minimal deprotection, as a small peak at 10.08 ppm can be seen in the ^{1}H NMR spectrum of the 6FDA-HAB-t-BOC film, indicating approximately 4% ± 0.5% hydroxyl functionality. The concomitant decrease in the t-BOC proton singlet peak at 1.25 ppm and the increase in the hydroxyl proton singlet peak at 10.08 ppm indicate that more t-BOC was removed with increasing time at a set temperature. As expected, for 1 or 2 h hold times, thermal treatments at 140 °C removed similar or more t-BOC than thermal treatments at 130 °C. For thermal treatments of 16 h, conversion was always approximately 95%, regardless of temperature, indicating a conversion limit for these samples.

Two additional peaks were occasionally observed in NMR spectra at 1.69 ppm and 4.66 ppm, which are associated with isobutylene. While the thermal decomposition products of t-BOC are CO_2 and isobutylene, the timescales of diffusion for these two molecules are vastly different. Time-lag experiments, which will be presented later, suggest that CO_2 diffuses completely from the film during thermal treatment, while these ^{1}H NMR results show the presence of some isobutylene after deprotection. HSQC spectroscopy was performed on t-BOC-130-1h to confirm the presence of isobutylene (**Section A.2**). ^{1}H NMR was also performed on a solution of

isobutylene gas dosed in DMSO-d_6 to further confirm the presence of isobutylene in thermally treated samples (**Section A.2**). Interestingly, the intensities of the isobutylene peaks decrease at longer conversion times and become negligible after 16 h treatments at each temperature because enough time was provided for isobutylene molecules to diffuse out of the film. An estimation of isobutylene content (**Section A.3**) revealed that only trace amounts of isobutylene remained in some samples prior to characterization. Within the uncertainty of our analysis procedure (±1%), no detectable isobutylene remained in six of our nine thermally treated samples prior to permeation testing. For the three samples with detectable isobutylene content, the highest content was about 3 wt% for t-BOC-160-5min. Therefore, experiments were run without further treatment to avoid complications that could result from physical aging and thermal annealing.

Table 2.2. Percent conversion of 6FDA-HAB-t-BOC films that underwent thermal treatment, as determined from ^{1}H NMR.

Treatment Temperature (°C)	Hold time	Percent conversion (%)
130	1 h	88.5 ± 0.5
	2 h	93 ± 1
	16 h	95.7 ± 0.9
140	1 h	93 ± 1
	2 h	95 ± 1
	16 h	95.5 ± 0.1
160	5 min	87 ± 2
	15 min	95.0 ± 0.5
	16 h	94 ± 1

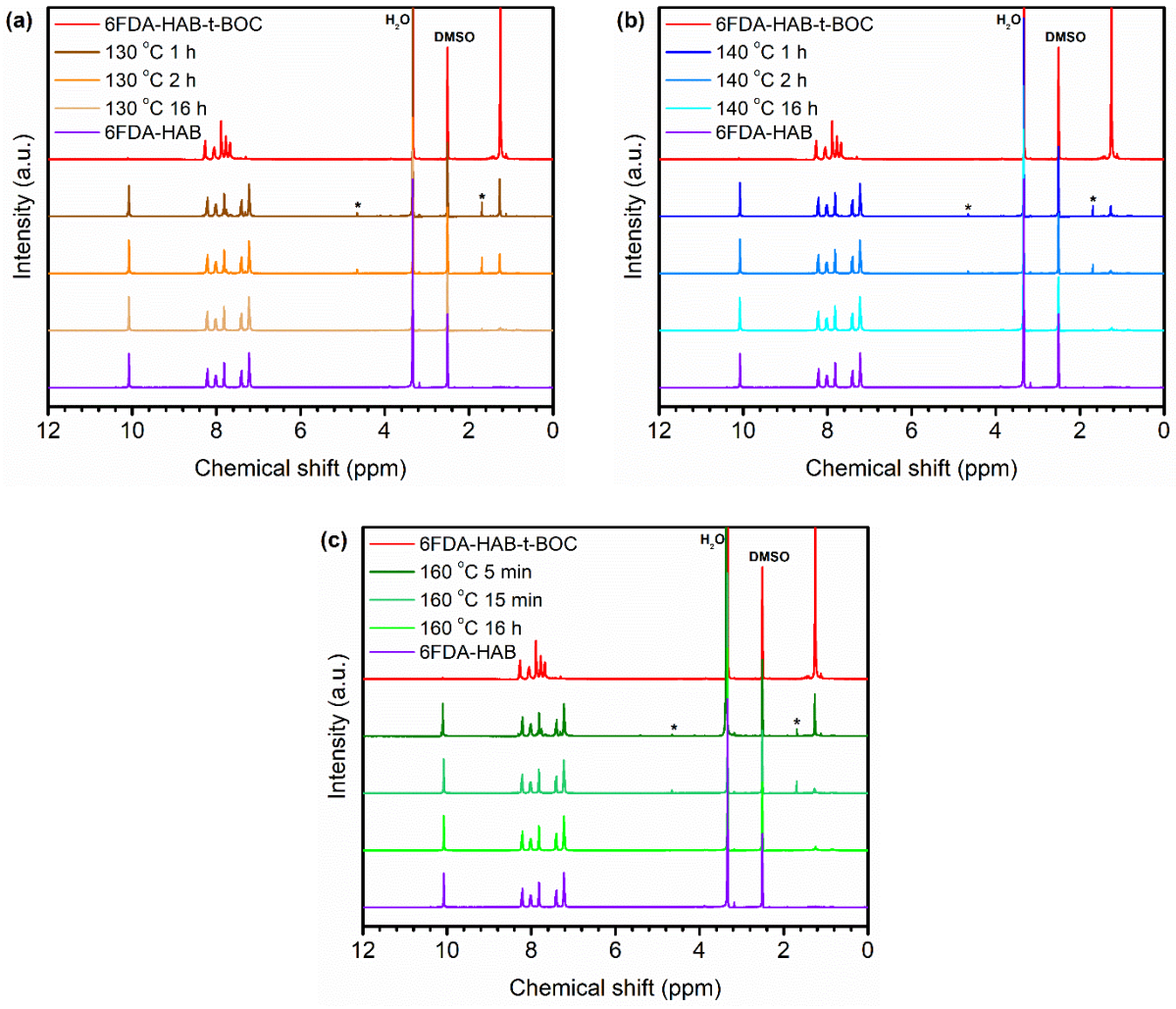

Figure 2.2. ^{1}H NMR spectra for 6FDA-HAB-t-BOC films undergoing thermal treatments at (a) 130 °C, (b) 140 °C, and (c) 160 °C. Peaks that are labeled with a "*****" are associated with the protons in isobutylene. ^{1}H NMR spectra of 6FDA-HAB and 6FDA-HAB-t-BOC are added for reference.

TGA scans for all films are shown in **Figure 2.3**. For all treatment temperatures, longer treatment times led to more t-BOC being removed from the polymer backbone, which is evident in the smaller decrease in weight percentage starting at 150 °C. In contrast to the TGA profile for the 6FDA-HAB-t-BOC powder shown in **Figure 2.1**, TGA scans for the 6FDA-HAB-t-BOC films showed a gradual mass loss over extended temperature ranges well beyond 150 °C. This finding

suggests that the higher accessible surface area of the powders reduces the time required for diffusion of gaseous byproducts. While CO_2 is a smaller gas and thus can diffuse more readily, isobutylene is significantly larger and will diffuse more slowly. Therefore, the slow decrease in weight percent as the sample is heated after t-BOC removal until the beginning of thermal rearrangement at approximately 400 °C can be predominantly attributed to slow diffusion of isobutylene. This slow decrease in weight percent is present in all thermally treated samples, and for this reason, it is challenging to accurately quantify the exact amount of t-BOC remaining on the polymer backbone using only TGA.

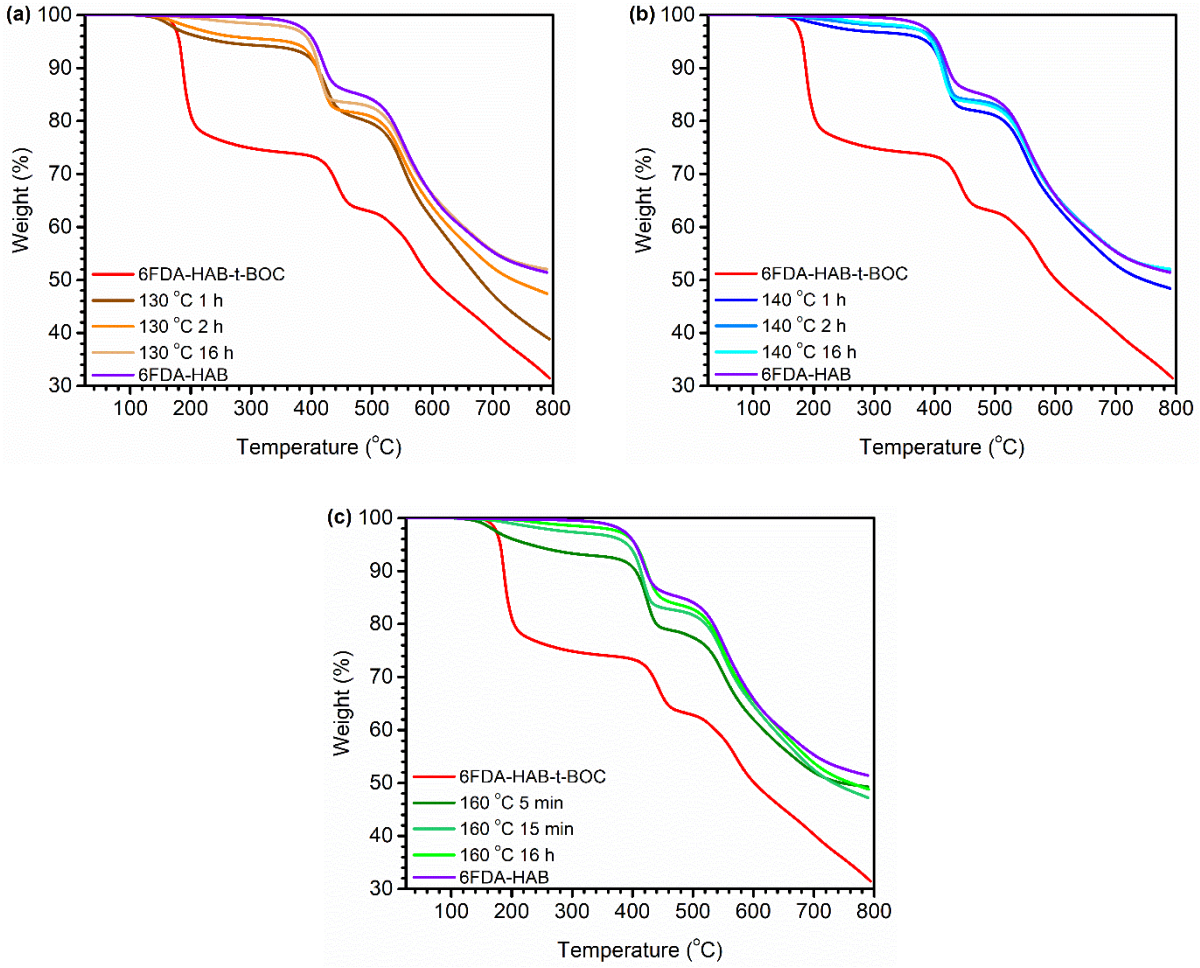

Figure 2.3. TGA scans for 6FDA-HAB and 6FDA-HAB-t-BOC reference samples, and 6FDA-HAB-t-BOC films that had previously undergone thermal treatments at (a) 130 °C, (b) 140 °C, and (c) 160 °C.

2.3.3. Effect of sample treatment on polymer chain packing

Fractional free volume (FFV) was calculated using the following equation:

$$FFV = \frac{V - 1.3V_w}{V} \tag{2.3}$$

where V is the molar volume of the polymer, and V_w is the van der Waals volume of the polymer determined using the group contribution method originally developed by Bondi.[71–73] For thermally

treated 6FDA-HAB-t-BOC samples, van der Waals volumes were estimated as the molar arithmetic sum of t-BOC and hydroxyl structural units that remained on each sample:

$$V_w = x_1 V_{w1} + x_2 V_{w2} \tag{2.4}$$

in which x_1 and x_2 are mole fractions and V_{w1} and V_{w2} are van der Waals volumes (1: 6FDA-HAB-t-BOC, 2: 6FDA-HAB), essentially treating the thermally-treated samples as a co-polymer.[136] The calculated FFV, oPs lifetimes (τ_3) and intensities (I_3), and average free volume element radii (R) calculated from the Tao-Eldrup equation are presented in **Table 2.3**.

Table 2.3. Density, fractional free volume (FFV), PALS results (τ_3 and I_3), and average free volume element radius (R) for 6FDA-HAB, 6FDA-HAB-t-BOC, and 6FDA-HAB-t-BOC after various thermal treatments.

Sample	Treatment Temperature (°C)	Hold time	Density (g/cm^3)	*FFV*	τ_3 (ns)	I_3 (%)	*R* (Å)
6FDA-HAB	n/a	n/a	1.50 ± 0.04	0.11 ± 0.03	2.35 ± 0.04	2.0 ± 0.1	3.15 ± 0.03
6FDA-HAB-t-BOC	n/a	n/a	1.32 ± 0.02	0.18 ± 0.01	2.74 ± 0.02	9.82 ± 0.07	3.45 ± 0.01
6FDA-HAB-t-BOC	130	1 h	1.39 ± 0.02	0.17 ± 0.01	2.68 ± 0.03	8.53 ± 0.08	3.41 ± 0.02
		2 h	1.39 ± 0.02	0.17 ± 0.01	2.66 ± 0.02	7.08 ± 0.05	3.38 ± 0.02
		16 h	1.48 ± 0.05	0.12 ± 0.03	2.89 ± 0.05	3.04 ± 0.05	3.54 ± 0.03
6FDA-HAB-t-BOC	140	1 h	1.50 ± 0.02	0.11 ± 0.01	2.63 ± 0.03	6.72 ± 0.07	3.37 ± 0.02
		2 h	1.49 ± 0.05	0.12 ± 0.03	2.62 ± 0.02	5.17 ± 0.05	3.36 ± 0.01
		16 h	1.47 ± 0.05	0.13 ± 0.03	2.75 ± 0.05	2.59 ± 0.07	3.46 ± 0.04
6FDA-HAB-t-BOC	160	5 min	1.42 ± 0.02	0.15 ± 0.01	2.56 ± 0.01	8.06 ± 0.08	3.32 ± 0.01
		15 min	1.515 ± 0.003	0.101 ± 0.002	2.53 ± 0.04	6.7 ± 0.1	3.29 ± 0.03
		16 h	1.54 ± 0.04	0.09 ± 0.02	2.71 ± 0.05	3.6 ± 0.1	3.43 ± 0.04

Graphical comparisons of percent conversion from 6FDA-HAB-t-BOC to 6FDA-HAB versus FFV are depicted in **Figure 2.4a**. There is a significant amount of scatter in this plot, indicating a poor correlation between FFV and percent conversion, but a few salient observations can be made. As expected, the FFV of 6FDA-HAB-t-BOC is higher than that of 6FDA-HAB due to the incorporation of t-BOC functional groups onto the polymer backbone. The bulkiness of this group is expected to reduce the efficiency of polymer chain packing in the film state, and the

elimination of hydrogen bonding after protection of hydroxyl functional groups would likewise be expected to decrease polymer–polymer interactions. Similar observations between functionalized and non-functionalized polymer films have been reported in other studies.[114,129,137] For example, in a study by Sanders et al., larger ortho-positioned groups appended to 6FDA-HAB led to disrupted chain packing, lower density, and higher FFV values.[129] A hydroxyl functional 6FDA-HAB sample had an FFV value of 13% ± 1%, but upon functionalization with acetate, propanoate, or pivalate, FFV increased to 14.6% ± 0.5%, 15.0% ± 0.7%, and 18.1% ± 0.8%, respectively.[129] We observed similar trends, including an FFV value of 18% ± 1% for 6FDA-HAB-t-BOC and 11% ± 3% for 6FDA-HAB.

A weak negative correlation was observed between FFV and percent conversion, implying that polymer chains are densifying through viscous conformational rearrangement to occupy the newly formed free volume elements. At similar conversions, samples treated at 130 °C generally exhibited higher FFV than samples treated at 140 °C and 160 °C. While t-BOC-160-5min and t-BOC-130-1h had similar conversions, the FFV value of t-BOC-130-1h was higher and had a comparable value to that of 6FDA-HAB-t-BOC. This finding reveals that higher temperatures induce more chain mobility and faster kinetics for the reorganization of the packed polymer structure, accelerating the reduction in FFV. While FFV was unchanged between the BOC protected sample and the samples treated at 130 °C for either 1 or 2 h, there were no indications of increased FFV during the porogen removal process.

Holding samples for 16 h at all three temperatures resulted in identical FFV values within the uncertainty of our analysis procedure. As previously noted in **Table 2.2**, these samples all had identical conversions, and when compared to 6FDA-HAB, all samples had the same values of FFV.

These findings indicate that the ensemble of packing structures accessible to these three samples average to approximately the same FFV as that determined for 6FDA-HAB.

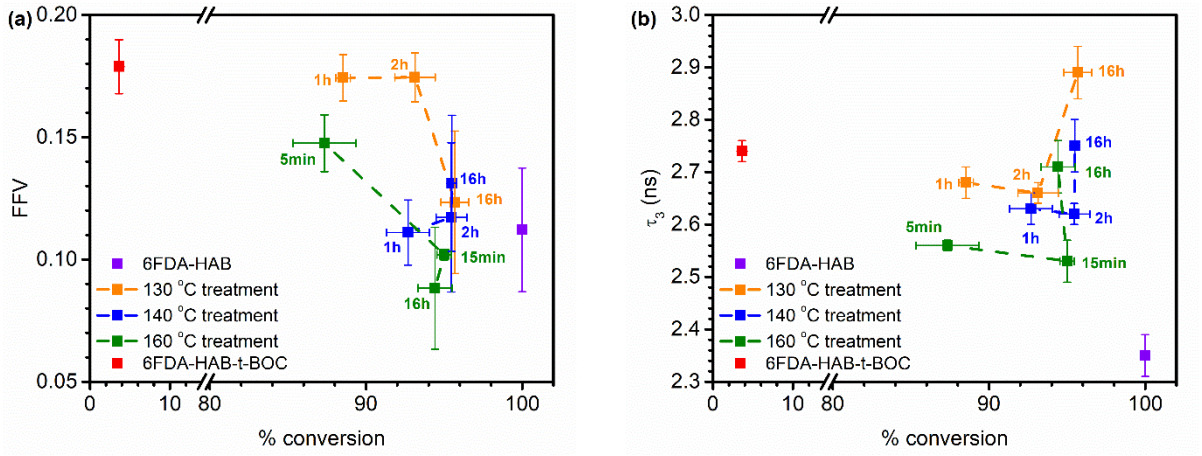

Figure 2.4. Percent conversion (from 6FDA-HAB-t-BOC to 6FDA-HAB) compared to (a) FFV and (b) τ_3 for all samples in this study. Thermally treated samples are labeled with their treatment times. Dashed lines have been added to guide the eye and are not representative of a predictive relationship.

While useful in estimating many bulk properties of polymers, because group contribution methods are compiled by averaging massive datasets, molecular-level details are often obscured by this approach.[73,138] Therefore, conclusions drawn from **Figure 2.4a** in regards to changes in polymer structure should be taken with caution, as FFV measurements from group contribution methods provide no direct indication of the free volume distribution. Instead, we used PALS to more accurately track changes in free volume and determine if trends derived from group contribution methods were relevant for analyzing this series of polymers. While certain high free volume polymers, such as PIMs, can be fit to PALS data using bimodal free volume size distributions,[99,139–141] a unimodal fit was found to most accurately represent all polymers in this

study, implying that deprotection did not create discrete free volume elements of significant intensity.

A graphical comparison of percent conversion versus τ_3 is presented in **Figure 2.4b**. Consistent with our FFV findings, PALS revealed that 6FDA-HAB displayed a smaller average τ_3 than that of 6FDA-HAB-t-BOC. In general, higher temperatures and longer treatment times resulted in smaller τ_3 values, and hence, reduced free volume element sizes, which aligns with our FFV interpretation. However, one notable difference was observed for τ_3 values for all 16 h treatments, regardless of treatment temperatures considered. Of note, t-BOC-130-16h contains free volume elements that are larger than those of 6FDA-HAB-t-BOC. This counterintuitive result is in contrast to trends derived from FFV and requires further investigation.

Three major possibilities exist to explain these findings. The first relates to slow diffusion of t-BOC decomposition products, the second relates to casting solvents and thermal conditioning, and the third relates to evidence of successful, albeit limited evidence of free volume manipulation. The first two possibilities are discussed here, and the third possibility is discussed in Section 2.3.4. As previously described, trace amounts of isobutylene are formed in the 6FDA-HAB-t-BOC polymer films as they undergo thermal deprotection. Although the presence of isobutylene is no longer detectable by NMR for many of our samples, it is possible that trace amounts of isobutylene conceal some limited anisotropy in the free volume packing structure of our polymers. Olefinic species, which are electron-rich, are known to inhibit positronium formation,[76] so small contributions of trapped isobutylene could inhibit the clear detection of porogen features. However, we expect these considerations to be minimal in our samples since any residual isobutylene remaining in each film would be vastly insufficient to occupy all of the porogen domains, but such

an effect could explain the slight increase in τ_3 values for all of the 16 h thermally treated samples, which would correspondingly have the lowest content of isobutylene.

The second possibility relates to casting solvents and thermal conditioning. For casting solvents, this consideration only applies for comparisons with 6FDA-HAB because this polymer could only be cast from high boiling point solvents, as discussed previously. All comparisons between deprotected analogues of 6FDA-HAB-t-BOC are fully self-consistent, since all of these samples underwent identical solvent removal procedures. Along these lines, changes in polymer packing structure due to different casting solvents have been noted previously, especially for high free volume polymers,[142] but the 16 h treatments were done consistently to 6FDA-HAB-t-BOC samples cast from identical solvents. Therefore, it is unlikely that the differences in τ_3 values could be attributed to solvent effects. Instead, these differences are much more likely related to slight differences in thermal annealing temperatures, as will be discussed in Section 2.3.4.

Despite the weak correlations in **Figure 2.4a** and **2.4b**, several conclusions can be made about applying the porogen approach to linear polyimides that have high T_g. Most importantly, exposure to elevated temperatures can sufficiently induce mobility of the 6FDA-HAB polymer matrix, causing both FFV and average free volume element size to decrease with increasing treatment temperature. As t-BOC is thermally removed, the regeneration of hydroxyl functional groups further induces matrix densification, as new opportunities for hydrogen bonding result.[60,143] Moreover, polymer relaxation processes appear to occur well below the T_g. Comer et al. have demonstrated the presence of sub-T_g transitions occurring for 6FDA-HAB around 150 °C,[144] so while long-range cooperative motion is suppressed below the T_g, these sub-T_g motions may result in the collapse of the newly created porogen architecture. In view of these complexities, while we conclude that the removal of t-BOC generates free volume elements, the generation of such free

volume elements drives the polymer further away from its theoretical chain packing equilibrium structure, which accelerates physical aging according to the Struik Model,[66] leading to the reorganization of polymer chains upon t-BOC removal induced by high temperature.

2.3.4. Effect of sample treatment on gas transport properties

The pure-gas permeabilities of He, H_2, CH_4, N_2, O_2, and CO_2 for all polymer films are tabulated in **Table 2.4**. Diffusion and sorption coefficients are also summarized in **Table 2.4**, and permselectivities of select gas pairs are shown in **Table 2.5**. A graphical comparison of percent conversion versus permeability for all six gases is presented in Figure S7. Analogous plots for diffusion and sorption coefficients for N_2, O_2, CH_4, and CO_2 are shown in Figures S8 and S9, respectively. Plots of diffusion coefficient versus effective diameter squared and sorption coefficient versus critical temperature for all samples are also included in Figures S10 and S11, respectively. Diffusion coefficients in all samples increased as follows: $D(CH_4) < D(CO_2) \sim D(N_2) < D(O_2)$, which follows the inverse order of effective diameter ((3.44 Å) O_2 < (3.63 Å) CO_2 ~ (3.66 Å) N_2 < (3.81 Å) CH_4), as expected for glassy polymers. Gas sorption coefficients in all samples increased with increasing critical temperatures of penetrant molecules as follows: $S(N_2) < S(O_2) < S(CH_4) < S(CO_2)$, which follows gas sorption trends for other polymers.[145]

Table 2.4. Pure-gas permeabilities (*P*), diffusion coefficients (*D*), and solubility coefficients (*S*) for 6FDA-HAB, 6FDA-HAB-t-BOC, and 6FDA-HAB-t-BOC after various thermal treatments

Sample	Treatment Temperature (°C)	Hold time		He	H_2	N_2	O_2	CH_4	CO_2
6FDA-HAB	n/a	n/a	*P*	53 ± 4	42 ± 3	0.37 ± 0.03	2.6 ± 0.2	0.17 ± 0.01	12.3 ± 0.9
			D	/	/	5.9 ± 0.8	28 ± 4	0.70 ± 0.05	6.5 ± 0.9
			S	/	/	0.47 ± 0.07	0.7 ± 0.1	1.8 ± 0.3	14 ± 2
6FDA-HAB-t-BOC	n/a	n/a	*P*	64 ± 2	61 ± 2	1.89 ± 0.05	8.4 ± 0.3	1.61 ± 0.05	42 ± 1
			D	/	/	40 ± 2	142 ± 8	10.9 ± 0.4	37 ± 2
			S	/	/	0.36 ± 0.02	0.45 ± 0.03	1.13 ± 0.09	8.7 ± 0.5
6FDA-HAB-t-BOC	130	1 h	*P*	59 ± 4	56 ± 4	1.09 ± 0.08	5.8 ± 0.4	0.49 ± 0.04	32 ± 2
			D	/	/	14 ± 2	63 ± 9	2.5 ± 0.2	14 ± 2
			S	/	/	0.6 ± 0.1	0.7 ± 0.1	1.5 ± 0.2	17 ± 3
		2 h	*P*	54 ± 5	51 ± 5	1.1 ± 0.1	4.7 ± 0.4	0.80 ± 0.08	24 ± 2
			D	/	/	14 ± 3	45 ± 9	2.6 ± 0.4	11 ± 2
			S	/	/	0.6 ± 0.1	0.8 ± 0.2	2.3 ± 0.3	17 ± 4
		16 h	*P*	51 ± 3	46 ± 3	0.55 ± 0.04	3.4 ± 0.2	0.22 ± 0.02	18 ± 1
			D	/	/	6.4 ± 0.9	29 ± 4	0.60 ± 0.06	7 ± 1
			S	/	/	0.7 ± 0.1	0.9 ± 0.1	2.8 ± 0.4	19 ± 3
6FDA-HAB-t-BOC	140	1 h	*P*	54 ± 5	50 ± 5	0.75± 0.07	4.2 ± 0.4	0.33 ± 0.03	22 ± 2
			D	/	/	11 ± 2	48 ± 9	1.2 ± 0.2	12 ± 2
			S	/	/	0.5 ± 0.1	0.7 ± 0.1	2.1 ± 0.4	15 ± 3
		2 h	*P*	66 ± 3	58 ± 2	0.73 ± 0.03	4.4 ± 0.2	0.26 ± 0.01	22.7 ± 0.9
			D	/	/	6.5 ± 0.5	34 ± 3	0.81 ± 0.04	8.3 ± 0.7
			S	/	/	0.85 ± 0.08	0.97 ± 0.09	2.4 ± 0.2	21 ± 2
		16 h	*P*	53 ±2	46 ± 1	0.50 ± 0.02	3.1 ± 0.1	0.183± 0.007	15.5 ± 0.5
			D	/	/	5.4 ± 0.3	26 ± 2	0.48 ± 0.02	7.0 ± 0.4
			S	/	/	0.70 ± 0.05	0.91 ± 0.06	2.9 ± 0.2	17 ± 1
6FDA-HAB-t-BOC	160	5 min	*P*	59 ± 5	58 ± 5	1.5 ± 0.1	7.5 ± 0.6	1.05 ± 0.09	45 ± 4
			D	/	/	27 ± 5	100 ±20	4.7 ± 0.8	28 ± 6
			S	/	/	0.42 ± 0.09	0.6 ± 0.1	1.7 ± 0.3	12 ± 3
		15 min	*P*	61 ± 4	57 ± 4	0.87 ± 0.05	5.0 ± 0.3	0.37 ± 0.03	27 ± 2
			D	/	/	11 ± 2	47 ± 6	1.4 ± 0.1	13 ± 2
			S	/	/	0.58 ± 0.09	0.8 ± 0.1	2.0 ± 0.2	16 ± 2
		16 h	*P*	48 ± 1	40.6 ± 0.9	0.43 ± 0.01	2.83 ± 0.07	0.164± 0.005	13.9 ± 0.3
			D	/	/	5.6 ± 0.2	27 ± 1	0.58 ± 0.02	7.0 ± 0.3
			S	/	/	0.58 ± 0.03	0.80 ± 0.04	2.2 ± 0.1	15.1 ± 0.7

Units: *P* (barrer = 10^{-10} cm^3(STP) cm cm^{-2} s^{-1} $cmHg^{-1}$ or 3.348 × 10^{-16} mol m m^{-2} s^{-1} Pa^{-1}), *D* (10^{-9} cm^2 s^{-1}), *S* (cm^3(STP) cm^{-3} atm^{-1}).

Table 2.5. Ideal permselectivities of select gas pairs for 6FDA-HAB, 6FDA-HAB-t-BOC, and 6FDA-HAB-t-BOC after various thermal treatments.

Sample	Treatment Temperature (°C)	Hold time	O_2/N_2	CO_2/CH_4	CO_2/N_2	H_2/CH_4	N_2/CH_4
6FDA-HAB	n/a	n/a	7.1 ± 0.7	74 ± 8	34 ± 3	250 ± 30	2.2 ± 0.2
6FDA-HAB-t-BOC	n/a	n/a	4.4 ± 0.2	26 ± 1	22 ± 1	38 ± 2	1.18 ± 0.05
6FDA-HAB-t-BOC	130	1 h	5.3 ± 0.5	66 ± 8	29 ± 3	120 ± 10	2.3 ± 0.3
		2 h	4.2 ± 0.6	30 ± 4	21 ± 3	64 ± 9	1.4 ± 0.2
		16 h	6.3 ± 0.6	80 ± 8	32 ± 3	210 ± 20	2.5 ± 0.3
6FDA-HAB-t-BOC	140	1 h	5.7 ± 0.7	67 ± 9	30 ± 4	150 ± 20	2.2 ± 0.3
		2 h	6.0 ± 0.4	89 ± 6	31 ± 2	230 ± 20	2.9 ± 0.2
		16 h	6.3 ± 0.3	85 ± 4	31 ± 1	250 ± 10	2.7 ± 0.1
6FDA-HAB-t-BOC	160	5 min	5.0 ± 0.6	42 ± 5	30 ± 4	55 ± 7	1.4 ± 0.2
		15 min	5.7 ± 0.5	72 ± 7	31 ± 3	150 ± 10	2.4 ± 0.2
		16 h	6.6 ± 0.2	85 ± 3	32 ± 1	248 ± 9	2.6 ± 0.1

As shown in **Table 2.4**, the permeabilities of all six gases tested for 6FDA-HAB-t-BOC are higher than those for 6FDA-HAB, while the selectivities for all gas pairs considered are lower. This increase in gas permeability is consistent with FFV and PALS data and suggests that the bulky t-BOC functional groups in 6FDA-HAB-t-BOC lead to less efficient polymer chain packing in the films. Moreover, diffusion coefficients in 6FDA-HAB-t-BOC are significantly higher than those in 6FDA-HAB, which is again consistent with the FFV and PALS data, as the t-BOC group can act as a bulky spacer to further expand the free volume and allow for increased gas diffusion.[146] These results are in accordance with the expected exponential correlation between fractional free volume and diffusion coefficients, $D = A\exp(-\frac{B}{FFV})$, where A and B are adjustable parameters.[72,147–150] However, sorption coefficients for 6FDA-HAB-t-BOC are lower than those for 6FDA-HAB, which is likely due to the presence of polar hydroxyl functional groups which can enhance chemical affinity of molecular diluents. The inclusion of polar functionality has led to increases in sorption for other polymers such as cellulose acetate,[151] poly(methyl methacrylate) (PMMA),[151] polysulfone,[152] and PIM-1.[153] Since the difference in diffusion coefficients is more

pronounced than the difference in sorption coefficients, there is an overall increase in permeability for 6FDA-HAB-t-BOC compared to 6FDA-HAB.

In order to visualize the effects of different thermal treatments on gas transport properties, Robeson upper bound plots for O_2/N_2 and CO_2/CH_4 gas pairs are shown in **Figure 2.5**. Additional Robeson plots for other gas pairs listed in **Table 2.5** can be found in **Section A.4**. As the t-BOC group is removed, permeability generally decreases and selectivity increases, implying that discrete free volume elements are not maintained. However, permeability is the product of sorption and diffusion, and a successful application of free volume manipulation would imply increases in diffusion as free volume is created by porogen removal.

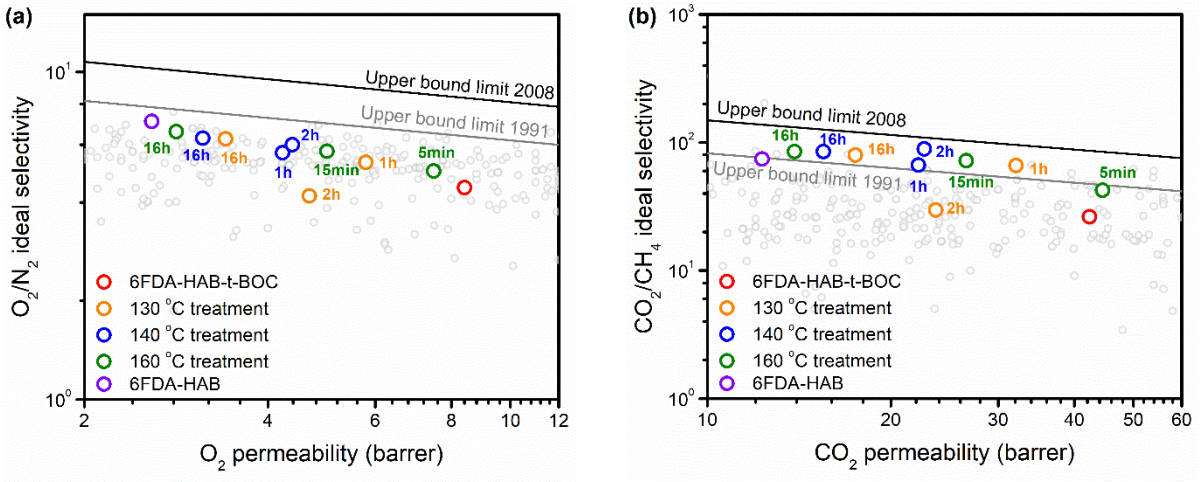

Figure 2.5. Robeson upper bound plots for (a) O_2/N_2, and (b) CO_2/CH_4 gas pairs. Thermally treated samples are labeled with their treatment times. The black and gray lines represent the 2008 and 1991 Robeson upper bounds, respectively.[46,47] Literature data are shown as open gray circles from Robeson's database.[46,47]

At each temperature treatment, as t-BOC is removed, permeabilities and diffusion coefficients generally decrease and approach those of 6FDA-HAB, while both sorption coefficients and permselectivities of all considered gas pairs generally increase. While these trends

indicate significant free volume reorganization, there are a few notable exceptions to these trends, and for the samples treated at 16 h, differences in FFV calculations and τ_3 values. These differences may indicate some limited evidence of FVM. Additionally, differences in free volume distribution could also explain how some samples (notably, t-BOC-130-16h, t-BOC-140-2h, and t-BOC-140-16h) have sorption coefficients that are higher than those for 6FDA-HAB, despite being chemically similar.

To investigate evidence of FVM, we turn to a few samples that exhibited morphological characteristics and/or transport effects that could support this interpretation. t-BOC-130-2h, in particular, was treated for a longer time than t-BOC-130-1h, yet the former possesses a lower selectivity for all gas pairs considered. In addition, the CH_4 permeability of t-BOC-130-2h (0.80 barrer) is higher than that of t-BOC-130-1h (0.49 barrer). These results can be explained by decoupling the permeability into diffusion and sorption coefficients. While t-BOC-130-1h and t-BOC-130-2h have identical CH_4 diffusion coefficients, the CH_4 sorption coefficient of t-BOC-130-2h (2.3 $cm^3(STP)\ cm^{-3}\ atm^{-1}$) is higher than that of t-BOC-130-1h (1.5 $cm^3(STP)\ cm^{-3}\ atm^{-1}$), which can be attributed to the higher conversion of t-BOC-130-2h (93% ± 1%) compared to t-BOC-130-1h (88.5% ± 0.5%). Because the FFV and τ_3 values are identical for these samples, differences in transport properties are governed by sorption effects and not indicative of significant FVM.

Another notable exception to the general trends was observed for t-BOC-140-1h and t-BOC-140-2h. Specifically, both the H_2 and He permeability coefficients of t-BOC-140-2h (66 and 58 barrer, respectively) are higher than those for t-BOC-140-1h (54 and 50 barrer, respectively). This result leads to a higher H_2/CH_4 selectivity for t-BOC-140-2h. For larger gases, diffusion coefficients decrease as treatment time at 140 °C increases, which correlates with the systematic

decrease in I_3, indicating a reduction in the number of free volume elements. However, O_2, N_2, and CO_2 sorption coefficients for t-BOC-140-2h exceed those for t-BOC-140-1h, even though the percent conversion, FFV, and τ_3 values are equivalent between the two samples. In addition, the sorption coefficients of all gases considered for t-BOC-140-2h exceed those for 6FDA-HAB. While t-BOC-140-2h can be considered chemically equivalent to 6FDA-HAB due to its conversion (95% ± 1%), the τ_3 value of t-BOC-140-2h is 11% ± 2% larger than that of 6FDA-HAB. A larger τ_3 value correlates with a larger average free volume element size, which indicates the presence of some excess volume in t-BOC-140-2h that does not exist in the directly formed 6FDA-HAB film. Since Robeson et al. have shown that excess free volume in polymers has a weak influence on sorption,[154] it is likely that the excess free volume found in t-BOC-140-2h contributes to higher sorption coefficients. While sorption coefficients for He and H_2 could not be determined, we would anticipate significantly higher sorption coefficients and permeabilities for these smaller gases in t-BOC-140-2h relative to 6FDA-HAB. While the effect is relatively small, these findings indicate some evidence of FVM for the 140 °C series. As one caveat, we refer to our earlier discussion on PALS results, where bimodal free volume distributions could not be fit for these samples. Therefore, conclusions of successful FVM in this series are somewhat nuanced, because sorption clearly increases from t-BOC-140-1h to t-BOC-140-2h, but both samples have similar FFV and τ_3 values.

Treatment temperatures of both 130 °C and 140 °C are below the prominent deprotection temperature of t-BOC, but the treatment temperature of 160 °C allows for the effects of faster deprotection on polymer chain rearrangement to be studied. When comparing samples that have similar conversions but different treatment conditions, it was generally found that with higher deprotection temperatures and longer treatment times, gas permeability decreases, coupled with

increases in selectivity. In particular, samples treated at 160 °C for significantly shorter times (5 min and 15 min) yield comparable gas transport results to those treated at 130 °C and 140 °C for longer times (1 h and 2 h). Although lower FFV values at similar conversions generally result in lower permeability, some exceptions were found that require further investigation. For example, while t-BOC-160-5min has a lower τ_3 value than t-BOC-130-1h, permeabilities for N_2, O_2, CH_4, and CO_2 are higher. This difference in permeability is mainly attributed to diffusion. A similar case is observed between t-BOC-140-2h and t-BOC-160-15min, in which the latter sample possesses a lower τ_3 value but higher permeabilities and diffusion coefficients for N_2, O_2, CH_4, and CO_2. The nearly equivalent FFV values between t-BOC-130-1h and t-BOC-160-5min and between t-BOC-140-2h and t-BOC-160-15min suggest that the free volume distribution between the two sample pairs differs, although these differences are again notably small.

As a final comparison, there are limited variations in diffusion coefficients for all four gases measured among the three samples annealed for 16 h. The independence of temperature on diffusion coefficients at a treatment time of 16 h is particularly interesting, as previous studies have shown that higher temperature treatments on polymer films can lead to larger decreases in diffusion coefficients.[60] There is a possibility that at 16 h, thermally-treated 6FDA-HAB-t-BOC has reached a state in which additional time may not warrant any obvious effects on the packing structure.[121] Such an interpretation would suggest that sub-T_g transitions, which are known to exist in 6FDA-HAB at our annealing temperatures,[144] have had sufficient time to reorganize the polymer packing structure such that the porogen templates have effectively been removed from the polymer matrix. A further study that examines the three thermal treatment temperatures used for times longer than 2 h, but shorter than 16 h, may elucidate this phenomenon.

2.4. Conclusions

In this study, the effect of thermal deprotection reactions on free volume manipulation (FVM) and gas transport properties was investigated. The control sample, 6FDA-HAB, was functionalized with t-BOC substituents to generate 6FDA-HAB-t-BOC, which was then cast into films. These films were subjected to thermal treatment conditions at various temperatures and times to study the effects of treatment conditions on polymer packing structure. Results were evaluated using FFV, PALS, and gas transport properties. Because deprotection reactions were all significantly below the glass transition temperature of 6FDA-HAB, we hypothesized that this method of FVM could generate free volume elements that were approximately the size of t-BOC. However, the results were far more nuanced, indicating that the thermally deprotected polymer underwent sufficient structural reorganization during thermal treatments, and complete retention of the created free volume elements could not be fully preserved. While certain samples showed some limited evidence of successful FVM, after sufficient thermal treatment, transport properties and physical characteristics of the deprotected samples closely resembled those of pure 6FDA-HAB. Extensive synthetic methods and characterization experiments demonstrate how this deprotection approach can be applied to high-T_g polymers with functional groups that can be protected. Applying these approaches to polymers with more restricted chain mobilities may enable more extensive manipulation and control to generate free volume elements from this top-down FVM approach.

Chapter 3. Polymers with side chain porosity for ultrapermeable and plasticization resistant materials for gas separations

Reprinted with permission from: He, Y.; Benedetti, F. M.; **Lin, S.**; Liu, C.; Zhao, Y.; Ye, H. Z.; Van Voorhis, T.; De Angelis, M. G.; Swager, T. M.; Smith, Z. P. Polymers with Side Chain Porosity for Ultrapermeable and Plasticization Resistant Materials for Gas Separations. *Adv. Mater.* **2019**, *31*, 1807871.

Polymer membranes with ultrahigh CO_2 permeabilities and high selectivities are needed to address some of the critical separation challenges related to energy and the environment, especially in natural gas purification and post-combustion carbon capture. However, very few solution-processable, linear polymers are known today that access these types of characteristics, and all of the known structures achieve their separation performance through the design of rigid backbone chemistries that concomitantly increase chain stiffness and interchain spacing, thereby resulting in ultramicroporosity in solid-state chain-entangled films. Herein we report the separation performance of a porous polymer obtained via Ring-Opening Metathesis Polymerization (ROMP), which possesses a flexible backbone with rigid, fluorinated side chains. This polymer exhibits ultrahigh CO_2 permeability (> 21,000 barrer) and exceptional plasticization resistance (CO_2 plasticization pressure > 51 bar). Compared to traditional polymers of intrinsic microporosity (PIMs), the rate of physical aging is slower, especially for gases with small effective diameters (*i.e.*, He, H_2, and O_2). This structural design strategy, coupled with studies on fluorination, demonstrates a generalizable approach to create new polymers with flexible backbones and pore-forming side chains that have unexplored promise for small molecule separations.

3.1. Introduction

Membranes are a promising platform technology for energy-efficient chemical separations. Unlike other separation processes, membranes do not require thermal regeneration, phase changes, or moving parts.[1] Increasing the permeability of polymer membranes used for gas separations is essential for enhancing productivity and reducing membrane areas required for large-scale gas and vapor separations.[155] Specific membrane applications include natural gas purification, hydrogen separations, air separation, and CO_2 capture from flue gas.[156,157]

Over the past decade, polymers of intrinsic microporosity (PIMs) have defined the state-of-the-art for gas separations.[67,158] Their rigid and contorted backbone structures lead to excellent separation performance for a variety of challenging binary separations (*e.g.*, CO_2/N_2, CO_2/CH_4, O_2/N_2, and H_2/CH_4).[158] Guided by the discovery that polymers of intrinsic miroporosity[159] now called PIMs were highly effective for gas separation,[86] researchers have sought to extend the database of accessible structures by designing and synthesizing ladder-type porous polymers containing more rigid backbones with even less conformational freedom.[88,160] Despite the advances in backbone rigidity of polymer chains, a relatively unexplored design strategy of creating porous polymers is to attach rigid, free-volume-generating sidechains to a flexible backbone to form a type of "bottlebrush" polymer. Recently, some of us have found that these polymers can be highly porous as a result of inefficient packing between rigid, non-compliant side chains.[161] In addition, since rigid macromonomers containing polymerizable units are synthesized before polymerization (**Scheme 3.1a**), it is easier to incorporate a variety of unique and pre-designed functionalities into this class of polymer as compared to PIM-1, which mainly relies on post-polymerization functionalization.[162,163] From a transport perspective, pre-designing side-chain structures can enhance the entropic ordering of ultramicropores, enabling easier access to

controlled entropic selectivities that are not currently considered from the activated state theory approach used to define the current polymer upper bound.[48]

It is well-known that fluorinated polymers introduce properties such as thermal stability and non-wettability, which have enabled commercial applications.[164] In terms of gas separation, previous studies have shown that the introduction of fluorinated moieties in aromatic polyimides can dramatically increase gas permeability with little impact on permselectivity.[95] In poly(organosiloxanes), it was found that CO_2 permeability and CO_2/CH_4 selectivity could increase simultaneously by incorporating fluorine-containing groups.[165] In all these cases, bulky hexafluoroisopropylidene functionality is used to contort the polymer backbone and generate free volume, thereby enhancing separation performance. Considering the synthetic versatility of using pore-forming macromonomers, the approach presented here enables a systematic comparison for studying the effect of fluorination on gas transport properties relative to that of hydrocarbon analogs in pre-designed ultramicropores. By doing so, a more direct deconvolution of the morphological and electronic contributions of fluorinated functionality on gas transport can be achieved.

This chapter describes the gas transport properties of two porous polymers obtained via Ring-Opening Metathesis Polymerization (ROMP), which both possess flexible poly(norbornene) backbones with rigid side chains. Films of CF_3-ROMP exhibited ultrahigh CO_2 permeability (> 21,000 barrer) and exceptional plasticization resistance (CO_2 plasticization pressure > 51 bar). The structures of two porous ROMP polymers are shown in **Scheme 3.1b** and are based on synthetic procedures published previously.[161] Side chains are made via an iterative Diels-Alder reaction, which generates a mixture of oligomers with different chain lengths (typically with 2–9 repeating units) (**Figure B.1** and **B.2**). The mixture of oligomers is directly used for ROMP

polymerization. Schematic representations of CF_3-ROMP are shown in **Scheme 3.1c**. Both CF_3-ROMP and OMe-ROMP are readily soluble in common organic solvents, allowing characterization by NMR and GPC (**Figure B.3** and **B.4**). The pre-casting CF_3-ROMP and OMe-ROMP powder showed significant microporosity via N_2 adsorption isotherms at 77 K, with a Brunauer–Emmett–Teller (BET) surface area of 700 $m^2\ g^{-1}$ and 146 $m^2\ g^{-1}$, respectively (**Figure B.6**). Solution casting from chloroform led to optically clear films (**Figure B.9**) suitable for gas permeation studies.

(a)

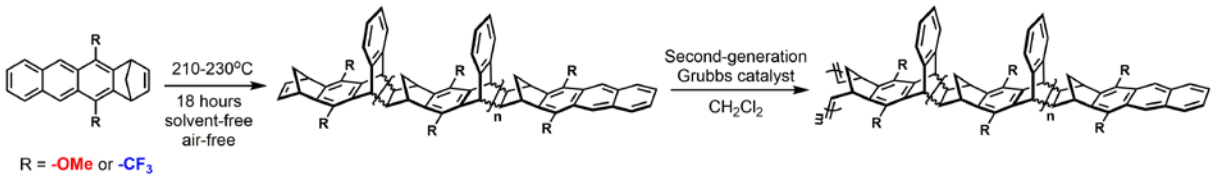

(b)

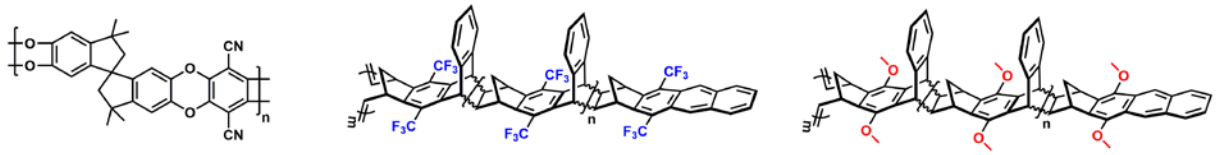

PIM-1 CF_3-ROMP OMe-ROMP

(c)

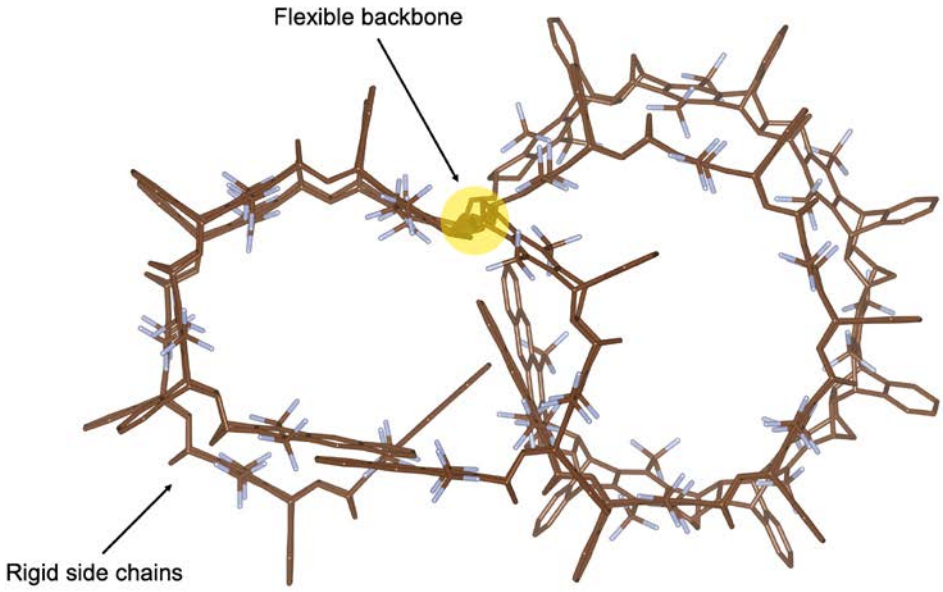

Uniform conformation for side chains

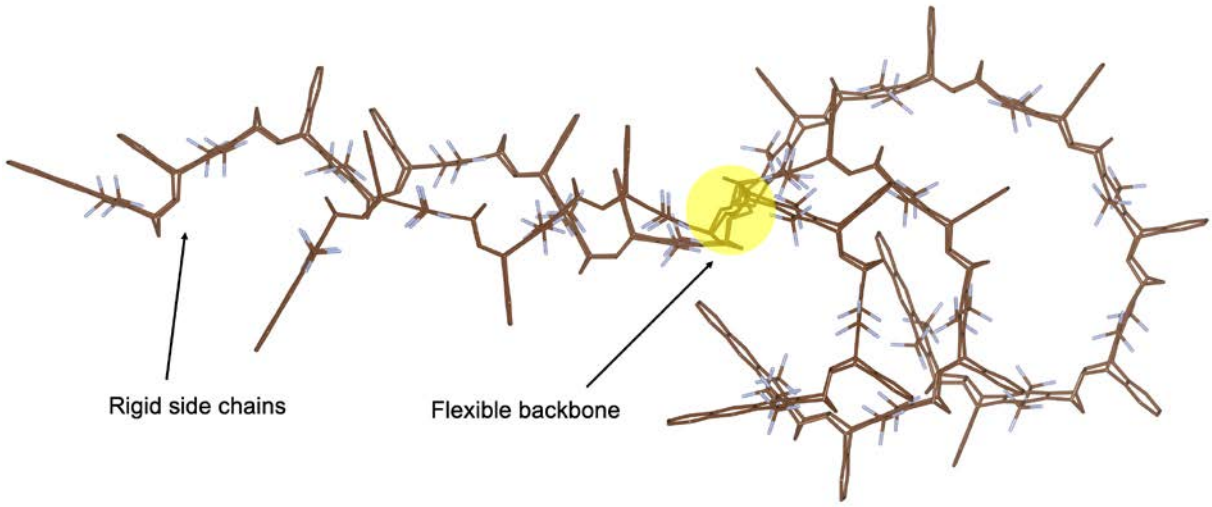

Mixed conformations for side chains

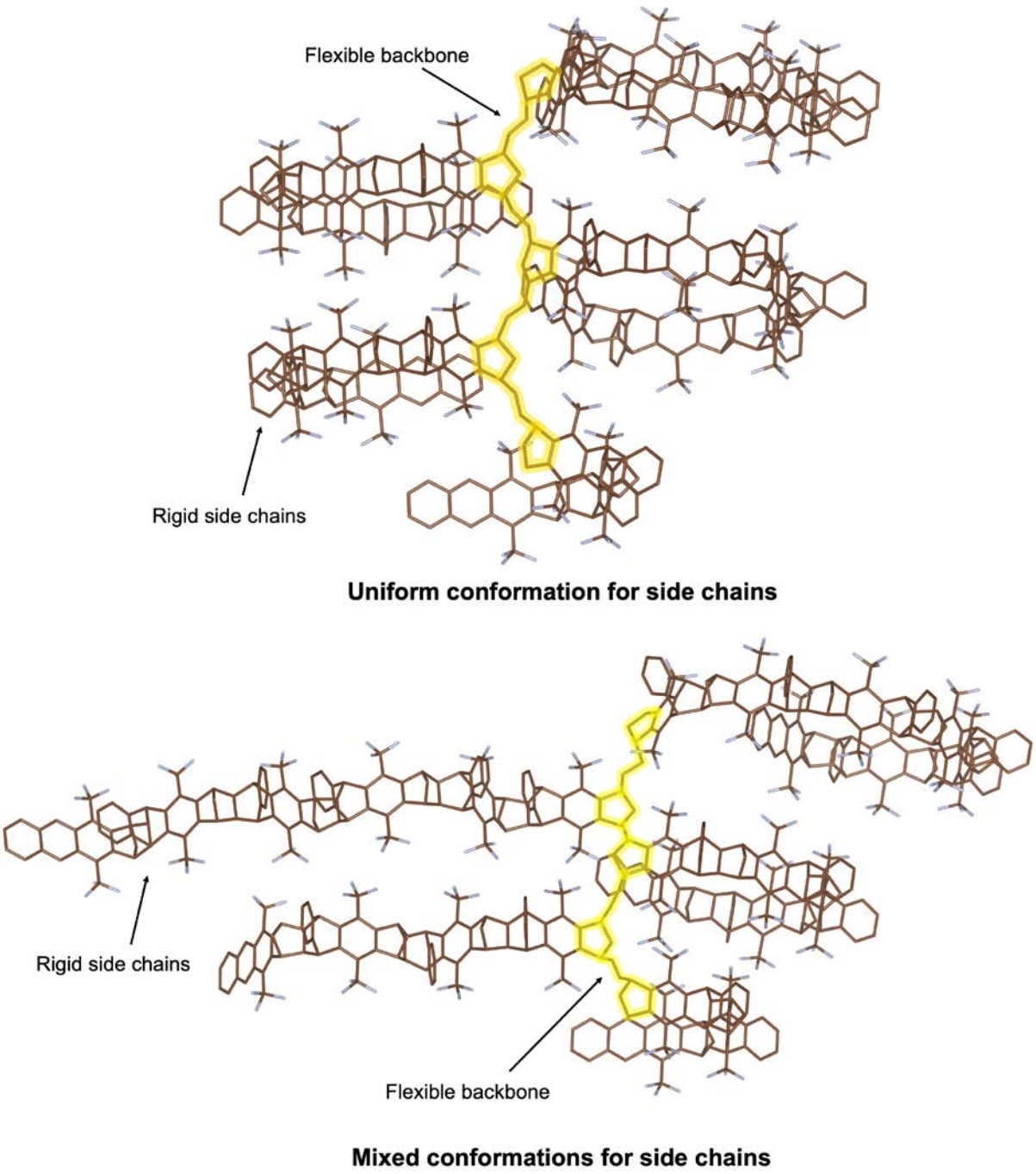

Scheme 3.1. (a) Generalized synthetic procedure for CF_3-ROMP and OMe-ROMP, (b) molecular structures of PIM-1, CF_3-ROMP, and OMe-ROMP, and (c) schematic representation of CF_3-ROMP with 5 repeating units (uniform conformation or mixed conformations for side chains).

3.2. Results and Discussion

The gas separation performance of CF_3-ROMP, OMe-ROMP, and PIM-1 are shown in **Figure 3.1** and **Table B.1**. Before permeation experiments, films were first soaked in ethanol for 48 h, dried at ambient conditions for 24 h, and then degassed in full vacuum for 8 h at 35 °C to remove residual solvent, as confirmed by TGA (**Figure B.10**).[166] The effect of different treatment conditions and film history were also investigated (**Section B.7**). The magnitude of gas permeability for CF_3-ROMP and OMe-ROMP followed the order of $CO_2 > H_2 > O_2 > He > CH_4 > N_2$, indicating a strong solubility contribution to permeation (**Figure B.11a**). CF_3-ROMP exhibited exceptionally high gas permeabilities across all gases tested, notably for CO_2 (~21,300 barrer) and H_2 (~8,300 barrer) for the non-aged film. These gas permeabilities were about 60 to 200% higher than the non-aged PIM-1 film under the same ethanol treatment and testing conditions, which makes CF_3-ROMP the third most permeable linear ultramicroporous polymer reported to date, behind PTMSP and PIM-TMN-Trip reported by Rose *et al.*[88] As a result, CF_3-ROMP surpassed the 2008 Robeson upper bound for H_2/CH_4 after physical aging, and was above the 1991 Robeson upper bound for all other gas pairs investigated (**Figure 3.1** and **B.12**).

In contrast, OMe-ROMP exhibited significantly lower gas permeabilities compared to CF_3-ROMP and PIM-1 but higher permselectivities (**Figure 3.1** and **B.11d**). These striking differences in transport properties are notable because CF_3-ROMP and OMe-ROMP are structurally very similar with the main exception being the $–CF_3$ versus –OMe functionality. Quantitatively, gas permeabilities are 7–10 fold higher, depending on the gas, for the CF_3-ROMP. This difference in performance can be rationalized by the higher BET surface area of CF_3-ROMP arising from the random configuration of CF_3- and OMe-substituted side chains. The pendant $–CF_3$ group is bulkier and stiffer than –OMe, which hinders interchain packing and reduces intrachain rotational freedom,

thus leading to higher porosity. Fluorine-containing moieties are also known to have high solubilities for light gases, which could subsequently increase permeabilities in the framework of the sorption–diffusion model.[3,41,167] It may be the combination of these two effects that leads to the significant increase in gas permeabilities, similar to trends reported for certain polyimides and polycarbonates.[168] Molecular mechanics simulations suggest side chain bending into "pocket-shapes" are a potentially pseudo-stable conformation (**Section B.4**). We also hypothesize that the pendant $–CF_3$ groups may form localized fluorine-rich domains between side chain segments as a result of the curvature of the side chain in 3D (**Scheme 3.1c**). However, the stereochemistry of Diels-Alder reaction during side chain formation is disordered and hence there is a distribution of the shape and size of the pockets.

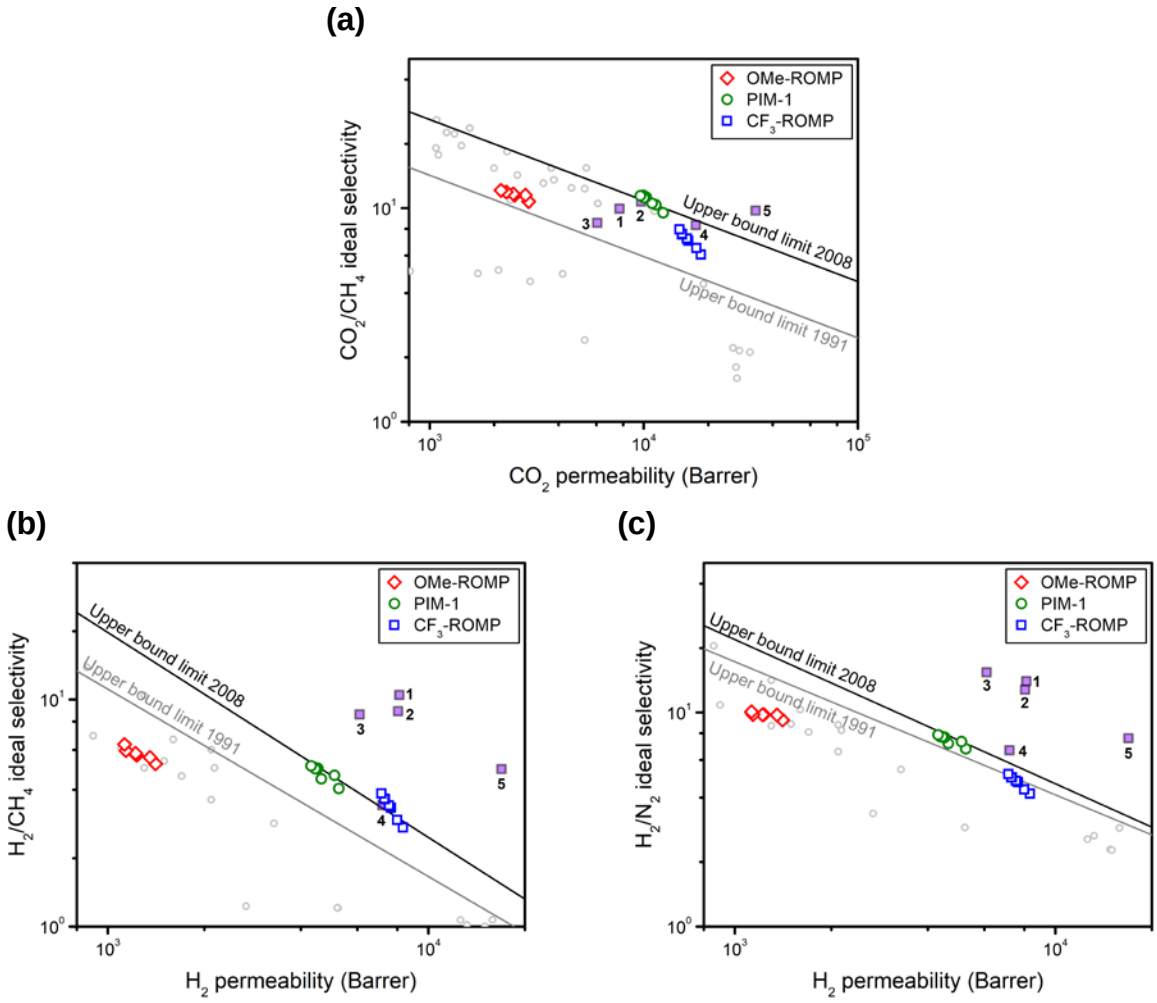

Figure 3.1. Robeson plots of CF_3-ROMP, OMe-ROMP, and PIM-1 for (a) CO_2/CH_4, (b) H_2/CH_4, and (c) H_2/N_2 gas pairs as a function of physical aging time. Black and gray lines represent 2008 and 1991 upper bounds, respectively.[46,47] Filled purple squares represent other highly permeable PIMs reported: 1) PIM-EA-TB, 2) PIM-Trip-TB, 3) PIM-TMN-SBI, 4) PIM-TMN-Trip-TB 5) PIM-TMN-Trip.[88,94]

Compared to PIM-1, CF_3-ROMP exhibited moderately lower selectivities for the gas pairs CO_2/CH_4, H_2/CH_4, and H_2/N_2. Diffusivity-selectivity and solubility-selectivity is presented in **Figure B.19** and **B.21**. According to **Figure 3.2**, **B.13**, and **B.14**, the solubility-selectivity of CF_3-ROMP is close to that of PIM-1 whereas its diffusivity-selectivity is lower for the majority of gas

pairs. Considering the difference in pore-size distribution between two polymers (**Figure B.6**), we hypothesize that the lower diffusivity-selectivity of CF_3-ROMP is most likely caused by polydispersity in length and stereochemistry of the side chains. Given this hypothesis, diffusivity-selectivity may be improved by homogenizing the length of side chains and devising systems that do not have structural variances as a result of the stereochemistry of the Diels-Alder reaction used in the side chain synthesis.

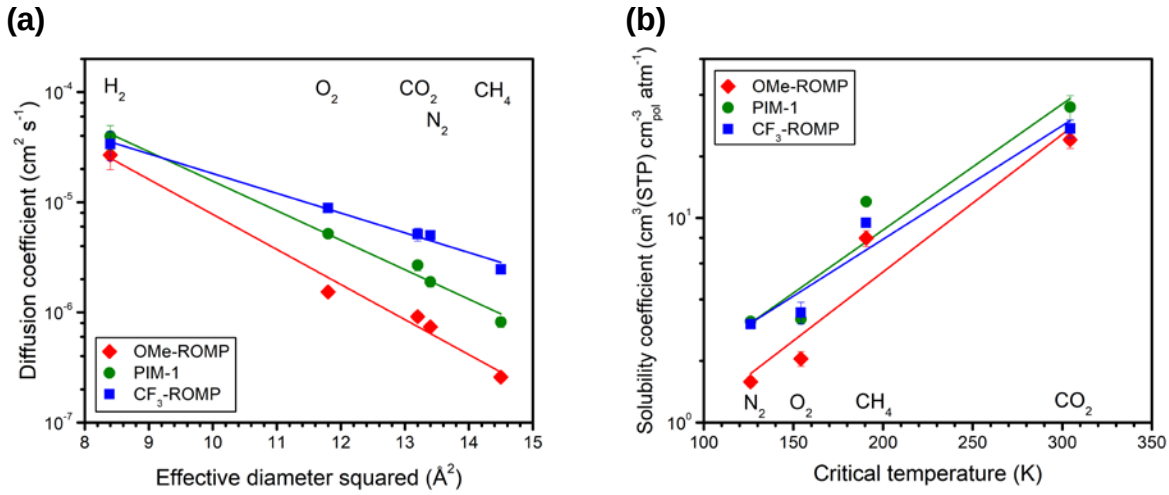

Figure 3.2. (a) Diffusion coefficient plotted against effective diameter squared for CF_3-ROMP, OMe-ROMP, and PIM-1 at 1 h aging after liquid ethanol soaking for 48 h, air-drying for 24 h, and subjecting to full vacuum for 8 h at 35 °C. The steepness of the slope indicates molecular sieving capabilities, thus molecular sieving capabilities decrease in the following order: –OMe > PIM-1 > $–CF_3$. (b) Solubility coefficient of N_2, O_2, CH_4, and CO_2 in polymers as a function of critical temperature.

In addition to evaluating performance relative to the upper bounds, determining the effects of penetrant-induced plasticization is an important concern in membrane-based gas separations.[169] Exposure of membranes to strongly interacting gases such as CO_2 at high pressures can reduce permselectivity as a result of sorption-induced swelling.[170] Thus, membranes that maintain stable

performance under high CO_2 feed pressures are desirable. In **Figure 3.3a**, CF_3-ROMP, OMe-ROMP and PIM-1 were subjected to CO_2 feed pressure up to 51 bar. Of note, CO_2 permeabilities of CF_3-ROMP decreased monotonically up to 51 bar even when using fugacity to account for non-idealities (**Figure B.25**). This result reveals that the plasticization pressure point, above which permeability starts to increase, was not reached under the conditions considered for these experiments. PIMs and many other non-crosslinked porous polymers exhibit plasticization pressure points at significantly lower pressures (**Figure B.23** and **Table B.2**), but the non-crosslinked CF_3-ROMP and OMe-ROMP have plasticization pressure points more characteristic to those of chemically-crosslinked polyimides.[171,172] Moreover, when the CO_2 feed pressure was gradually decreased, the hysteresis induced by conditioning up to 51 bar was ~35% of the original CO_2 permeability. OMe-ROMP shows similar anti-plasticization behavior with plasticization pressure points >51 bar, but the hysteresis (~50%) is slightly higher than CF_3-ROMP. As a comparison, the plasticization pressure point for PIM-1 when tested under identical conditions was ~27 bar, and it shows a significantly larger hysteresis effect (up to 95% increased permeability) when CO_2 feed pressure is released. These results indicate that the interchain cohesive energy for ROMPs is larger than that of PIM-1. This feature may originate from both a fluorophilic interaction between $–CF_3$ moieties and a greater rigidity-promoting "physical interlocking" between side chains typical of both ROMPs. Such an interpretation is in agreement with the results of Swaidan *et al.*, wherein interchain rigidity contributed to CO_2 plasticization resistance.[162,173] To further investigate the plasticization resistance of CF_3-ROMP, 50:50 vol.% CO_2/CH_4 mixed-gas permeation experiments were run, and the details can be found in **Section B.11**.

It is well-known that the relaxation of non-equilibrium free volume elements in PIMs proceeds rapidly in the first ~10 days after swelling in a non-solvent (*e.g.*, alcohols).[174] To evaluate

such behavior in the samples considered here, physical aging of CF_3-ROMP, OMe-ROMP, and PIM-1 was monitored by gas permeation measurements and wide-angle X-ray scattering (WAXS) for 2000 h. **Figure 3.3c** displays helium permeability as a function of the time, and it is clear that CF_3-ROMP, OMe-ROMP, and PIM-1 age at different rates. For smaller gases like He, H_2, and O_2, CF_3-ROMP aged the slowest among samples considered, while OMe-ROMP aged the fastest with PIM-1 displaying intermediate behavior (**Figure B.17**). Notably, the aging rate of CF_3-ROMP is significantly lower than that of state-of-the-art PIMs, although the alcohol treatment was slightly different (ethanol vs. methanol).[88,96] For instance, helium permeability decreased by ~45 % after 1000 h aging for PIM-TMN-Trip, whereas CF_3-ROMP only decreased by ~10 %. Moreover, the CF_3-ROMP films considered here are thinner than PIM-TMN-Trip (119 μm vs. 192 μm), and physical aging is accelerated for thinner films.[117] For larger molecules like CO_2, N_2, and CH_4, there was no significant difference in aging rates between the three polymers compared in this work (**Figure B.17a**). These findings suggest that using permeability as a proxy for assessing aging rates instead of diffusion is a limitation for more strongly sorbing components that also have significant solubility contributions to permeability.

Previous studies have shown that the introduction of fluorinated moieties can suppress physical aging in aromatic polyimides.[175,176] In the case at hand, despite its higher BET surface area, the aging rate of CF_3-ROMP was considerably lower than that of OMe-ROMP for gases with smaller effective diameters. The WAXS of CF_3-ROMP displays a decrease in scattering intensity only over the larger *d*-spacing regime during physical aging, whereas OMe-ROMP exhibited a decrease in scattering intensity across the entire *d*-spacing range (**Figure B.22**). This trend suggests that subtle differences in polymer chemistry for a similar polymer design may result in multiple, complex aging pathways. The reduced aging rate for CF_3-ROMP compared to OMe-ROMP likely

results from a stability of CF_3-ROMP to contraction of smaller free volume elements (**Figure B.15** and **B.16**).

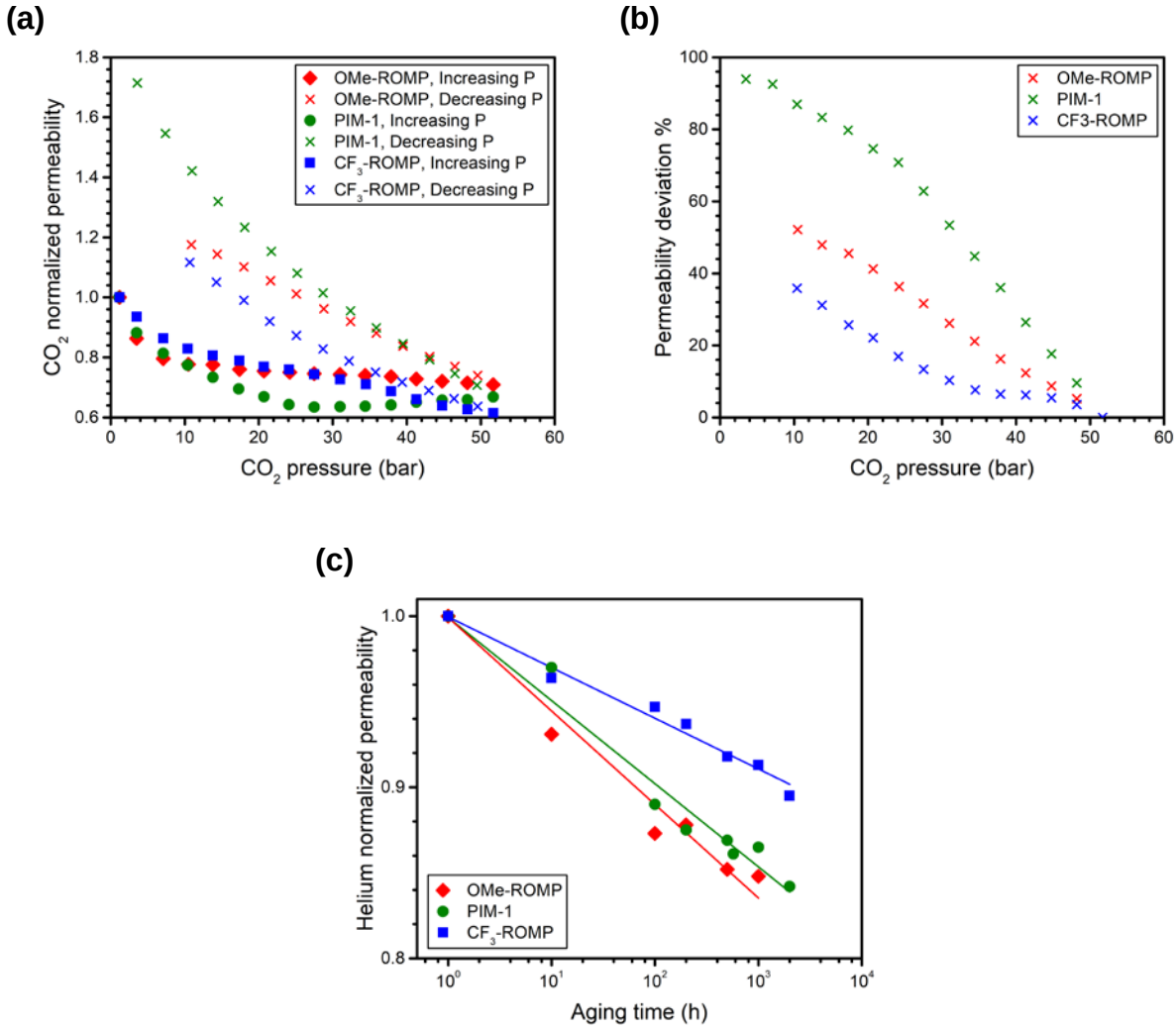

Figure 3.3. (a) CO_2 plasticization study and (b) hysteresis induced by conditioning of the film at 51 bar of CO_2 for CF_3-ROMP, OMe-ROMP, and PIM-1. (c) Physical aging study of helium by monitoring permeability over time for CF_3-ROMP, OMe-ROMP, and PIM-1 between 1 and 2000 h after liquid ethanol treatment.

3.3. Conclusions

In summary, we have demonstrated a versatile approach to achieve ultrahigh CO_2 permeabilities and selective size-sieving behavior for gas-phase separations by using pore-forming side chains attached to flexible polymer backbones. Pendent $–CF_3$ groups enhance gas permeability and reduce physical aging compared to their –OMe counterparts. The different performance metrics as a function of pendent groups on the side chain reveal that these features can be used to tailor gas separation performance. Outstanding plasticization resistance is a common feature for both of the ROMP polymers presented, indicating that this new structural design may provide a material platform to systematically address challenges with plasticization. Moreover, CF_3-ROMP exhibited a reduction in physical aging rate compared to PIM-1 even though it is characterized by significantly higher intrinsic permeabilities. The formation of porous polymers based on flexible backbones and rigid free volume promoting side chains represents a promising new platform of materials for addressing fundamental limitations in current design strategies for membrane materials.

3.4. Materials and Methods

Synthesis of Porous ROMP polymers: Synthetic procedures for CF_3-ROMP and OMe-ROMP have been previously reported by Zhao and He *et al*.[161]

Modelling and Gas Transport Properties: The 3D structure of CF_3-ROMP is optimized using the MMFF 94 force field as implemented in Avogadro 1.2.0.

Gas Transport Properties: Self-standing films of CF_3-ROMP, OMe-ROMP, and PIM-1 were prepared by slow evaporation of a 3 wt % polymer solution in chloroform using a flat aluminum Petri dish. The as-cast film was soaked in liquid ethanol before testing gas permeability

and WAXS. TGA analysis was performed to ensure the complete removal of residual solvents from the films and to determine their thermal stability. The thicknesses of CF_3-ROMP, OMe-ROMP, and PIM-1 films, as measured with a digital micrometer, were 119 μm, 160 μm, and 119 μm, respectively. Permeability was measured at 35 °C with a fixed-volume variable-pressure Maxwell Robotics automated permeation system from the slope of the curve (p, t) in the steady-state region after 6 times the time lag (θ). Pressure was measured with a MKS transducer (Model 622C, 10 Torr limit). The diffusion coefficient, $\mathcal{D}$, was determined by applying the time-lag method: $\mathcal{D} = l^2/6\theta$ where l is the film thickness. The solubility coefficient, $\mathcal{S}$, was determined in the framework of the solution-diffusion model where $\mathcal{S} = \mathcal{P}/\mathcal{D}$. Aging experiments were systematically performed on samples subjected to the same treatment and storage conditions, experiencing the same history for up to 2000 h. CO_2-induced plasticization experiments were performed by pressurizing samples up to 51 bar and depressurizing down to 1 bar to evaluate the hysteresis.

Chapter 4. Elucidating the role of side-chain length and dispersity in ROMP polymers with pore-generating side chains for gas separations

Reprinted from Benedetti, F. M.; Wu, Y.-C.; **Lin, S.**; He, Y.; Flear, E.; Liu, C.; Zhao, Y.; Swager, T. M.; Smith, Z. P. Elucidating the role of side-chain length and dispersity in ROMP polymers with pore-generating side chains for gas separations. *In preparation.*

Polymers with flexible backbones and rigid side chains of varying length synthesized via ring-opening metathesis polymerization (ROMP) have shown ultrahigh CO_2 permeability and plasticization resistance. We report gas transport properties of a methoxy (OMe) functionalized ROMP polymer with uniform side-chain lengths ranging from n = 2–5 repeat units in order to elucidate the role of both side-chain length and dispersity on gas transport properties and plasticization resistance. As side-chain length increased, both Brunauer–Emmett–Teller (BET) surface area and gas permeability increased with minimal losses in gas selectivity. Increased plasticization resistance was also observed with increasing side-chain length, which can be attributed to increased interchain rigidity from longer side chains. Controlling the side-chain length was revealed to be an effective strategy to rationally optimize the performance of ROMP polymers for CO_2-based gas separations.

4.1. Introduction

The use of membranes for gas separations is a promising alternative to traditional industrial separations due to their energy efficiency, low capital investment, and operational simplicity (i.e., no moving parts or phase changes).[1,177] In order to be suitable for scale-up and operation, such membranes must be solution-processable, as well as highly permeable and selective.[3] In recent years, polymers of intrinsic microporosity (PIMs) have emerged to define the state of the art in pure-gas performance for gas separations due to their rigid and contorted backbones that lead to inefficient packing and concomitant pore generation, which results in very high gas permeabilities.[86,88,142,158,178] Since the discovery of PIMs, a range of design strategies (e.g., the incorporation of rigid groups such as iptycenes, Tröger's base, Hünlich's base, and polybenzoxazole motifs through thermally rearranged (TR) polymers) have been used to generate pores for improved separation performance.[23,62,94–98,179]

We have recently introduced an alternative method of pore generation using a "bottlebrush" type of polymer with a flexible poly(norbornene) backbone containing rigid, free-volume-generating side chains.[161,180] A variety of functionalities can be incorporated into the rigid macromonomers prior to their polymerization via ring-opening metathesis polymerization (ROMP), allowing for the effects of these functionalities on polymer packing and gas transport properties to be studied. To that end, we studied the gas transport properties of two porous polymers generated via ROMP with two different chemical substituents (CF_3-ROMP and OMe-ROMP), and found that CF_3-ROMP possessed ultrahigh CO_2 permeability (> 21,000 barrer) and exceptional plasticization resistance (CO_2 plasticization pressure > 51 bar).[180] While OMe-ROMP also displayed similar exceptional plasticization resistance, CO_2 permeability was lower (~2,900 barrer).[180] Although these polymers achieved plasticization resistance previously unreported for

un-crosslinked glassy polymers, the combinations of permeabilities and selectivities of both CF_3-ROMP and OMe-ROMP were not high enough to surpass the 2008 Robeson upper bound for a majority of gas pairs studied.[47,180] Mechanistically, it was determined that the reason behind these findings related to the diffusivity-selectivity of CF_3-ROMP being lower than that of PIM-1 for a majority of gas pairs.[180] This finding is potentially related to the non-uniformity in side-chain length and the stereochemistry of the rigid side chains Thus, we hypothesized that creating side chains of uniform length could potentially improve diffusivity-selectivity in ROMP polymers for gas separations (**Figure 4.1a**).

In this study, we report gas transport properties of OMe-ROMP with uniform side chains ranging from n = 2–5 repeat units. It was found that increasing side-chain length (i.e. the value of n) led to increased pure-gas permeability and diffusion coefficients for all gases considered, with minimal loss in selectivity. While it was hypothesized that forming side chains of uniform length could improve diffusivity selectivity, the dispersity of side chain length in samples did not seem to influence gas transport properties, as those of OMe-ROMP (which had an average n = 4.5) fell between those of poly(OMe 4-mer; n = 4) and poly(OMe 5-mer; n = 5). When measuring plasticization resistance using high-pressure pure-gas CO_2 permeation tests, poly(OMe 5-mer) and poly(OMe 4-mer) were found to have higher plasticization resistance than poly(OMe 3-mer), which displayed a plasticization pressure of ~10 bar.

4.2. Experimental

4.2.1. Materials and methods

Dicyclopentadiene, sodium hydride, methyl iodide, and Grubbs 2nd-generation catalyst were purchased from commercial sources and used as received. Anhydrous dimethylformamide (DMF)

was purchased from Sigma–Aldrich in SureSeal bottles and dried over 4-Å molecular sieves prior to use. Anhydrous dichloromethane (DCM) was obtained from an INERT PureSolv MD5 solvent purification system and stored under Ar over 4-Å molecular sieves. All other solvents were purchased at ACS grade or higher and used as received. 1,4-Anthraquinone was purified with a silica plug (using dichloromethane as the eluent) prior to use.

Silica gel chromatography: Silica gel chromatography was performed on a Biotage Isolera flash chromatography system with Biotage SNAP Ultra columns containing HP-Sphere 25μm silica.

Nuclear magnetic resonance (NMR) spectroscopy: ^{1}H and ^{13}C NMR spectra were acquired using Bruker Avance spectrometers at 400 or 600 MHz (100 or 150 MHz) for ^{1}H (^{13}C), in deuterated solvents as specified, and referenced to the residual solvent signal. Spectra for quantitative integration were recorded using 16 scans and 5-s relaxation time.

Size exclusion chromatography (SEC): SEC was performed in HPLC-grade tetrahydrofuran using an Agilent 1260 Infinity system with a guard column (Agilent PLgel; 5μm; 50 x 7.5 mm) and three analytical columns (Agilent PLgel; 5μm; 300 x 7.5 mm; 105, 104, and 103 Å pore sizes). The instrument was calibrated with polystyrene standards between 1.7 and 3150 kg•mol^{-1}. All runs were performed at 1.0 mL•min^{-1} flow rate and 35 ºC. Molecular weight values were calculated using ChemStation GPC Data Analysis Software (Rev. B.01.01) based on the refractive index signal.

Matrix-assisted laser desorption/ionization (MALDI)–time of flight (TOF) mass spectrometry (MS): MALDI–TOF MS was performed on a Bruker Autoflex Speed machine using reflector mode and positive ionization. *trans*-2-[3-(4-*tert*-Butylphenyl)-2-methyl-2-propenylidene]malononitrile (DCTB) was used as the matrix.

Brunauer–Emmett–Teller (BET) surface area: BET surface areas of polymers were measured using N_2 sorption at 77 K using a Micromeritics ASAP 2020 analyzer. Powder samples were degassed under high vacuum at 120 °C for at least 4 hours prior to analysis.

4.2.2. Synthetic procedures

The synthetic procedures for the OMe monomer, oligomerization, and polymerization were previously reported[161,180] and used without modification other than the separation step. Representative procedures are presented below.

OMe oligomer: OMe monomer was added to an oven-dried Schlenk flask, which was evacuated and backfilled with Ar three times. The monomer was heated at 220 °C for 18 h.

Separation of oligomers: The oligomer mixture was separated by silica gel chromatography using a Biotage Isolera flash chromatography system. Generally a solvent gradient of 5% to 40% EtOAc/hexanes was successful in providing sufficient separation. R_f decreases with increasing *n*. Crucially, the isolated oligomers were dissolved in a small amount of DCM and precipitated in MeOH prior to polymerization in order to remove impurities, presumably from the evaporated solvent used for chromatography. OMe *n*-mers were dried in the vacuum oven at 60 °C for at least 3 h.

Polymerization: OMe 4-mer (168 mg, 0.14 mmol, 1 equiv.) was added to an oven-dried Schlenk flask, which was evacuated and backfilled with Ar three times, and then dissolved in DCM (1 mL). In a separate oven-dried vial, Grubbs 2nd-generation catalyst (1.18 mg, 0.0014 mmol, 0.01 equiv.) was dissolved in DCM (0.4 mL). The catalyst solution was transferred by syringe into the oligomer solution, and the reaction mixture was stirred at room temperature for 18 h. The flask was unsealed and 1 drop of ethyl vinyl ether was added to quench the catalyst. The polymer

solution was precipitated in methanol, and the solid was collected by vacuum filtration, washed with methanol, and dried under vacuum.

4.2.3. Membrane fabrication and treatment

Self-standing films of poly(OMe *n*-mer)s were made by dissolving polymer in chloroform to create a ~3 wt% polymer solution. The solution was then cast onto a Norton® fluorinated ethylene propylene (FEP) Film petri dish liner with a diameter of 50 mm, which was then placed on a flat-bottomed glass dish. After 4–5 days of slow evaporation at room temperature in a fumehood, a stable and defect-free film was formed with a thickness of ~150 μm.

Two different treatments were employed on the self-standing films. Thermally treated films were dried at 120 °C for 24 h under vacuum to remove residual solvent. Alcohol-treated films were soaked in either ethanol (poly(OMe 2-mer)) or methanol (poly(OMe 3-mer) to poly(OMe 5-mer)) for 48 h. After alcohol treatment, films were air-dried in a fumehood for 24 h before testing in the permeation system.

4.2.4. Pure-gas permeability measurements

Pure-gas permeability measurements of samples were done using an automated constant-volume, variable-pressure permeation system from Maxwell Robotics. Polymer films were cut, placed on top of a hole in the center of a brass disk, and glued to the brass disk using epoxy glue (Devcon 5 min Epoxy). The glue was left to dry for at least 30 min. After, the polymer sample were sealed inside a stainless steel permeation cell (Millipore), which was immersed in a water bath set to 35 °C by an immersion circulator (ThermoFisher SC150L). All gases used for testing (He, H_2, CH_4, N_2, O_2, and CO_2) were ultra-high purity from Airgas.

The permeabilities of the six aforementioned gases were determined at ~1 bar. Before testing permeation, the testing chamber was dosed with ~2 bar of helium gas to ensure that no residual gas remained in the system. Then, the sample was held under vacuum at 35 °C for 8 h. Before switching to a new permeating gas for testing, samples were again dosed with ~2 bar of helium gas and held under vacuum for at least 1 h.

Pure-gas permeability (P) was calculated using the following equation:

$$P = \frac{V_d l}{p_2 ART}\left(\frac{dp}{dt}\right)_{ss} \tag{4.1}$$

in which V_d is the volume downstream of the film, l is the film thickness, p_2 is the upstream pressure, A is the area of film exposed to the gas, R is the ideal gas constant, T is the absolute experimental temperature, and $\left(\frac{dp}{dt}\right)_{ss}$ is the rate of pressure rise in the permeate at steady state. The ideal gas selectivity ($\alpha_{i,j}$) was taken to be the ratio of the pure-gas permeabilities of the more permeable gas, i, to that of the less permeable gas, j (i.e., $\frac{P_i}{P_j}$). Diffusion coefficients for each gas were determined using the time-lag method, $D = \frac{l^2}{6\theta}$, in which θ is the time lag.[134] Since the diffusion coefficients for smaller gases (i.e., He and H_2) were sometimes within the resolution of the acquisition time of the permeation system, which was typically 1–2 s, diffusion coefficients for these two gases are not reported in. By assuming the sorption–diffusion model to be valid ($S = \frac{P}{D}$),[41] sorption coefficients could be determined. Error bars for permeability, diffusion coefficients, and sorption coefficients were determined using the error propagation method.

4.3. Results and Discussion

Figure 4.1a depicts a comparison of our previous study,[180] described in Chapter 3, to the work presented in this chapter. OMe-ROMP polymers with uniform side-chain lengths (*n*), which we term poly(OMe *n*-mer)s, were synthesized from their respective oligomers of uniform lengths. The pure but stereoirregular OMe *n*-mers of uniform lengths were in turn obtained by using silica gel column chromatography to separate the OMe-oligomer mixture obtained from Diels–Alder oligomerization. We were able to separate out the OMe *n*-mers of $n = 1 – 5$, whereas higher *n*-mers began to coelute ($n = 1$ corresponds to the unreacted monomer and was not further studied). Unfortunately, the fluorophilic CF_3 oligomers did not separate well on silica gel under all solvents considered. After isolation of the OMe *n*-mers, their identity and purity were confirmed by nuclear magnetic resonance (NMR) spectroscopy and matrix-assisted laser desorption/ionization–time-of-flight mass spectrometry (MALDI–TOF MS). In addition to MALDI (**Figure 4.1c**), ^{1}H NMR integration ratios were used to confirm the identity of the separated OMe *n*-mers. **Figure C.1** demonstrates the method used for NMR integration, and **Table C.1** shows the expected and experimentally obtained ratios. NMR integral ratios of each *n*-mer were consistent with the expected values (**Figure C.1** and **Table C.1**), and each MALDI–TOF MS spectrum demonstrates the expected mass of each *n*-mer with minimal impurities (**Figure 4.1c**). Additionally, we found that precipitation of the isolated oligomers from dichloromethane solution into methanol was crucial for removing residual impurities (such as trace amounts of alkenes) from the column chromatography solvent that would otherwise interfere with the ROMP reaction, leading to lower molecular weights. With the purified OMe *n*-mers in hand, ROMP using Grubbs 2nd-generation catalyst provided the corresponding poly(OMe *n*-mer)s (**Figure 4.1b**). Monomer-to-initiator ratios ([M]/[I], based on molar concentrations) between 100 and 150 produced polymers of high

molecular weights ($M_n \geq 75$ kDa; see **Table C.2**) that were suitable for producing free-standing films via solution casting.

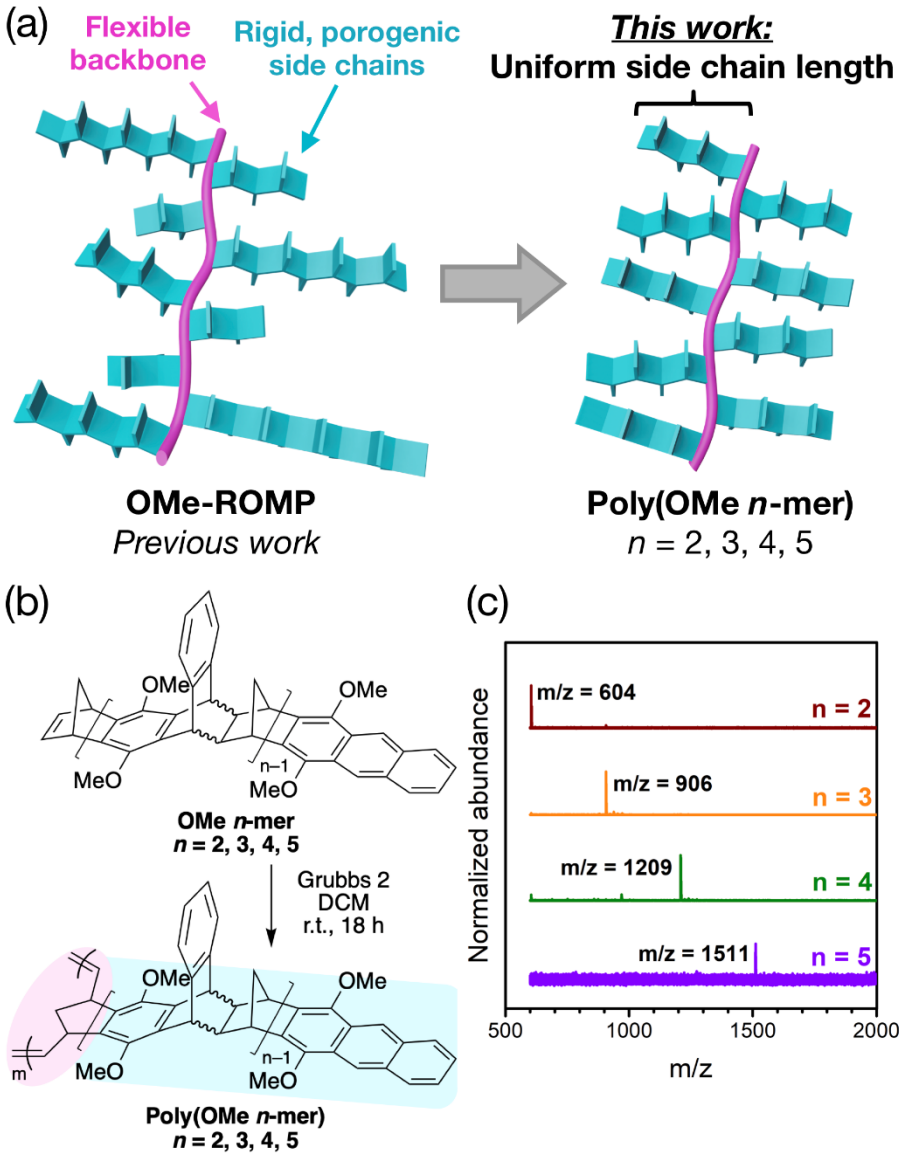

Figure 4.1. (a) Comparison of polymer structure between previous study[180] and this study; (b) reaction conditions to polymerize OMe *n*-mers; (c) MALDI–TOF MS spectrum of each *n*-mer in this work.

Brunauer–Emmett–Teller (BET) surface areas of poly(OMe 2-mer) – poly(OMe 5-mer) were obtained from N_2 adsorption isotherms (**Figure C.2**) at 77 K and are shown in **Table 4.1**.

The BET surface areas show an increasing trend with increasing *n*, demonstrating the porogenic nature of the rigid side chains, with the higher *n*-mers producing materials with higher BET surface areas. The BET surface area of OMe-ROMP falls between those of poly(OMe 4-mer) and poly(OMe 5-mer), which is consistent with an average *n* of 4.5 in OMe-ROMP as determined by NMR integration ratio.

Table 4.1. BET surface areas of poly(OMe 2-mer) through poly(OMe 5-mer).

	BET Surface Area (m^2/g)
OMe 2-mer	30
OMe 3-mer	147
OMe 4-mer	430
OMe 5-mer	574
OMe-ROMP	484

The gas separation performance of all poly(OMe *n*-mer)s are shown in **Figure 4.2** and **Table C.3**. Before testing, films were soaked in methanol for 48 h, dried in ambient conditions for 24 h, and then degassed under full vacuum at 35 °C for 8 h. Since poly(OMe 2-mer) films were unable to withstand methanol treatment for permeation tests, ethanol treatment was used instead. Similar to methanol treatment, ethanol treatment has also been shown to swell polymer membranes and thereby increase free volume and gas permeability.[166,181–184]

Data for OMe-ROMP was reported in our previous study and is included in **Figure 4.2** here for comparison.[180] This sample was soaked with ethanol instead of methanol but otherwise underwent identical treatments conditions relative to the other samples considered in this study. For all samples tested, gas permeability increased as follows: $P(N_2) < P(CH_4) < P(O_2) < P(He) < P(H_2) < P(CO_2)$, which indicates a strong sorption component to permeability. As *n* increases, permeabilities for all gases increase, while the selectivities for gas pairs considered decrease slightly, which is consistent with BET data presented. In addition, the gas separation performance

of OMe-ROMP is in between those of poly(OMe 4-mer) and poly(OMe 5-mer), which is again consistent with the average *n* of 4.5 for OMe-ROMP. Gas separation performance for poly(OMe *n*-mer) samples that underwent thermal treatment instead of solvent treatment (120 °C under full vacuum for 24 h before drying in ambient conditions for 24 h and then degassing under full vacuum at 35 °C for 8 h) can be found in **Appendix C** (**Figure C.3** and **Table C.3**).

In order to determine whether our original hypothesis that forming side chains of uniform length could lead to increased diffusivity selectivity, we decoupled permeability into diffusion and sorption coefficients in the framework of the sorption–diffusion model ($P = DS$).[41] Diffusion coefficients were determined using the time-lag method ($D = l^2/6\theta$)[134] where l is the film thickness. Since the time-lags of He and H_2 were outside of the resolution of our permeation system (1–2 s), diffusion and sorption coefficients are not reported for these gases. Tabulated diffusion and sorption coefficients for all samples in this study can be found in **Table C.3**.

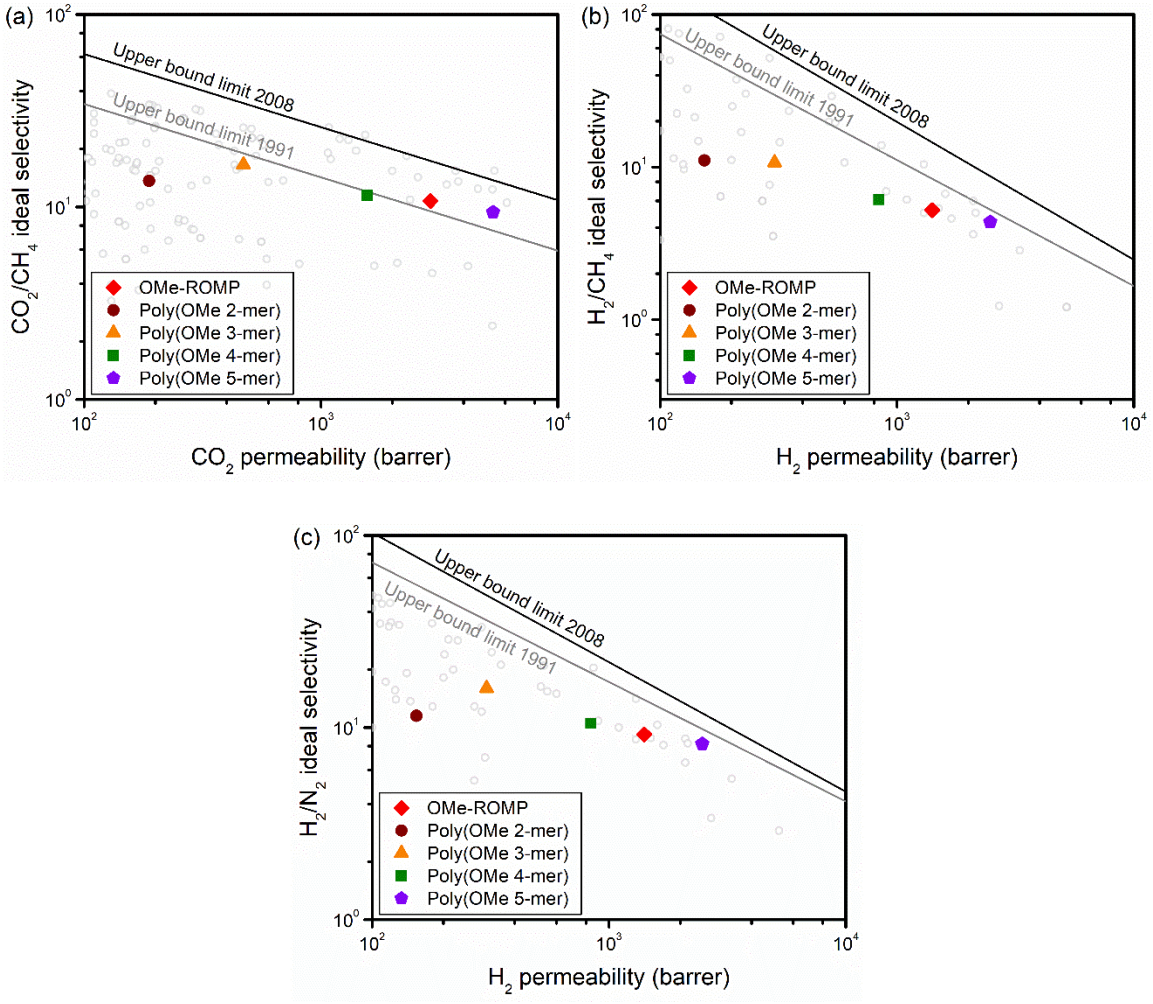

Figure 4.2. Robeson plots of alcohol-treated poly(OMe *n*-mer)s and OMe-ROMP for (a) CO_2/CH_4, (b) H_2/CH_4, and (c) H_2/N_2 gas pairs. Black and gray lines represent the 2008 and 1991 Robeson upper bounds, respectively.[46,47] Open gray circles represent permeation data from Robeson's database.[46,47]

The effects of *n* on diffusion coefficient for O_2 is shown in **Figure 4.3** for both thermally treated and methanol-treated samples. Analogous plots for N_2, CH_4, and CO_2 are shown in **Figure C.4**. It can be seen that, for the four gases considered in this study, as the side-chain length increases from $n = 2$ to $n = 5$, the diffusivity increases in an exponential manner, which is in agreement with free volume theory.[145,150] Thus, plots are presented with a logarithmic y-axis for

linearization,[185] and the slopes of the semilog plots are displayed on each figure. For each gas, thermally treated samples experience a smaller increase in diffusion coefficient as *n* increases compared to samples that underwent methanol treatment, as evident by the smaller slope. In addition, the slopes of the semilog plots for thermally treated samples for each gas remain largely invariant, indicating that the change in diffusivity with respect to *n* is similar across all gases considered. However, for methanol-treated samples, the slopes of the semilog plots increase ((0.38 ± 0.03) O_2 < (0.42 ± 0.03) CO_2 < (0.47 ± 0.07) N_2 < (0.53 ± 0.06) CH_4) in accordance with the effective diameter of the gas ((3.44 Å) O_2 < (3.63 Å) CO_2 ~ (3.66 Å) N_2 < (3.81 Å) CH_4). Methanol treatment of polymer membranes results in swelling, leading to an increase in free volume size and gas permeability.[139] Thus, changes in diffusivity coefficient from side-chain length will be more pronounced in methanol treated samples because of the swelling nature of this processing method.

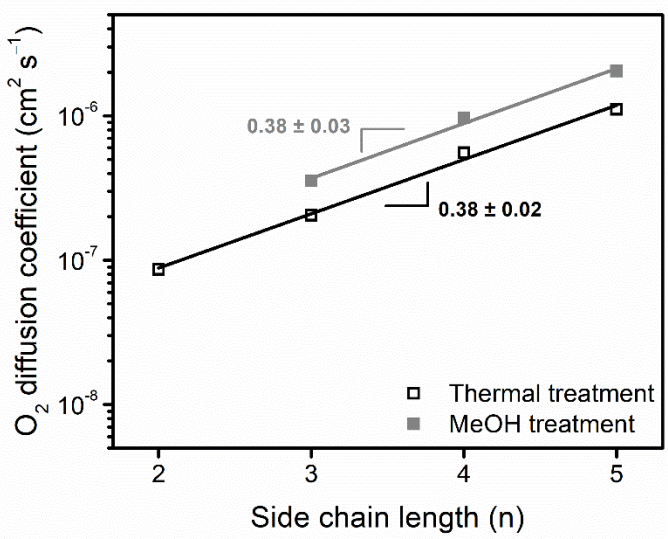

Figure 4.3. Side-chain length (*n*) versus O_2 diffusion coefficient for both thermal and methanol-treated poly(OMe *n*-mer) samples. Slopes and errors were calculated using the Origin 9.1 fitting tool.

As ROMPs have shown exceptional plasticization resistance,[180] poly(OMe *n*-mer)s undergoing methanol treatment were also subjected to plasticization studies. In particular, samples were exposed to CO_2 feed pressures of up to 51 bar at 35 °C, and results are shown in **Figure 4.4**. The hysteresis induced by conditioning samples at 51 bar CO_2 is also shown (**Figure C.5**). Data for OMe-ROMP is included for comparison. While poly(OMe 4-mer) and poly(OMe 5-mer) show excellent plasticization resistance similar to OMe-ROMP (i.e., no plasticization pressure detected up to 51 bar), poly(OMe 3-mer) exhibits a plasticization pressure of ~10 bar. Since poly(OMe 2-mer) films could not withstand the methanol treatment used for the other samples in this study, the plasticization study was conducted on thermally treated poly(OMe 2-mer), which showed a plasticization pressure of ~15 bar. With increasing side-chain length, a decrease in the hysteresis (i.e., the difference in permeability at the same feed pressure before and after conditioning at 51 bar CO_2) is also observed, with the hysteresis of poly(OMe 5-mer) being up to ~30% (compared to ~50% for OMe-ROMP). In our previous work, we hypothesized that large interchain cohesive energy present in ROMPs contributed to the plasticization resistance.[180] Our results in this study indicate that higher *n* (i.e., longer rigid side chains) lead to stronger interchain cohesive energy and greater interchain rigidity. Detailed mixed-gas studies to deepen an understanding on the plasticization resistance exhibited by ROMPs will be the subject of future studies.

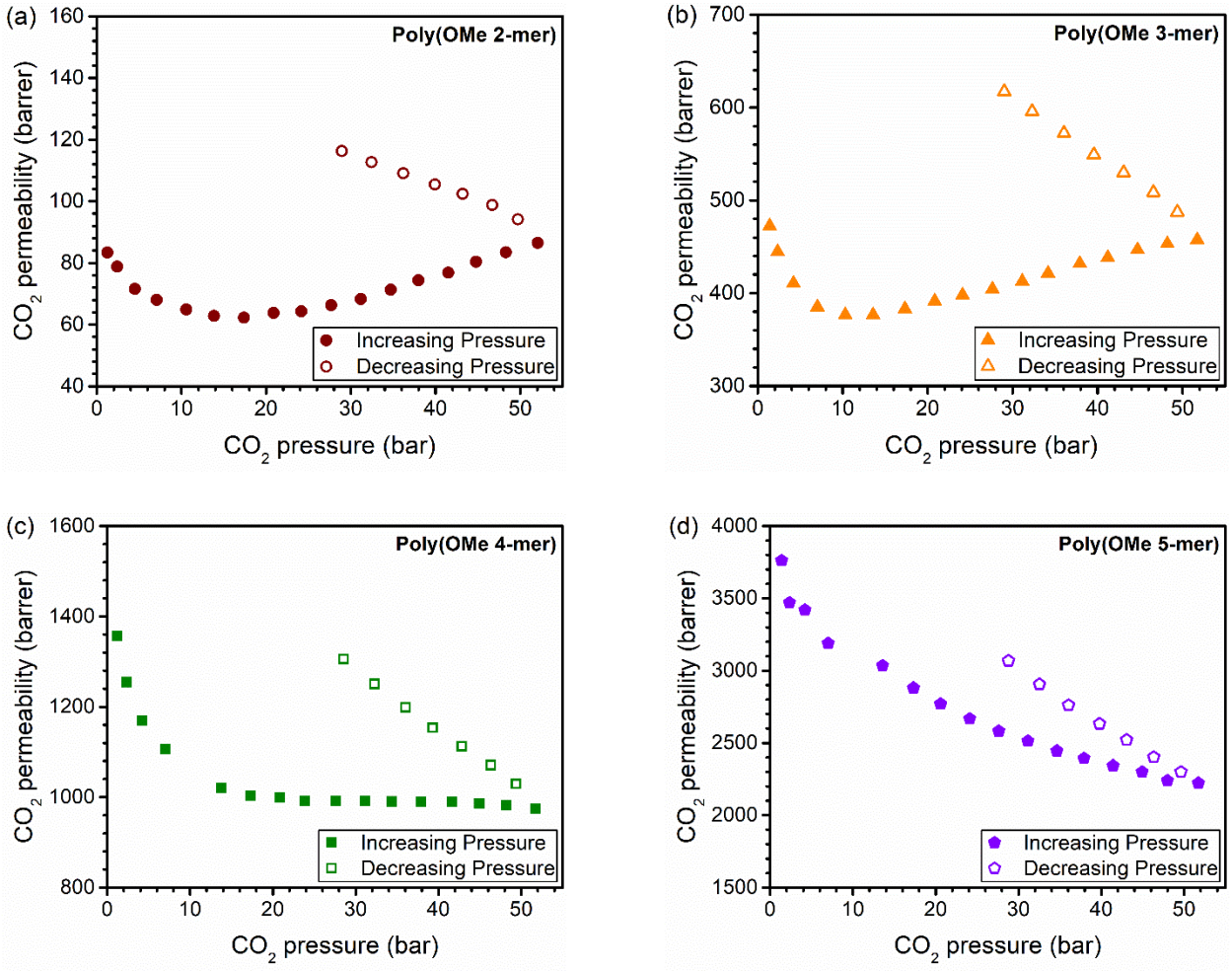

Figure 4.4. High-pressure pure-gas CO_2 permeability experiments conducted on (a) poly(OMe 2-mer), (b) poly(OMe 3-mer), (c) poly(OMe 4-mer), and (d) poly(OMe 5-mer).

4.4. Conclusions

In conclusion, we have polymerized discrete OMe oligomers with side-chain length (n) of 2 – 5 to study the effects of n on gas transport properties in these bottlebrush ROMP polymers. BET and gas transport measurements indicated that both surface area and gas permeability increased as n increased, and the properties of the OMe-ROMP with non-uniform side chains, which has non-uniform side chains of average n = 4.5, lay in between those of n = 4 and n = 5. Whereas diffusivity

increased exponentially as *n* increased, there was not an appreciable effect on selectivity. Additionally, we found that forming uniform side-chain length did not lead to improved diffusivity selectivity as was originally hypothesized, and thus selectivity remained largely unaffected. Moreover, the plasticization resistance (as determined by high-pressure pure-gas CO_2 permeation tests) was revealed to increase with increasing side-chain length, suggesting that the exceptional stability of ROMPs is attributed to the inclusion of long and rigid side chain units. Longer side chains than what have been studied here could further improve property sets such as permeability and plasticization resistance.

Chapter 5. Role of side-chain length in gas transport of CO_2/CH_4 mixtures in polymers with side chain porosity

Reprinted from **Lin, S.**; Storme, K. R.; Wu, Y.-C.; Benedetti, F. M.; Swager, T. M.; Smith, Z. P. Role of side-chain length in gas transport of CO_2/CH_4 mixtures in polymers with side chain porosity. *In preparation.*

Recently, the effect of the rigid side-chain length on the free volume and gas transport properties of a methoxy (OMe) functionalized polymer generated via ring-opening metathesis polymerization (ROMP) was reported. In this study, we elaborate further on the role of side-chain length in this polymer, henceforth referred to as OMe-ROMP. It was previously found that increasing side-chain length led to increased BET surface areas and pure-gas permeabilities. Increased diffusion coefficients with increasing side-chain length were also observed. In this study, the hypothesis that increasing side-chain length led to increased amounts of free volume was further corroborated by pure-gas sorption measurements. In addition, the plasticization resistance of OMe-ROMP with varying side-chain lengths was studied using high-pressure mixed-gas CO_2/CH_4 permeation experiments. A deeper understanding of the role of side-chain length on polymer packing and plasticization resistance can be used to optimize the structure and chemistry of ROMP polymers for gas separations.

5.1. Introduction

Over the past 25 years, natural gas processing has become one of the most widespread industrial applications for gas separations, with the world using close to 100 trillion scf (standard cubic feet) of natural gas every year.[16,186] Compared to other established technologies, polymer membranes are an energy-efficient method for gas separations due to their processability, small footprint, and scalability[1,3]. However, polymer membrane-based separations only occupy about 10% of the natural gas processing market.[2,16] This limited industrial adoption is primarily due to the trade-off that polymer membranes experience between permeability and selectivity. Most commercial membranes for gas separations currently are based on polymers with moderate selectivity but low permeability.[1,96]

Another major issue that precludes adoption of polymer membranes for gas separations is plasticization. When exposed to high pressures of condensable gases (such as CO_2), polymer chains will reorganize and swell, which increases gas permeability but reduces selectivity.[57,59,187] This issue is particularly relevant for natural gas separations, in which separation of CH_4 from CO_2 and other gases is the primary separation.[16] Since plasticization involves molecular chain movements, there have been efforts to mitigate plasticization by increasing polymer chain rigidity either through incorporating interchain interactions (such as cross-linking,[171,188–190] the formation of charge transfer complexes (CTCs),[191–194] and the introduction of hydrogen-bonding functionalities[60,61,63,64,125,192,195,196]) or restricting intrachain mobility (which include the incorporation of rigid groups like triptycene,[63,95,136,141,197] Tröger's base,[94,96,198,199] and ethanoanthracene[200] into the polymer backbone).

One strategy to address current materials limitations of polymer membranes has been the development of polymers of intrinsic microporosity (PIMs). These polymers have rigid backbones

and contorted structure that allow for inefficient packing, enhancing separation performance for a number of gas pairs.[88,93,158] Further advances have been made by incorporating bulky groups into PIM-based materials to increase rigidity even further.[62,94–96,141,173] While the incorporation of interchain interactions has seen some success in mitigating plasticization, enhancements in intrachain rigidity alone has not proven sufficient in suppressing plasticization.[162] Of note, polymers with increased intrachain rigidity, such as PIM-based materials, often have high fractional free volume that leads to increased sorption capacity for condensable gases, which likely exacerbates plasticization effects.

Recently, our group has introduced a different type of bulky structure by using ring-opening metathesis polymerization (ROMP), incorporating rigid side chains on a flexible poly(norbornene) backbone.[161,180] CF_3-ROMP and OMe-ROMP, which were named for their functionality, both showed gas transport properties that were comparable to state-of-the-art PIMs for a number of commonly-tested gas pairs. When both ROMP polymers were tested under high-pressure pure-gas CO_2 permeation up to a feed pressure of 51 bar, neither exhibited a detectable "plasticization pressure" in this pressure range, indicating that the CO_2 permeability continued to decrease with increasing pressure. A follow-up study investigated the influence of rigid side-chain length on OMe-ROMP on both the gas transport properties and plasticization resistance.[201] These polymers are referred to as poly(OMe *n*-mer), in which *n* ranged from 2 to 5. As the side-chain length increased from $n = 2$ to $n = 5$, gas permeability increased with minimal losses in permselectivity. Increasing the side-chain length also led to increased plasticization resistance. While poly(OMe 2-mer) and poly(OMe 3-mer) exhibited plasticization pressures of ~15 and ~10 bar CO_2, respectively, both poly(OMe 4-mer) and poly(OMe 5-mer) did not show any plasticization pressure up to 51 bar CO_2. In addition, the hysteresis induced by conditioning

samples at 51 bar CO_2 was ~25% at a CO_2 pressure of ~25 bar for poly(OMe 5-mer), compared to ~30% for poly(OMe 4-mer), ~55% for poly(OMe 3-mer), and ~80% for poly(OMe 2-mer). The increased plasticization resistance of monodispersed OMe-ROMP samples with increasing side-chain length was attributed to stronger interchain cohesive energy and greater intrachain rigidity.

However, high-pressure pure-gas tests in search of a plasticization pressure are not sufficient to determine whether a polymer is plasticization-resistant or not. The plasticization pressure alone does not indicate anything about the change in permselectivity for a binary separation. Even when no plasticization pressure is detected in the range of pressures tested, CO_2 can still act as a plasticizer that will swell the polymer chains and increase the diffusion coefficients of less condensable gases such as CH_4, ultimately increasing permeability of the less condensable gas and decreasing permselectivity with increasing pressure under mixed-gas conditions.[202,203] Some studies have shown that the less condensable CH_4 permeability increased and the CO_2/CH_4 permselectivity decreased with increasing pressure in CO_2/CH_4 mixed-gas tests, unambiguously indicating plasticization.[65,204,205]

In addition to permeation tests, direct sorption measurements are also a way to analyze the behavior of polymer membranes under aggressive CO_2 feed pressures. Similar to high-pressure CO_2 permeation tests, high-pressure CO_2 sorption tests involve pressurization, conditioning at a maximum feed pressure, and then depressurization. The hysteresis induced by conditioning at a high feed pressure can provide information on the effects of condensable gases on the polymer chain packing. If plasticization occurred, the sorption of penetrants can increase from before to after conditioning at high pressures of condensable gas.[206]

In this work, we further expand upon the claim that ROMP polymers are plasticization-resistant by measuring both the pure-gas sorption capacity and mixed-gas CO_2/CH_4 permeation of

monodispersed poly(OMe *n*-mer) samples with side-chain lengths ranging from $n = 2$ to $n = 5$. Fractional free volume (FFV) measurements were also measured to determine the effect of side-chain length on amount of excess free volume. CH_4 and CO_2 pure-gas sorption measurements were performed up to a feed pressure of ~50 atm, and dual-mode sorption parameters were determined for each sample. CO_2/CH_4 mixed-gas data at varying feed compositions and pressures were also conducted to determine gas transport behavior at more realistic industrial conditions.

5.2. Experimental

5.2.1. Materials

Dicyclopentadiene, sodium hydride, methyl iodide, and Grubbs 2nd-generation catalyst were purchased from commercial sources and used as received. Anhydrous dimethylformamide (DMF) was purchased from Sigma–Aldrich in SureSeal bottles and dried over 4-Å molecular sieves prior to use. Anhydrous dichloromethane (DCM) was obtained from an INERT PureSolv MD5 solvent purification system and stored under Ar over 4-Å molecular sieves. All other solvents were purchased at ACS grade or higher and used as received. 1,4-Anthraquinone was purified with a silica plug (using dichloromethane as the eluent) prior to use.

Size exclusion chromatography (SEC): SEC was performed in HPLC-grade tetrahydrofuran using an Agilent 1260 Infinity system with a guard column (Agilent PLgel; 5µm; 50 x 7.5 mm) and three analytical columns (Agilent PLgel; 5µm; 300 x 7.5 mm; 105, 104, and 103 Å pore sizes). The instrument was calibrated with polystyrene standards between 1.7 and 3150 kg•mol^{-1}. All runs were performed at 1.0 mL•min^{-1} flow rate and 35 ºC. Molecular weight values were calculated using ChemStation GPC Data Analysis Software (Rev. B.01.01) based on the refractive index signal.

5.2.2. Polymer synthesis

The polymer synthesis has been previously described[161,180] and will be summarized as follows. First, the OMe monomer was added to an oven-dried Schlenk flask, which was evacuated and backfilled with Ar three times. The monomer was heated at 140 °C (n = 2) or 220 °C (n = 3–5) for 18 h. The oligomer mixture was then separated by silica gel chromatography using a Biotage Isolera flash chromatography system with Biotage SNAP Ultra columns containing HP-Sphere 25μm silica. A solvent gradient of 5% to 40% EtOAc/hexanes was successful in providing sufficient separation. R_f decreases with increasing n. Isolated oligomers were dissolved in a small amount of DCM and precipitated in methanol prior to polymerization in order to remove impurities, presumably from the evaporated solvent used for chromatography. OMe n-mers were dried in the vacuum oven at 60 °C for at least 3 h.

For the polymerization, OMe n-mer (168 mg, 0.14 mmol, 1 equiv.) was added to an oven-dried Schlenk flask, which was evacuated and backfilled with Ar three times, and then dissolved in DCM (1 mL). In a separate oven-dried vial, Grubbs 2nd-generation catalyst (1.18 mg, 0.0014 mmol, 0.01 equiv.) was dissolved in DCM (0.4 mL). The catalyst solution was transferred by syringe into the oligomer solution, and the reaction mixture was stirred at room temperature for 18 h. The flask was unsealed and 1 drop of ethyl vinyl ether was added to quench the catalyst. The polymer solution was precipitated in methanol, and the solid was collected by vacuum filtration, washed with methanol, and dried under vacuum.

5.2.3. Polymer film preparation and characterization

Polymers were dissolved in chloroform (2 wt%) and cast onto a 50mm Norton skin on a flat-bottomed glass dish. The dish was then covered with aluminum foil, and another glass dish was

placed on top of the foil, allowing slow solvent evaporation and enabling film formation inside a chemical fumehood for 4 days. Afterward, the formed films were dried at 120 °C for 24 h under full vacuum to remove residual solvent. The thicknesses of all film samples were ~150 μm, as measured by a digital micrometer.

Polymer film density was determined using Archimedes' principle using *n*-hexane as the buoyant liquid, since the density of water was expected to be close to the sample density. Measurements were conducted using a density measurement kit from Mettler Toledo (ME-DNY-4). The fractional free volume (FFV) was then calculated for each sample using the following equation:

$$FFV = \frac{V - 1.3V_w}{V} \tag{5.1}$$

where V is the molar volume of the polymer ($cm^3\ mol^{-1}$) and V_w is the van der Waals volume of the polymer ($cm^3\ mol^{-1}$) determined using group contribution methods first developed by Bondi,[71] van Krevelen,[73] and Park and Paul[72] and updated by Wu, et al.[74]

5.2.4. High-pressure pure-gas sorption measurements

CH_4 and CO_2 high-pressure sorption isotherms were collected for all poly(OMe *n*-mer) samples at 35 °C using a dual-volume, dual-transducer automated pressure decay system from Maxwell Robotics. Approximately 0.15–0.2 g of polymer film was loaded into the sample cell that was then sealed with a VCR gasket. The system was then degassed for 8 h to remove any residual dissolved gases in the films. The temperature was controlled using a built-in air heating system. For CH_4 and CO_2, isotherms were measured up to 48–51 atm. Additionally for CO_2, depressurization isotherms were subsequently collected back down to ~1 atm in order to measure the change in sorption capacity after exposure to high pressures of CO_2. Equilibrium hold times for each pressure point

were set to 2.5 h for CH_4 and 2 h for CO_2. After measuring the sorption isotherm of CH_4, the system was held under vacuum for 6 h before measuring the sorption isotherm of CO_2. In order to correct for nonidealities, fugacity is reported based on the second virial equation of state.[207]

To generate sorption isotherms, the amount of moles sorbed into the polymer was determined for each equilibrium fugacity point using a mole balance between the initial and equilibrium conditions.[42] Isotherms were then fit using the dual-mode sorption (DMS) model:

$$C = k_D f + \frac{C'_H b f}{1 + b f} \tag{5.2}$$

where C is the concentration of gas in the polymer (cm^3_{STP} cm^{-3}_{pol}), f is the equilibrium fugacity (atm), k_D is Henry's constant (cm^3_{STP} cm^{-3}_{pol} atm^{-1}), C'_H is the Langmuir capacity constant (cm^3_{STP} cm^{-3}_{pol}), and b is the Langmuir affinity constant (atm^{-1}). The fit was performed via a nonlinear optimization using the χ^2 parameter as the objective function, and uncertainties used for the χ^2 parameter were determined from error propagation.[135] Each gas–polymer pair was optimized independently. Error bars for k_D, C'_H, and b were determined by varying each parameter (while all other parameters are fixed) about a quadratic estimation of χ^2 with respect to the varied parameter.[208,209]

The sorption coefficient can be calculated by dividing the concentration by the corresponding fugacity:

$$S = \frac{C}{f} = k_D + \frac{C'_H b}{1 + b f} \tag{5.3}$$

The sorption coefficient at infinite dilution (i.e., the sorption behavior of the first penetrant in the polymer matrix) can be determined by taking the limit of Equation 5.3 as fugacity approaches zero:

$$\lim_{f \to 0} S = S_\infty = k_D + C'_H b \tag{5.4}$$

5.2.5. Mixed-gas permeation measurements

Mixed-gas permeation tests were performed with CO_2/CH_4 mixtures at 35 °C using an automated constant-volume, variable-pressure systems from Maxwell Robotics with an in-line Agilent 7890B gas chromatograph (GC) to measure gas composition in the feed and permeate streams. The temperature was maintained using a built-in air-heating system. After loading the sample into a stainless steel permeation cell, the system was degassed overnight to remove residual dissolved gases in the film.

The upstream pressure was set using a proportional–integral–derivative (PID) controller. Feed mixtures were generated at the desired composition with Bronkhorst mass flow controllers that maintained gas flow at high rates (300–800 sccm) in order to avoid concentration polarization. The maximum stage cut value (ratio of permeate flow to sweep flow) was <1%. First, pure gas permeability measurements of CH_4 and CO_2 at ~1.1 atm were measured for each sample. Then, three CO_2/CH_4 mixture compositions (20:80, 80:20, and 50:50) were tested at a total mixed-gas feed pressure of ~2.2 atm. Afterward, the feed composition was fixed at 50:50 CO_2/CH_4 and the total mixed-gas feed pressure was increased from 2.2 to ~24 atm. For each mixed-gas step, gas was collected in a downstream volume that was previously degassed. Once the downstream pressure reached ~13.5 torr, the gas was injected into the GC for analysis.

The molar composition of gas in the downstream was calculated using the GC calibration curves. In order to calculate permeability for gas *i*, the following equation was used:

$$P_i = \frac{V_d}{RT}\frac{l}{A}\frac{1}{x_i p_2} \times y_i \frac{dp_1}{dt} \tag{5.5}$$

where V_d is the downstream volume, R is the ideal gas constant, T is the absolute experimental temperature, l is the film thickness, A is the area of film exposed to the gas, p_2 is the upstream pressure, $\frac{dp_1}{dt}$ is the rate of pressure rise in the downstream at steady state, and x and y are the mole

fractions of gas *i* in the upstream and downstream, respectively. Note that for a pure-gas case, both x_i and y_i would equal 1, which leaves Equation 5.5 to be equal to the pure-gas permeability equation:

$$P_i = \frac{V_d}{RT}\frac{l}{A}\frac{1}{p_2}\frac{dp_1}{dt} \tag{5.6}$$

5.3. Results and Discussion

Density values, van der Waals volumes, and FFV measurements of all poly(OMe *n*-mer) samples in this study are shown in **Table 5.1**. FFV as a function of *n* is also shown in **Figure 5.1**. Two different methods were used to calculate the van der Waals volume of the polymer. The first method (labeled as "Method 1") used group contribution methods developed by Bondi[71] and further expanded by van Krevelen[73] and Park and Paul,[72] while the second method (labeled as "Method 2") is an updated method developed by Wu et al.[74] In "Method 2", overlap volume between groups is taken into account, which generally leads to a smaller V_w and larger FFV value.

Table 5.1. Density, van der Waals volumes (V_w), and fractional free volume (FFV) of poly(OMe *n*-mer) samples from *n* = 2–5. "Method 1" refers to group contribution methods developed by Bondi, van Krevelen, and Park and Paul.[71–73] "Method 2" refers to an updated group contribution method developed by Wu et al.[74]

n	**Density (g cm^{-3})**	**$V_{w,Method\ 1}$ (cm^3 mol^{-1})**	**$V_{w,Method\ 2}$ (cm^3 mol^{-1})**	**FFV (Method 1)**	**FFV (Method 2)**
2	1.184 ± 0.005	362.64	325.508	0.077 ± 0.004	0.171 ± 0.004
3	1.134 ± 0.009	529.11	482.150	0.140 ± 0.007	0.216 ± 0.007
4	1.11 ± 0.02	695.58	638.792	0.17 ± 0.02	0.24 ± 0.02
5	1.12 ± 0.01	862.05	795.434	0.17 ± 0.01	0.23 ± 0.01

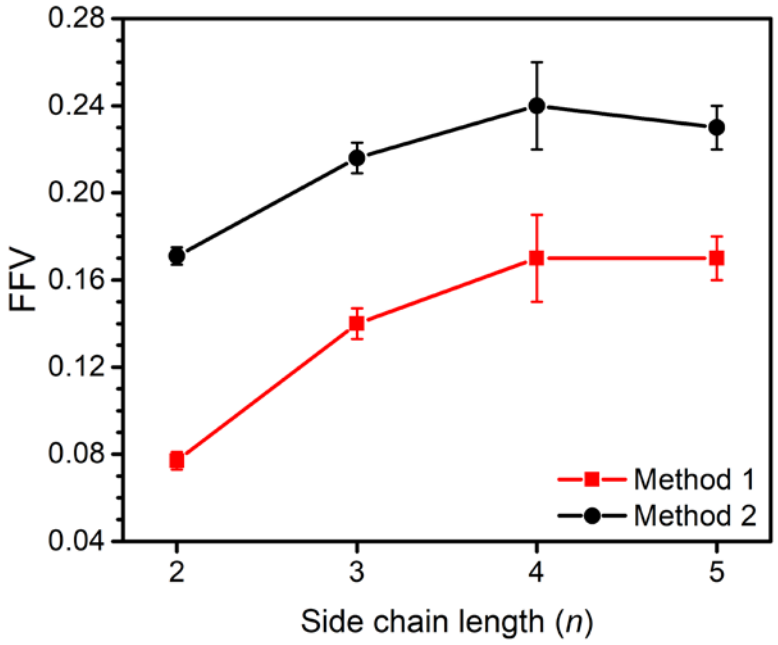

Figure 5.1. Fractional free volume (FFV) as a function of side-chain length (*n*). Red squares represent calculations using "Method 1".[71–73] Black circles represent calculations using "Method 2".[74]

There is a clear increase of FFV from $n = 2$ to $n = 4$, which suggests that the increasing rigidity from longer side chains leads to more frustrated chain packing. However, the FFV values for poly(OMe 4-mer) and poly(OMe 5-mer) are equivalent, regardless of the method used for the calculation. While group contribution methods are useful in estimating a number of bulk properties of polymers, including FFV, molecular-level details such as free volume size, shape, and distribution can be obscured by this approach.[138] We have previously reported that gas permeability increases with increasing *n*,[201] and similar correlations can be made here for gas permeability and FFV.[72,74] Different methods to probe free volume, such as positron annihilation lifetime spectroscopy (PALS) and molecular dynamics (MD) simulations,[210] would be useful tools to further understand the effects of *n* on polymer chain packing.

CH_4 and CO_2 sorption isotherms are shown in **Figure 5.2** for all poly(OMe *n*-mer) samples. The dual-mode sorption (DMS) model was used to fit sorption isotherms.[42] Sorption trends for all samples follow the trend of condensable gases having higher sorption ($S_{CO_2} > S_{CH_4}$), which is consistent with other polymers reported in the literature.[142,211] In addition, all samples show good fits to the dual-mode sorption model. After conditioning each sample at a CO_2 fugacity of ~39–41 atm and depressurizing, poly(OMe 2-mer) exhibited the largest hysteresis of all samples (i.e., the difference between the concentration of gas in the polymer before and after conditioning), while poly(OMe 5-mer) showed the smallest hysteresis. At an equilibrium fugacity of ~1 atm, there was a ~110% difference in concentration before and after conditioning for poly(OMe 2-mer) and poly(OMe 3-mer), while this difference was ~45% and ~23% for poly(OMe 4-mer) and poly(OMe 5-mer), respectively. Smaller hystereses indicate increased plasticization resistance,[212,213] suggesting that poly(OMe *n*-mer) samples with longer side chains are more plasticization resistant due to the increased rigidity from increasing side-chain length and "physical interlocking" between side chains that promote interchain rigidity and reduce CO_2-induced swelling. Similar results have been found in the past, where adding functionalities that engage in interchain hydrogen bonding to polymer backbones increase plasticization resistance.[60,61,63–65]

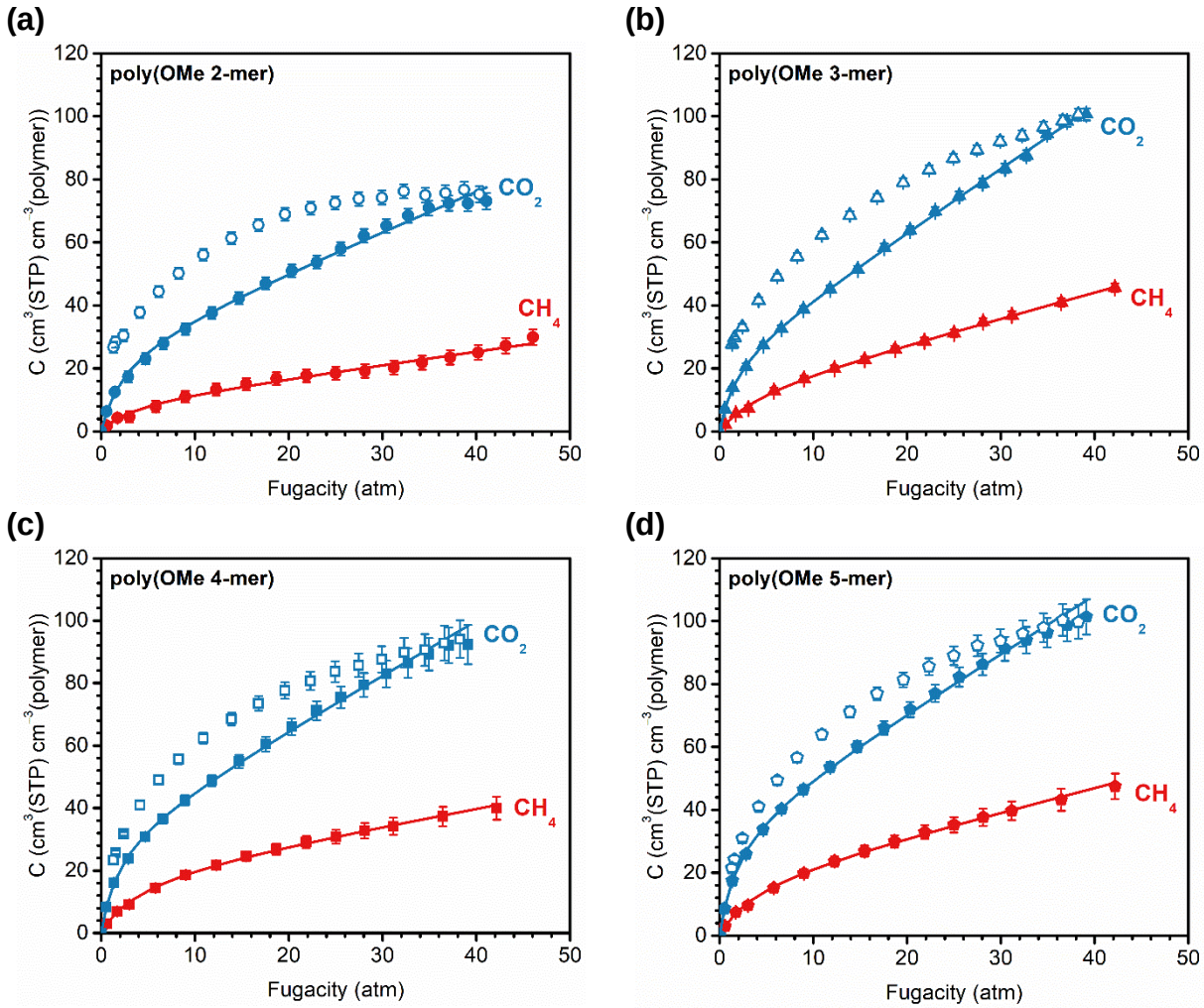

Figure 5.2. Pure-gas sorption isotherms as a function of fugacity (atm) for (a) poly(OMe 2-mer), (b) poly(OMe 3-mer), (c) poly(OMe 4-mer), and (d) poly(OMe 5-mer). Red points indicate CH_4, while blue points indicate CO_2. Filled points indicate increasing fugacity, while open points indicate decreasing fugacity. Individual points represent experimental data, while lines represent dual-mode model fits.

Dual-mode parameters are shown below for poly(OMe *n*-mer) samples in **Table 5.2**. k_D describes the sorption in the Henry's domain, which represents a hypothetical equilibrium sorption mode in the polymer.[214] As seen in **Table 5.2**, k_D for both gases considered increases from n = 2 to n =3, suggesting an increase in Henry sorption with longer side chains. However, from n = 3 to

n = 4, k_D for both gases decreased. This finding could be due to the shorter side chains in poly(OMe 3-mer) allowing for greater polymer packing efficiency, and hence, more equilibrium character compared to the longer and more rigid side chains in poly(OMe 4-mer). A similar result was found by Swaidan et al., in which the more flexible PIM-PI-1 had a higher k_D values than KAUST-PI-1 for both C_3H_6 and C_3H_8.[214] However, as side-chain length increases from n = 4 to n = 5, k_D increased for both CH_4 and CO_2, again suggesting increased Henry sorption. Taken together, these findings indicate that the dual-mode model provides limited guiding details on the packing structure of these unusual side-chain polymers.

C_H' describes the sorption in the Langmuir mode, and due to its higher condensability, CO_2 has a higher C_H' value than for CH_4 in all cases. In general, C_H' values also increase steadily with increasing n, which indicates increasing amounts of excess free volume that can accommodate more gases readily.[215] This is also consistent with the increasing diffusion coefficients previously reported[201] and increasing FFV with increasing n. The b parameter is the Langmuir affinity constant, which represents an equilibrium constant that describes the relative rates of surface adsorption to desorption to the Langmuir mode.[216] For both CH_4 and CO_2, b appears to be invariant as n increases, which is expected as the chemical composition of samples are not altered significantly with increasing n. $C_H'b$, which represents the overall nonequilibrium contribution to sorption, generally increases with increasing n, which is consistent with the FFV trends shown earlier. In addition, S^{∞}, which describes the sorption at infinite dilution, also increases with both gases with increasing n.

The ratio of nonequilibrium sorption to equilibrium sorption at infinite dilution ($C_H'b/k_D$), which is also presented in **Table 5.2**, describes a gas molecule's preference to sorb in the polymer matrix versus nonequilibrium free volume.[211] The trend between n and $C_H'b/k_D$ appears to be

invariant. This suggests that while, overall, longer side-chain length will create more excess free volume for gases to sorb onto, the amount of Henry sorption sites is also increasing.

However, it is important to note that since the dual-mode model is an additive model between Henry and Langmuir sorption sites, its validity in accurately describing the physical behavior of gas sorption has been debated.[43] In addition, plasticization effects are not accounted for in the model.[217] Therefore, while the model provides a sufficient preliminary platform to understand the effect of rigid side-chain length on the sorption capacity of the polymer, additional analysis using more complex models such as the nonequilibrium lattice fluid (NELF) model, which assumes a pseudo-equilibrium state in glassy polymers,[43,44,218] can provide a better understanding of the sorption behavior of ROMPs.

Table 5.2. Dual-mode sorption model parameters for all poly(OMe n-mer) samples. Units of k_D are in cm^3(STP) cm^{-3}(polymer) atm^{-1}, units of C'_H are in cm^3(STP) cm^{-3}(polymer), units of b are in atm^{-1}, and units of S^∞ are in cm^3(STP) cm^{-3}(polymer).

n	Gas	k_D	C'_H	b	$C'_H b$	S^∞	$C'_H b/k_D$
2	CH_4	0.41 ± 0.04	10 ± 1	0.3 ± 0.1	3 ± 1	3 ± 1	7 ± 3
	CO_2	1.24 ± 0.04	28 ± 1	0.41 ± 0.06	12 ± 2	13 ± 2	9 ± 1
3	CH_4	0.79 ± 0.03	13.5 ± 0.8	0.25 ± 0.05	3.4 ± 0.7	4.2 ± 0.7	4.3 ± 0.9
	CO_2	1.99 ± 0.03	25.1 ± 0.7	0.56 ± 0.05	14 ± 1	16 ± 1	7.2 ± 0.7
4	CH_4	0.54 ± 0.06	20 ± 1	0.24 ± 0.04	4.9 ± 0.8	5.4 ± 0.8	9 ± 2
	CO_2	1.71 ± 0.08	33 ± 1	0.52 ± 0.05	17 ± 2	19 ± 2	10 ± 1
5	CH_4	0.75 ± 0.07	19 ± 1	0.26 ± 0.04	4.9 ± 0.9	5.7 ± 0.9	6 ± 1
	CO_2	1.83 ± 0.07	37 ± 1	0.50 ± 0.07	19 ± 1	20 ± 1	10.2 ± 0.9

While useful in many aspects, pure-gas data is often not representative of realistic conditions. Mixed-gas data can differ significantly from pure-gas data, especially in mixtures that contain condensable gases such as CO_2. In some cases, the change in performance from pure- to mixed-gas measurements is favorable. Condensable gases that have high polymer affinity can

effectively hinder the transport of less condensable gases, increasing overall permselectivity. For example, Swaidan et al. demonstrated that a thermally-annealed PIM-polyimide (TPDA-APAF) exhibited mixed-gas CO_2/CH_4 permselectivities 10–20% higher than those under pure-gas conditions due to competitive sorption of CO_2 over CH_4.[60] Du et al. reported increases in CO_2/N_2 permselectivity of TZ-PIM-1 from the pure- to mixed-gas case of over 30% due to favorable sorption of CO_2.[163]

However, the change in performance from the pure- to mixed-gas scenario can also be unfavorable. The presence of a condensable gas can cause swelling, which in turn results in an upturn the permeability isotherm of non-condensable gases. For example, Swaidan et al. reported that in a 50:50 CO_2/CH_4 mixture, the CH_4 permeability of PIM-1 was up to 60% higher than in the pure-gas case.[65] This increase in CH_4 permeability also led to a decrease in CO_2/CH_4 permselectivity, with the CO_2/CH_4 permselectivity of PIM-1 dropping about 38% from 4 to 20 bar total pressure.[65] Similar effects have been observed for other microporous polymers and carbon molecular sieve derivatives.[162,205]

In a previous study, the effect of side-chain length of poly(OMe *n*-mer) on pure-gas CO_2 permeability as a function of pressure was evaluated. It was found that longer side chains exhibited less hysteresis after conditioning at 51 bar CO_2 feed pressure, suggesting that increased rigidity of longer side chains contribute to increased plasticization resistance.[201] Here, this claim is further elucidated using mixed-gas CO_2/CH_4 tests. First, the pure-gas CH_4 and CO_2 permeabilities for all poly(OMe *n*-mer) samples were tested at ~1.1 atm. Then, samples were tested with a 20:80, 80:20, and 50:50 CO_2/CH_4 mixture at ~2.2 atm. All data is presented in **Table 5.3**. As shown in **Figure 5.3**, a rise in CO_2/CH_4 permselectivity is observed from the pure- to mixed-gas case for all samples considered, regardless of mixture composition. This can be attributed to competitive sorption, in

which CO_2 preferentially sorbs into the polymer over CH_4, lowering CH_4 sorption and permeability. This phenomena is also evident in the drop in CH_4 permeability from the pure- to mixed-gas case. Slightly lower CO_2 permeabilities in the mixed-gas case compared to the pure-gas case are also observed for all samples, due to some competitive sorption with CH_4.

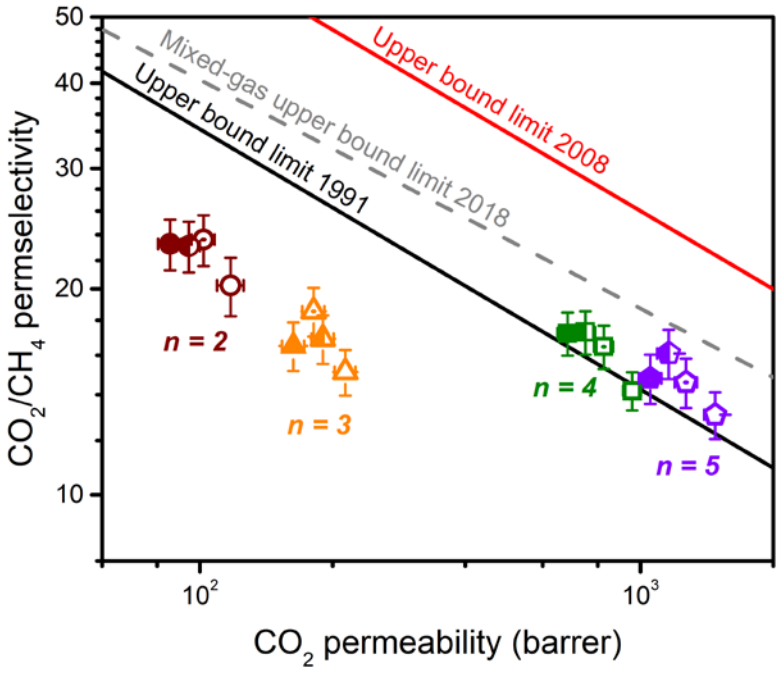

Figure 5.3. Robeson upper bound plots of all poly(OMe *n*-mer) samples. Open symbols represent pure-gas data collected at ~1.1 atm feed pressure. Symbols with a dot in the center (20:80 CO_2/CH_4), half-filled symbols (50:50 CO_2/CH_4), and filled symbols (80:20 CO_2/CH_4) represent mixed-gas data collected at ~2.2 atm total feed pressure. All data were obtained at 35 °C. Solid red line represents the 2008 Robeson upper bound,[47] solid black line represents the 1991 Robeson upper bound,[46] and gray dashed line represents the 2018 mixed-gas upper bound.[52]

Table 5.3. CO_2/CH_4 gas transport properties of all poly(OMe *n*-mer) samples at ~1.1 atm feed pressure (for pure gases) or ~2.2 atm total feed pressure (for mixtures). Permeability (***P***) is given in barrer (10^{-10} cm^3(STP) cm cm^{-2} s^{-1} $cmHg^{-1}$). All data were obtained at 35 °C.

n	**Mixture composition (CO_2/CH_4)**	P_{CO_2}	P_{CH_4}	α_{CO_2/CH_4}
2	Pure	117 ± 8	5.8 ± 0.4	20 ± 2
	20:80	102 ± 6	4.3 ± 0.3	24 ± 2
	50:50	94 ± 6	4.1 ± 0.3	23 ± 2
	80:20	86 ± 5	3.7 ± 0.2	23 ± 2
3	Pure	210 ± 10	14.1 ± 0.8	15 ± 1
	20:80	180 ± 10	9.8 ± 0.6	19 ± 2
	50:50	190 ± 10	11.2 ± 0.7	17 ± 1
	80:20	163 ± 9	9.9 ± 0.6	17 ± 1
4	Pure	960 ± 40	67 ± 3	14.2 ± 0.9
	20:80	830 ± 40	42 ± 2	16 ± 1
	50:50	750 ± 40	43 ± 2	17 ± 1
	80:20	680 ± 40	40 ± 2	17 ± 1
5	Pure	1480 ± 80	113 ± 6	13 ± 1
	20:80	1270 ± 70	87 ± 5	15 ± 1
	50:50	1160 ± 60	71 ± 4	16 ± 1
	80:20	1050 ± 70	72 ± 4	15 ± 1

Poly(OMe 4-mer) and poly(OMe 5-mer) were then tested with a 50:50 CO_2/CH_4 mixture at 35 °C up to a total feed pressure of ~24 atm. As previously reported, these two samples did not show a plasticization pressure up to a pure-gas CO_2 feed pressure of 51 bar.[201] Mixed-gas CO_2 and CH_4 permeabilities are shown in **Figure 5.4**, while mixed-gas CO_2/CH_4 permselectivities are shown in **Figure 5.5**. Gas transport measurements are also summarized in **Table D.1**. For both samples, CO_2 and CH_4 permeabilities initially decreased with increasing pressure, which is due to preferential sorption of the Langmuir mode and the subsequent reduction of the sorption coefficient.[215] For poly(OMe 4-mer), while CO_2 permeability continues to decrease up to a CO_2 partial pressure of ~12 atm, CH_4 permeability begins to increase at a CO_2 partial pressure of ~3.4 atm. This phenomenon of increasing permeability, which is referred to as "CH_4-creep", is an

unambiguous indication of CO_2-induced plasticization.[60] In fact, over the pressure range tested, CH_4 permeability increases by about 25% (**Figure 5.4a**). CO_2/CH_4 permselectivity rapidly begins to decrease after a CO_2 partial pressure of ~4 atm (**Figure 5.5a**), and the total decrease in permselectivity over the tested pressure range is ~50%.

For poly(OMe 5-mer), at around a CO_2 partial pressure of 7 atm partial pressure, CH_4 permeability began to increase slightly. However, poly(OMe 5-mer) experienced an overall ~10% decrease in CH_4 permeability over the pressure range tested (**Figure 5.4b**), as well as a ~30% decrease in CO_2/CH_4 permselectivity (**Figure 5.5b**). Compared to poly(OMe 4-mer), poly(OMe 5-mer) exhibited more plasticization resistance, as both the CH_4 permeability increase and the CO_2/CH_4 permselectivity decrease over the tested pressure range is much less extreme.

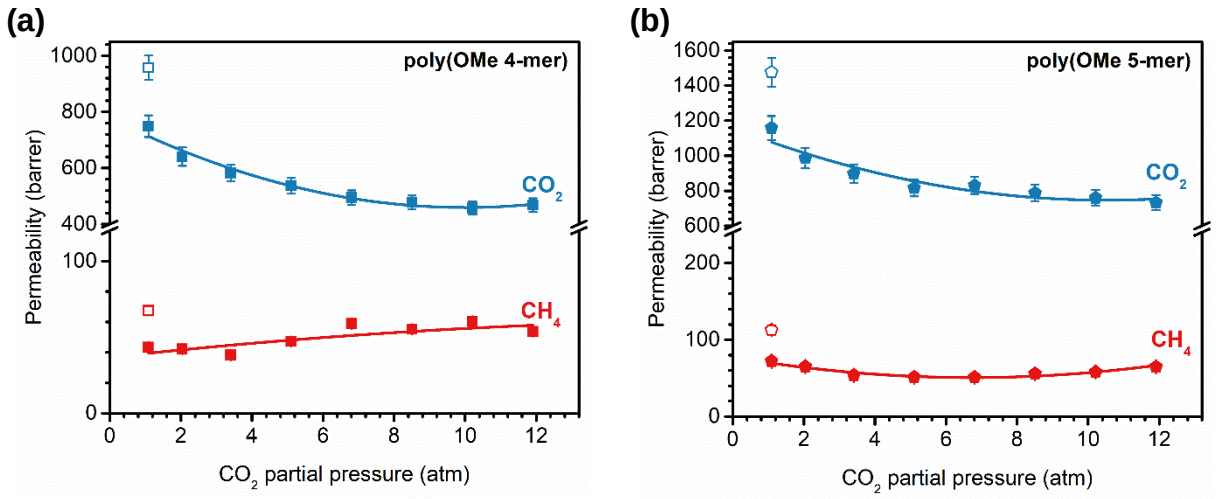

Figure 5.4. Mixed-gas CO_2 (blue) and CH_4 (red) permeabilities as functions of CO_2 partial pressure (50:50 CO_2/CH_4 mixture at 35 °C) for (a) poly(OMe 4-mer) and (b) poly(OMe 5-mer). Open symbols represent pure-gas data at ~1.1 atm, and filled symbols represent mixed-gas data. Lines are drawn to guide the eye.

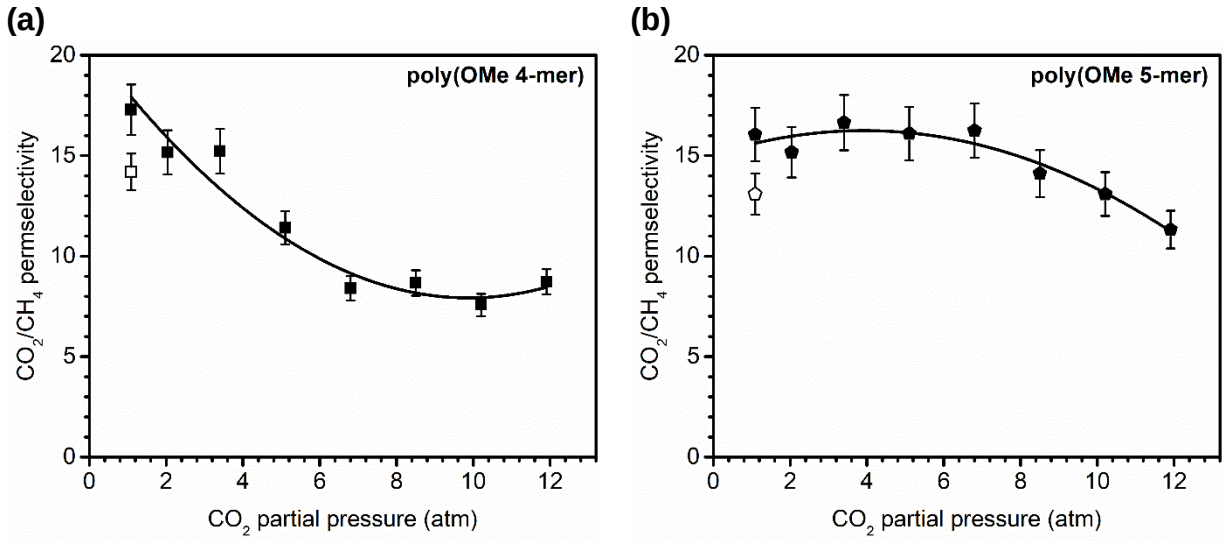

Figure 5.5. Mixed-gas CO_2/CH_4 permselectivity as a function of CO_2 partial pressure (50:50 CO_2/CH_4 mixture at 35 °C) for (a) poly(OMe 4-mer) and (b) poly(OMe 5-mer). Open symbols represent pure-gas data at ~1.1 atm, and filled symbols represent mixed-gas data. Lines are drawn to guide the eye.

5.4. Conclusions

Fractional free volume (FFV) estimates were determined for poly(OMe *n*-mer) samples (*n* = 2–5) using group contribution methods, and results indicated that FFV generally increased with increasing *n*, suggesting increasing free volume with increasing side-chain length and rigidity. Pure-gas CH_4 and CO_2 sorption measurements on all poly(OMe *n*-mer) samples revealed that increasing *n* led to increasing sorption via the Langmuir mode. In addition, with increasing *n*, hysteresis from sorption experiments decreased, indicating that longer rigid side chains contribute to decreased swelling in the presence of CO_2. Lastly, mixed-gas CO_2/CH_4 permeation tests on poly(OMe *n*-mer) samples were conducted, and it was found that at low pressures, both CO_2 and CH_4 permeability decreased and CO_2/CH_4 permselectivity increased from the pure- to mixed-gas

case for all samples, which is due to competitive sorption effects. High-pressure mixed-gas tests up to a feed pressure of ~24 atm were also performed for poly(OMe 4-mer) and poly(OMe 5-mer), as previous studies showed that these two samples did not show a plasticization pressure up to a pure-gas CO_2 feed pressure of 51 bar. For mixture tests, poly(OMe 4-mer) experienced a ~25% increase in CH_4 permeability and a ~50% decrease in CO_2/CH_4 permselectivity over the pressure range tested. However, poly(OMe 5-mer) displayed more plasticization resistance with a ~10% decrease in CH_4 permeability and a ~30% decrease in CO_2/CH_4 permselectivity over the pressure range tested.

Chapter 6. Conclusions and Future Directions

6.1. Thesis Summary

This thesis aims to discuss alternative methods to manipulate the free volume architecture of polymer membranes, with the end application being that of gas separations. Two different approaches were discussed: a “top down” method that involves thermal treatments to remove functional groups and subsequently generate porosity in a polymer film, and a “bottom up” method which explores a different type of polymer architecture of rigid, pore-generating side chains on a flexible polymer backbone.

Chapter 2 described the “top down” method in which a 6FDA-HAB polyimide was functionalized with tert-butoxycarbonyl (t-BOC) and later exposed to varying thermal treatments in order to selectively remove different amounts of t-BOC. While the original hypothesis of this study was that thermal treatments well below the polymer glass transition temperature would be able to remove thermally labile functionalities without altering the rest of the polymer structure, it was found that the polymer still underwent structural rearrangements during thermal treatments. Free volume generated from thermal deprotection thus could not be retained. However, applying this technique to more rigid polymer systems may allow for more controlled free volume manipulation.

Chapter 3 introduced a type of polymer architecture that had not before been studied for gas separation applications. Polymers with rigid, pore-generating side chains appended on a flexible backbone were generated via ring-opening metathesis polymerization (ROMP). The two polymers in this study, CF_3-ROMP and OMe-ROMP (named for their functionalities), showed gas transport properties similar to state-of-the-art PIM materials, as well as unprecedented resistance to both CO_2-induced plasticization and physical aging.

Chapter 4 expanded upon the results presented in Chapter 3 by elucidating the role of side-chain length and dispersity on gas transport properties. In the previous study, side-chain lengths of both CF_3-ROMP and OMe-ROMP ranged from $n = 2$ to $n = 9$ repeat units, with an average side-chain length of ~4.5. In this study, OMe-ROMP with uniform side chains ranging from $n = 2$ to $n = 5$ repeat units were synthesized. As side-chain length increased, both BET surface area and gas permeability increased, with minimal losses in permselectivity for all common gas pairs considered. BET surface area and gas permeability for polydispersed OMe-ROMP, with an average side-chain length of $n = 4.5$, aligned well with the trends found for BET surface area and permeability versus side-chain length, indicating no significant effect of dispersity on polymer packing and gas transport. In addition, high-pressure pure-gas CO_2 permeation tests were run on all samples to determine the effect of side-chain length on plasticization resistance. Increasing side-chain length resulted in more plasticization resistance, with the disappearance of a detectable plasticization pressure and decreasing hysteresis after conditioning at a feed pressure of 51 bar CO_2.

In Chapter 5, the unprecedented plasticization resistance of ROMP polymers was analyzed even further using pure-gas sorption and mixed-gas tests. First, FFV estimates were calculated from group contribution measurements on poly(OMe *n*-mer) samples ($n = 2$–5), and it was found that increasing side-chain length generally lead to higher FFV values, indicating that the increasing rigidity of longer side chains contributed to excess free volume. Pure-gas CO_2 and CH_4 sorption measurements were then performed on all samples, and sorption isotherms were fit using the dual-mode sorption (DMS) model. In addition, CO_2 sorption isotherms of all samples after conditioning at ~39–41 atm CO_2 were collected. While poly(OMe 2-mer) showed the largest hysteresis (i.e., difference in CO_2 sorption before and after conditioning), indicating plasticization, poly(OMe 5-

mer) showed the smallest hysteresis, which support the claim that longer and more rigid side chains can contribute to plasticization resistance. DMS model fitting also indicated that increasing side-chain length led to increased sorption in the Langmuir mode. Lastly, CO_2/CH_4 mixed-gas tests were performed on all samples, and results at a pure-gas feed pressure of ~1.1 atm and a mixed-gas feed pressure of ~2.2 atm were compared. It was found that both CO_2 and CH_4 permeability decreased while CO_2/CH_4 permselectivity increased from the pure- to mixed-gas cases for all poly(OMe *n*-mer) samples, which is indicative of competitive sorption effects. Poly(OMe 4-mer) and poly(OMe 5-mer) were also exposed to a mixed-gas CO_2/CH_4 feed of up to ~24 atm total feed pressure, and while poly(OMe 4-mer) showed signs of plasticization with increasing CH_4 permeability and decreasing permselectivity, poly(OMe 5-mer) still exhibited excellent plasticization resistance.

6.2. Future Directions

While the original "top down" method to free volume manipulation via thermal treatments to remove functionalities did not yield results that aligned with the original hypothesis, a greater understanding of polymer chain architecture when exposed to elevated temperatures was gained. More rigid polymer systems, such as cross-linked polymers with thermally labile functionalities could be considered in future studies. The increased rigidity could allow the free volume elements formed from deprotection to be preserved. Appendix E describes an initial study utilizing a co-polymer of 6FDA-HAB-t-BOC and BTDA-DAM, which contains a UV cross-linkable benzophenone functionality that has been previously explored in literature.[219–221]

In addition, alternative methods to remove chemical functionalities could be explored in order to eliminate additional effects thermal treatments can have on polymer membranes. It has

been shown in the past that thermal treatments can accelerate physical aging, which consequently lowers the free volume and permeability of polymer membranes even below the glass transition temperature. As such, using functional groups that can be easily removed via acid treatments or UV treatments, such as o-nitrobenzyl, could be studied.[222,223]

In this thesis, a different "bottom up" method to manipulate free volume was also described. Polymers were synthesized using ring-opening metathesis polymerization (ROMP), and the gas transport properties of both CF_3-ROMP and OMe-ROMP were described. Since the difference in functionality led to vastly different gas transport properties, it is hypothesized that gas transport properties can be tuned based on functionality. Since PIM-1, which is a state-of-the-art polymer that is commonly studied in gas transport applications, contain nitrile (–CN) functional groups, CN-ROMP can be synthesized to be more directly comparable to PIM-1. In particular, since PIM-1 has shown high sorption to CO_2,[142,224] direct sorption measurements of both CN-ROMP and PIM-1 can be performed. If CN-ROMP shows an increased CO_2 affinity compared to CF_3-ROMP and OMe-ROMP, mixed-gas tests can also be performed to determine whether increased CO_2 sorption may compromise the plasticization resistance seen in ROMP polymers so far. Additional functionalization with different groups such as amine,[153,224,225] amide,[226] carboxylic acid,[211,227,228] and tetrazole[163] that have been considered for PIM-1 could be studied for the ROMP class of polymers as well.

As ROMP polymers have shown unprecedented plasticization resistance, additional condensable gases that are relevant in industry, such as H_2S, C_3H_6, and C_3H_8, and their transport through these polymers can be studied. In particular, in mixtures containing CO_2, CH_4, and H_2S, plasticization can occur since H_2S is more condensable than CO_2. However, the presence of H_2S may actually have benefits, as H_2S/CH_4 permselectivity has been shown to increase with

increasing feed pressure due to the dominance of sorption selectivity over diffusion selectivity.[229,230] Poly(OMe 5-mer) displayed excellent plasticization resistance even in a CO_2/CH_4 mixture, and thus its interesting properties can be studied in more complex gas mixtures.

Appendix A. Supporting Information for Chapter 2

Reprinted with permission from **Lin, S.**; Joo, T.; Benedetti, F. M.; Chen, L. C.; Wu, A. X.; Mizrahi Rodriguez, K.; Qian, Q.; Doherty, C. M.; Smith, Z. P. Free Volume Manipulation of a 6FDA-HAB Polyimide Using a Solid-State Protection/Deprotection Strategy. *Polymer* **2021**, *212*, 123121.

A.1. Characterization of 6FDA-HAB, 6FDA-HAB-t-BOC, and thermally treated samples

The ^{1}H NMR spectra of both 6FDA-HAB and 6FDA-HAB-t-BOC powder samples are shown below in **Figure A.1**. Water (H_2O) and DMSO peaks are labeled accordingly. The ^{1}H NMR results for 6FDA-HAB match those reported in literature.[98] The proton labeled "H" correspond to the protons in the t-BOC group, while the proton labeled "A" corresponds to the proton in the hydroxyl group. The protons labeled "B" through "G" have slightly different chemical shifts between 6FDA-HAB and 6FDA-HAB-t-BOC, which relates to small differences in shielding effects that are expected as a result of different ortho-positioned functional groups on the diamine. The shift of protons labeled "E", "F", and "G" is significantly more prominent because of their proximity to the ortho-positioned functional group on the diamine.

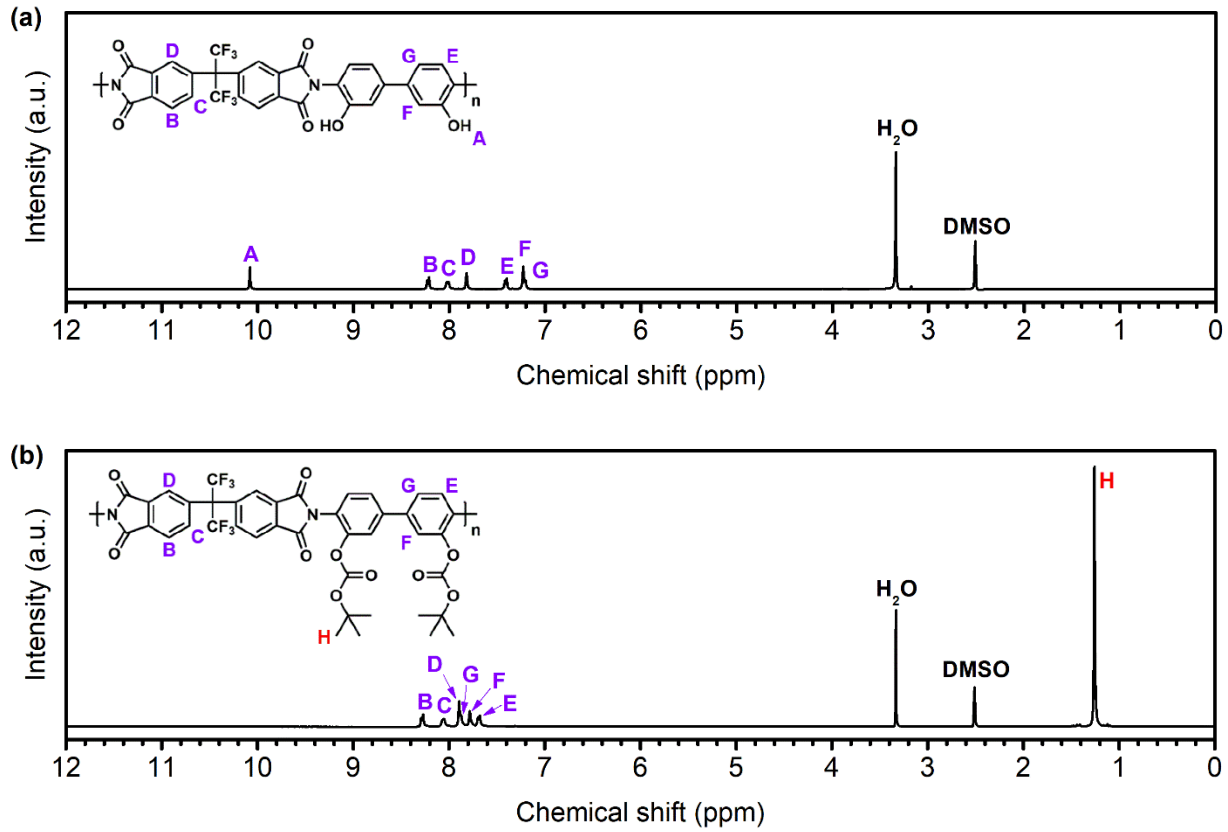

Figure A.1. ^{1}H NMR spectra of (a) 6FDA-HAB and (b) 6FDA-HAB-t-BOC powders in DMSO-d_6.

Table A.1. GPC data for 6FDA-HAB and 6FDA-HAB-t-BOC.

Polymer	M_n **(kDa)**	M_w **(kDa)**	**PDI**
6FDA-HAB	81.8	189	2.30
6FDA-HAB-t-BOC	95.6	184	1.92

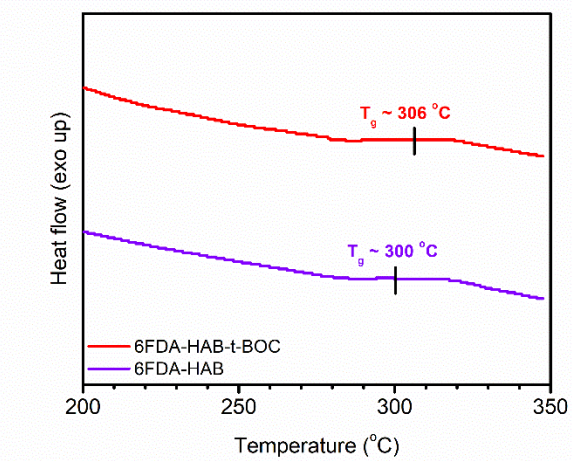

Figure A.2. DSC scans of 6FDA-HAB and deprotected 6FDA-HAB-t-BOC films. Glass transition temperature (T_g) values are labeled for each sample. Scans are offset for ease of viewing.

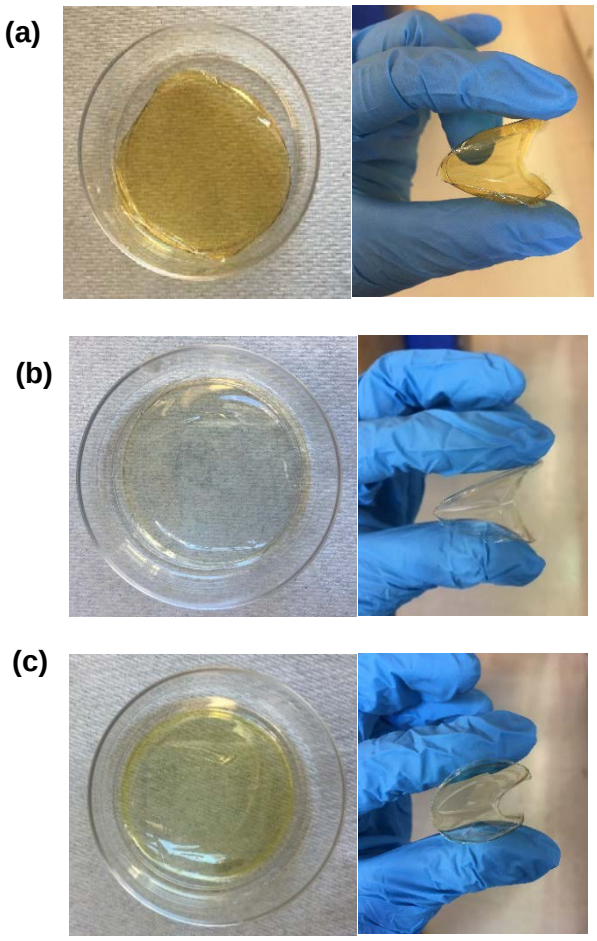

Figure A.3. Films of (a) 6FDA-HAB, (b) 6FDA-HAB-t-BOC, and (c) thermally treated 6FDA-HAB-t-BOC. Films were cast in 5 cm flat-bottom glass dishes. Heating of 6FDA-HAB-t-BOC films caused a slight color change (from optically transparent to slightly yellow), but flexibility was maintained.

The changes in chemical structure as 6FDA-HAB-t-BOC films underwent thermal treatment was also tracked using FTIR, as presented in **Figure A.4**. In the FTIR spectrum for 6FDA-HAB-t-BOC, a C–H stretching peak associated with the methyl functionality on t-BOC is observed at approximately 3000 cm^{-1}. This C–H peak decreased in intensity as 6FDA-HAB-t-BOC was thermally treated for longer periods of time. In its place, a weak and broad band characteristic of O–H stretching between 3200 cm^{-1} and 3600 cm^{-1} became more noticeable as exposure time to thermal treatment increased. This O–H stretch is also present in the FTIR spectrum for 6FDA-HAB, which further confirms that thermal treatment converts 6FDA-HAB-t-BOC to 6FDA-HAB.

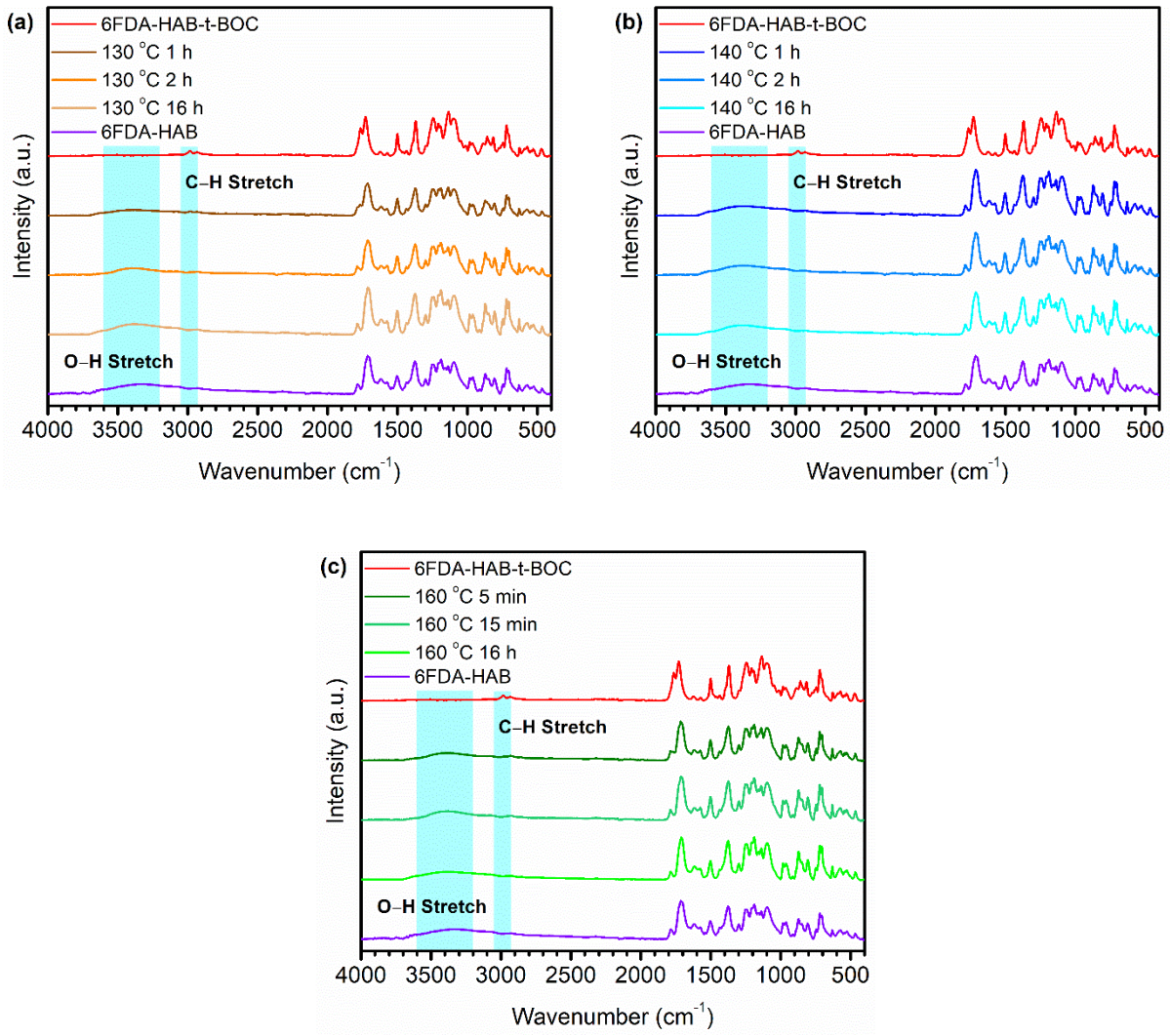

Figure A.4. FTIR spectra of 6FDA-HAB and 6FDA-HAB-t-BOC reference samples, and 6FDA-HAB-t-BOC films that had previously undergone thermal treatments at (a) 130 °C, (b) 140 °C, and (c) 160 °C. Bands of interest for C–H and O–H peaks are highlighted in light blue and labeled accordingly.

A.2. Heteronuclear single quantum correlation (HSQC) and NMR spectra

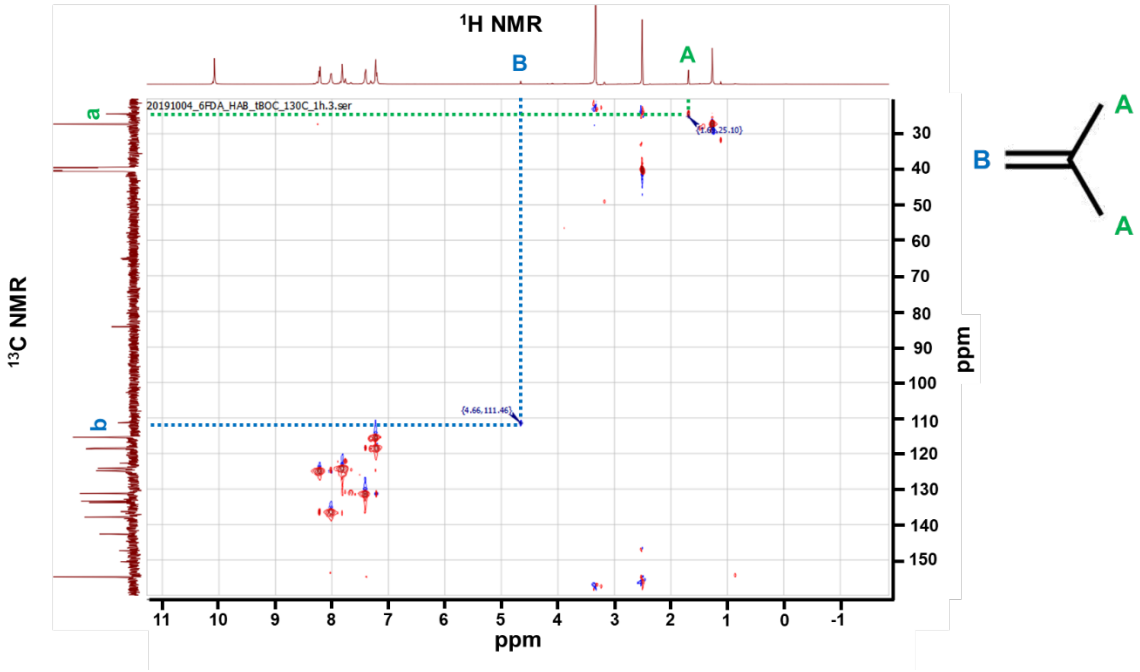

Figure A.5. HSQC of 6FDA-HAB-t-BOC films treated at 130 °C, 1h (t-BOC-130-1h) in DMSO-d_6, with the chemical structure of isobutylene for reference. Isobutylene peaks are labeled accordingly.

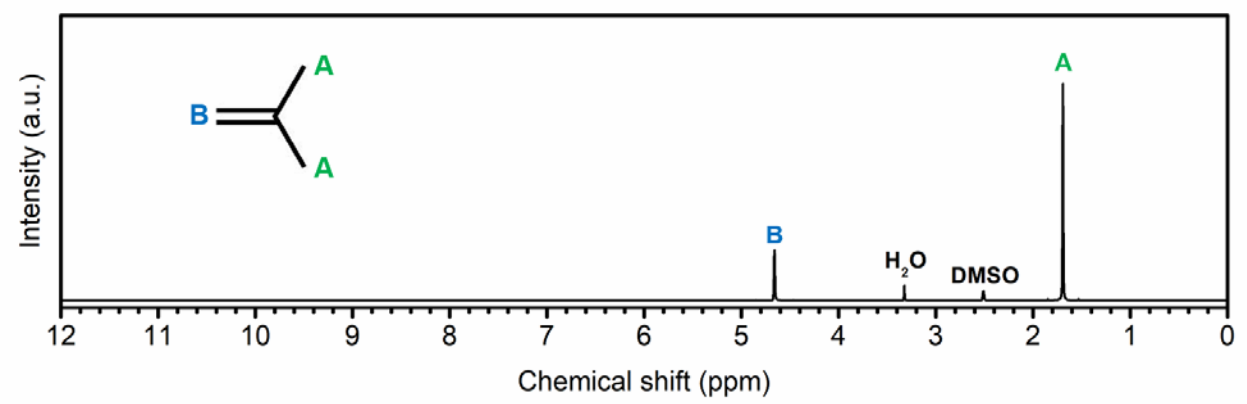

Figure A.6. ^{1}H NMR spectra of isobutylene in DMSO-d_6. Water, DMSO, and isobutylene peaks are labeled accordingly. Labeled isobutylene peaks (at 1.69 ppm and 4.66 ppm) further conclude the presence of isobutylene in 6FDA-HAB-t-BOC samples undergoing thermal treatment.

A.3. Estimation of isobutylene amount after thermal treatment

The amount of isobutylene remaining in the polymer matrix after thermal treatments ($wt\%\ trapped\ isobutylene$) was estimated to determine if the residual gas could have a notable impact on measurements performed in this study. Data from both TGA scans in **Figure 2.3** and NMR results in **Figure 2.2** were used. The $wt\%\ loss\ before\ 300\ °C$, from TGA, for each sample is shown in **Table A.2**, and can be assumed to be the sum of the $wt\%\ t\text{-}BOC\ after\ treatment$ and the $wt\%\ trapped\ isobutylene$, as shown below:

$$wt\%\ loss\ before\ 300\ °C = (wt\%\ t\text{-}BOC\ after\ treatment) + (wt\%\ trapped\ isobutylene) \quad (A.1)$$

In order to determine the $wt\%\ t\text{-}BOC\ after\ treatment$, the $\%\ t\text{-}BOC\ after\ treatment$ was found using NMR data from **Table 2.2**:

$$\%\ t\text{-}BOC\ after\ treatment = 100 - Percent\ Conversion \quad (A.2)$$

Molecular weights of each sample were also calculated:

$$MW\ of\ sample = (MW\ of\ 6FDA\text{-}HAB) * (Percent\ Conversion) + (MW\ of\ 6FDA\text{-}HAB\text{-}t\text{-}BOC) * (\%\ t\text{-}BOC\ after\ treatment) \quad (A.3)$$

in which $MW\ of\ 6FDA\text{-}HAB$ is equal to 624.36 g/mol and $MW\ of\ 6FDA\text{-}HAB\text{-}t\text{-}BOC$ is equal to 824.69 g/mol. The $wt\%\ of\ t\text{-}BOC\ after\ treatment$ was then determined:

$$wt\%\ of\ t\text{-}BOC\ after\ treatment = \frac{MW\ of\ sample - MW\ of\ 6FDA\text{-}HAB}{MW\ of\ sample} \quad (A.4)$$

The $wt\%\ trapped\ isobutylene$ could then be determined from Equation A.1. Results are tabulated in **Table A.2** for each sample.

Table A.2. Approximate amount of isobutylene remaining in thermally treated samples.

Sample Name	**wt% loss before 300 °C**	**% t-BOC after treatment**	**MW of sample**	**wt% t-BOC after treatment**	**wt% trapped isobutylene**
t-BOC-130-1h	5.56	11.48	647.35	3.55	2.01
t-BOC-130-2h	4.32	6.87	638.12	2.16	2.16
t-BOC-130-16h	1.56	4.32	633.01	1.37	0.19
t-BOC-140-1h	3.12	7.31	639.01	2.29	0.83
t-BOC-140-2h	1.88	4.54	633.45	1.43	0.45
t-BOC-140-16h	1.56	4.51	633.39	1.43	0.13
t-BOC-160-5min	6.54	12.66	649.73	3.90	2.64
t-BOC-160-15min	2.57	5.00	634.38	1.58	0.99
t-BOC-160-16h	1.41	5.58	635.54	1.76	-0.35

A.4. Effect of treatment on gas transport properties

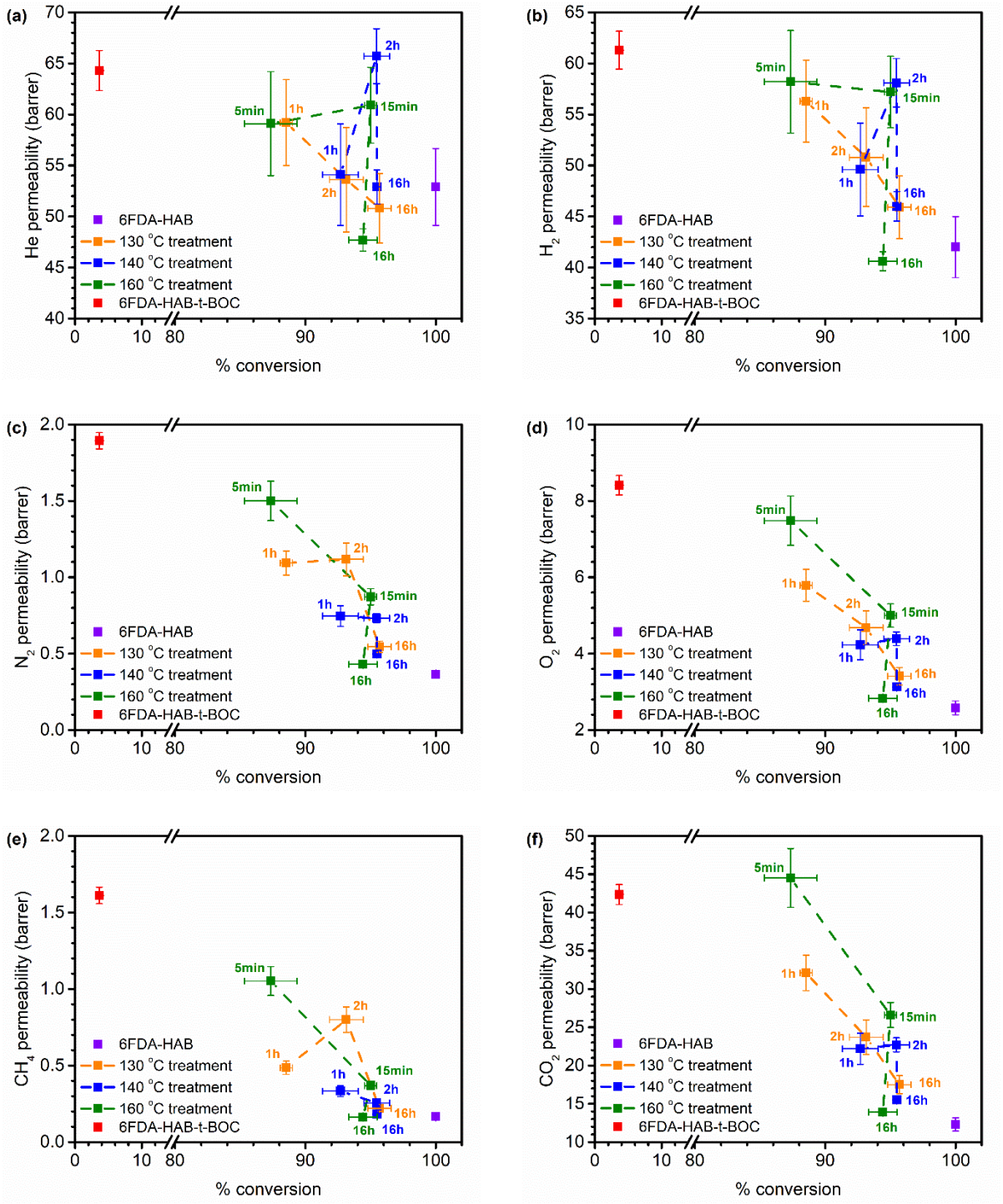

Figure A.7. Percent conversion compared to permeability for (a) He, (b) H_2, (c) N_2, (d) O_2, (e) CH_4, and (f) CO_2. Dashed lines have been added to guide the eye.

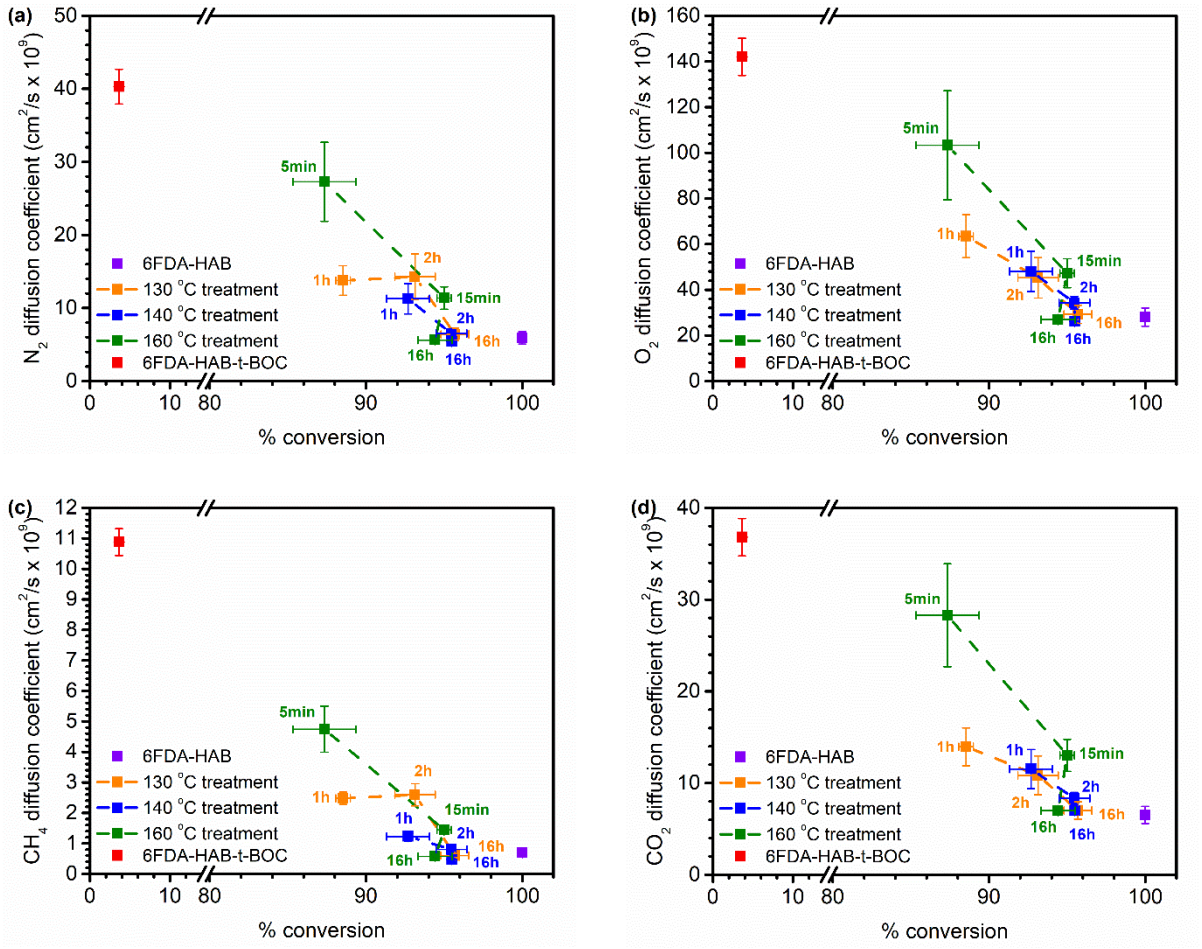

Figure A.8. Percent conversion compared to diffusion coefficients for (a) N_2, (b) O_2, (c) CH_4, and (d) CO_2. Dashed lines have been added to guide the eye.

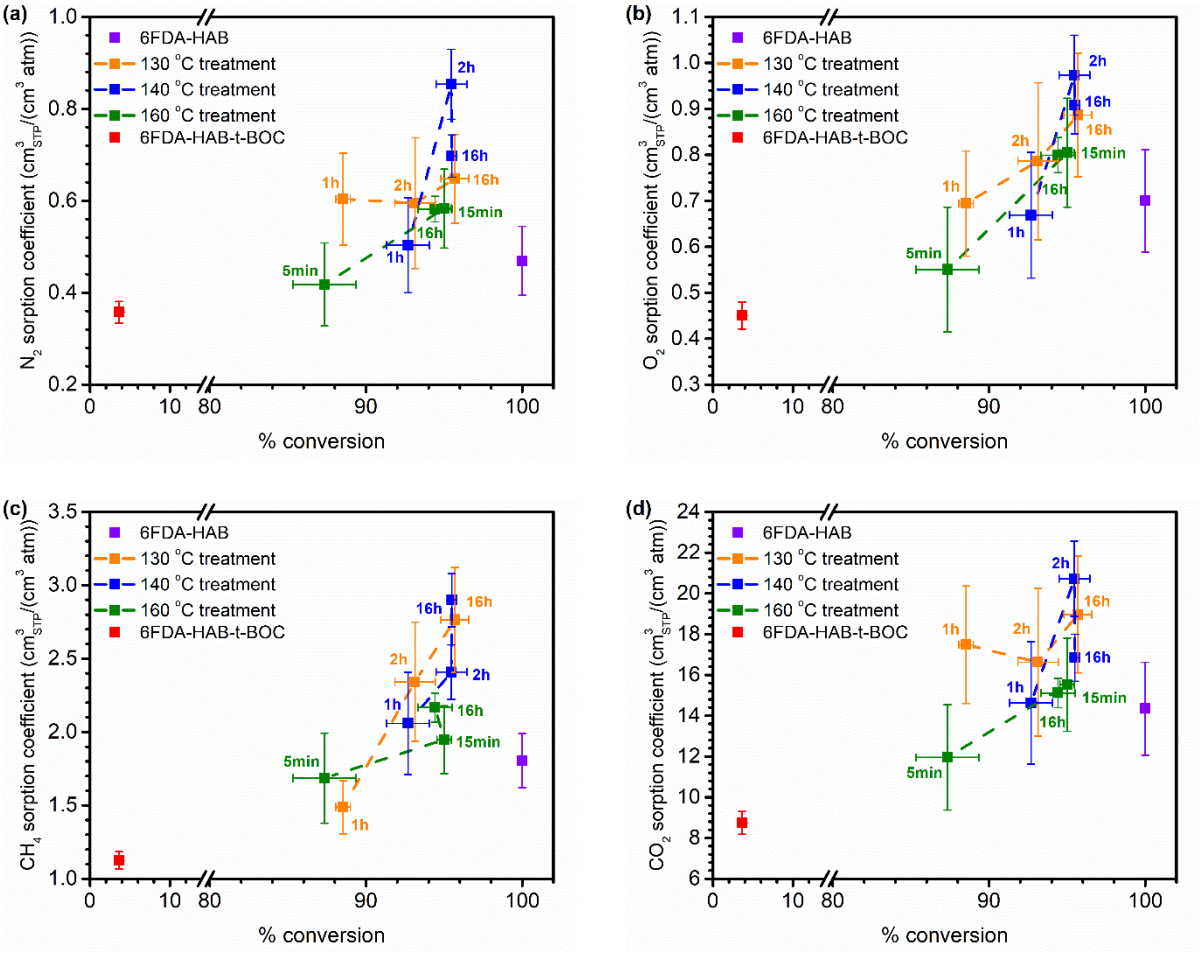

Figure A.9. Percent conversion compared to sorption coefficients for (a) N_2, (b) O_2, (c) CH_4, and (d) CO_2. Dashed lines have been added to guide the eye.

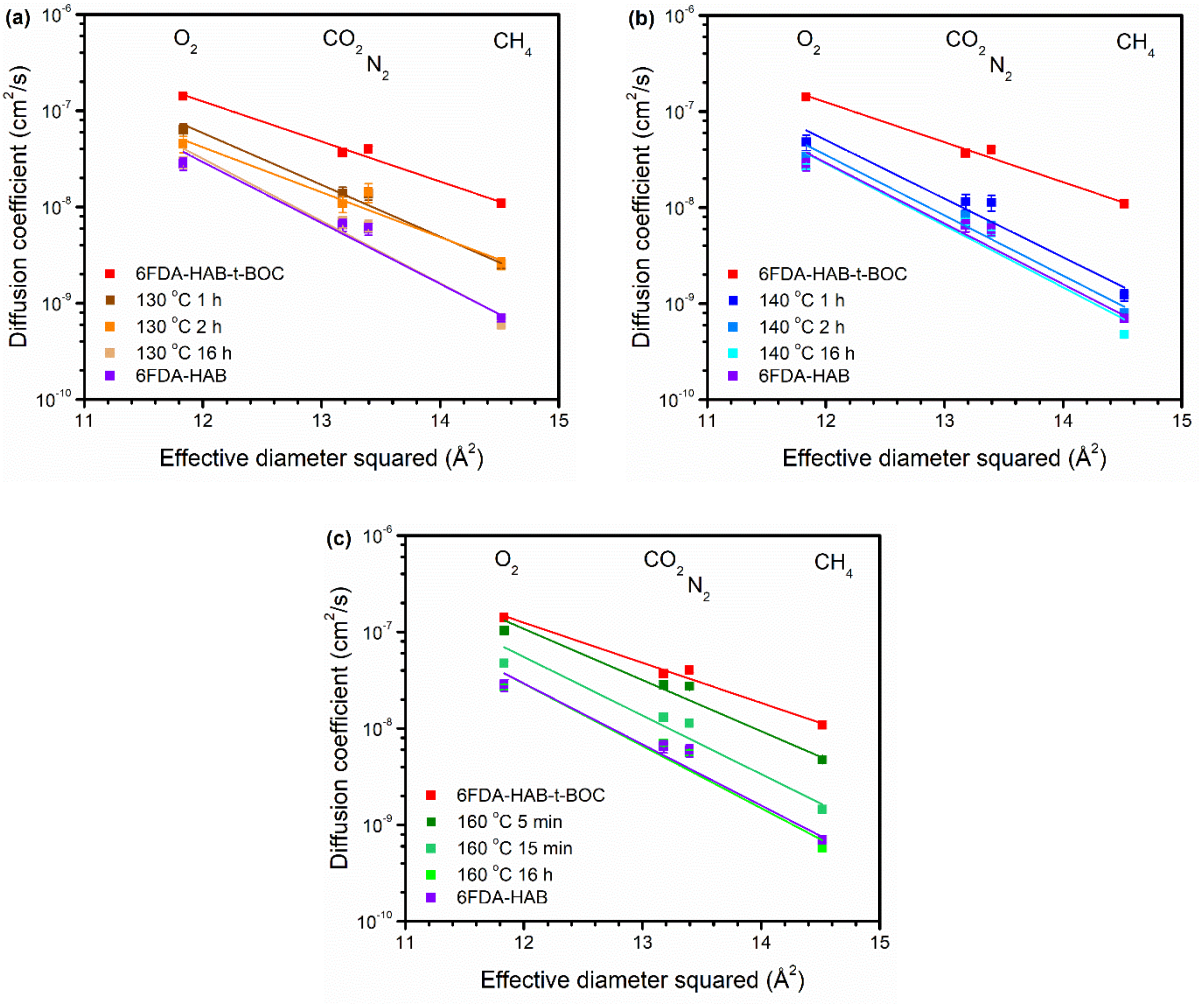

Figure A.10. Diffusivity plotted against effective diameter squared for 6FDA-HAB-t-BOC films that underwent different thermal treatments at (a) 130 °C, (b) 140 °C, and (c) 160 °C. Data for 6FDA-HAB and 6FDA-HAB-t-BOC are added for reference.

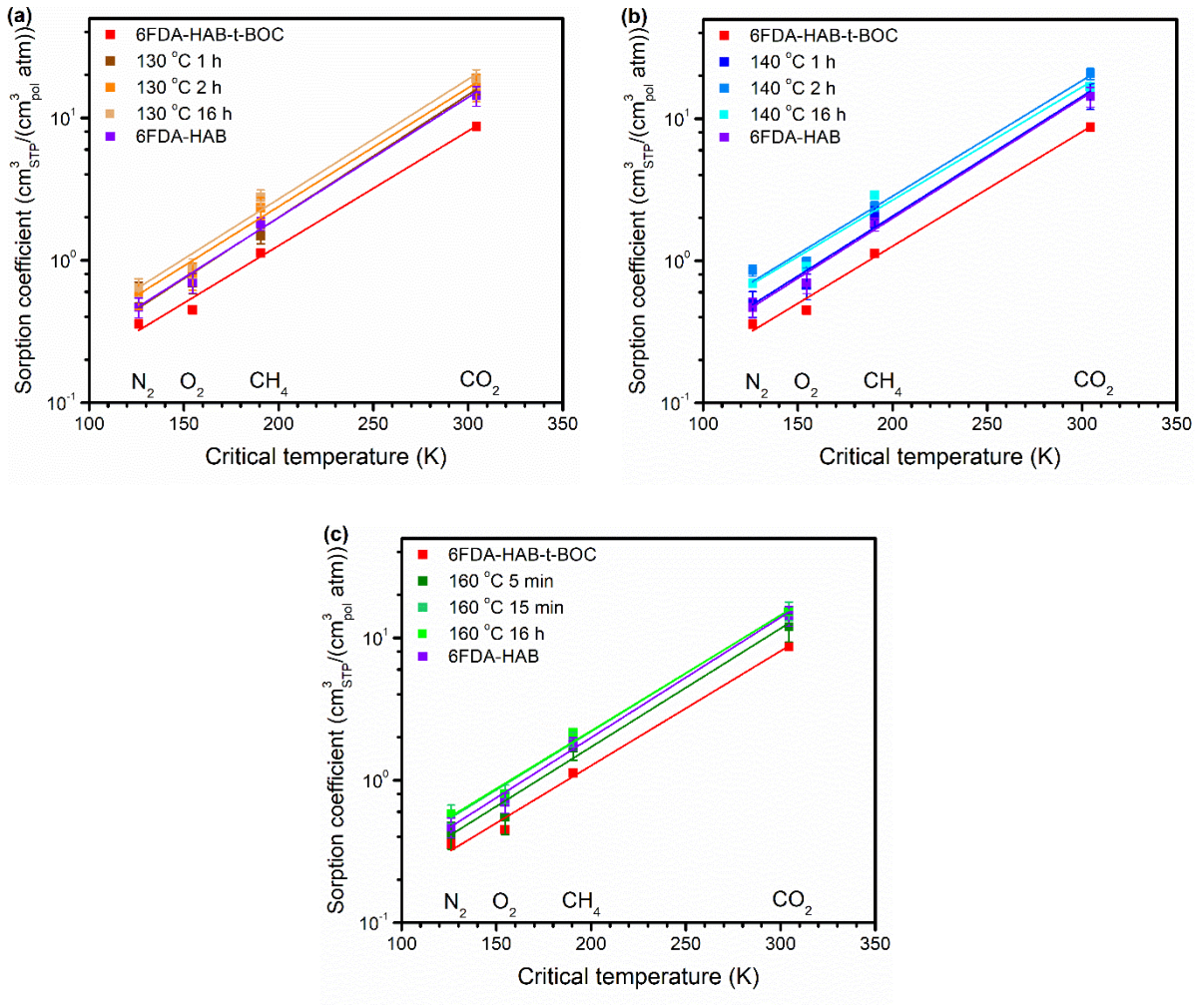

Figure A.11. Sorption coefficients plotted against critical temperature for 6FDA-HAB-t-BOC films that underwent different thermal treatments at (a) 130 °C, (b) 140 °C, and (c) 160 °C. Data for 6FDA-HAB and 6FDA-HAB-t-BOC are added for reference.

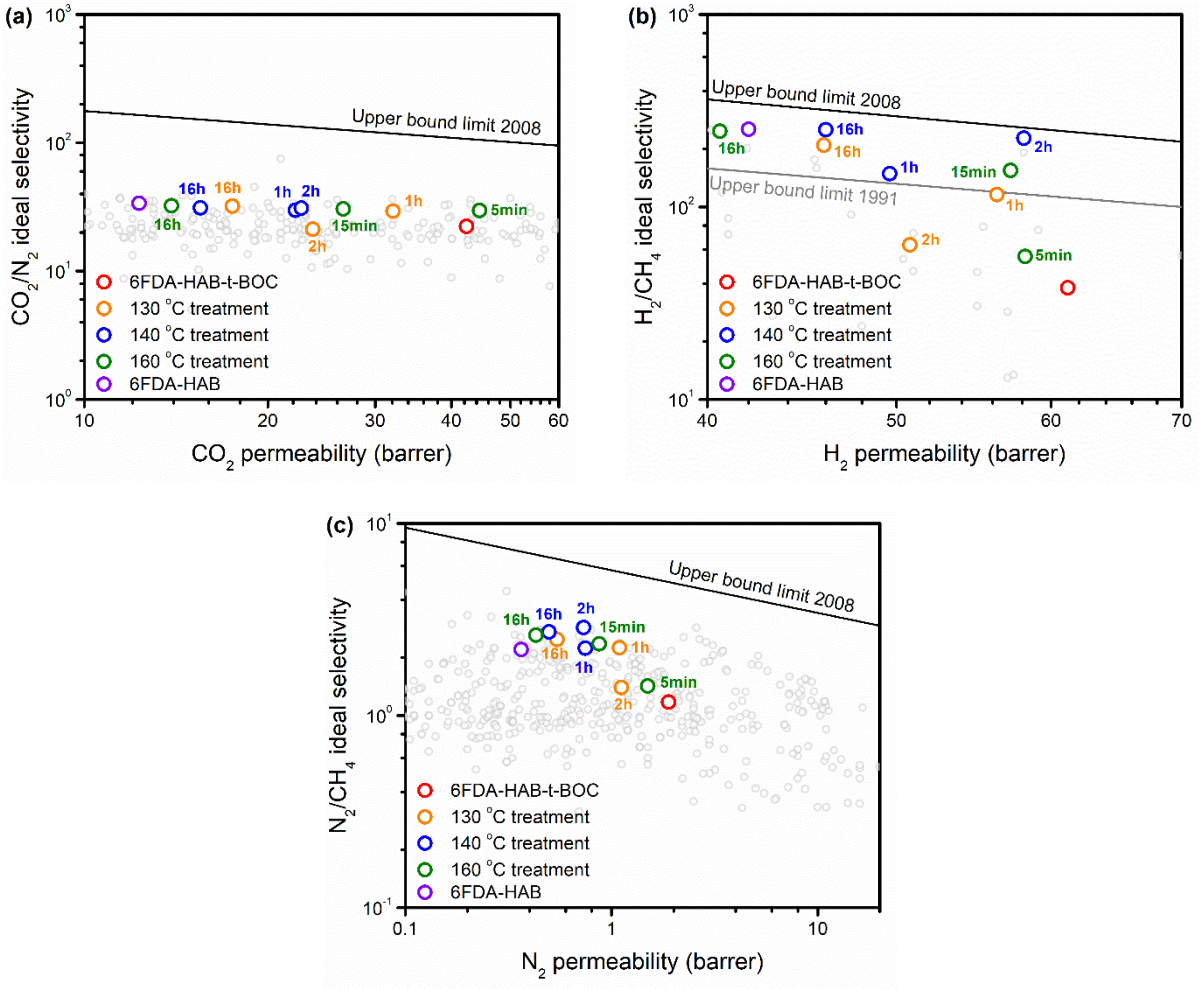

Figure A.12. Robeson plots for (a) CO_2/N_2, (b) H_2/CH_4, and (e) N_2/CH_4 gas pairs. Thermally treated samples are labeled with their treatment times. The black and gray lines represent the 2008 and 1991 Robeson upper bounds, respectively.[46,47] Literature data are shown as open gray circles from Robeson's database.[46,47]

Appendix B. Supporting Information for Chapter 3

Reprinted with permission from: He, Y.; Benedetti, F. M.; **Lin, S.**; Liu, C.; Zhao, Y.; Ye, H. Z.; Van Voorhis, T.; De Angelis, M. G.; Swager, T. M.; Smith, Z. P. Polymers with Side Chain Porosity for Ultrapermeable and Plasticization Resistant Materials for Gas Separations. *Adv. Mater.* **2019**, *31*, 1807871.

B.1. General materials and methods

Materials: All solvents, including methanol and ethanol, were of ACS reagent grade or better unless otherwise noted.

NMR Spectroscopy: ^{1}H- and ^{13}C-NMR spectra for all compounds were acquired in $CDCl_3$ on a Bruker Avance Spectrometer operating at 400 and 100 MHz for ^{1}H-NMR and ^{13}C-NMR, respectively. Chemical shifts (δ) are reported in parts per million (ppm) and referenced with TMS for ^{1}H-NMR and $CDCl_3$ for ^{13}C-NMR.

Gel permeation chromatography (GPC): Measurements were carried out in HPLC-grade tetrahydrofuran using an Agilent 1260 Infinity system with variable-wavelength diode array (254, 450, and 530 nm) and refractive index detectors, guard column (Agilent PLgel; 5μm; 50 x 7.5 mm), and three analytical columns (Agilent PLgel; 5μm; 300 x 7.5 mm; 105, 104, and 103 Å pore sizes). The instrument was calibrated with narrow-dispersity polystyrene standards between 1.7 and 3150 kg mol^{-1}. All runs were performed at 1.0 mL min^{-1} flow rate and 35 ºC. Molecular weight values were calculated using Chemsta-tion GPC Data Analysis Software (Rev. B.01.01) based on the refractive index signal.

Thermogravimetric analysis (TGA): TGA measurements were carried out under nitrogen atmosphere (Airgas, ultra-high purity grade) using a TGA 550 from TA Instruments. The ramp speed was 10 ℃ min^{-1}, and isotherms were performed from room temperature to 900 ℃.

Brunauer–Emmett–Teller (BET): BET surface area of polymers was measured with N_2 sorption at 77 K using a Micromeritics ASAP 2020. Powder samples (CF_3-ROMP, OMe-ROMP, and PIM-1) were degassed under high vacuum at 120 °C for 5 hours prior to analysis. Analysis of pore-size distributions was performed using Non-Local Density Functional Theory (NLDFT) model for carbon slit pore geometry provided by ASAP 2020.

Pure-gas permeabilities: Pure-gas permeabilities of polymer films were determined using a fixed-volume variable-pressure Maxwell Robotics automated permeation system. Polymer films were inserted into a stainless-steel permeation cell, which was then vacuum sealed and immersed in a water bath that was temperature-controlled at 35 °C using an immersion circulator (ThermoFisher SC 150L). All gases used for testing (He, H_2, CH_4, N_2, O_2, and CO_2) were ultra-high purity gases from Airgas.

Nanoindentation: Nanoindentation was done on a Hysitron TriboIndenter 950 with the Berkovich tip. The load control was 300 μN for all samples tested with a loading time of 10 s, holding time of 5 s, and unloading time of 10 s.

B.2. Synthesis and characterization of CF_3-ROMP, OMe-ROMP, and PIM-1

Synthesis and characterization of CF_3-ROMP and OMe-ROMP were previously reported by Zhao and He *et al.*[161] PIM-1 was synthesized according to previously published procedures.[86,231,232] A representative procedure for the oligomerization of OMe- and CF_3-monomer, as well as for the ring opening metathesis polymerization of OMe- and CF_3-ROMP, are reported as follows.

For OMe-oligomers and OMe-ROMP: OMe-monomer was heated at 220 °C for 18 h under Ar. A small amount of OMe-monomer was sublimed during thse reaction and condensed on the sidewall of the flask. The sublimed OMe-monomer was removed with cotton soaked with DCM.

The OMe-oligomer was used directly for ROMP without further purification. To a 25 mL Schelenk flask were added OMe-oligomer (300 mg, 0.285 mmol, 1.0 equiv.) and 2 mL of dry DCM. Subsequently, Grubbs 2nd generation catalyst (1.21 mg, 0.00143 mmol, 0.005 equiv.) in 1 mL of dry DCM was injected all at once. The reaction was left stirring for 12 hrs at room temperature and quenched with ethyl vinyl ether. Upon completion, corresponding polymer was precipitated in methanol, filtered, and washed with methanol for 3 times. The white solid OMe-ROMP was dried in vacuum oven at 80 °C for overnight before characterization.

For CF_3-oligomers and CF_3-ROMP: CF_3-monomer was heated at 220 °C for 18 h under Ar. A small amount of CF_3-monomer was sublimed during the reaction and condensed on the sidewall of the flask. The sublimed CF_3-monomer was removed with cotton soaked with DCM. The CF_3-oligomer was used directly for ROMP without further purification. To a 25 mL Schelenk flask were added CF_3-oligomer (500 mg, 0.389 mmol, 1.0 equiv.) and 2 mL of dry DCM. Subsequently, Grubbs 2nd generation catalyst (3.3 mg, 0.00389 mmol, 0.01 equiv.) in 1 mL of dry DCM was injected all at once. The reaction was left stirring for 12 hrs at room temperature and quenched with ethyl vinyl ether. Upon completion, corresponding polymer was precipitated in methanol, filtered, and washed with methanol for 3 times. The light yellow solid CF_3-ROMP was dried in vacuum oven at 80 °C for overnight before characterization.

GPC and MALDI-TOF for CF_3- and OMe-substituted side chains are shown in **Figures B.1** and **B.2**, respectively. ^{1}H-NMR, GPC, and DSC of corresponding polymers, CF_3-ROMP and OMe-ROMP, as well as field-emission SEM images of fabricated membranes used in gas permeation tests, are shown below in **Figures B.3** and **B.4**. **Figure B.5** presents comparative results for PIM-1.

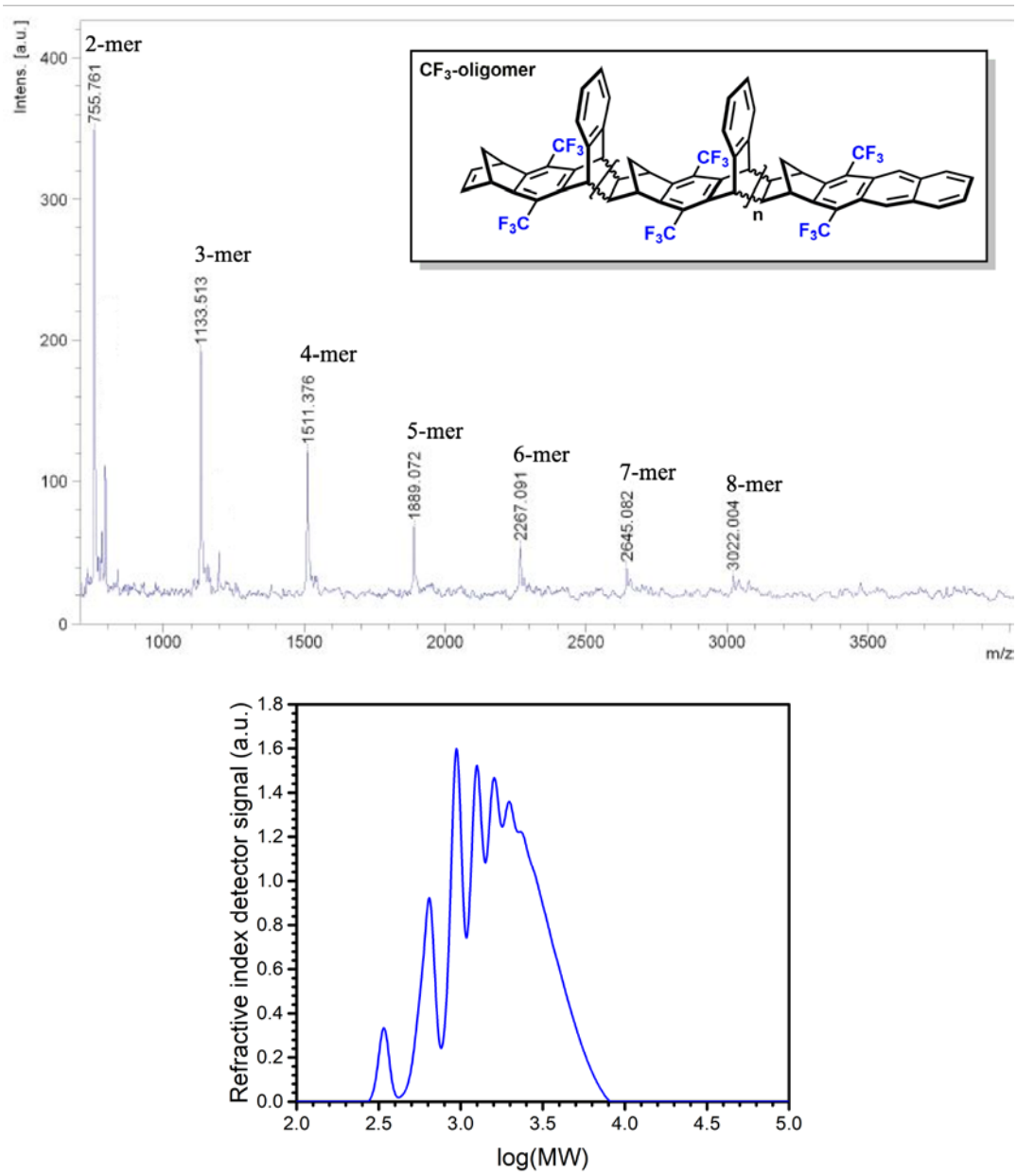

Figure B.1. MALDI-TOF and GPC of CF_3-oligomer.

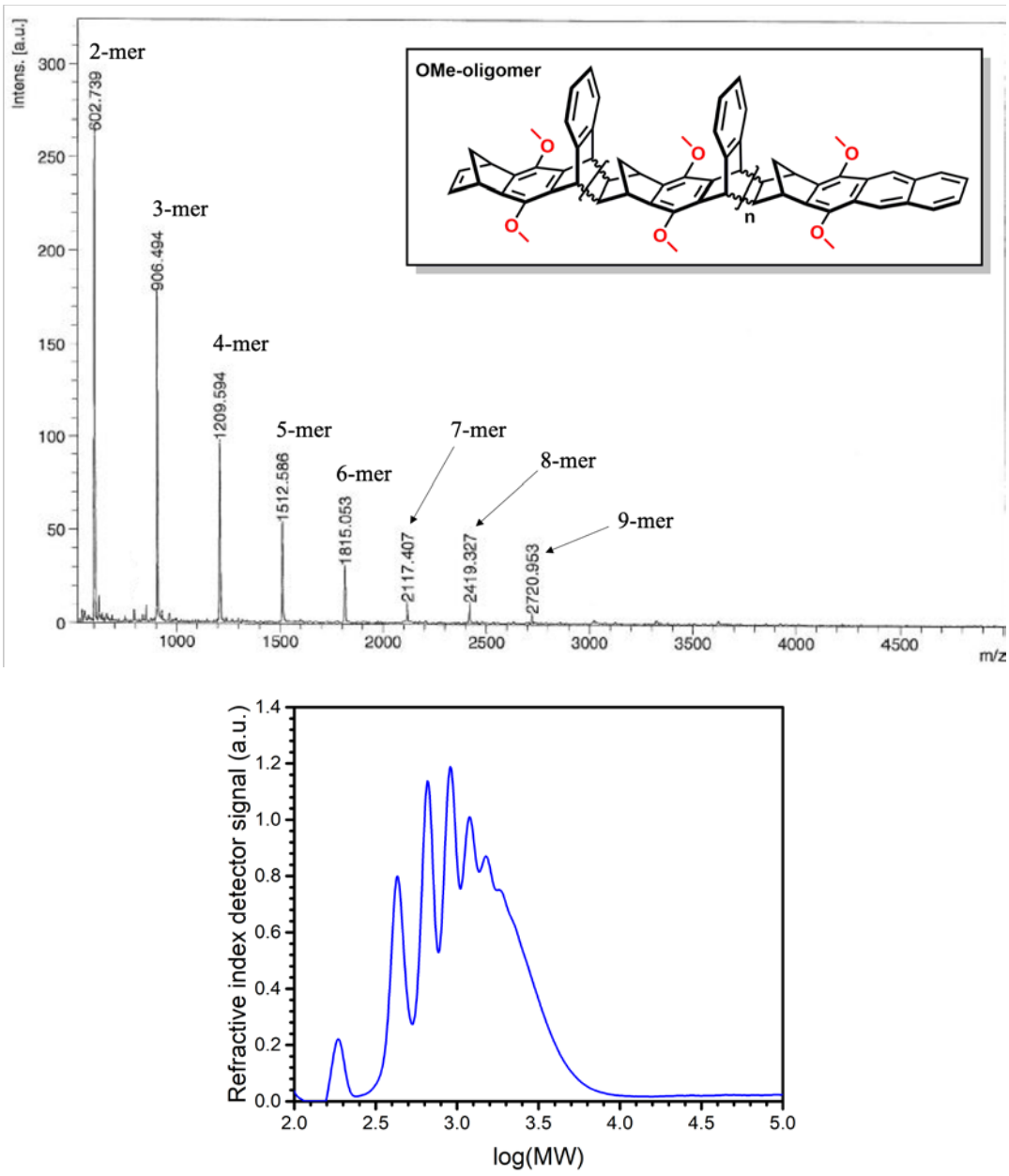

Figure B.2. MALDI-TOF and GPC of OMe-oligomer.

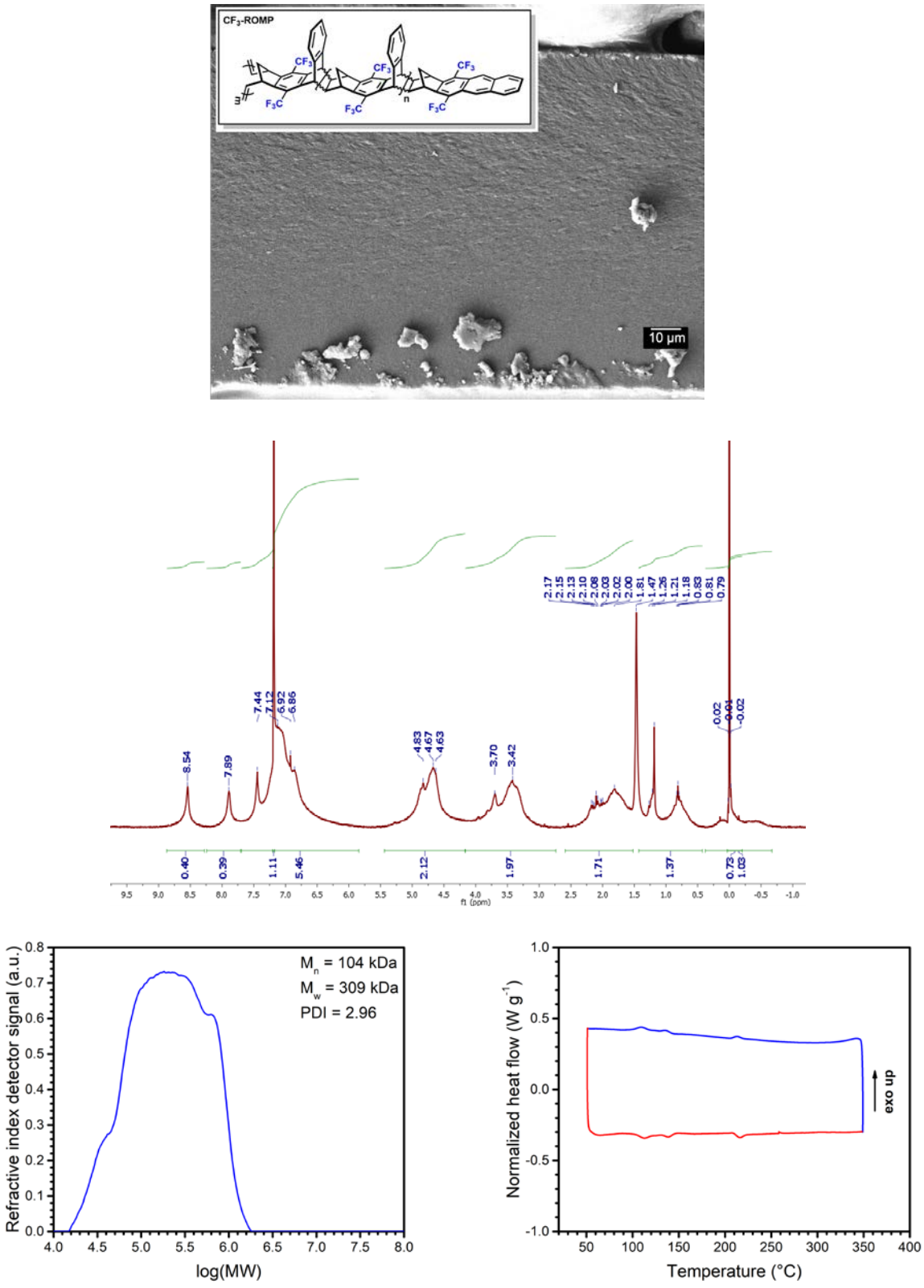

Figure B.3. SEM image, ^{1}H-NMR, GPC, and DSC for CF_3-ROMP.

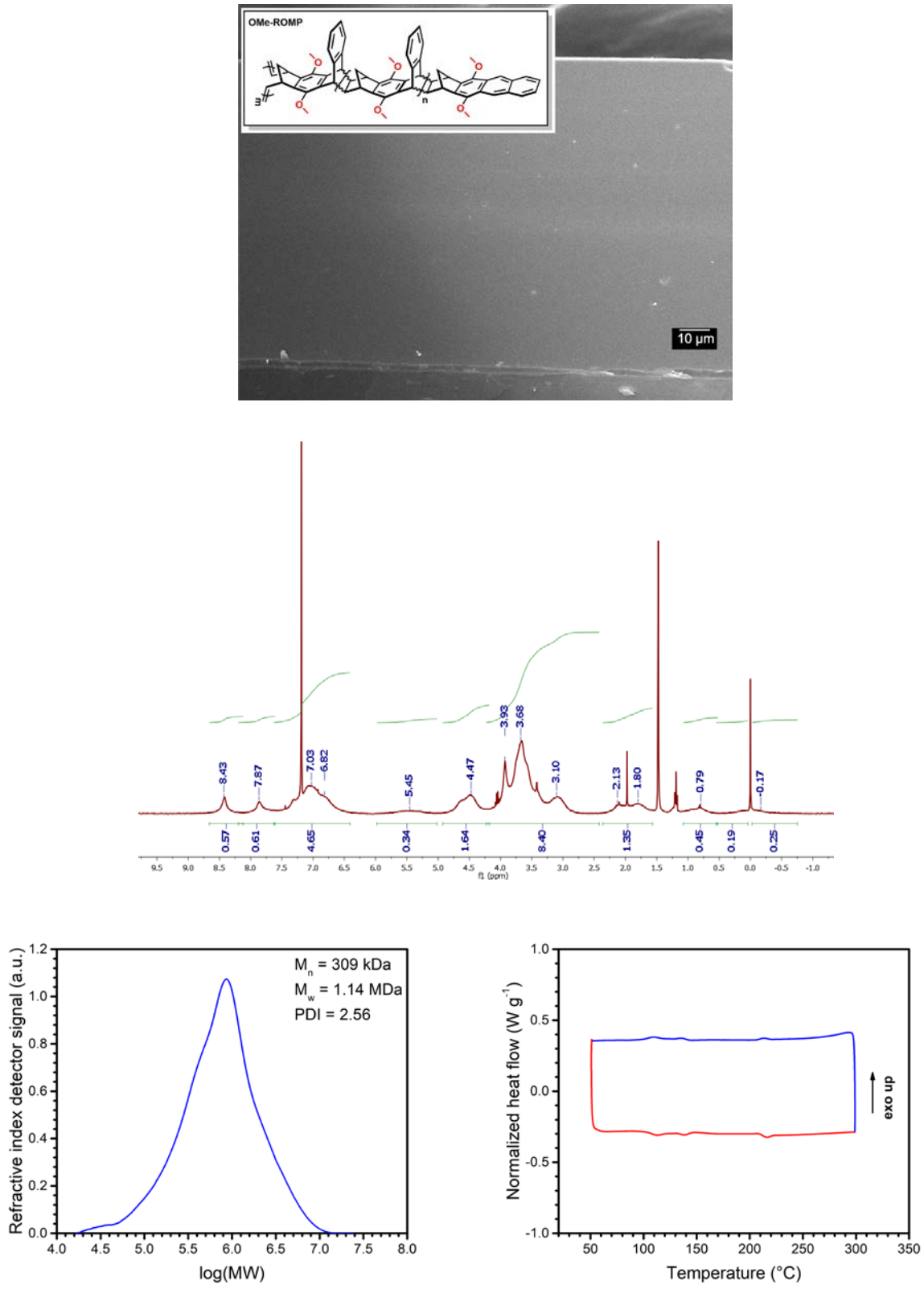

Figure B.4. SEM image, ^{1}H-NMR, GPC, and DSC for OMe-ROMP.

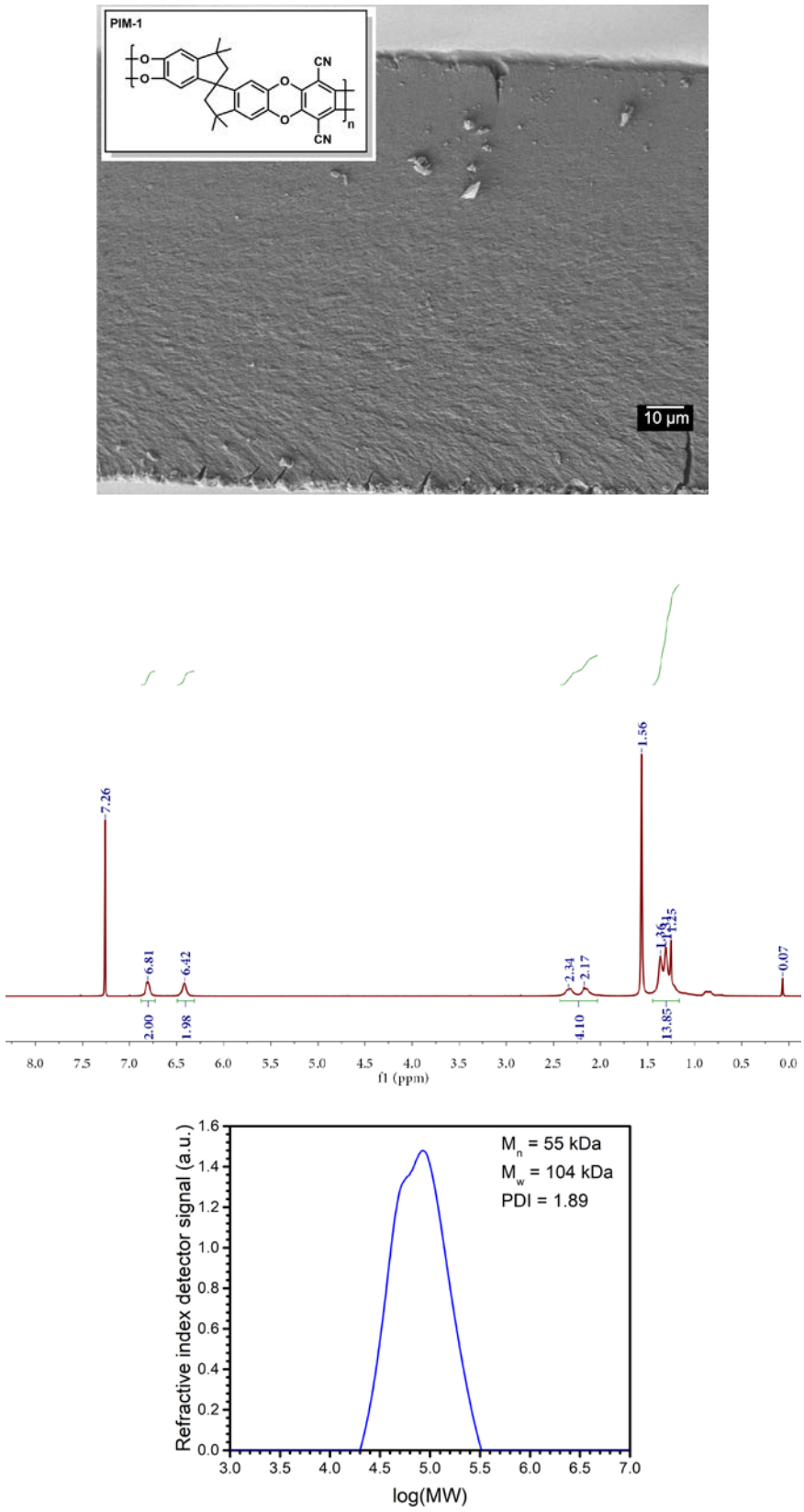

Figure B.5. SEM image, ^{1}H-NMR, and GPC for PIM-1.

B.3. BET and pore-size distribution for CF_3-ROMP, OMe-ROMP, and PIM-1

The porosity of CF_3-ROMP, OMe-ROMP, and PIM-1 powder was measured using nitrogen adsorption isotherm at 77 K with a saturation pressure of p_0 = 1 bar. BET surface area was calculated based on a p/p_0 range from 0.06 to 0.20 for the adsorption measurement. CF_3-ROMP, OMe-ROMP, and PIM-1 have a Brunauer–Emmett–Teller (BET)[233] internal surface area of 700 $m^2\ g^{-1}$, 146 $m^2\ g^{-1}$, and 800 $m^2\ g^{-1}$, respectively. Pore-size distributions were analyzed using NLDFT based on the adsorption part of isotherm and carbon slit pore geometry. Results are reported in **Figure B.6**.

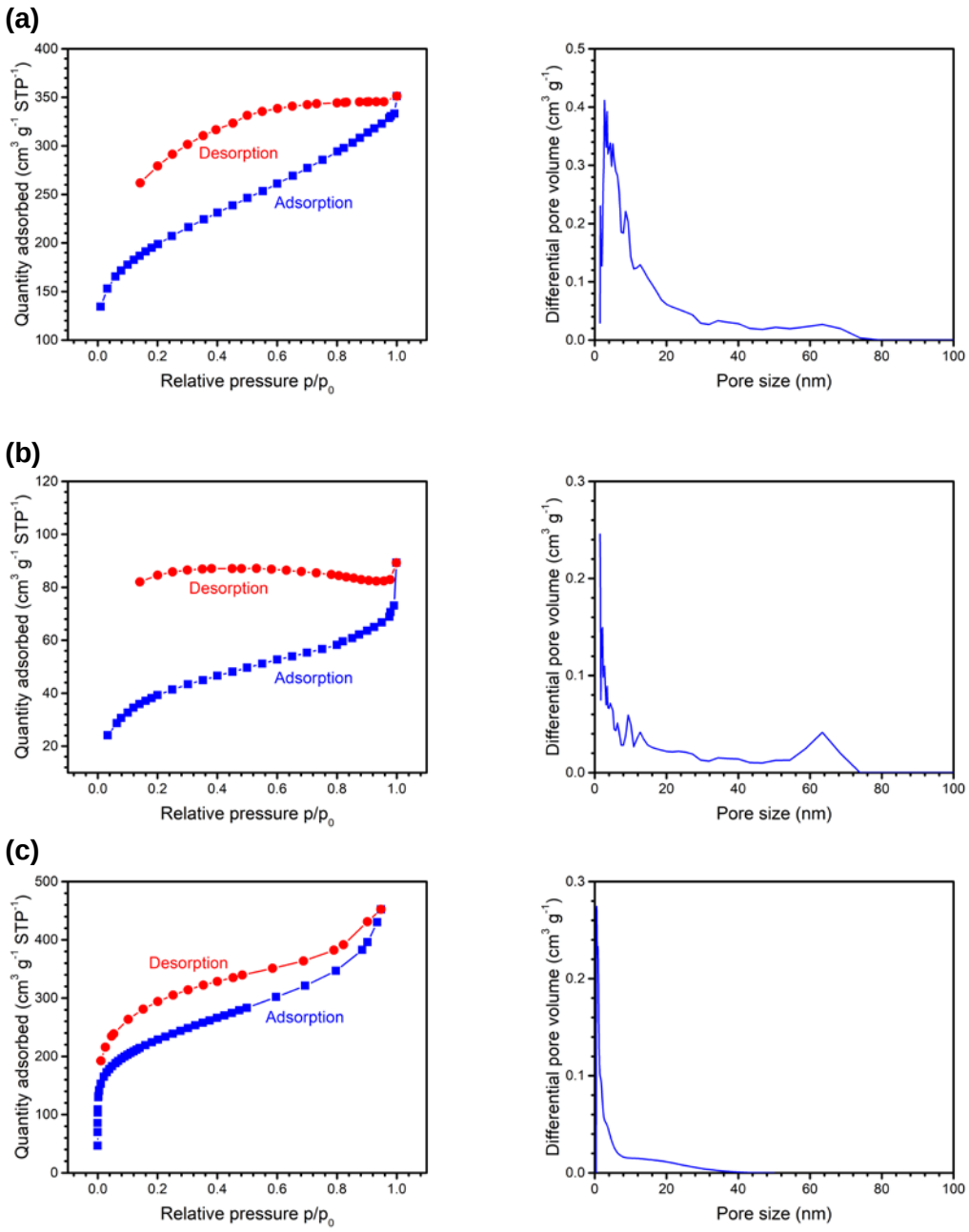

Figure B.6. BET and pore size distribution analysis of (a) CF_3-ROMP, (b) OMe-ROMP, and (c) PIM-1.

B.4. Representative conformations of side chains

Due to the complexity of the Diels-Alder (D-A) reaction, the side chains exhibit versatile stereochemistry depending on the orientation of the phenyl and methylene groups. Here, we select

three representative conformations and use molecular mechanics simulation to investigate their stable structures. All conformations were geometrically optimized using the MMFF94 force field[234–236] implemented in Avogadro.[237] For complex organic compounds, the stable structures found in this way could be biased by the initially guessed structures. To avoid this bias, for each conformer, we start the geometry optimization from many different configurations.

We first consider a conformation where all phenyl and methylene groups point towards the same side. Shown in **Figure B.7** are the optimized structures for n = 1–5. Circular structures are obtained for all n values even starting with chain-shaped initial guesses. For n = 1 and 2, the stable structures are unique, while there are two isomers for $n \geq 3$, depending on the end phenyl group curving inwards or outwards. We also note that n = 3 is the minimal length of forming a circle-shaped structure.

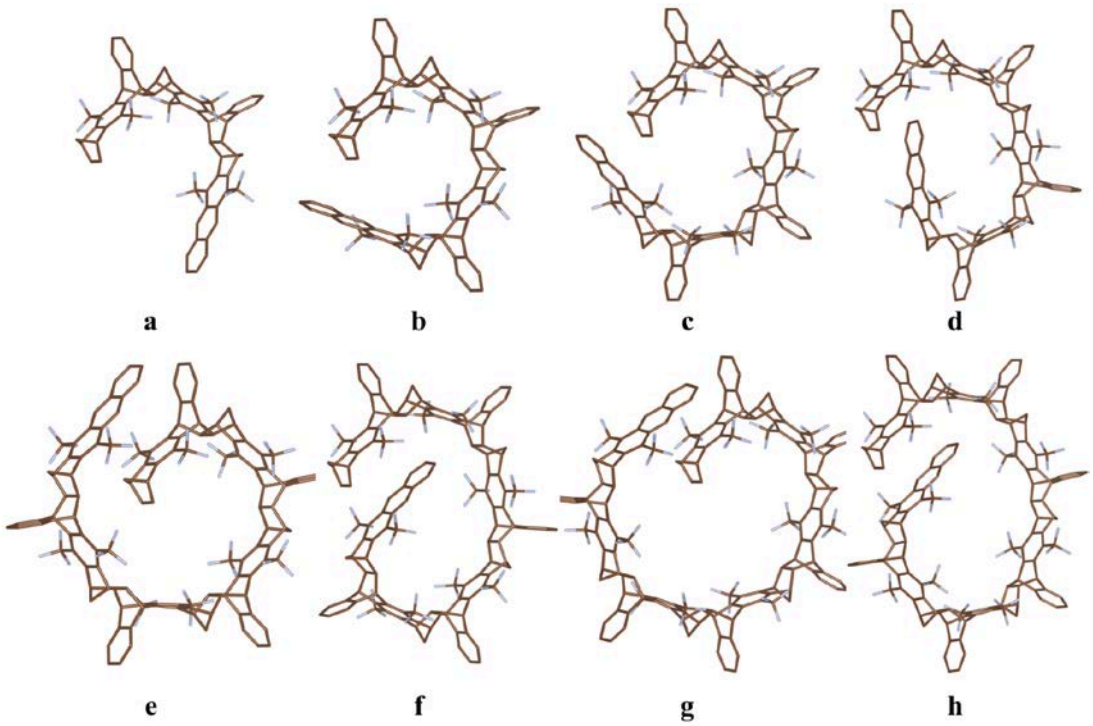

Figure B.7. Molecular mechanics optimized structures for one of the conformations of the side chain for n = (a) 1, (b) 2, (c) and (d) 3, (e) and (f) 4, and (g) and (h) 5.

We then consider two other conformers for n = 4, where the orientation of the phenyl groups and methylene groups alternates, respectively. One stable structure is found for each of them, and the results are shown in **Figure B.8**. We can see that the stereochemistry of both the methylene and phenyl groups has a large effect on the topology of the side chain: alternating these functional groups changes the structure from being circular to wiggling chains.

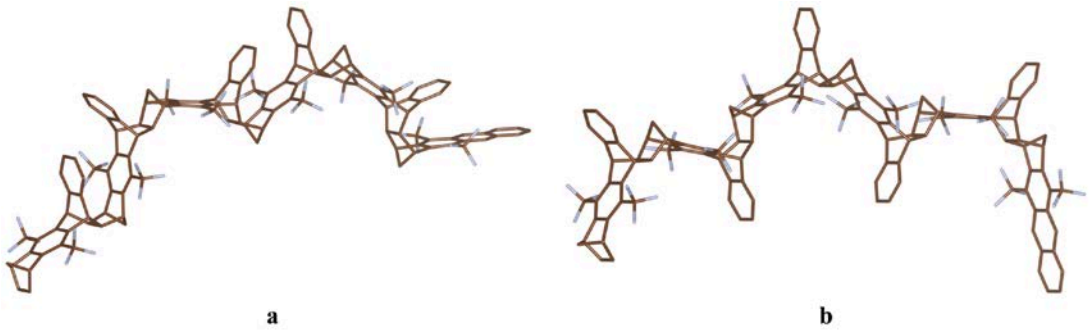

Figure B.8. Molecular mechanics optimized structures for two other conformations for n = 4.

B.5. Membrane fabrication and treatments

Self-standing films of ROMP polymers and PIM-1 were obtained following the method in the experimental section of Chapter 3. **Figure B.9** shows a CF_3-ROMP and an OMe-ROMP membrane obtained by solution casting ~3 wt% polymer solution in chloroform onto aluminum Petri dishes. Films are approximately 5 cm in diameter. A slow evaporation of the solvent allowed for the formation of stable and defect-free films in the thickness range of 74 to 180 μm.

(a) **(b)**

Figure B.9. (a) CF_3-ROMP and (b) OMe-ROMP films as cast from chloroform solutions.

After 4 days, films were ready for post-casting treatment. Different treatments, which are described below, were performed on the films to investigate their effects on the transport properties:

(A) Soaking in liquid ethanol for 48 h, air-drying for 24 h, and applying dynamic vacuum at 35 °C for 4 h;

(B) Soaking in liquid ethanol for 48 h, air-drying for 24 h, and applying dynamic vacuum at 35 °C for 8 h;

(C) Thermal treatment at 120 °C for 24 h under dynamic vacuum, vapor methanol treatment at 180 mbar (partial pressure of methanol) for 12 h, and applying dynamic vacuum at 100 °C for 16 h;

(D) Thermal treatment at 120 °C for 24 h under dynamic vacuum, vapor methanol treatment at 160 mbar to 200 mbar (partial pressure of methanol) for 12 h, and applying dynamic vacuum at 70 °C overnight;

(E) Thermal treatment at 120 °C for 24 h and applying dynamic vacuum;

The dynamic vacuum provided by Welch DuoSeal 1405 vacuum pumps was < 0.01 torr. **Table B.1** in **Section B.7** summarizes key results obtained for CF_3-ROMP, OMe-ROMP, and

PIM-1 after following the protocols described above. Measurements were performed immediately after the end of the treatment methods.

B.6. TGA experiments

Thermogravimetric analysis (TGA) was used to assess the thermal stability of ROMP polymers and PIM-1 and to verify that all the casting solvent (chloroform) and the non-solvent used in the post-casting treatment (ethanol or methanol), were completely removed from the films before performing gas permeation experiments. **Figure B.10a** shows three heating profiles for CF_3-ROMP, OMe-ROMP, and PIM-1 after all samples were subjected to an identical treatment method, **(B)**.[238] These samples were used to perform aging experiments. There was no detectable mass loss up to 350 °C for each polymer, which indicated that neither chloroform nor non-solvent were present in the films at the end of post-casting treatment (**Figure B.10a**). Furthermore, both ROMP polymers showed excellent thermal stability. CF_3-ROMP degradation started at ~380 °C, while OMe-ROMP degradation started at ~350 °C. This result suggests that these polymers may possess thermal stability needed for industrial applications that operate at high temperatures.

Different treatments, described in **Section B.5**, were applied to films made from new ROMP polymers to investigate how transport properties changed as a function of the post-casting treatment as reported in **Table B.1**. Among those treatments, TGA was performed on samples that underwent treatment **(B)**, **(D)**, and **(E)** and additional heating profiles are shown in **Figure B.10b** and **B.10c**. Within experimental error, all the curves essentially overlapped, indicating that all the treatments led to membranes free of casting solvent and swelling agents.

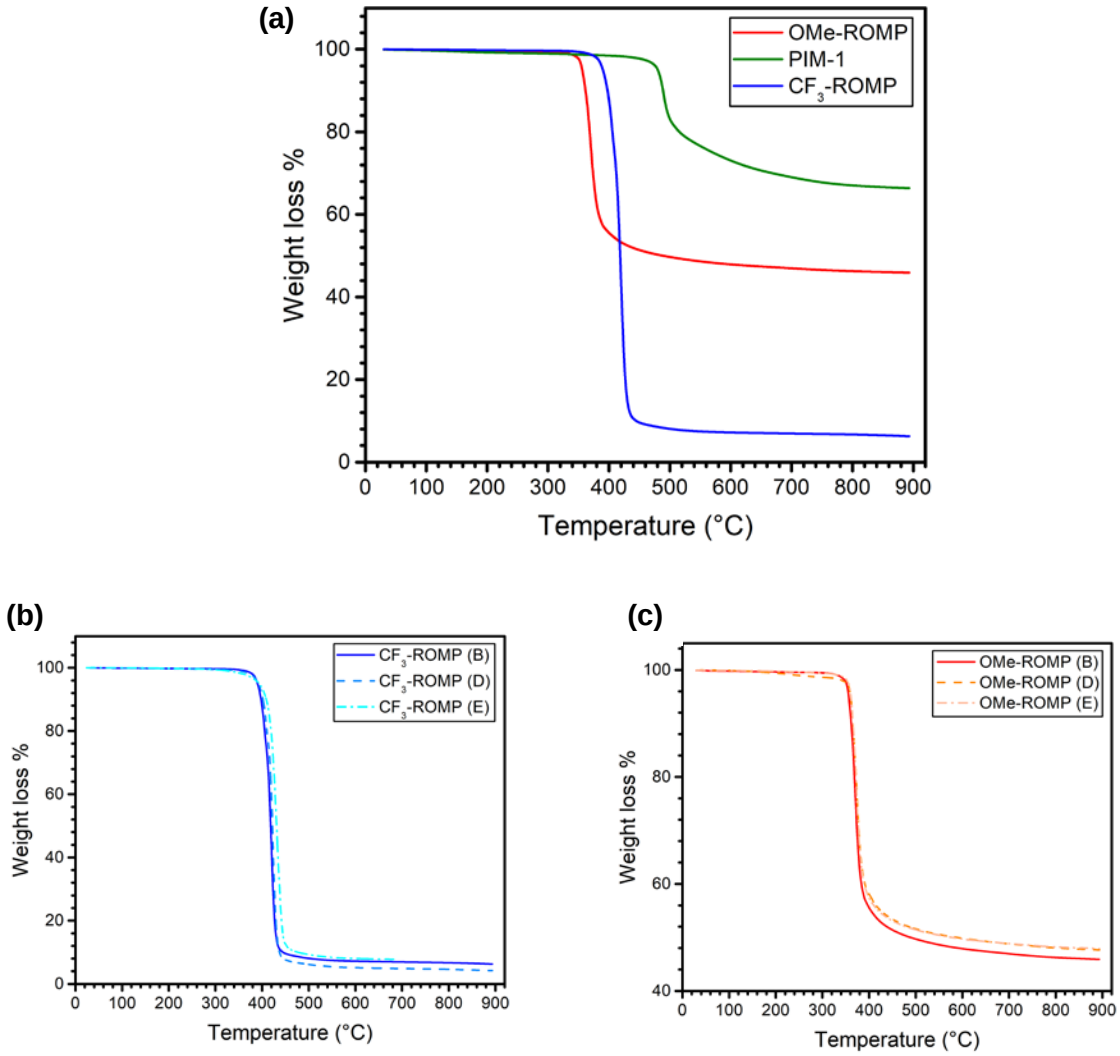

Figure B.10. (a) TGA comparison between CF_3-ROMP, OMe-ROMP, and PIM-1 samples that underwent treatment **(B)**; TGA of different (b) CF_3-ROMP and (c) OMe-ROMP samples, respectively, treated following different procedures: **(B)**, **(D)**, and **(E)**.

B.7. Gas transport properties and effect of the post-casting treatment

To characterize samples for gas transport performance, permeabilities were determined by direct permeation experiments and diffusivities were estimated from time-lag measurements. Six light gases (He, H_2, CH_4, N_2, O_2, and CO_2) were considered at 35 °C and ~1 bar. It is known that for glassy polymers, including PIMs, transport properties are dependent on film history and time,

which can lead to a wide distribution of values for permeability and diffusivity.[88,139] For this reason, the change in permeability for different post-casting treatment methods were carefully tracked over time. Results obtained are summarized in **Table B.1**.

Since the initial downstream pressure, p_d, was assumed to be full vacuum, permeability can be evaluated at pseudo-steady state from the linear portion of the pressure versus time curve, when $\frac{dp_d}{dt}$ is constant, by using the following equation:

$$\mathcal{P} = \frac{V}{RT}\frac{l}{A}\frac{1}{(p_u - \bar{p}_d)}\left(\frac{dp_d}{dt}\right) \tag{B.1}$$

in which R is the gas constant, T is the operative absolute temperature, l is the film thickness, p_u is the upstream pressure, and $\bar{p}_d$ is the average downstream pressure of the considered gas.

The ideal permselectivity between gas A and B, $\alpha_{A/B}$, is given by Equation B.3 and can be split in two contributions: $\alpha_{A/B}^{\mathcal{D}}$, which is the diffusivity selectivity, and $\alpha_{A/B}^{\mathcal{S}}$, which is the solubility selectivity in the framework of the solution-diffusion model, which is represented by Equation B.2:[41]

$$\mathcal{P} = \mathcal{D}\mathcal{S} \tag{B.2}$$

$$\alpha_{A/B} = \frac{y_{A,d}/y_{B,d}}{y_{A,u}/y_{B,u}} \cong \frac{\mathcal{P}_A}{\mathcal{P}_B} = \frac{\mathcal{D}_A}{\mathcal{D}_B}\frac{\mathcal{S}_A}{\mathcal{S}_B} = \alpha_{A/B}^{\mathcal{D}}\alpha_{A/B}^{\mathcal{S}} \tag{B.3}$$

The parameters $y_{A,d}$ and $y_{B,d}$ are the molar fractions at the downstream side of the film for gases A and B, respectively, while $y_{A,u}$ and $y_{B,u}$ are those at the upstream side of the film. $\mathcal{P}_A$ is the permeability of the more permeable gas and $\mathcal{P}_B$ is that of the less permeable one.

Time-lag, θ, was evaluated for all gases by extrapolating the linear portion of the pressure-versus-time curve to the time axis. Since experiments were performed starting from an initial

concentration of gas across the membrane equal to zero, θ can be related to the diffusivity, $\mathcal{D}$, through the following equation:

$$\mathcal{D} = \frac{l^2}{6\theta} \tag{B.4}$$

Since the permeabilities of the ROMP polymers and PIM-1 were remarkably high, in some cases, time-lag values obtained were often less than 2 seconds, which is close to the resolution of the acquisition time of the permeation system. For this reason, diffusion coefficients are not reported in **Table B.1** when θ was too small to be determined within the resolution of these experiments, typically for He, H_2, and sometimes O_2 and CO_2.

The highest values of permeability were obtained from films freshly soaked in liquid ethanol. In particular, CF_3-ROMP and OMe-ROMP achieved CO_2 permeabilities of > 21,000 barrer and 2,900 barrer, respectively. However, when considering membranes at different aging stages or films not soaked in ethanol, CO_2 permeability measured was in the range of 6–21×10^3 barrer for CF_3-ROMP and in the range of 10–29×10^2 barrer for OMe-ROMP. Vapor methanol treatment was designed to provide an alternative, less invasive way to erase history from films. Partial pressures of 160 mbar to 200 mbar of methanol were reached after thermally treating the films at 120 °C for 24 h under vacuum. This approach led to considerably different results with respect to the traditional treatment procedure involving liquid alcohols. The permeability of ROMP polymers that underwent vapor methanol treatment was approximately halved, while selectivity was generally higher. For example, CO_2/N_2 selectivity increased from 18.9 to 23.4 for OMe-ROMP. PIM-1, which was used as a benchmark to compare ROMP polymers with the current state-of-the-art, gave a similar response to the change of treatment.

Table B.1. Gas permeability and diffusivity values for CF_3-ROMP, OMe-ROMP, and PIM-1 measured from films with different history: **(A)** Soaking in liquid ethanol for 48 h, air-drying for 24 h, and applying dynamic vacuum at 35 °C for 4 h, **(B)** Soaking in liquid ethanol for 48 h, air-drying for 24 h, and applying dynamic vacuum at 35 °C for 8 h, **(C)** Thermal treatment at 120 °C for 24 h under dynamic vacuum, vapor methanol treatment at 180 mbar (partial pressure of methanol) for 12 h, and applying dynamic vacuum at 100 °C for 16 h, **(D)** Thermal treatment at 120 °C for 24 h under dynamic vacuum, vapor methanol treatment at 160 mbar to 200 mbar (partial pressure of methanol) for 12 h, and applying dynamic vacuum at 70 °C overnight, **(E)** Thermal treatment at 120 °C for 24 h and applying dynamic vacuum.

Permeability ($\mathcal{P}_x$) in Barrer (10^{-10} cm^3(STP) cm cm^{-2} s^{-1} $cmHg^{-1}$), Diffusion Coefficient ($\mathcal{D}_x$) in 10^{-8} cm^2 s^{-1}. All data were calculated at 35 °C and upstream pressure ~1 bar.

Polymer	Treatment	Aging (h)	Thickness (μm)	$\mathcal{P}_{He}$ ($\mathcal{D}_{He}$)	$\mathcal{P}_{H_2}$ ($\mathcal{D}_{H_2}$)	$\mathcal{P}_{CH_4}$ ($\mathcal{D}_{CH_4}$)	$\mathcal{P}_{N_2}$ ($\mathcal{D}_{N_2}$)	$\mathcal{P}_{O_2}$ ($\mathcal{D}_{O_2}$)	$\mathcal{P}_{CO_2}$ ($\mathcal{D}_{CO_2}$)
CF_3-ROMP	(A)	1	148	4296 (/)	8303 (/)	3970 (319)	2367 (570)	4354 (995)	21266 (633)
	"	830	"	/ (/)	6816 (/)	2942 (263)	1825 (493)	/ (/)	16148 (/)
	(B)	1	119	4372 (/)	8327 (3376)	3053 (245)	1993 (509)	4035 (888)	18490 (513)
	"	1000	"	3993 (/)	7285 (/)	1995 (154)	1464 (366)	3326 (632)	15104 (418)
	(C)	1	80	/ (/)	4535 (/)	/ (/)	980 (287)	2072 (/)	/ (/)
	"	500	"	2685 (/)	4736 (/)	/ (/)	935 (209)	2088 (/)	9919 (/)
	(D)	80	109	/ (/)	4864 (/)	1778 (188)	1195 (460)	2346 (/)	11144 (461)
	"	100	"	/ (/)	4844 (/)	1718 (173)	/ (/)	/ (/)	10910 (514)
	"	300	110	/ (/)	4719 (/)	1648 (225)	1098 (/)	2285 (/)	10815 (429)
	"	310	"	/ (/)	4708 (/)	1598 (214)	/ (/)	/ (/)	/ (/)
	"	600	"	/ (/)	4679 (/)	1501 (202)	1039 (/)	2220 (/)	10490 (436)
	"	610	"	/ (/)	4677 (/)	/ (/)	/ (/)	2258 (640)	/ (/)
	"	1100	"	/ (/)	4661 (/)	1419 (134)	1008 (410)	2187 (/)	10324 (443)
	(E)	120	141	/ (/)	3048 (2820)	703 (81.9)	523 (211)	1244 (429)	6361 (257)
OMe-ROMP	(B)	1	160	664 (/)	1409 (2679)	270 (25.8)	153 (73.6)	414 (153)	2900 (91.4)
	"	1000	"	563 (/)	1127 (1955)	178 (18.0)	112 (60.6)	313 (134)	2154 (74.3)

	(C)	1	74	/ (/)	535 (/)	/ (/)	46 (21.1)	141 (78.4)	/ (/)
	“	500	“	/ (/)	535 (/)	/ (/)	42 (19.4)	131 (63.8)	/ (/)
	(D)	100	157	/ (/)	698 (2038)	101 (15.6)	58 (45.4)	181 (120)	1357 (97.4)
	“	110	“	/ (/)	697 (1844)	/ (/)	/ (/)	/ (/)	1319 (94.8)
	“	150	144	/ (/)	696 (1697)	119 (16.4)	69 (41.3)	182 (95.2)	1343 (61.7)
	(E)	48	180	/ (/)	587 (1501)	85 (7.81)	52 (25.7)	150 (54.5)	1072 (36.0)
	“	60	“	/ (/)	578 (924)	83 (7.45)	51 (30.5)	/ (/)	1053 (38.5)
PIM-1	(B)	1	119	2176 (/)	5251 (3971)	1297 (81.9)	777 (189)	2177 (517)	12318 (268)
	“	1000	“	1882 (/)	4437 (/)	896 (58.7)	576 (155)	1736 (450)	10005 (293)
	(C)	1	126	/ (/)	3293 (/)	/ (/)	444 (191)	1258 (/)	/ (/)
	“	500	“	1481 (/)	3325 (/)	/ (/)	417 (153)	1213 (/)	/ (/)

Figure B.11 visually reveals the performance differences among the polymers investigated. Data reported refers to samples that underwent treatment **(B)** with identical aging history. Standard deviations were calculated using the error propagation approach.[135] It is clear that a small variation on the ladder-type side chain functionality in ROMP polymers (*i.e.*, $–CF_3$ versus –OMe), led to sensitive variations in gas transport properties. CF_3-ROMP permeability was one order of magnitude higher than that of OMe-ROMP and almost double that of PIM-1. By looking at the diffusivity and solubility contributions to permeability, **Figure B.11b** shows that high diffusion coefficient values for each gas for CF_3-ROMP were the primary reason behind the high permeability values for this sample. **Figure B.11c** illustrates that while PIM-1 solubility coefficients exceeded those of both ROMPs for CO_2 and CH_4, PIM-1 and CF_3-ROMP had similar solubility for N_2 and O_2. As expected from the trade-off usually observed in glassy polymers, selectivity follows the opposite trend with respect to permeability among samples. **Figure B.11d** shows that OMe-ROMP is the most selective polymer for almost all gas pairs. Further explanation to this finding is found in the main part of this communication.

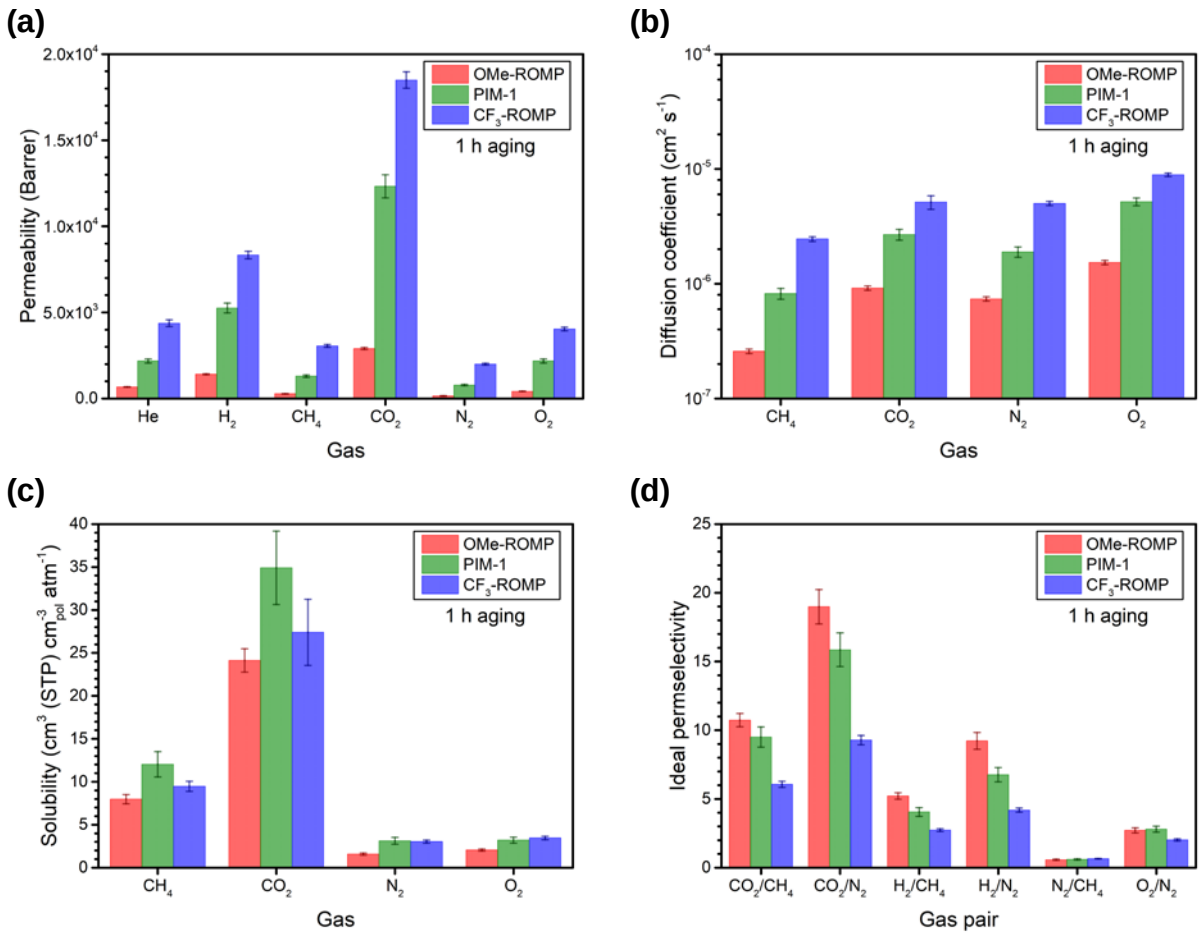

Figure B.11. Transport properties of ROMP polymers and PIM-1 at 35 °C and 1 bar upstream pressure that underwent treatment **(B)** after 1 h aging: a) permeability, b) diffusion coefficient, c) solubility coefficient, and d) permselectivity.

About 30 years ago, Robeson popularized a way to represent polymer performance for a large database of property sets and compare them to one another.[46] Permeability-based graphs were already reported in **Figure 3.1**. Here, we feature more complete versions in which we include performance obtained from treatments **(A)**, **(C)**, **(D)**, and **(E)** (**Figure B.12**).

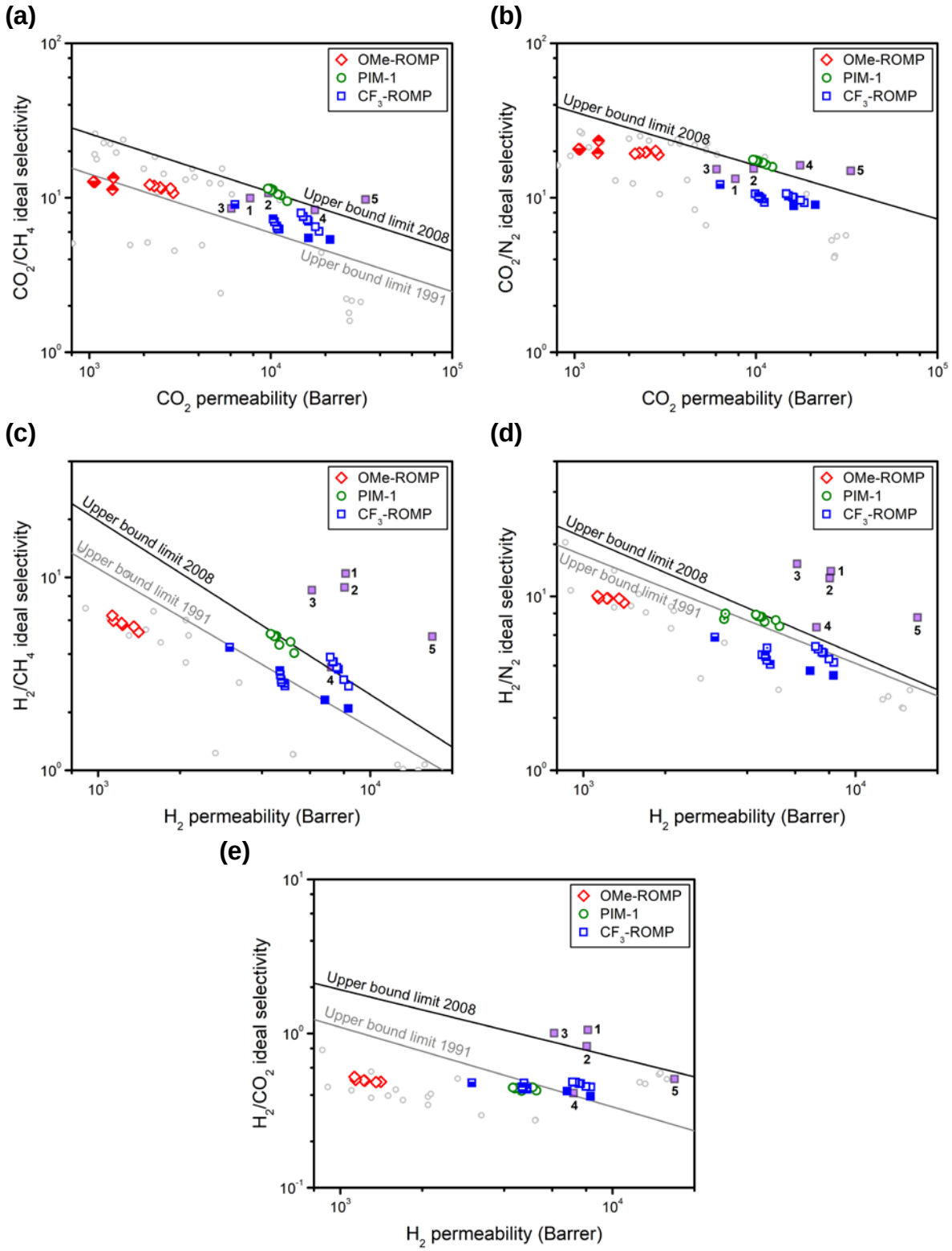

Figure B.12. Permeability trade-off in Robeson plots for (a) CO_2/CH_4, (b) CO_2/N_2, (c) H_2/CH_4, (d) H_2/N_2, and (e) H_2/CO_2. Different treatments: Filled marks **(A)**, Outline with white fill **(B)**, Dot

in center **(C)**, Top half filled **(D)**, and Bottom half filled **(E)**. 1) PIM-EA-TB,[94] 2) PIM-Trip-TB,[94] 3)PIM-TMN-SBI,[88] 4) PIM-TMN-Trip-TB,[88] and 5) PIM-TMN-Trip.[88] Gray dots are data from the Robeson database.[46,47] All other data points represented are reported in **Table B.1**.

Similar plots can be developed for diffusion (**Figure B.13**) and solubility (**Figure B.14**). We compared diffusivity and solubility results for ROMPs and PIM-1 on Robeson-like plots with a large database from the literature for a series of gas pairs.[154] As with Robeson upper bound plots for permeability, ideal materials should be located in the upper right corner of the graph.

Molecular diffusivity can change by orders of magnitude among different polymers for light gases, while solubility generally experiences a narrower variation. Additionally, permeability upper bound selectivity values are mostly determined by diffusivity selectivity over solubility selectivity.[48] As anticipated in **Figure B.11b**, CF_3-ROMP has exceptionally high diffusivity. In fact, blue markers representing CF_3-ROMP are on the extreme upper-right front of the populated data points on the following graphs, while most of the other polymers from this work and from literature are distributed to the lower-left of the front. For gas pairs like CO_2/CH_4, CO_2/N_2, N_2/CH_4, O_2/N_2, O_2/CH_4, and O_2/CO_2, high values of diffusivity were accompanied by modest diffusivity selectivity, placing CF_3-ROMP on the upper limit with respect to other polymers with some of the highest combinations of diffusivity and diffusivity selectivity (**Figure B.13**).

Exceptional results can be obtained if high diffusivity selectivity is coupled with very high gas solubility.[239] Robeson-like solubility plots in **Figure B.14** reveal how the solubility of CO_2 is relatively low in ROMP polymers. The improvement of solubility would lead this new class of polymers to be even more competitive in terms of separation performance. This outcome would be particularly beneficial towards compounds like CO_2 as can be observed in **Figure B.14**.

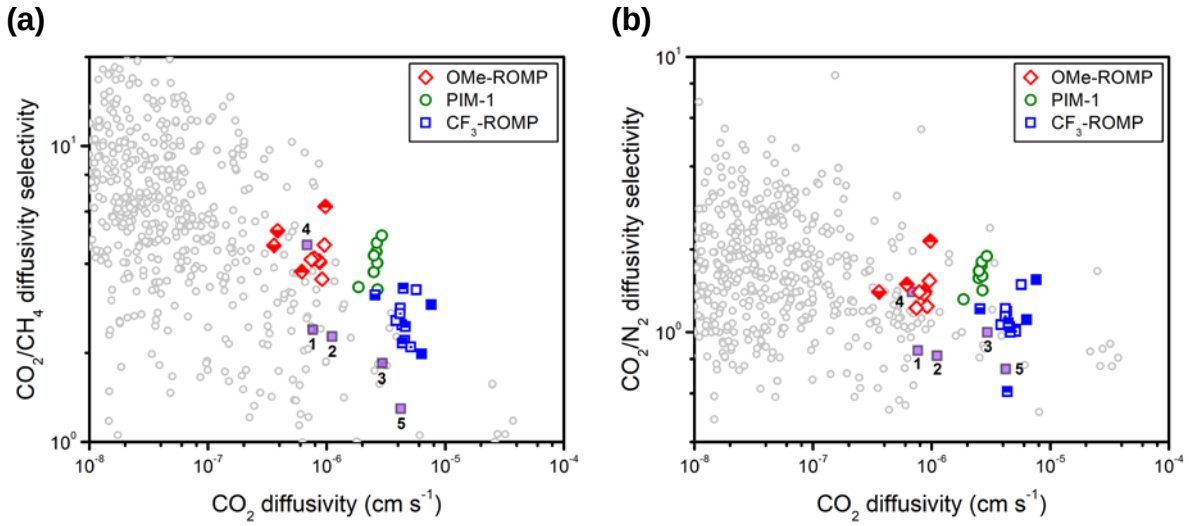

Figure B.13. Diffusivity trade-off in Robeson-like plots for (a) CO_2/CH_4 and (b) CO_2/N_2. Different treatments: Filled marks **(A)**, Outline with white fill **(B)**, Dot in center **(C)**, Top half filled **(D)**, and Bottom half filled **(E)**. 1) PIM-EA-TB,[94] 2) PIM-Trip-TB,[94] 3)PIM-TMN-SBI,[88] 4) PIM-TMN-Trip-TB,[88] and 5) PIM-TMN-Trip.[88] Gray dots are data from the Robeson database,[46,47] rearranged to determine diffusivity and diffusivity selectivity.

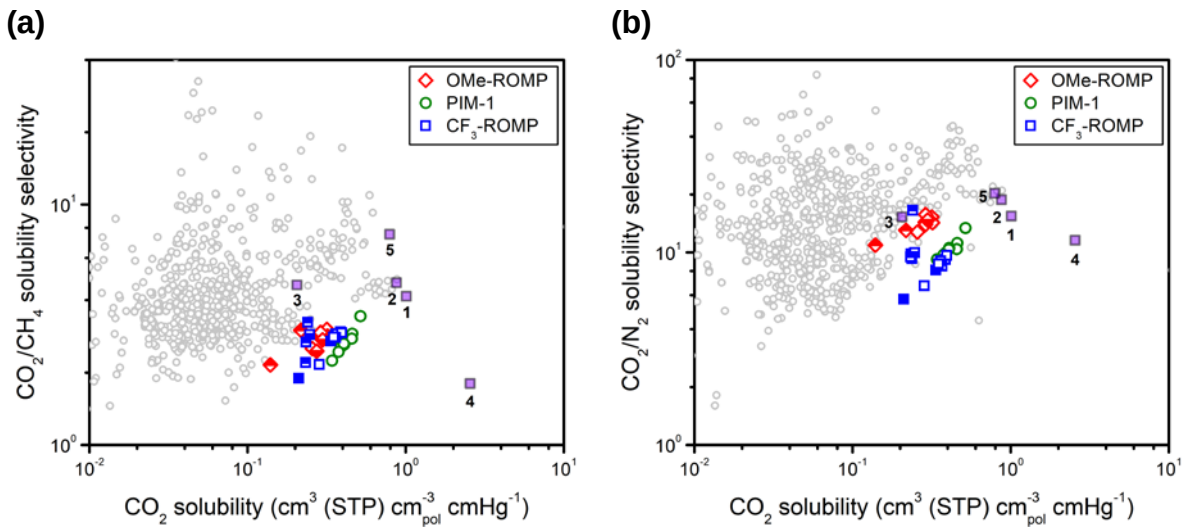

Figure B.14. Solubility trade-off in Robeson-like plots for (a) CO_2/CH_4 and (b) CO_2/N_2. Different treatments: Filled marks **(A)**, Outline with white fill **(B)**, Dot in center **(C)**, Top half filled **(D)**, and Bottom half filled **(E)**. 1) PIM-EA-TB,[94] 2) PIM-Trip-TB,[94] 3)PIM-TMN-SBI,[88] 4) PIM-TMN-

Trip-TB,[88] and 5) PIM-TMN-Trip.[88] Gray dots are data from the Robeson database,[46,47] rearranged to determine diffusivity and diffusivity selectivity.

B.8. Physical aging study

Physical aging is a phenomenon that typically occurs in glassy polymers such as ROMPs and PIMs since they are not in their equilibrium packing configuration at temperatures below their glass transition.[66] As a consequence, the specific volume of the material decreases over time, leading to many property changes. In this study, changes in permeability over time were the primary metric used to glean information on the effects of physical aging of films previously soaked in liquid ethanol. Of note, exposure to ethanol, such as that described in **Section B.5**, is known to further increase excess specific volume in glassy polymers, thereby leading to a more pronounced physical aging rate.[174,240] For this study, we considered the effects of physical aging on polymers that underwent treatment method **(B)**. A decrease in permeability was experienced over time for each gas tested for both ROMP samples and PIM-1. As shown in **Figure B.15**, an approximately linear trend was observed in double logarithmic charts in which permeability was plotted as a function of the aging time. Similar linear behaviors have been observed by other authors.[117,118] The decrease in permeability was accompanied by an increase in permselectivity for some of the most relevant gas couples, *i.e.*, CO_2/N_2, CO_2/CH_4, H_2/N_2, H_2/CH_4, O_2/N_2, and N_2/CH_4 (**Figure B.16**). This finding relates to the trade-off between permeability and selectivity described by Robeson.[46] Notably, CF_3-ROMP reached the highest permeability for each gas, while OMe-ROMP was the most selective for all gas pairs. As indicated in **Table B.1**, the CF_3-ROMP sample used for the physical aging study featured an initial CO_2 permeability of 18,490 barrer, a value lower than that of the sample subjected to treatment **(A):** 21,266 barrer. This is due to the

variability among different samples and the longer dynamic vacuum which the less permeable film was exposed to before testing.

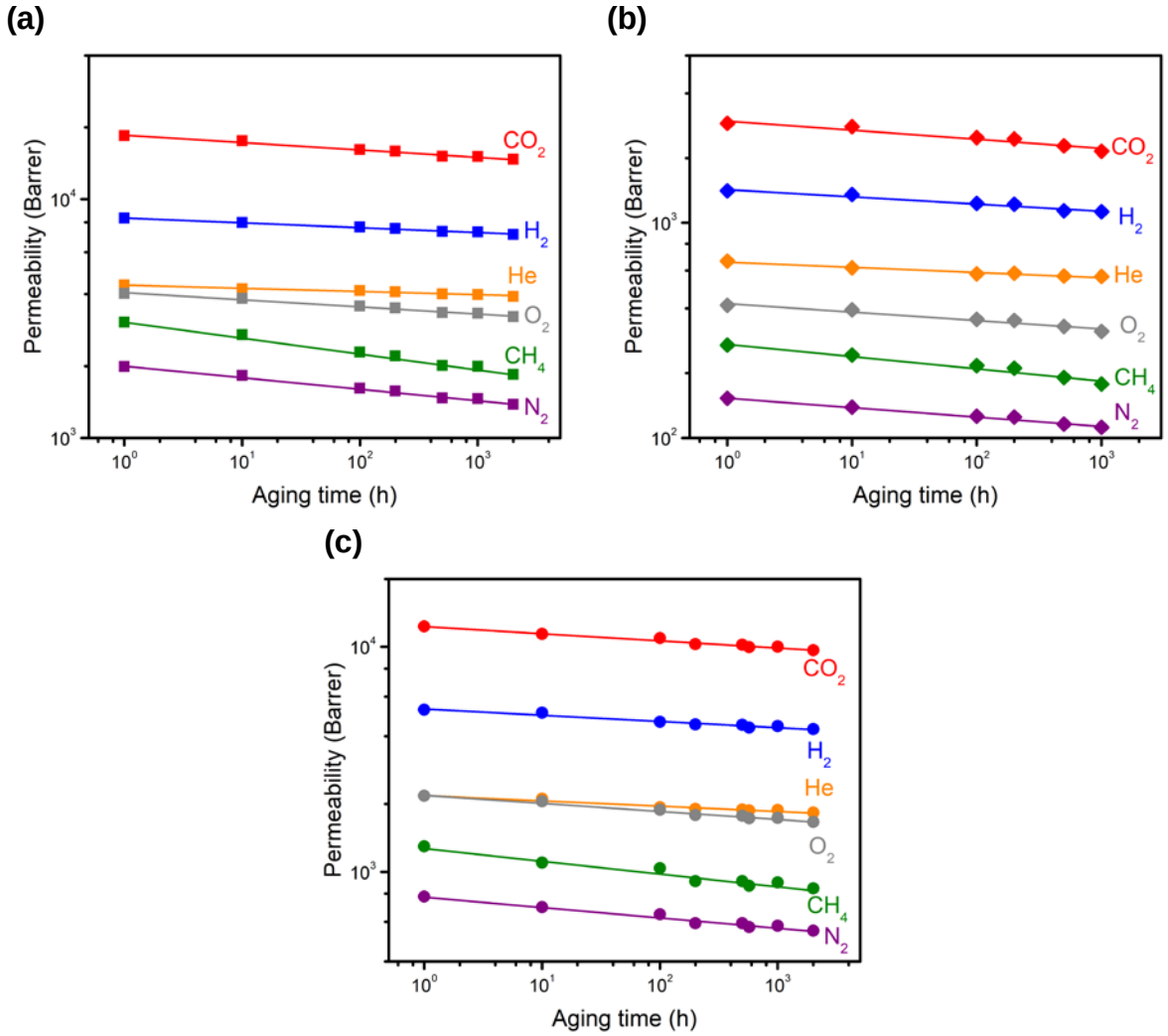

Figure B.15. Permeability as a function of time. Data were collected at 35 °C and 1 bar upstream pressure for (a) CF_3-ROMP, (b) OMe-ROMP, and (c) PIM-1.

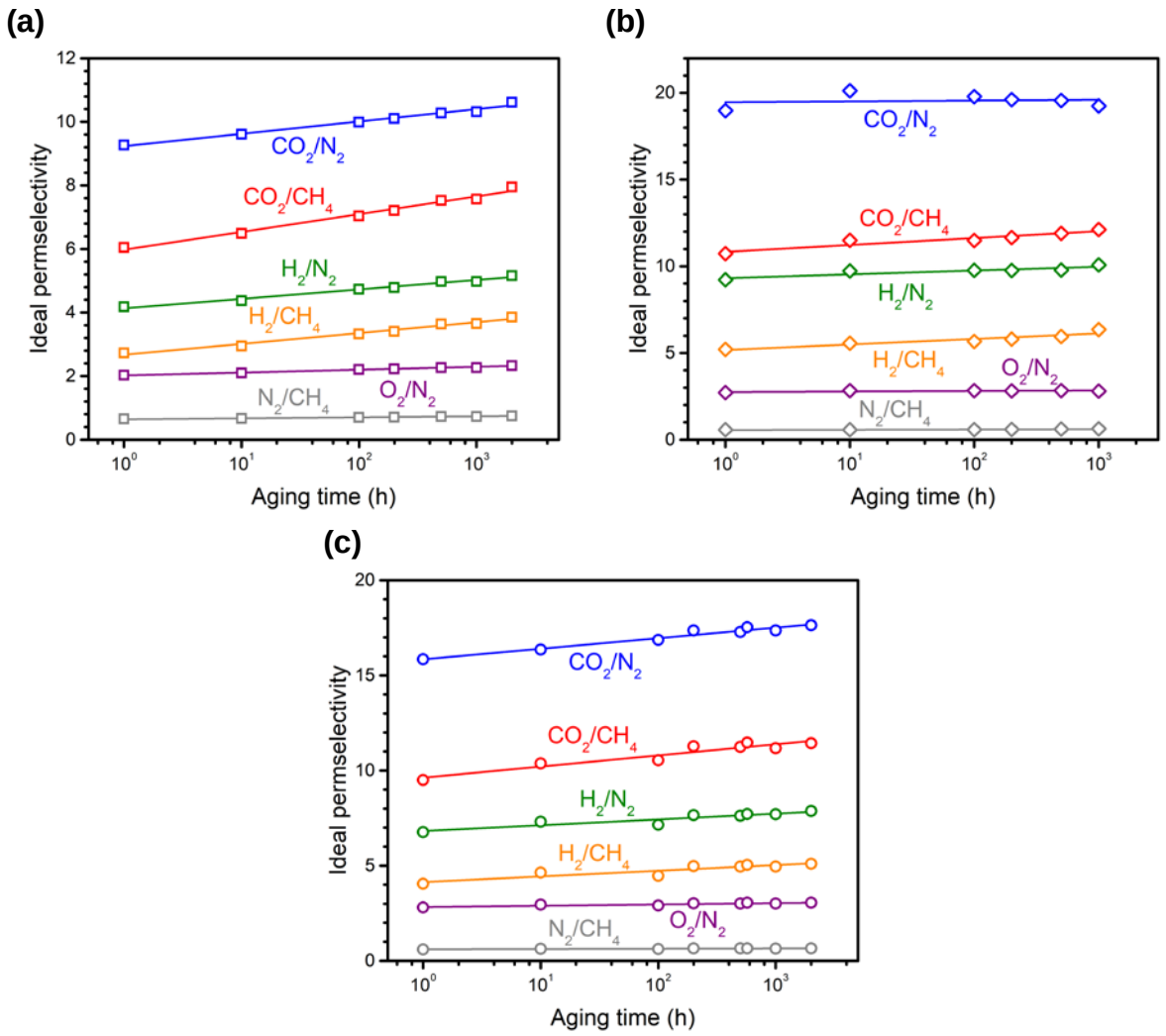

Figure B.16. Ideal permselectivity as a function of time. Data were collected at 35 °C and 1 bar upstream pressure for (a) CF_3-ROMP, (b) OMe-ROMP, and (c) PIM-1.

The graphs in **Figure B.17a** reveal that the permeabilities of larger gases decreased more than those of smaller gases as the materials aged. Furthermore, aging rates for each gas followed the same order of the effective diameter (He < H_2 < O_2 < CO_2 < N_2 < CH_4), as shown in **Figure B.17b** for CF_3-ROMP. The permeability loss that each gas experienced over time was plotted as a function of effective diameter squared, and the slope of this line can be calculated for each set of experiments at each time. **Figure B.17c** shows that this slope increased over time. Interestingly, the rate by which it evolved was very different among the three materials, and this result is related

to the way polymer chains pack over time. In other words, it gave us information about the evolution of the fractional free volume as the polymer transitioned towards its equilibrium density that minimizes the Gibbs free energy of the system. CF_3-ROMP showed the highest values of these slopes because small gases (*i.e.*, He, H_2, O_2) experienced a smaller permeability drop over time compared to OMe-ROMP and PIM-1, while for larger gases (*i.e.*, CO_2, N_2, CH_4) the drop in permeability is comparable (**Figure B.17a**). This finding reflects on the fact that H_2/X and He/X permselectivity (X = generic other gas), increased remarkably over time without compromising H_2 and He permeability, often surpassing the Robeson Upper Bounds (**Figure 3.1**).[46,47] This result was further supported by evidence from WAXS experiments. More details about WAXS will follow in **Section B.9**.

(a)

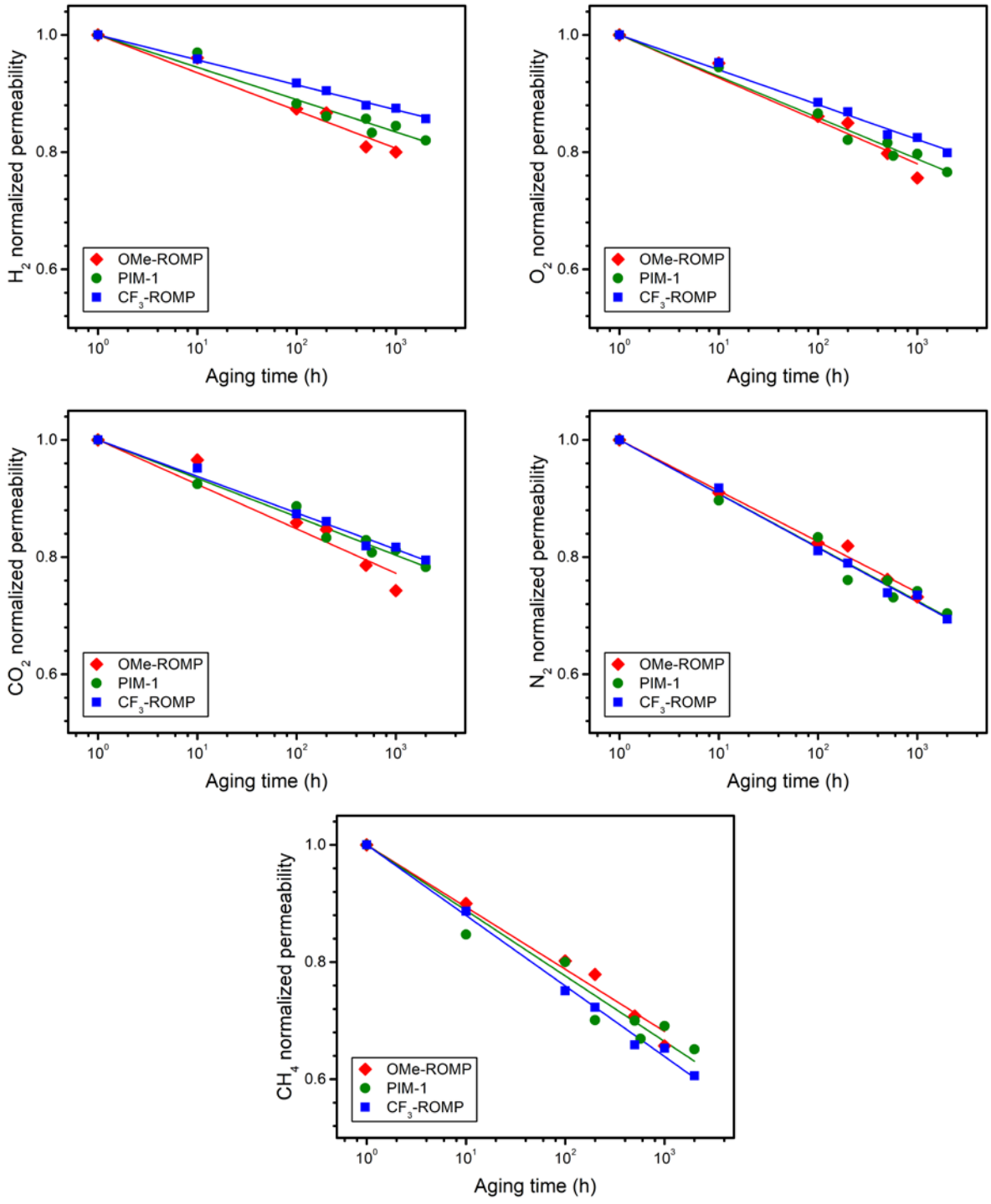
H2 normalized permeability
O2 normalized permeability
CO2 normalized permeability
N2 normalized permeability
CH4 normalized permeability
Aging time (h)
OMe-ROMP
PIM-1
CF3-ROMP

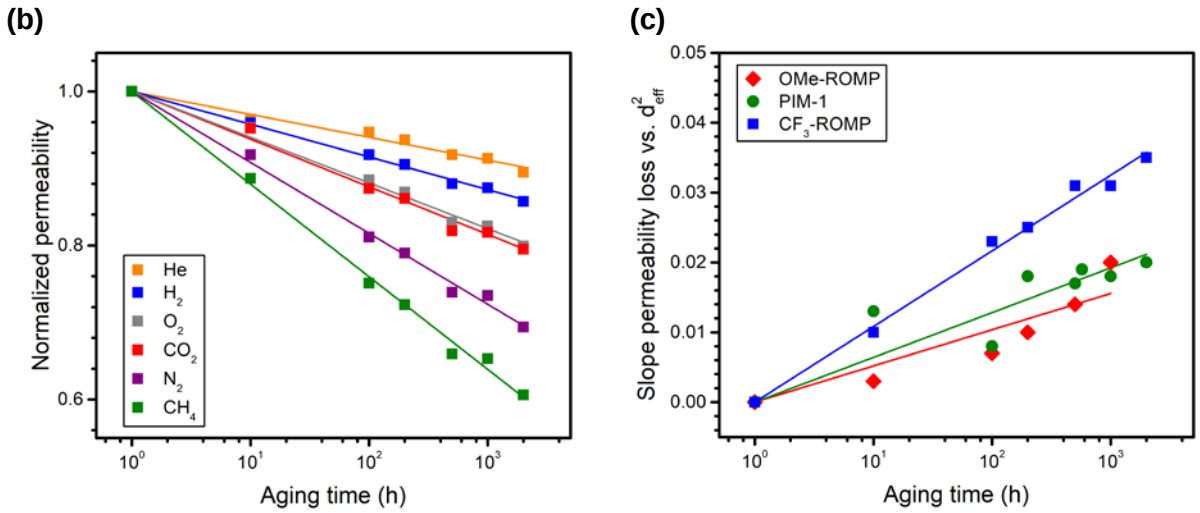

Figure B.17. Physical aging data. (a) CF_3-ROMP, OMe-ROMP, and PIM-1 comparison of normalized permeability against aging time for H_2, O_2, CO_2, N_2, and CH_4, (b) CF_3-ROMP aging data and (c) Data calculated evaluating the slope of permeability loss against effective diameter squared at each time (1, 10, 100, 200, 500, 1000, and 2000 h), and plotted against aging time.

Diffusivity coefficients were monitored while films aged over time, and results are shown in **Figure B.18**. He and H_2 values are not represented in the figures because the time-lag was too short for accurate calculations. Diffusion coefficients decreased according to what was expected from aging experiments. These changes contribute to the overall decrease in permeability. For ROMP polymers, the magnitude of diffusivity values, follows the inverse order of the effective diameter: (3.44 Å) O_2 < (3.63 Å) CO_2 < (3.66 Å) N_2 < (3.81 Å) CH_4. Diffusivity selectivity increased over time, as shown in **Figure B.19**, and this change is the biggest contribution to the increase in permselectivity that allows these ROMPs to overcome the upper bound for some gas pairs. OMe-ROMP showed diffusivity selectivity higher than PIM-1 for CO_2/CH_4 and N_2/CH_4 separation.

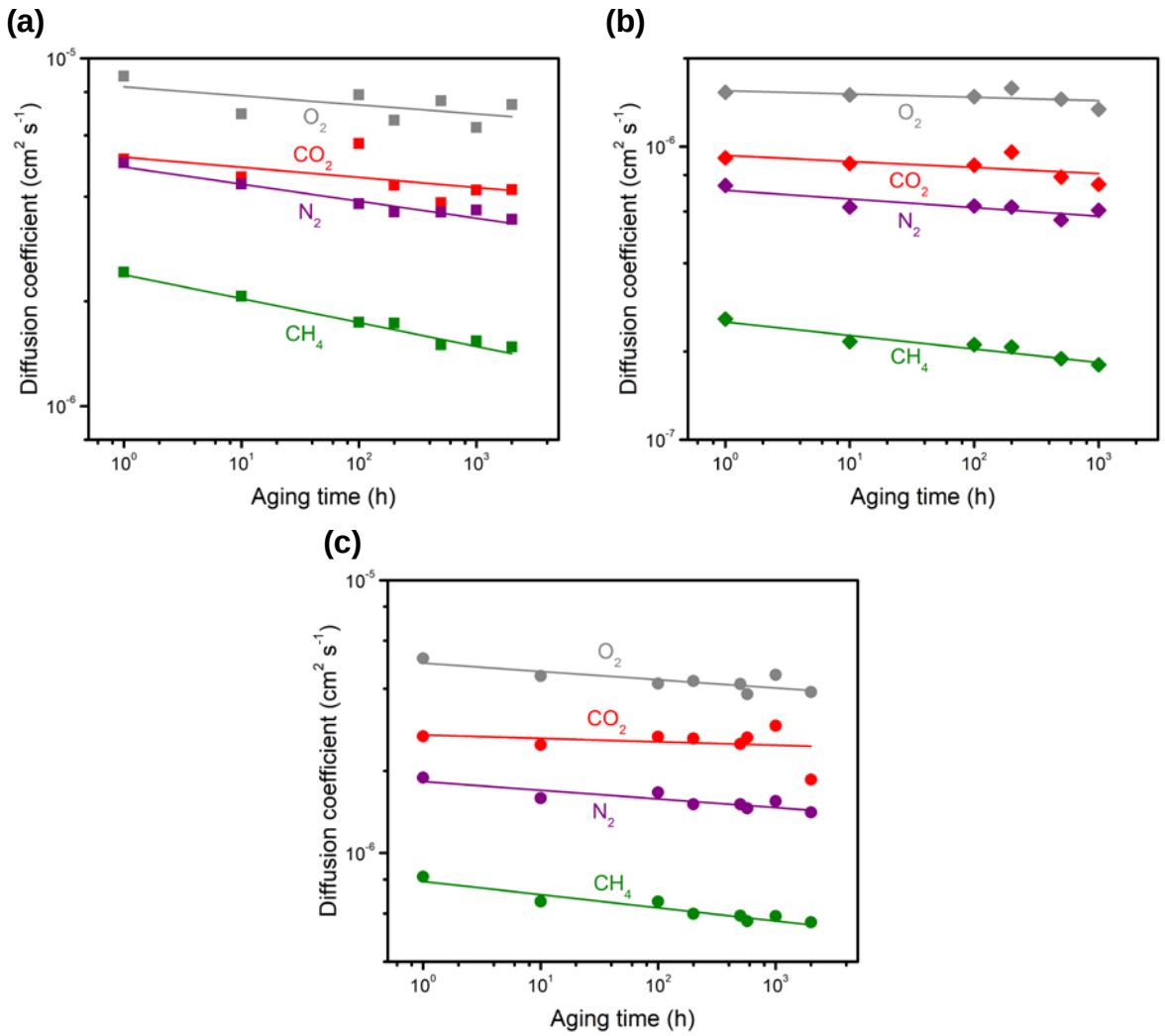

Figure B.18. Diffusion coefficient as a function of time. Data were collected at 35 °C and 1 bar upstream pressure for (a) CF_3-ROMP, (b) OMe-ROMP, and (c) PIM-1. He and H_2 data were not plotted because time lags were less than 2 s.

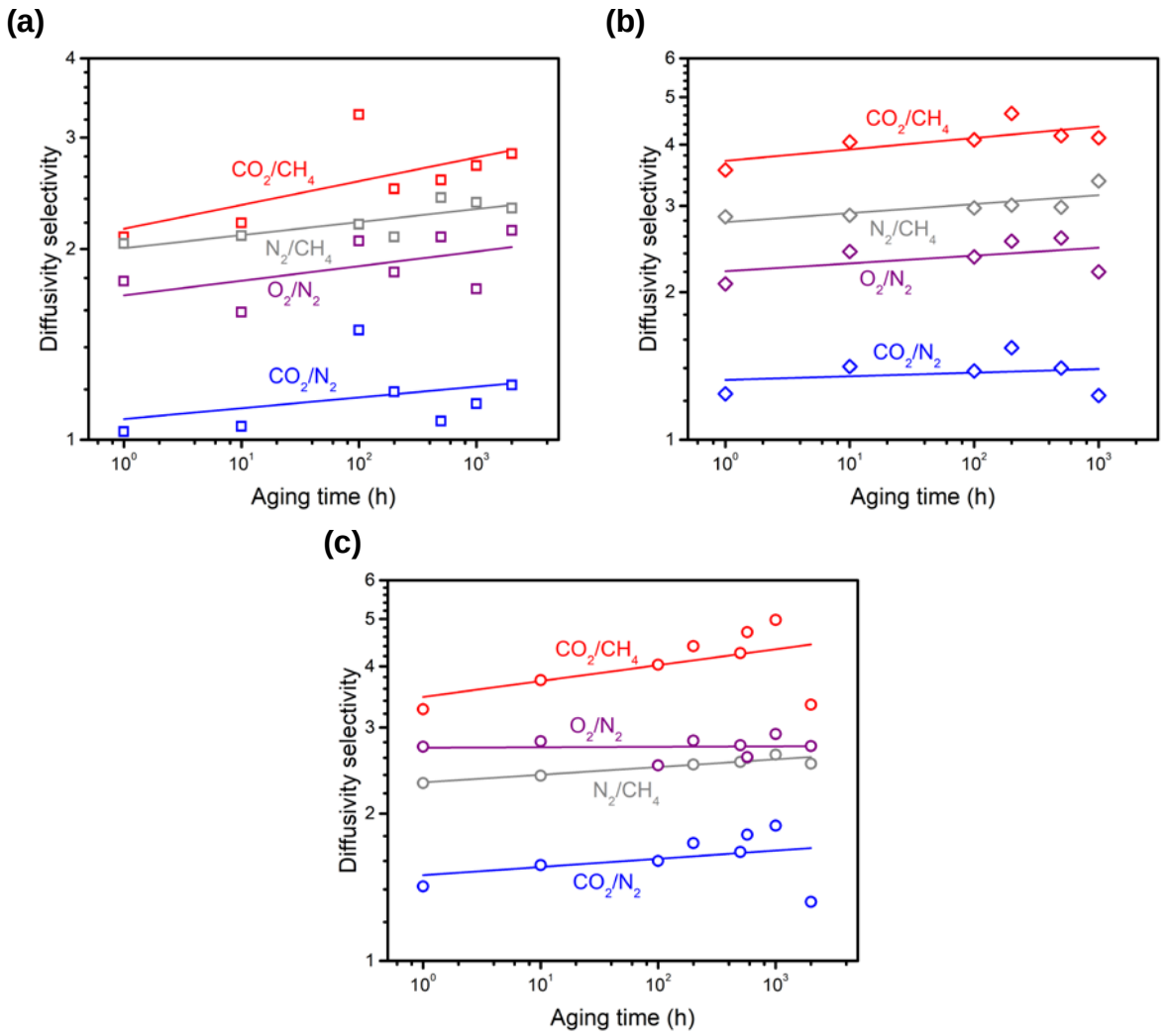

Figure B.19. Diffusivity selectivity as a function of time. Data were collected at 35 °C and 1 bar upstream pressure for (a) CF_3-ROMP, (b) OMe-ROMP, and (c) PIM-1. He/X and H_2/X data were not plotted because time lags were less than 2 s.

Solubility coefficients and solubility selectivity were also calculated to evaluate their trend over time using a reverse formula of Equation B.2:

$$\mathcal{S} = \frac{\mathcal{P}}{\mathcal{D}} \tag{B.5}$$

Solubility and solubility selectivity values appear to oscillate around an approximate average value over time, as seen in **Figure B.20** and **Figure B.21**, respectively. CF_3-ROMP and PIM-1 showed

similar results for solubility selectivity, while OMe-ROMP recorded higher values of CO_2/N_2 and CH_4/N_2.

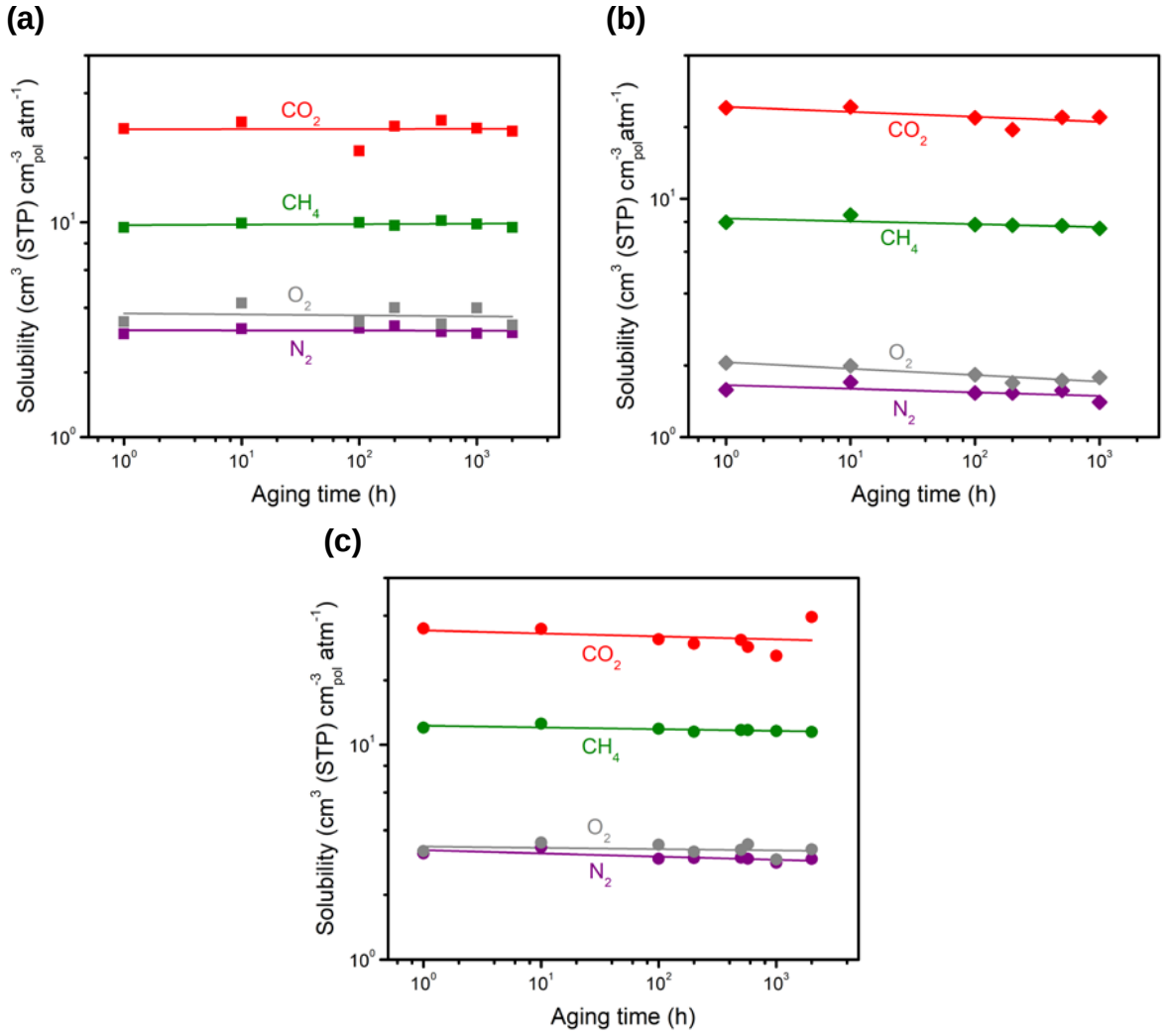

Figure B.20. Solubility as a function of time. Data were collected at 35 °C and 1 bar upstream pressure for (a) CF_3-ROMP, (b) OMe-ROMP, and (c) PIM-1. He and H_2 data were not plotted because time lags were less than 2 s and the calculation of S depends on D (Eq. 5).

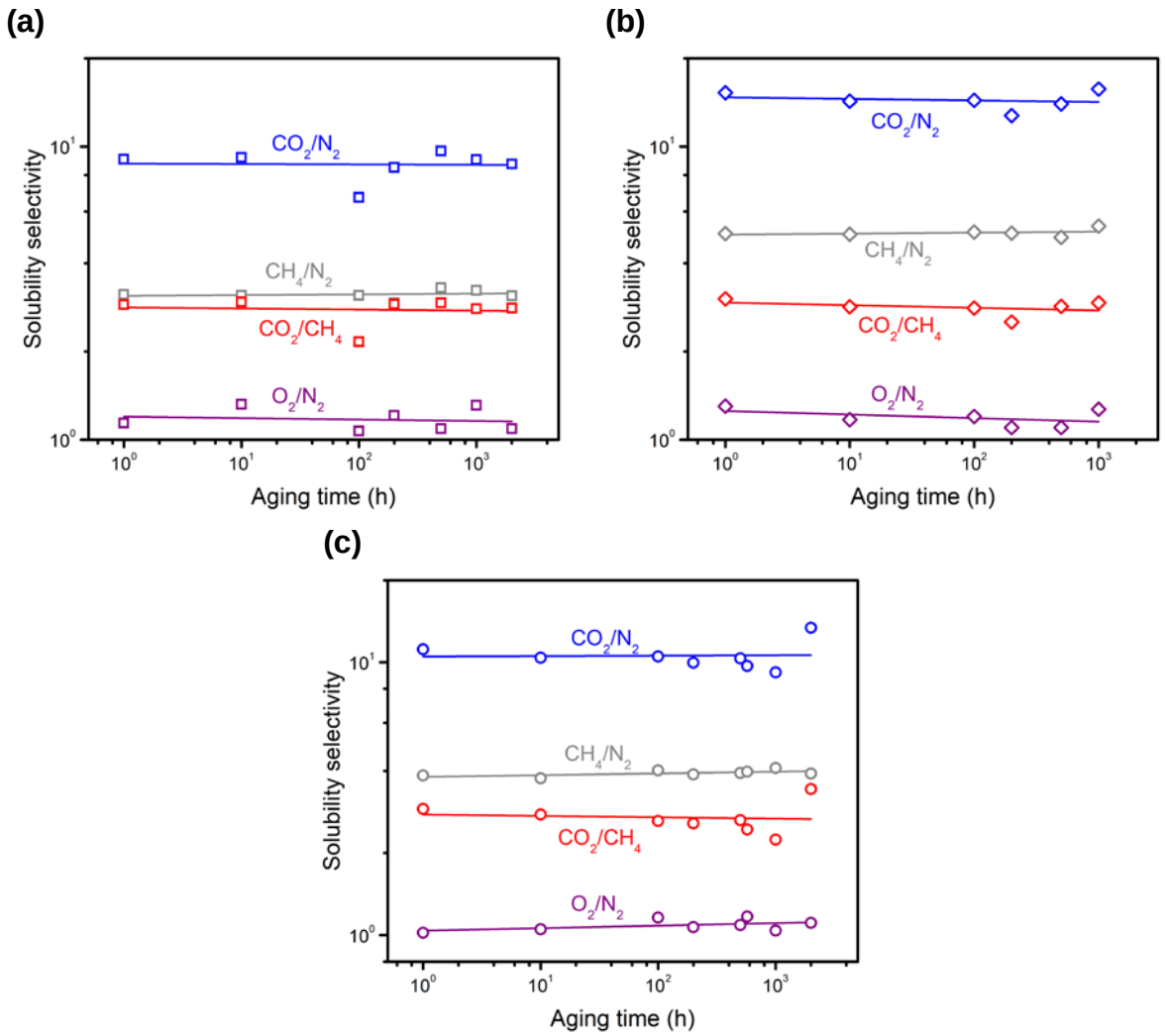

Figure B.21. Solubility selectivity as a function of time. Data were collected at 35 °C and 1 bar upstream pressure for a) CF_3-ROMP, b) OMe-ROMP, and c) PIM-1. He/X and H_2/X data were not plotted because time lags were less than 2 s and the calculation of S depends on D (Eq. B.5).

B.9. Wide-angle X-ray scattering (WAXS) study

Physical aging was also monitored by Wide-angle X-ray scattering. X-ray scattering methods are suitable for studying internal structural changes of CF_3-ROMP, OMe-ROMP, and PIM-1 because of their high fractional free volume and relevant pore-size distribution. For WAXS, d (Bragg spacing) and q (scattering vector) are correlated as follows:

$$d = \frac{2\pi}{q} \tag{B.6}$$

It is important to note that these WAXS experiments were performed in conjunction with gas permeation experiments during the course of 2000 h on samples from the same film, so the aging history was identical and results could be directly correlated. The same sample was used for WAXS throughout the entire 2000 h so the scattering intensity can be compared on a relative-basis. **Figure B.22** shows that CF_3-ROMP (a) is the polymer that experienced less aging in internal free volume, especially in the range where q is larger than 1 $Å^{-1}$ (*d*-spacing < 3.14 Å), which means smaller pores were preserved over time after soaking in liquid ethanol. This result is consistent with the fact that smaller gases (*e.g.*, He and H_2) showed slower physical aging rates (**Figure B.17a**) and correlates with the different rates in permeability drop (**Figure B.17b-c**).

Conversely, OMe-ROMP (b) and PIM-1 (c) showed a larger decrease in the absolute scattering intensity across all ranges of pore size ($0.1\ Å^{-1} < q < 2\ Å^{-1}$), which supports our findings that these polymers possess faster aging rates for small gases (*e.g.*, He and H_2) and similar aging rates for larger gases (*e.g.*, N_2 and CH_4) compared to CF_3-ROMP. The contraction of larger pores has a much larger impact on the transport of larger gas molecules compared to smaller ones.

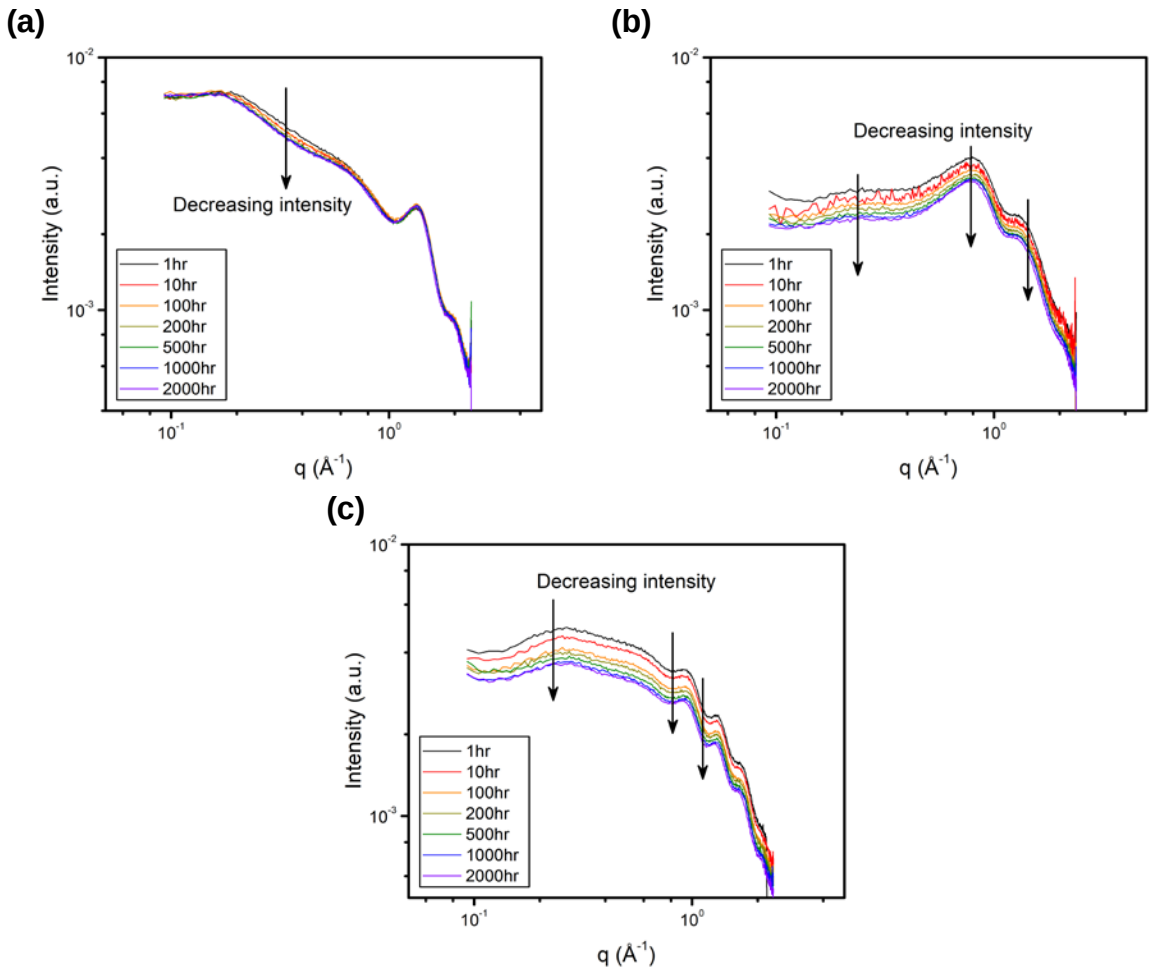

Figure B.22. WAXS patterns for (a) CF_3-ROMP, (b) OMe-ROMP, and (c) PIM-1 as a function of time up to 2000 h, for films treated using method **(B)**.

B.10. CO_2-induced plasticization study

Plasticization is a frequently investigated phenomenon in the field of membrane science.[57,241] It is typically recognized through a decrease in glass transition temperature and an increase in gas permeability as the upstream pressure increases. Plasticization is especially relevant when operating with high pressure feed streams (*e.g.*, natural gas processing). Among the gases investigated in this study, CO_2 is the only quadrupolar gas and it has the highest critical temperature. For these reasons, separate permeation experiments were performed with CO_2 pressures up to 17, 20.5, 25, and 51 bar. One of the most undesirable consequences of plasticization is a significant

reduction in membrane mixed-gas selectivity.[191,242] It is important to determine the extent to which materials can resist plasticization to ensure steady and reliable performance even when plasticizing agents are present in high concentrations. The ROMP samples and PIM-1 plasticization performance can be compared with results previously obtained in the literature at different conditions. Since plasticization pressure usually decreases with increasing thickness,[56] a direct comparison can be made just among thick films.

Table B.2 contains a broad collection of CO_2-induced plasticization data. CO_2 permeability from the first point of the plasticization curve, which usually was taken at an upstream pressure between 1 and 2 bar, is reported to give a sense of the performance of different polymers, which ranges over 4 orders of magnitude. The so-called plasticization pressure is a parameter that is commonly considered to compare the plasticization resistance of polymers. Polymers that showed a plasticization point are compared in **Figure B.23**. Excluded from this figure, but included in **Table B.2**, is data for a crosslinked Matrimid® film (treated at 350 °C for 30 minutes), which shows no plasticization pressure point up to 44 bar and a steady high-pressure plateau in permeability of 3.5 barrer.28 For non-crosslinked polymers, polysulfone (PSf) and polycarbonate (PC) had the highest plasticization pressures. For a PSf thick film, the plasticization pressure point was ~34 bar,27 and for a PSf thin film, the plasticization pressure point was ~24 bar,[243] while for a PC thick film it was ~34 bar.[244] However, CF_3-ROMP and OMe-ROMP are the only polymers whose permeabilities exhibit continuously decreasing values after reaching 51 bar of CO_2. CF_3-ROMP and OMe-ROMP results described in **Chapter 3** show unprecedented results.

Table B.2. CO_2 plasticization pressure in glassy polymers from this work and from the literature.

Polymer	CO_2 Permeability @ 1-2 bar (Barrer)	Peculiarities (treatment, thickness)	Plasticization pressure	Reference
CF_3-ROMP	**14477**	**119 µm, ethanol treatment, 2100 h aged**	**> 51 bar**	**This work**
OMe-ROMP	**1425**	**153 µm, ethanol treatment, 300 h aged**	**> 51 bar**	**This work**
PIM-1	**10558**	**119 µm, ethanol treatment, 2000 h aged**	**~27.5 bar**	**This work**
6FDA-6FmDA	5.5		~21 atm	[245]
6FDA-6FpDA	75.5		~10 atm	[245]
6FDA-6FpDA	78		~16.5 bar	[242]
6FDA-6FpDA/DABA 2:1	47	Uncrosslinked	~10.3 bar	[242]
6FDA-DAM:DABA 2:1		Rapid quench from T_g+15 °C	~34.5 bar	[172]
AD 60	400	Annealed above T_g, 335 nm	~8 bar	[246]
AF 2400	2400	As-cast, 258 nm	~12 bar	[246]
AF 2400	3800	Annealed above T_g, 17 µm	~10 bar	[246]
BPA-PC	7.5		~31 bar	[57]
BPZ-PC	2.5		~24 bar	[57]
C-CoPIM-TB-1	5400	Pure-gas and 50:50 CO_2/CH_4	> 20 atm	[247]
C-CoPIM-TB-2	4200	Pure-gas and 50:50 CO_2/CH_4	> 20 atm	[247]
CA	6.5 - 9		11-13 bar	[57,162]
CTA	8		~10 bar	[57]
HFPC	34		~21 bar	[244]
KAUST-PI-1	2400	Pure-gas and 50:50 CO_2/CH_4	< 2 bar	[162]
KAUST-PI-5	1500	Pure-gas and 50:50 CO_2/CH_4	~12 bar	[162]
Matrimid	9	182 nm	~6 atm	[56]
Matrimid	9.2	20 µm	~14 atm	[56]
Matrimid	5	Crosslinked, 30' at 350 °C	> 44 bar	[191]
P84	1		~22 bar	[57]
PC	7.5	127 µm	~34 bar	[244]

PEI	1		~28 bar	[57]
PES	3.4		~27 bar	[57]
PIM-1	450	200 nm	< 2 bar	[248]
PIM-1	10600	30 µm	~8 bar	[248]
PIM-1	5500-5600	50-102 µm	> 10 bar	[142,173]
PIM-Trip-TB	8400	Pure-gas and 50:50 CO_2/CH_4	> 20 atm	[247]
PMMA	0.5		< 2 bar	[249]
PPO	95	18 – 45 µm	~14 bar	[57]
PPO	41.5	192 nm	~6 bar	[243]
PSf	4.7	18 – 45 µm	~34 bar	[57]
PSf	9.2	191 nm	~24 bar	[243]
PTMSP	35500	115 µm	> 28 atm	[250]
TMBPA-PC	15		~13 bar	[57]
TMPC	22.5		~21 bar	[244]
TPIM-1	1500	Pure-gas and 50:50 CO_2/CH_4	< 2 bar	[173]
TPIM-2	450	Pure-gas and 50:50 CO_2/CH_4	N/A, constant profile up to 15 bar	[173]

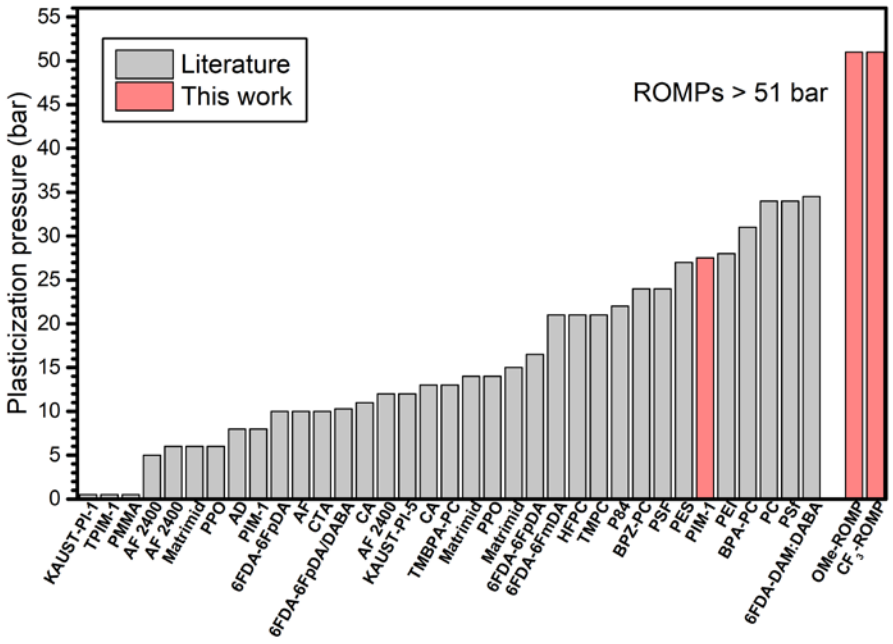

Figure B.23. Collection of CO_2-induced plasticization pressure results obtained for uncrosslinked polymers in pure-gas conditions from the literature (gray bars), and comparison with polymers investigated in this study (red bars).

CO_2-induced plasticization curves obtained with a maximum pressure lower than 51 bar are shown in **Figure B.24**. The duration of each experiment in the increasing pressure stage (filled markers) was 12 minutes and 15 minutes for CF_3-ROMP and OMe-ROMP, respectively, and 18 minutes and 21 minutes for CF_3-ROMP and OMe-ROMP, respectively, in the decreasing pressure stage (hysteresis), to ensure that pseudo-steady state was reached to calculate permeability.

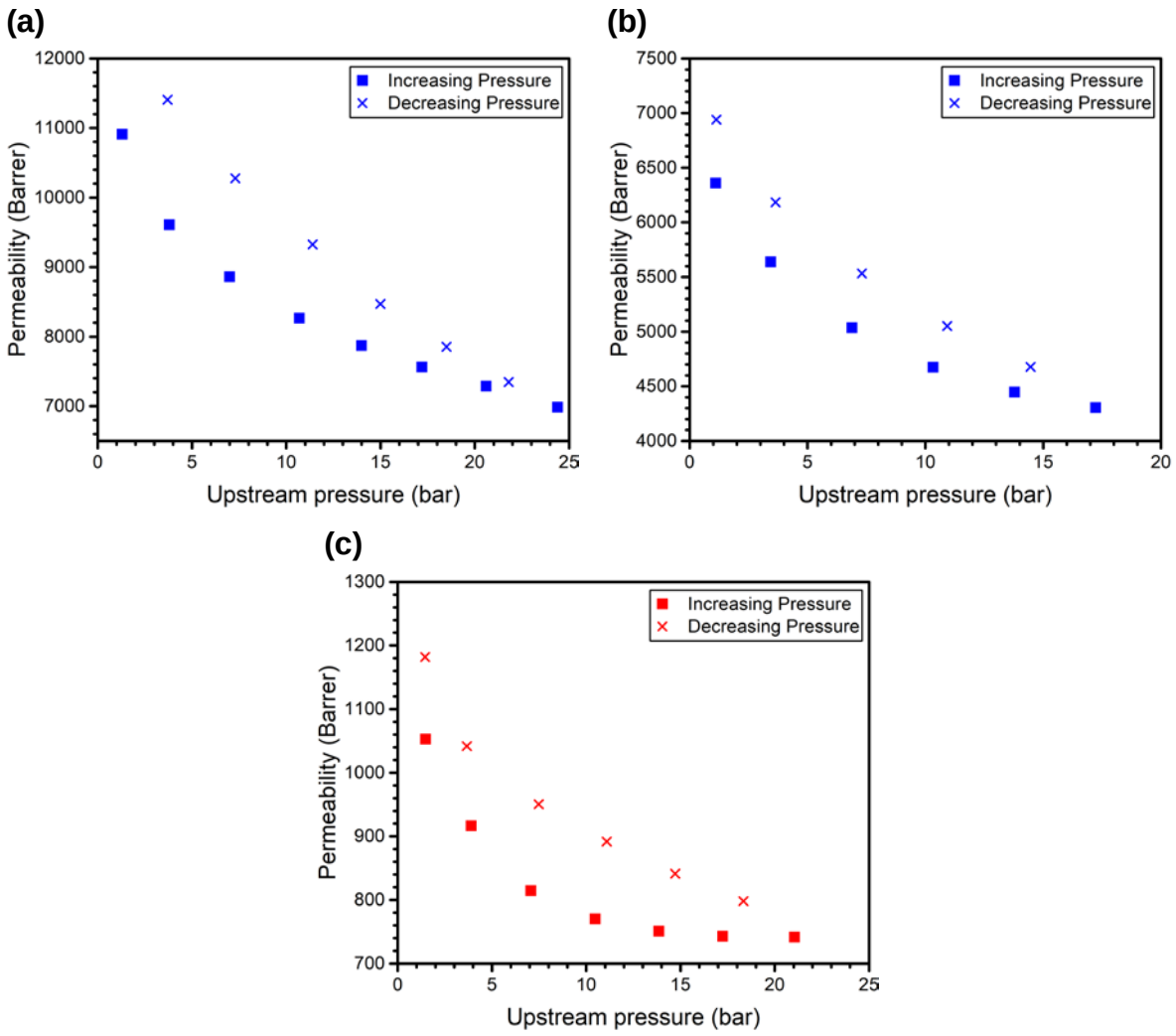

Figure B.24. CO_2 plasticization study (a) CF_3-ROMP, treatment **(D)**, tested up to 24 bar, 90 h aged, (b) CF_3-ROMP, treatment **(E)**, tested up to 17 bar, 48 h aged, (c) OMe-ROMP, treatment **(E)**, tested up to 20.5 bar, 60 h aged.

Considering the high upstream pressures reached during CO_2-induced plasticization experiments, it is important to correct for the non-ideal behavior of CO_2. Permeability can be calculated modifying Equation B.1 by using fugacity, f, instead of pressure, as indicated in Equation B.7:

$$\mathcal{P}' = \frac{V}{RT}\frac{l}{A}\frac{1}{(f_u - \bar{f}_d)}\left(\frac{df_d}{dt}\right) \quad \text{(B. 7)}$$

The fugacity was calculated by means of Peng-Robinson Equation of State.[251] **Figure B.25** shows the results reported in the main communication, recalculated on a fugacity-based fashion. The permeability of CF_3-ROMP revealed to be decreasing with fugacity up to 40 bar, the whole range investigated, while OMe-ROMP showed a minimum at around 10 bar that was not experienced when permeability was calculated based on pressure instead of fugacity (**Figure 3.3a**). PIM-1 results, instead, confirmed that a minimum value of permeability was obtained at a fugacity of ~21 bar.

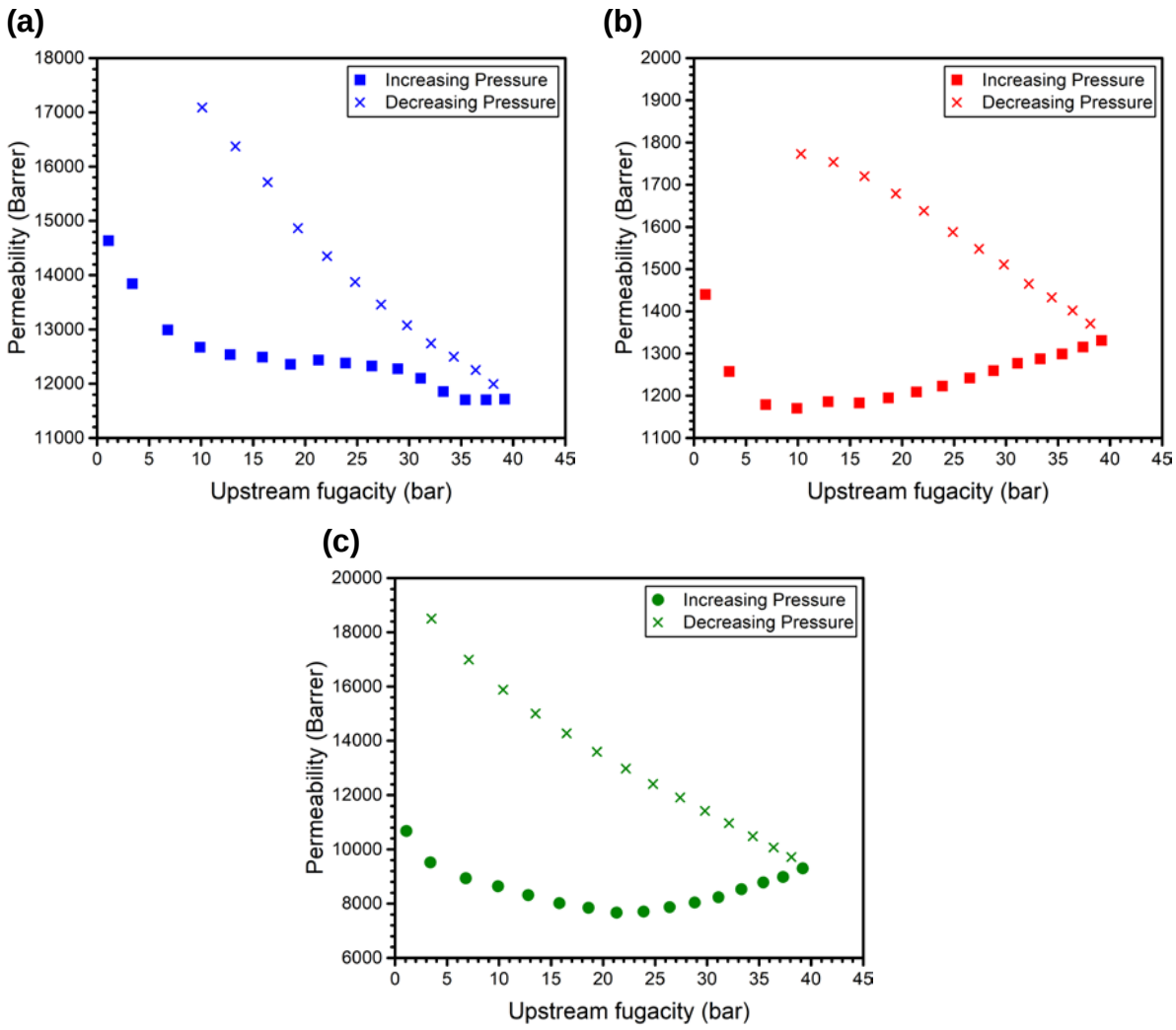

Figure B.25. Fugacity-based CO_2 plasticization curves for liquid ethanol treated samples: (a) CF_3-ROMP aged 2100 h, (b) OMe-ROMP aged 300 h, and (c) PIM-1 aged 2000 h.

B.11. Mixed-gas permeation

Mixed-gas permeation measurements of CO_2/CH_4 were carried out with CF_3-ROMP, the most permeable polymer in this study that also showed unprecedented plasticization resistance, using a 50:50 vol.% CO_2/CH_4 mixture. Mixed-gas feed pressures of 1 and 2 bar were tested, thus 0.5 and 1 bar or partial pressure of CO_2, respectively. A gas chromatograph (GC) (INFICON 3000 Micro GC) was used in order to measure the concentration of gas in the feed, residue, and permeate streams. A hold time of 30 minutes was found to be sufficient to reach steady state by monitoring the concentration of the permeate stream over time until a constant composition was reached. This is due to the very high diffusion coefficients of CF_3-ROMP as measured in pure-gas permeation studies (**Figure B.13** and **Table B.1**). Additionally, helium was used as a carrier gas to sweep permeate from the membrane surface. The following Equation B.8 was used to calculate the mixed-gas permeability, $\boldsymbol{\mathcal{P}_A}$:

$$\mathcal{P}_A = \frac{x_A^P F l}{x_{He}^P A (p_2 x_A^F - p_1 x_A^P)} \tag{B.8}$$

in which x_A^P is the mole fraction of gas A in the permeate stream, F is the sweep gas flow rate, l is the thickness of the membrane, x_{He}^P is the mole fraction of helium in the permeate stream, A is the area of membrane exposed to the gas stream, x_A^F is the mole fraction of gas A in the feed stream, and p_2 and p_1 are the upstream and downstream total pressures, respectively.[42,252]

Three different treatment conditions for CF_3-ROMP were tested to examine their effects on mixed-gas transport properties:

(E) As reported in **Section B.5**;

(F) Vacuum drying at room temperature for 24 h;

(G) Soaking in liquid ethanol for 36 h, air-drying for 48 h, and full vacuum at room temperature for 4 h;

Table B.3 summarizes results obtained from these three treatment methods for a 50:50 vol.% CO_2/CH_4 mixture at the feed pressures mentioned above. Pure CO_2 and CH_4 measurements were also conducted at 1 bar using the above described technique for the mixed-gas experiments. These tests can be directly compared to 50:50 vol.% mixed-gas permeability experiments performed at 2 bar, so that the partial pressure of each gas is 1 bar in both pure- and mixed-gas conditions.

Table B.3. CO_2 and CH_4 permeability values for CF_3-ROMP with different treatment conditions: **(E)** Thermal treatment at 120 °C for 24 h and applying dynamic vacuum, **(F)** vacuum drying at room temperature for 24 h, and **(G)** soaking in liquid ethanol for 36 h, air-drying for 48 h, and full vacuum at room temperature for 4 h. Feed pressure is reported in bar, and permeability ($\boldsymbol{\mathcal{P}_X}$) is reported in Barrer (10^{-10} cm^3(STP) cm cm^{-2} s^{-1} $cmHg^{-1}$). All data were calculated at 35 °C.

Mixture Composition	Treatment	Feed Pressure (bar)	$\mathcal{P}_{CH_4}$	$\mathcal{P}_{CO_2}$
Pure-Gas	(E)	1	644	6377
	(F)	1	1086	8867
	(G)	1	2368	13418
50:50 vol.% CO_2/CH_4	(E)	1	598	6373
		2	779	7063
	(F)	1	1005	9925
		2	1151	9266
	(G)	1	2279	15707
		2	2183	15036

CO_2/CH_4 Robeson plots for both pure-gas and 50:50 vol.% CO_2/CH_4 mixtures at a CO_2 partial pressure of 1 bar are shown below in **Figure B.26**. From the Robeson plots, there appears to be a systematic, albeit small, increase in permeability from the pure-gas case to the mixed-gas case. In **Figure B.26c**, which depicts the performance of CF_3-ROMP that underwent treatment **(G)**,

an increase in the separation factor of around 21.5% is also recorded from the pure-gas case to the mixed-gas case. This may be due to an increase in CO_2/CH_4 solubility-selectivity, due to the fact that the more condensable gas, CO_2, tends to exclude CH_4 from the polymer matrix.[253] The plasticization-resistant nature of CF_3-ROMP reduces the swelling induced by CO_2, possibly preventing a significant increase of the CH_4 diffusion coefficient that would be observed otherwise.[254,255] This would reduce the decrease in CO_2/CH_4 diffusivity-selectivity generally experienced from the pure-gas case to the mixed-gas case.[254,255] Thus, the increase in solubility-selectivity may outweigh the decrease in diffusivity-selectivity, leading to the overall increase in the CO_2/CH_4 permselectivity that we reported. This result seems to be emphasized by the ethanol treatment.

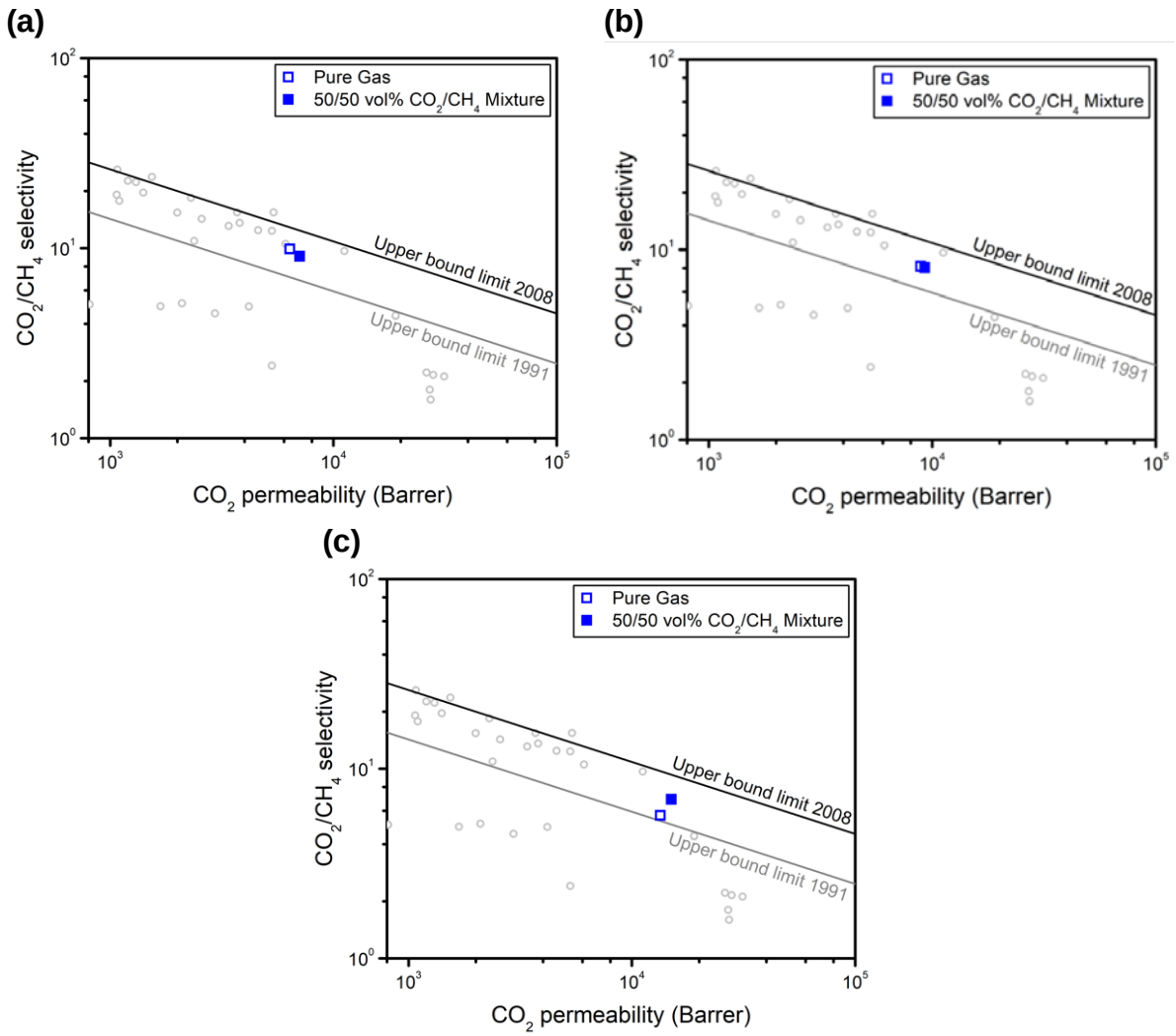

Figure B.26. CO_2/CH_4 Robeson plots for CF_3-ROMP films undergoing three different treatments: (a) treatment **(E)**, (b) treatment **(F)**, and (c) treatment **(G)**. Gray dots are data from the Robeson database.[46,47]

Table B.4 contains CO_2/CH_4 permselectivities reported in literature for various polymers during mixed-gas experiments. Feed pressures and temperatures are also reported, as well as treatment methods, if applicable. At a feed pressure of 2 bar, the ideal CO_2/CH_4 permselectivity of PIM-1 was reported to be 16, while that of AO-PIM-1 was reported to be 34.[65] When exposed to a equimolar CO_2/CH_4 mixture with a CO_2 partial pressure of 2 bar, the CO_2/CH_4 permselectivities of PIM-1 and AO-PIM-1 decreased to 12 and 24, respectively.[65] A similar decrease in CO_2/CH_4

permselectivity from the pure-gas case with feed pressures of 2 bar to the mixed-gas case with a CO_2 partial pressure of 2 bar and an equimolar CO_2/CH_4 mixture feed was observed with TPIM-1 (31 to ~30) and 6FDA-DAP (92 to ~87).[173,186] However, the CO_2/CH_4 permselectivity of TPIM-2 slightly increased from the pure-gas case to the mixed-gas case (21 to ~23).[173] TPIM-2 was reported to have high plasticization resistance, as the CH_4 permeability increased by less than 10% from the pure-gas case to the mixed-gas case.[173] Similarly, the CH_4 permeability in the mixed-gas case for the plasticization-resistant CF_3-ROMP was around 6% higher than the pure-gas value at a CH_4 partial pressure of 1 bar for sample **(F)**, while for the sample that underwent treatment **(G)**, it revealed to be around 8% smaller. As a consequence, the latter film experienced a CO_2/CH_4 permselectivity increased up to around 21.5%. A similar increased in mixed-gas permselectivity was experienced before by HAB-6FDA and its thermally rearranged analogous.[204]

Table B.4. CO_2 plasticization pressure in glassy polymers from this work and from the literature. Feed pressure is reported in bar, temperature is reported in °C, while permeability ($\boldsymbol{\mathcal{P}_X}$) is reported in Barrer (10^{-10} cm^3(STP) cm cm^{-2} s^{-1} $cmHg^{-1}$).

Polymer	CO_2/CH_4 Mixture Composition	Feed Pressure (bar)	Temperature	Treatment Method	% α_{CO_2/CH_4} change[a]	Reference
CF_3-ROMP	50:50	2	35	Soaking in liquid ethanol for 36 h, air-drying for 48 h, and full vacuum at room temperature for 4 h;	+22%	This work
PIM-1	50:50	4	35	Drying at 45 °C for 2 days, soaking in liquid methanol for 24 h, air-drying, and heating at 120 °C for 24 h under high vacuum	-25%	65
AO-PIM-1	50:50	4	35	Drying at 45 °C for 2 days, soaking in liquid methanol for 24 h, air-drying, and heating at 120 °C for 24 h under high vacuum	-29%	65
PIM-1	50:50	4	35	Drying at 120 °C under vacuum for 12 h, soaking in liquid methanol for 24 h, and drying at 120 °C under vacuum for 24 h	-13%	173
TPIM-1	50:50	4	35	Drying at 120 °C under vacuum for 12 h, soaking in liquid methanol for 24 h, and drying at 120 °C under vacuum for 24 h	-6%	173
TPIM-2	50:50	4	35	Drying at 120 °C under vacuum for 12 h, soaking in liquid methanol for 24 h, and drying at 120 °C under vacuum for 24 h	+14%	173
TZPIM-2	50:50 or 80:20	~4	25	Soaking in liquid methanol and drying at 120 °C in vacuum oven for 24 h.	-7.6	163
6FDA-*m*PDA	50:50	~4	35	Soaking in liquid methanol for 12 h, air-drying, and drying at 120 °C in a vacuum oven for 24 h	+1%	186
6FDA-DAP	50:50	~4	35	Drying at 120 °C and post-drying at 200 °C in a vacuum oven for 24 h	-3%	186
6FDA-DAR	50:50	~4	35	Drying at 120 °C and post-drying at 200 °C in a vacuum oven for 24 h	-1%	186

HAB-6FDA	50:50	~4	35	Drying at 80 °C under partial vacuum for 24 h and post-drying at 200 °C under full vacuum for 24 h	+26%	[204]
TR450	50:50	~4	35	HAB-6FDA films heated under flowing N_2 at 300 °C for 1 h and at 450 °C for 1 h.	+20%	[204]

[a]This column refers to the percentage difference between CO_2/CH_4 permselectivity from the pure-gas to the mixed-gas case.

For the polymers reported here from literature, CO_2/CH_4 permselectivity generally decreased as feed pressure was increased. While competitive sorption can result in a lower CO_2 permeability, plasticization of the polymer when exposed to higher pressures can lead to an increase in CH_4 permeability, which collectively can decrease the CO_2/CH_4 permselectivity.[173] When increasing the feed pressure from 4 bar to 20 bar, PIM-1 was shown to have a mixed-gas CO_2/CH_4 permselectivity that decreased by approximately 38%, while the CO_2/CH_4 permselectivity of AO-PIM-1 decreased by only 13%.[65] The polyimide 6FDA-*m*PDA experienced a CO_2/CH_4 permselectivity drop of 40% as feed pressure was increased from ~4 to ~40 bar, while the CO_2/CH_4 permselectivities of hydroxyl-functionalized polyimides 6FDA-DAP and 6FDA-DAR decreased by approximately 30% across the same feed pressure range.[186] Similar results were recorded for HAB-6FDA and TR polymers.[204] The unprecedented plasticization results of CF_3-ROMP may indicate that its CO_2/CH_4 permselectivity will not significantly change as the feed pressure increases. Future mixed-gas studies on both CF_3-ROMP and OMe-ROMP will be conducted in order to evaluate their performance and potential in realistic industrial conditions.

B.12. Mechanical properties

Due to the brittleness of CF_3-ROMP and OMe-ROMP, polymer films fractured during the clamping process of dynamic mechanical analysis (DMA), which rendered the measurements not possible. Instead, we measured the reduced Young's modulus (E_r) of CF_3-ROMP, OMe-ROMP,

and PIM-1 using nanoindentation. Corresponding data is shown below (**Figure B.27** and **Figure B.28**). While CF_3-ROMP has a larger E_r than OMe-ROMP, 2.6 GPa and 1.1 GPa respectively, both of them lie in the GPa range, which is on par with most polymers of intrinsic microporosity (*e.g.*, 2.9 GPa for PIM-1). Differences between CF_3-ROMP and OMe-ROMP might be due to different packing states of rigid side chains attached to the polymer backbone.

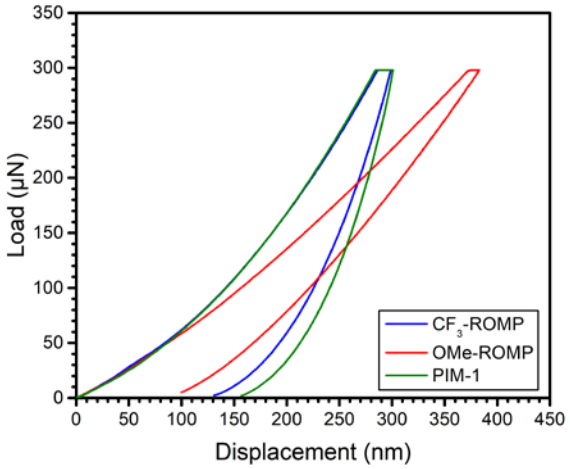

Figure B.27. Load-displacement relationship for CF_3-ROMP, OMe-ROMP, and PIM-1.

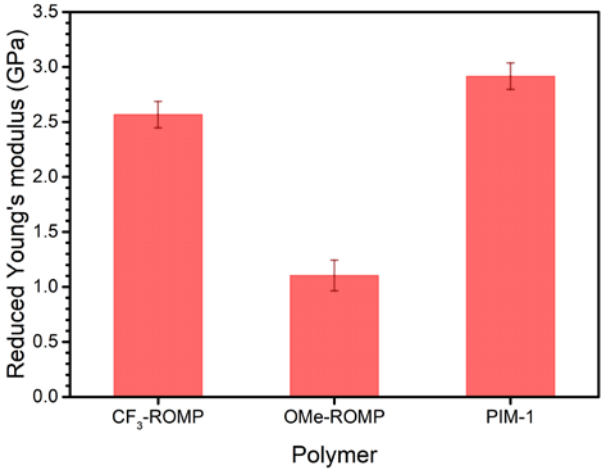

Figure B.28. Reduced Young's modulus (E_r) for CF_3-ROMP, OMe-ROMP, and PIM-1.

Appendix C. Supporting Information for Chapter 4

Reprinted from Benedetti, F. M.; Wu, Y.-C.; **Lin, S.**; He, Y.; Flear, E.; Liu, C.; Zhao, Y.; Swager, T. M.; Smith, Z. P. Elucidating the role of side-chain length and dispersity in ROMP polymers with pore-generating side chains for gas separations. *In preparation.*

C.1. Polymer characterizations

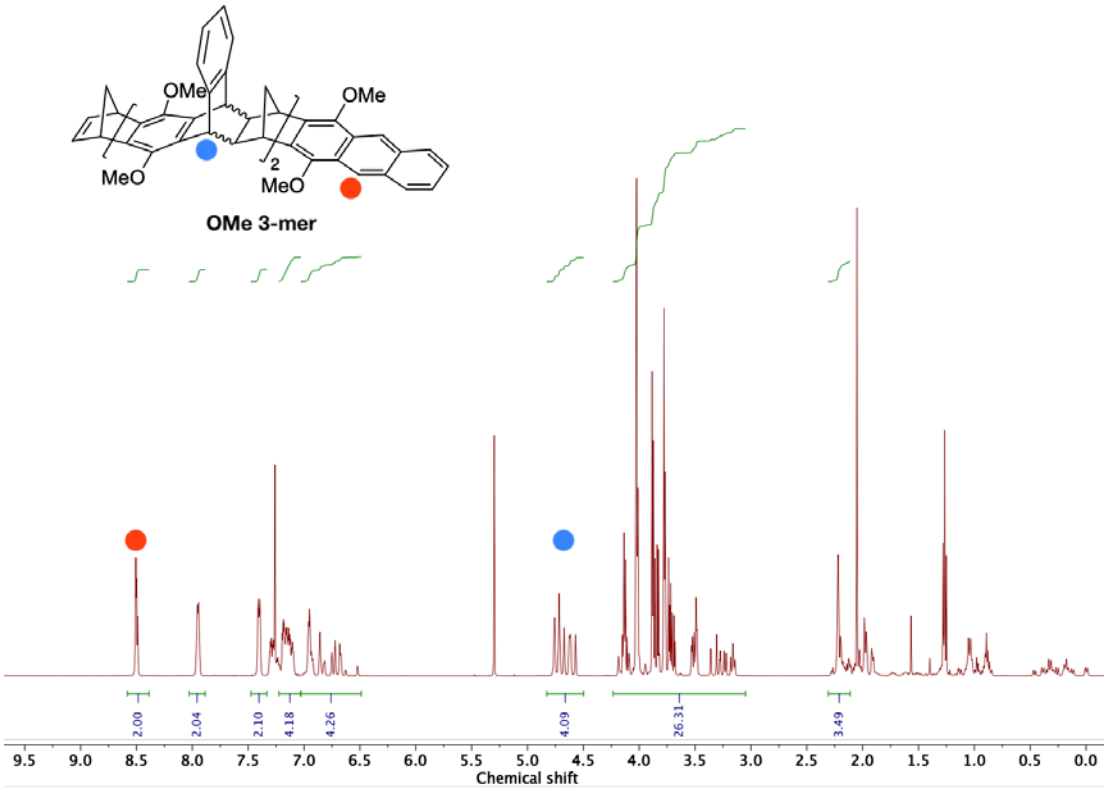

Figure C.1. Example of the method used to obtain NMR integration ratios.

Table C.1. NMR integration ratios of OMe *n*-mers.

	Expected ratio	Experimental ratio
OMe 2-mer	1	1.03
OMe 3-mer	2	2.05
OMe 4-mer	3	3.27
OMe 5-mer	4	4.20

Table C.2. Molecular weights of poly(OMe *n*-mer)s considered in this study.

	[M]/[I]	M_n **(kDa)**	$Đ$
OMe 2-mer	150	76	1.9
OMe 3-mer	150	76	1.9
OMe 4-mer	125	116	2.7
OMe 5-mer	100	84	2.6

(a)

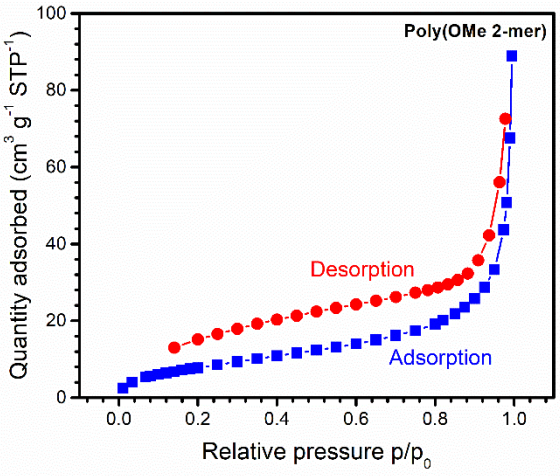
Poly(OMe 2-mer)
Desorption
Adsorption
Quantity adsorbed (cm3 g-1 STP-1)
Relative pressure p/p0

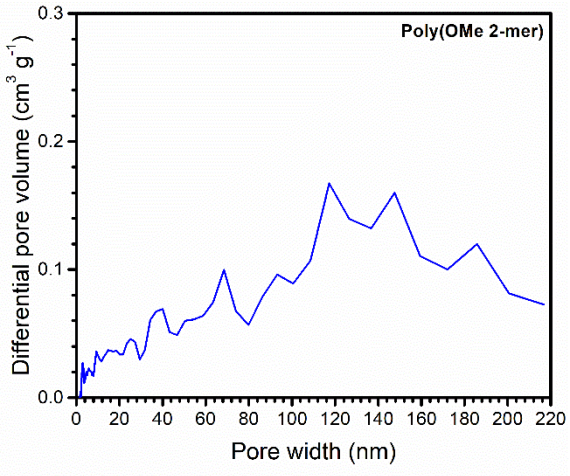
Poly(OMe 2-mer)
Differential pore volume (cm3 g-1)
Pore width (nm)

(b)

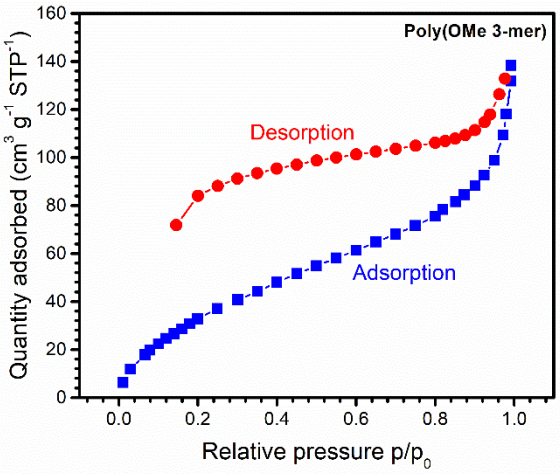
Poly(OMe 3-mer)
Desorption
Adsorption
Quantity adsorbed (cm3 g-1 STP-1)
Relative pressure p/p0

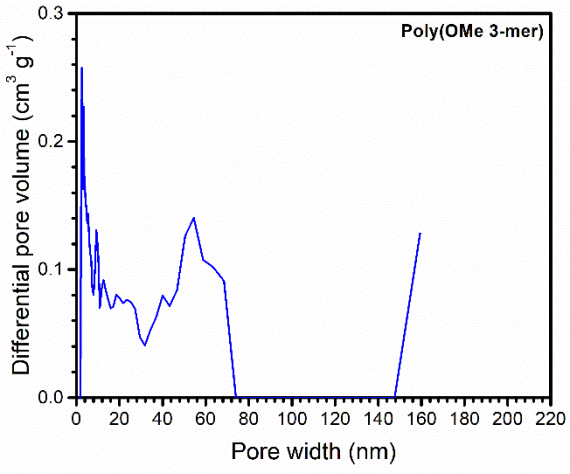
Poly(OMe 3-mer)
Differential pore volume (cm3 g-1)
Pore width (nm)

(c)

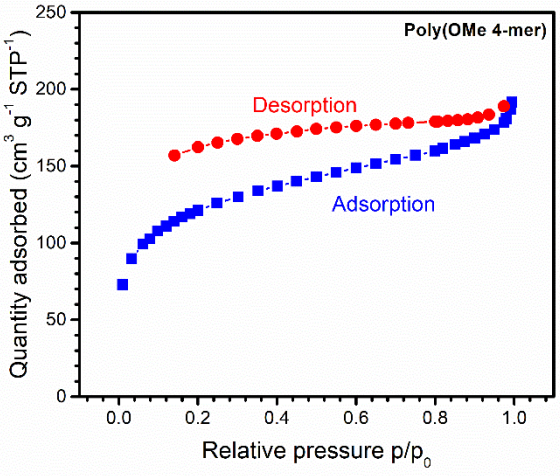
Poly(OMe 4-mer)
Desorption
Adsorption
Quantity adsorbed (cm3 g-1 STP-1)
Relative pressure p/p0

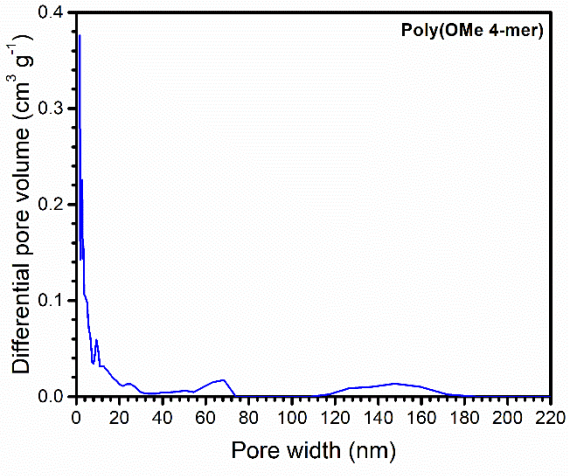
Poly(OMe 4-mer)
Differential pore volume (cm3 g-1)
Pore width (nm)

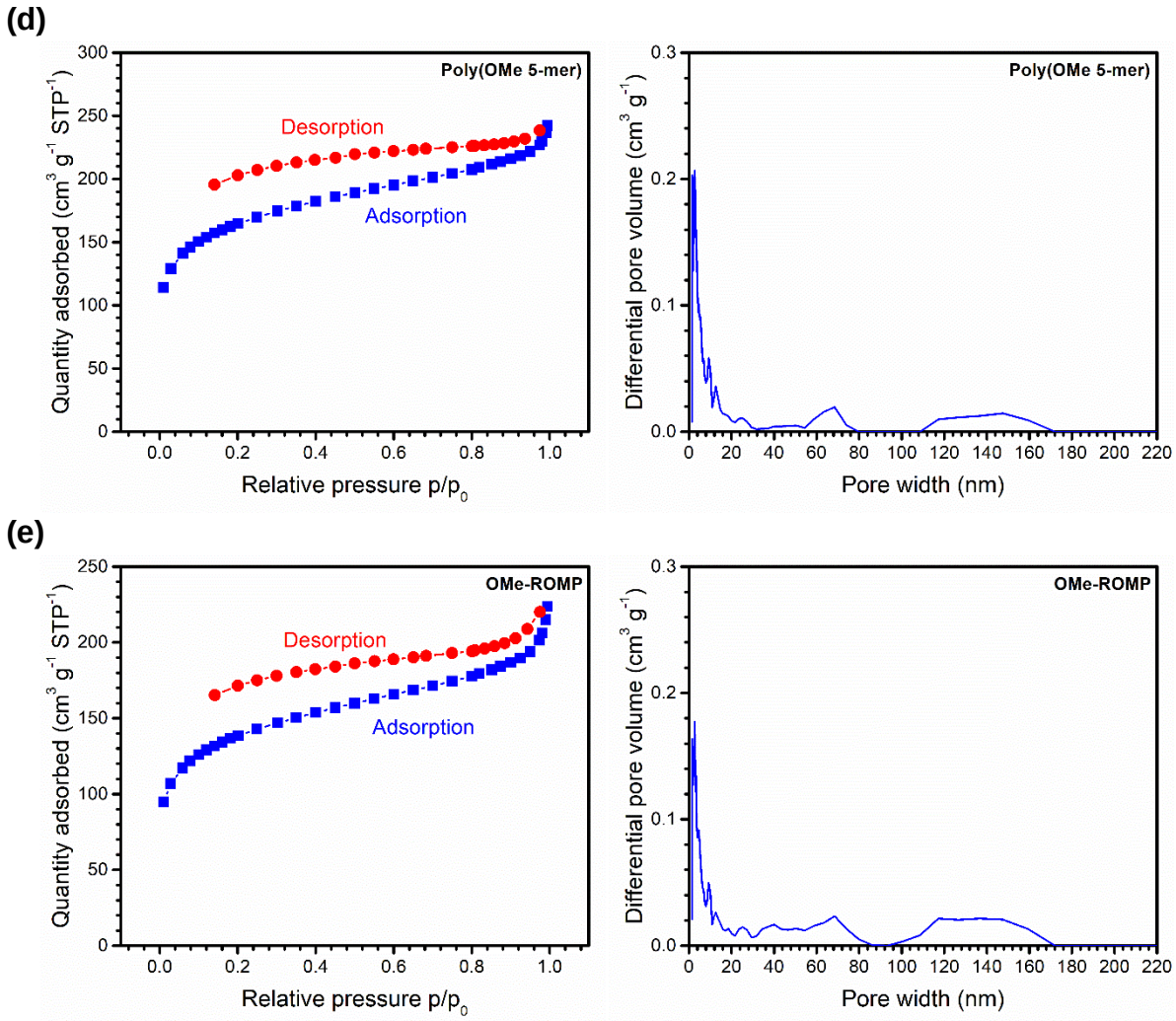

Figure C.2. N_2 adsorption isotherms and pore size distributions (PSDs) of (a) poly(OMe 2-mer), (b) poly(OMe 3-mer), (c) poly(OMe 4-mer), (d) poly(OMe 5-mer), and (e) polydispersed OMe-ROMP obtained from Brunauer–Emmett–Teller (BET) analysis.

C.2. Pure-gas permeability data

Table C.3. Gas separation performance of all poly(OMe *n*-mer)s in this study. Permeability (***P***) is given in barrer (10^{-10} cm^3(STP) cm cm^{-2} s^{-1} $cmHg^{-1}$), diffusion coefficient (***D***) is given in 10^{-8} cm^2 s^{-1}, and sorption coefficient (***S***) is given in cm^3(STP) cm^{-3} atm^{-1}. All data were obtained at 35 °C and ~1 bar upstream pressure.

Polymer	**Treatment**		**He**	**H_2**	**N_2**	**O_2**	**CH_4**	**CO_2**
Poly(OMe 2-mer)	120 °C 24 h vacuum, 1 day aged	***P***	53.16	79.93	3.58	12.71	4.69	83.41
		D	/	/	3.57	8.66	0.91	4.26
		S	/	/	0.76	1.12	3.90	14.87
Poly(OMe 2-mer)	EtOH treat 48 h, air-dry 24 h, 1 day aged	***P***	106.62	153.82	13.36	33.05	13.92	190.13
		D	/	/	13.15	34.16	4.51	13.68
		S	/	/	0.77	0.74	2.34	10.56
Poly(OMe 3-mer)	120 °C 24 h vacuum, 1 day aged	***P***	81.87	135.14	5.37	26.28	8.48	177.79
		D	/	/	6.10	20.56	2.00	9.90
		S	/	/	0.67	0.97	3.23	13.64
Poly(OMe 3-mer)	EtOH treat 48 h, air-dry 24 h, 1 day aged	***P***	160	294	19	64	31	455
		D	/	/	/	/	/	/
		S	/	/	/	/	/	/
Poly(OMe 3-mer)	MeOH treat 48 h, air-dry 24 h, 14 days aged	***P***	168.92	304.43	18.99	65.72	28.46	470.74
		D	/	/	11.63	35.35	3.50	18.89
		S	/	/	1.24	1.41	6.18	18.94
Poly(OMe 4-mer)	120 °C 24 h vacuum, 1 day aged	***P***	242.57	462.36	36.03	112.15	58.38	829.50
		D	/	/	22.27	55.57	6.71	33.37
		S	/	/	1.23	1.53	6.62	18.89
Poly(OMe 4-mer)	120 °C 24 h vacuum, 34 days aged	***P***	242.46	450.71	34.45	107.55	55.55	787.91
		D	/	/	19.47	49.59	6.10	29.84
		S	/	/	1.34	1.65	6.92	20.07
Poly(OMe 4-mer)	120 °C 24 h vacuum, MeOH treat 48 h, air-dry 24 h, 1 day aged	***P***	421.49	839.12	79.77	224.32	136.62	1568.76
		D	/	/	44.98	96.80	14.92	55.82
		S	/	/	1.35	1.76	6.96	21.36
Poly(OMe 4-mer)	120 °C 24 h vacuum, MeOH treat 48 h, air-dry 24 h, 3 days aged	***P***	348.26	716.94	62.51	188.64	108.65	1355.17
		D	/	/	35.53	89.46	12.05	54.01
		S	/	/	1.34	1.60	6.85	19.07
Poly(OMe 5-mer)	120 °C 24 h vacuum, 10 days aged	***P***	496.57	1076.87	106.89	309.18	185.09	2246.57
		D	/	/	45.51	110.96	16.15	67.84
		S	/	/	1.79	2.12	8.71	25.17
Poly(OMe 5-mer)	120 °C 24 h vacuum, MeOH treat 48 h, air-dry 24 h, 1 day aged	***P***	715.64	1655.74	213.69	551.68	404.02	3761.76
		D	/	/	69.18	146.04	28.57	81.72
		S	/	/	2.35	2.87	10.75	34.98
Poly(OMe 5-mer)	120 °C 24 h vacuum, MeOH treat 48 h, air-dry 24 h, 2 days aged	***P***	1075.66	2476.11	301.40	796.56	567.32	5324.12
		D	/	/	101.69	203.37	39.91	128.60
		S	/	/	2.25	2.98	10.80	31.47

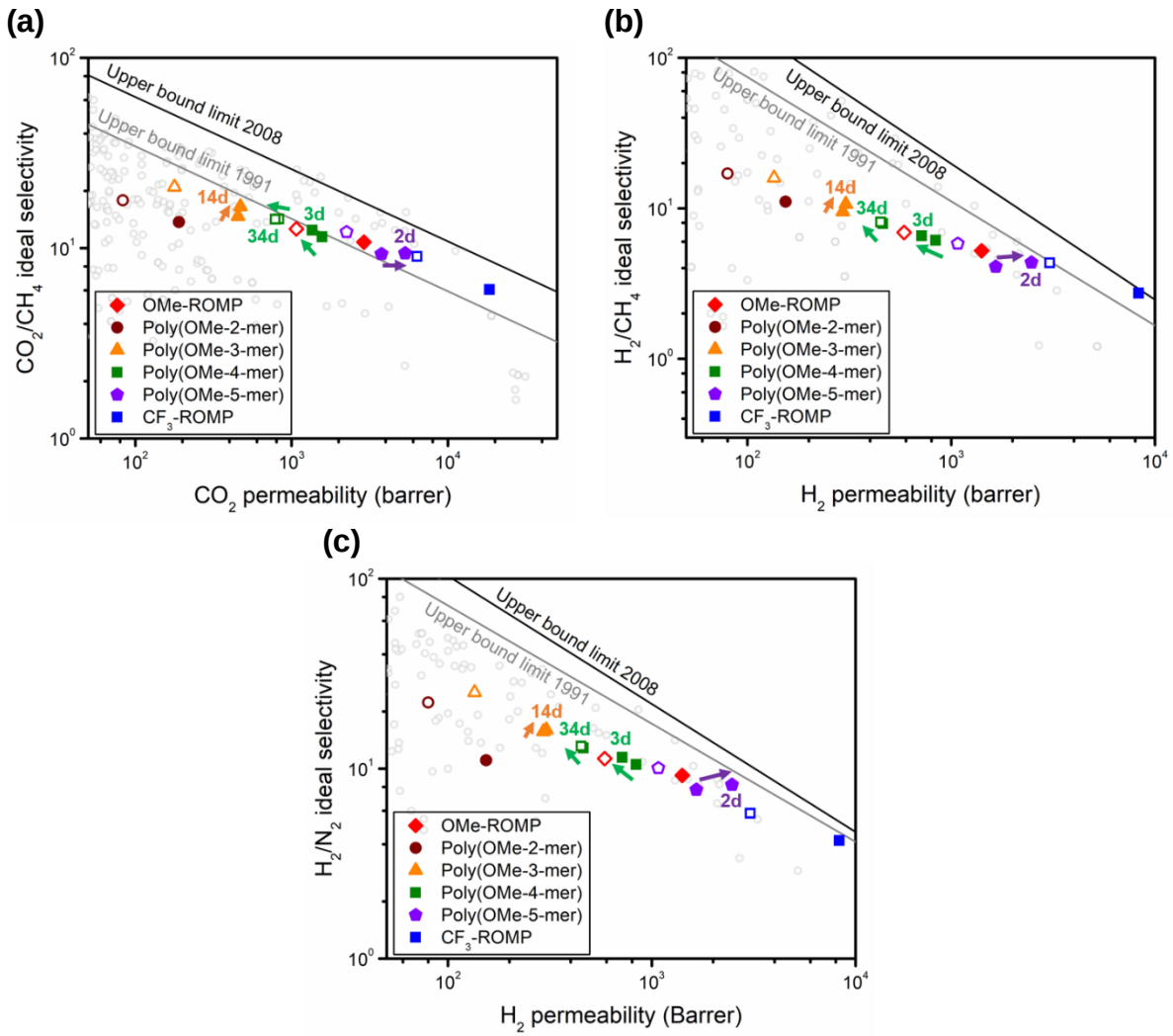

Figure C.3. Robeson plots of poly(OMe *n*-mer)s, OMe-ROMP, and CF_3-ROMP for (a) CO_2/CH_4, (b) H_2/CH_4, and (c) H_2/N_2 gas pairs. Black and gray lines represent the 2008 and 1991 Robeson upper bounds, respectively.[46,47] Filled shapes represent alcohol-treated samples, and open shapes represent thermally-treated samples. Aged samples are indicated with their aging time, and arrows point from the 1 day aged sample to the older sample. Open gray circles represent permeation data from Robeson's database.[46,47]

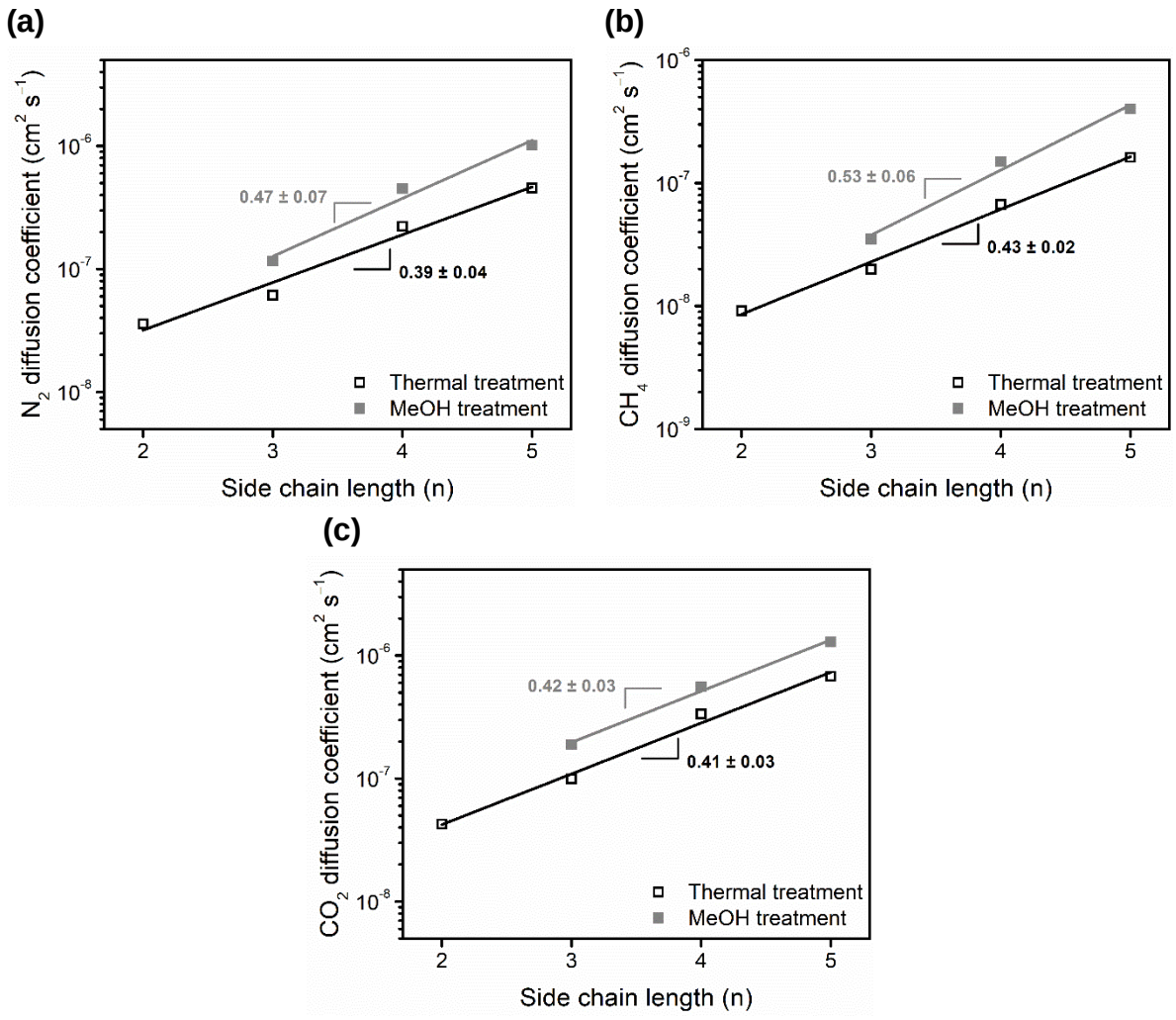

Figure C.4. Side-chain length (*n*) versus diffusion coefficient for (a) N_2, (b) CH_4, and (c) CO_2.

C.3. CO_2-induced plasticization study

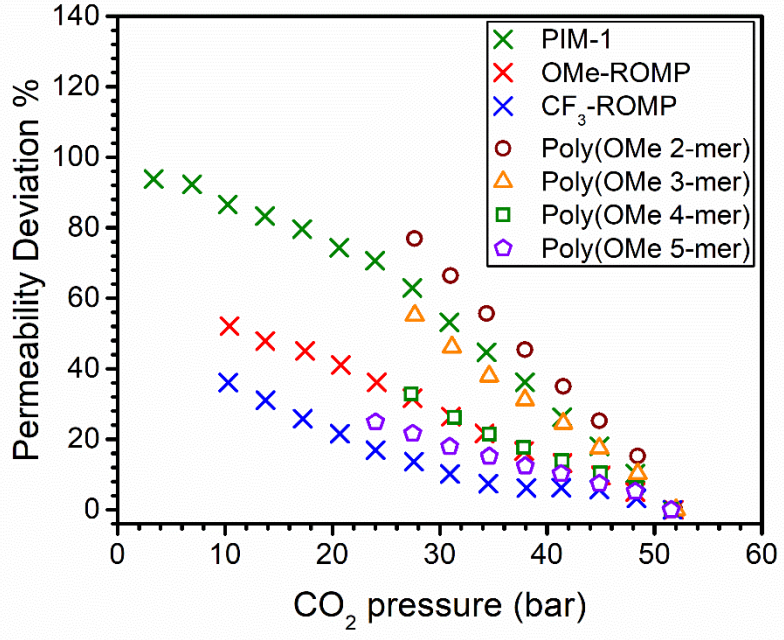

Figure C.5. Hysteresis induced by conditioning of the film at 51 bar of CO_2 for all samples in this study. Results for CF_3-ROMP, OMe-ROMP, and PIM-1 from our previous work[180] are included here for comparison.

Appendix D. Supporting Information for Chapter 5

Reprinted from **Lin, S.**; Storme, K. R.; Wu, Y.-C.; Benedetti, F. M.; Swager, T. M.; Smith, Z. P. Role of side-chain length in gas transport of CO_2/CH_4 mixtures in polymers with side chain porosity. *In preparation.*

Table D.1. Variable pressure CO_2/CH_4 mixed-gas separation performance of poly(OMe 4-mer) and poly(OMe 5-mer). Mixture composition was set at 50:50. Permeability (***P***) is given in barrer (10^{-10} cm^3(STP) cm cm^{-2} s^{-1} $cmHg^{-1}$). All data were obtained at 35 °C.

n	**CO_2 partial pressure (atm)**	P_{CO_2}	P_{CH_4}	α_{CO_2/CH_4}
4	1.09	750 ± 40	43 ± 2	17 ± 1
	2.04	640 ± 30	42 ± 2	15 ± 1
	3.40	580 ± 30	38 ± 2	15 ± 1
	5.10	540 ± 30	47 ± 2	11.4 ± 0.8
	6.80	490 ± 30	59 ± 3	8.4 ± 0.6
	8.51	480 ± 20	55 ± 3	8.7 ± 0.6
	10.21	460 ± 20	60 ± 3	7.6 ± 0.6
	11.91	470 ± 20	54 ± 3	8.8 ± 0.6
5	1.09	1160 ± 70	72 ± 4	16 ± 1
	2.04	990 ± 60	65 ± 4	15 ± 1
	3.40	900 ± 50	54 ± 3	17 ± 1
	5.10	830 ± 50	51 ± 3	16 ± 1
	6.80	830 ± 50	51 ± 3	16 ± 1
	8.51	790 ± 50	56 ± 3	14 ± 1
	10.21	760 ± 40	58 ± 3	13 ± 1
	11.91	730 ± 40	64 ± 4	11.3 ± 0.9

Appendix E. Combined photochemical crosslinking and thermal deprotection for the free volume manipulation of polyimides

Reprinted from **Lin, S.**; Joo, T.; Gwozdz, E. J.; Smith, Z. P. Combined photochemical crosslinking and thermal deprotection for the free volume manipulation of polyimides. *In preparation.*

Previously, it was hypothesized that reintroducing hydroxyl functionality after t-BOC deprotection, along with sub-T_g motions, led to the collapse of free volume elements otherwise formed from deprotection.[256] Therefore, crosslinking was deemed as a potential solution to maintain free volume architecture. Past studies have indicated successes with porogen formation from thermal crosslinking after deprotection.[105–108] However, we seek to determine if UV crosslinking can provide the same benefits without the need to heat the polymer system to extreme temperatures.

Lin et al. proposed a UV crosslinking mechanism involving benzophenone-containing polyimides, in which the benzophenone group is exposed to UV irradiation, radicalized, and crosslinked with a CH_2 radical,[220] as shown below in **Figure E.1**.

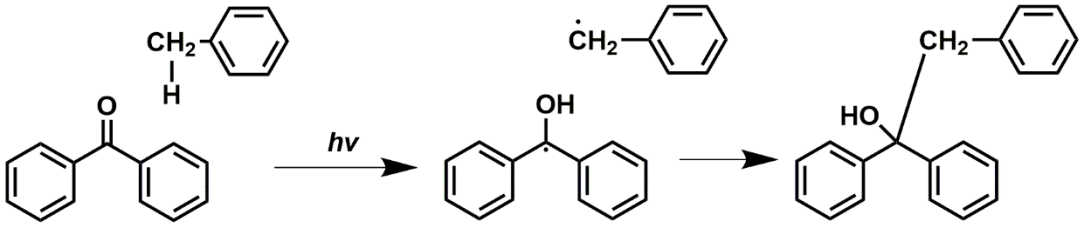

Figure E.1. Crosslinking reaction between a benzophenone group and a benzyl methyl group.[220] UV irradiation generates the radical in both the benzophenone and benzyl methyl group, which facilitates crosslinking.

Park et al. developed a polyimide-poly(dimethylsiloxane) co-polymer with 6FDA and BTDA dianhydrides in a 7:3 molar ratio, with the diamine DAM and varying amounts of siloxane oligomer.[219] To generate crosslinks between the benzophenone group in the BTDA monomer and

the benzyl methyl groups in the DAM monomer, the co-polymer films were exposed to broad-spectrum UV irradiation for 3 minutes.[219] While the films were found to be thermally stable up to 300 °C, densification increased as a result of UV crosslinking, which subsequently decreased the amount of free volume and increased CO_2/N_2 permselectivity.[219] The strategy of using co-polymerization to further modify UV crosslinked polymers for gas separations has also been explored by other groups.[257,258]

In a similar fashion, co-polymers with 6FDA-HAB-t-BOC and BTDA-DAM will be synthesized. As done by Park et al.,[219] the benzophenone group in BTDA will be crosslinked to the benzyl methyl groups in DAM via UV irradiation. The proposed structure of the co-polymer is shown below in **Figure E.2**.

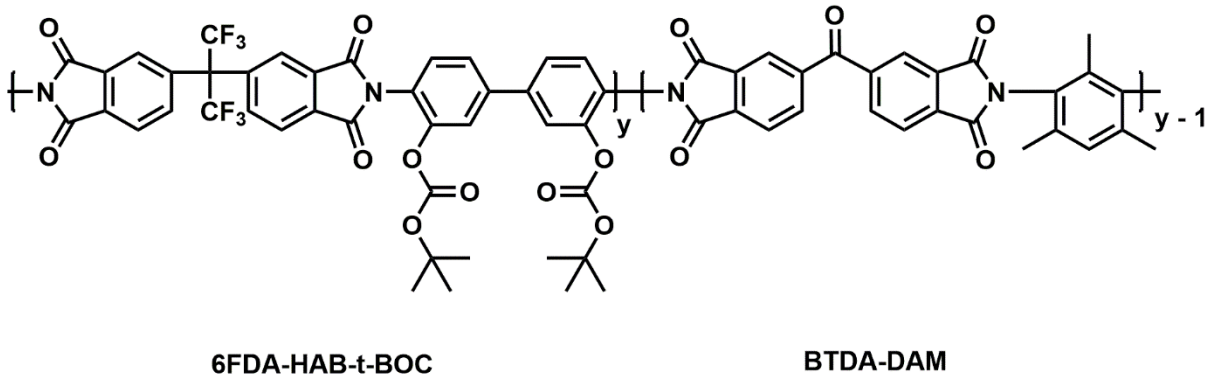

Figure E.2. Structure of the 6FDA-HAB-t-BOC/BTDA-DAM co-polymer.

Since BTDA-DAM shows limited solubility in chloroform,[259] which was the solvent of choice to make 6FDA-HAB-t-BOC films previously,[256] the 6FDA-HAB-t-BOC/BTDA-DAM co-polymer was synthesized in both a 90:10 and 80:20 molar ratio. Both sets of synthesized co-polymers dissolved readily in chloroform, and were therefore cast into films. Characterizations such as TGA, DSC, FTIR, NMR, and permeation experiments can be done to confirm the chemical

structure and gas transport properties. After UV treatment, these same characterization techniques can be used, as well as gel fraction content measurements to determine the degree of crosslinking.

References

(1) Galizia, M.; Chi, W. S.; Smith, Z. P.; Merkel, T. C.; Baker, R. W.; Freeman, B. D. 50th Anniversary Perspective : Polymers and Mixed Matrix Membranes for Gas and Vapor Separation: A Review and Prospective Opportunities. *Macromolecules* **2017**, *50* (20), 7809–7843. https://doi.org/10.1021/acs.macromol.7b01718.

(2) Qian, Q.; Asinger, P. A.; Lee, M. J.; Han, G.; Mizrahi Rodriguez, K.; Lin, S.; Benedetti, F. M.; Wu, A. X.; Chi, W. S.; Smith, Z. P. MOF-Based Membranes for Gas Separations. *Chem. Rev.* **2020**, *120* (16), 8161–8266. https://doi.org/10.1021/acs.chemrev.0c00119.

(3) Sanders, D. F.; Smith, Z. P.; Guo, R.; Robeson, L. M.; McGrath, J. E.; Paul, D. R.; Freeman, B. D. Energy-Efficient Polymeric Gas Separation Membranes for a Sustainable Future: A Review. *Polymer* **2013**, *54* (18), 4729–4761. https://doi.org/10.1016/j.polymer.2013.05.075.

(4) Sholl, D. S.; Lively, R. P. Seven Chemical Separations to Change the World. *Nature* **2016**, *532* (7600), 435–437. https://doi.org/10.1038/532435a.

(5) U.S. Department of Energy. Materials for Separation Technologies: Energy and Emission Reduction Opportunities. **2005**.

(6) Association, C. G. *Handbook of Compressed Gases*, 4th ed.; Springer: Norwell, MA, 1999.

(7) Gunardson, H. *Industrial Gases in Petrochemical Processing: Chemical Industries*; Marcel Dekker, Inc.: New York, NY, 1998.

(8) Eldridge, R. B. Olefin/Paraffin Separation Technology: A Review. *Ind. Eng. Chem. Res.* **1993**, *32* (10), 2208–2212. https://doi.org/10.1021/ie00022a002.

(9) Zhu, X.; Li, S.; Shi, Y.; Cai, N. Recent Advances in Elevated-Temperature Pressure Swing Adsorption for Carbon Capture and Hydrogen Production. *Prog. Energy Combust. Sci.* **2019**, *75*, 100784. https://doi.org/10.1016/j.pecs.2019.100784.

(10) Lee, K. B.; Beaver, M. G.; Caram, H. S.; Sircar, S. Reversible Chemisorbents for Carbon Dioxide and Their Potential Applications. *Ind. Eng. Chem. Res.* **2008**, *47* (21), 8048–8062. https://doi.org/10.1021/ie800795y.

(11) Sircar, S. Pressure Swing Adsorption. *Ind. Eng. Chem. Res.* **2002**, *41* (6), 1389–1392. https://doi.org/10.1021/ie0109758.

(12) Raganati, F.; Chirone, R.; Ammendola, P. CO_2 Capture by Temperature Swing Adsorption: Working Capacity As Affected by Temperature and CO_2 Partial Pressure. *Ind. Eng. Chem. Res.* **2020**, *59* (8), 3593–3605. https://doi.org/10.1021/acs.iecr.9b04901.

(13) Kikkinides, E. S. S.; Yang, R. T. T.; Cho, S. H. H. Concentration and Recovery of CO_2 from Flue Gas by Pressure Swing Adsorption. *Ind. Eng. Chem. Res.* **1993**, *32* (11), 2714–2720. https://doi.org/10.1021/ie00023a038.

(14) Chuah, C. Y.; Goh, K.; Yang, Y.; Gong, H.; Li, W.; Karahan, H. E.; Guiver, M. D.; Wang,

R.; Bae, T. H. Harnessing Filler Materials for Enhancing Biogas Separation Membranes. *Chemical Reviews*. 2018, pp 8655–8769. https://doi.org/10.1021/acs.chemrev.8b00091.

(15) Prasad, R.; Notaro, F.; Thompson, D. R. Evolution of Membranes in Commercial Air Separation. *J. Memb. Sci.* **1994**, *94* (1), 225–248. https://doi.org/10.1016/0376-7388(93)E0193-N.

(16) Baker, R. W.; Lokhandwala, K. Natural Gas Processing with Membranes: An Overview. *Ind. Eng. Chem. Res.* **2008**, *47* (7), 2109–2121. https://doi.org/10.1021/ie071083w.

(17) Ünveren, E. E.; Monkul, B. Ö.; Sarıoğlan, Ş.; Karademir, N.; Alper, E. Solid Amine Sorbents for CO_2 Capture by Chemical Adsorption: A Review. *Petroleum*. 2017, pp 37–50. https://doi.org/10.1016/j.petlm.2016.11.001.

(18) Wang, Q.; Luo, J.; Zhong, Z.; Borgna, A. CO_2 Capture by Solid Adsorbents and Their Applications: Current Status and New Trends. *Energy and Environmental Science*. 2011, pp 42–55. https://doi.org/10.1039/c0ee00064g.

(19) D'Alessandro, D. M.; Smit, B.; Long, J. R. Carbon Dioxide Capture: Prospects for New Materials. *Angew. Chemie - Int. Ed.* **2010**, *49* (35), 6058–6082. https://doi.org/10.1002/anie.201000431.

(20) Beil, M.; Beyrich, W. *Biogas Upgrading to Biomethane*; 2013. https://doi.org/10.1533/9780857097415.3.342.

(21) Yu, C. H.; Huang, C. H.; Tan, C. S. A Review of CO_2 Capture by Absorption and Adsorption. *Aerosol Air Qual. Res.* **2012**, *12* (5), 745–769. https://doi.org/10.4209/aaqr.2012.05.0132.

(22) Olajire, A. A. CO_2 Capture and Separation Technologies for End-of-Pipe Applications - A Review. *Energy* **2010**, *35* (6), 2610–2628. https://doi.org/10.1016/j.energy.2010.02.030.

(23) Corrado, T.; Guo, R. Macromolecular Design Strategies toward Tailoring Free Volume in Glassy Polymers for High Performance Gas Separation Membranes. *Mol. Syst. Des. Eng.* **2020**, *5* (1), 22–48. https://doi.org/10.1039/C9ME00099B.

(24) Loeb, S.; Sourirajan, S. Sea Water Demineralization by Means of an Osmotic Membrane. *Advances in Chemistry Series* **1962**, *38*, 117–132. https://doi.org/10.1021/ba-1963-0038.ch009.

(25) Baker, R. W. *Membrane Technology and Applications*; John Wiley & Sons, Ltd: Chichester, UK, 2004. https://doi.org/10.1002/0470020393.

(26) Koros, W. J.; Pinnau, I. Membrane Formation for Gas Separation Processes. In *Polymeric Gas Separation Membranes*; Paul, D. R., Yampol'skii, Y. P., Eds.; CRC Press: Boca Raton, 1994. https://doi.org/10.1201/9781351075886.

(27) Lonsdale, H. K. The Growth of Membrane Technology. *J. Memb. Sci.* **1982**, *10* (2–3), 81–181. https://doi.org/10.1016/S0376-7388(00)81408-8.

(28) Baker, R. W. Future Directions of Membrane Gas Separation Technology. *Ind. Eng. Chem. Res.* **2002**, *41* (6), 1393–1411. https://doi.org/10.1021/ie0108088.

(29) Baker, R. W.; Low, B. T. Gas Separation Membrane Materials: A Perspective. *Macromolecules* **2014**, *47* (20), 6999–7013. https://doi.org/10.1021/ma501488s.

(30) AirProducts. *Advanced Prism® Membrane Systems For Cost Effective Gas Separations*.

(31) Stookey, D. J.; Patton, C. J.; Malcolm, G. L. Membranes Separate Gases Selectively. *Chem. Eng. Prog.* **1986**, *82* (11), 36–40.

(32) Baker, R. W.; Pinnau, I.; He, Z.; Amo, K. D.; Da Costa, A. R.; Daniels, R. Nitrogen Gas Separation Using Organic-Vapor-Resistant Membranes. 6579341, 2003.

(33) Baker, R. W.; Pinnau, I.; He, Z.; Amo, K. D.; Da Costa, A. R.; Daniels, R. Carbon Dioxide Gas Separation Using Organic-Vapor-Resistant Membranes. 6572680, 2003.

(34) Merkel, T. C.; Pinnau, I.; Prabhakar, R.; Freeman, B. D. Gas and Vapor Transport Properties of Perfluoropolymers. In *Materials Science of Membranes for Gas and Vapor Separation*; Yampolskii, Y. P., Pinnau, I., Freeman, B. D., Eds.; Wiley: Chichester, UK, 2006.

(35) Gottschlich, D. E.; Roberts, D. L. *Energy Minimization of Separation Processes Using Conventional/Membrane Hybrid Systems*; 1990. https://doi.org/10.2172/6195331.

(36) Sanders Jr., E. S.; Clark, D. O.; Jensvold, J. A.; Beck, H. N.; Libscomb, G. G.; Coan, F. L. Process for Preparing POWADIR Membranes from Tetrahalobisphenol A Polycarbonates. 4772392, 1988.

(37) Campos, A. C. C.; Dos Reis, R. A.; Ortiz, A.; Gorri, D.; Ortiz, I. A Perspective of Solutions for Membrane Instabilities in Olefin/Paraffin Separations: A Review. *Ind. Eng. Chem. Res.* **2018**, *57* (31), 10071–10085. https://doi.org/10.1021/acs.iecr.8b02013.

(38) Ren, Y.; Liang, X.; Dou, H.; Ye, C.; Guo, Z.; Wang, J.; Pan, Y.; Wu, H.; Guiver, M. D.; Jiang, Z. Membrane-Based Olefin/Paraffin Separations. *Advanced Science*. 2020, pp 1–29. https://doi.org/10.1002/advs.202001398.

(39) Boulamanti, A.; Moya, J. A. Production Costs of the Chemical Industry in the EU and Other Countries: Ammonia, Methanol and Light Olefins. *Renewable and Sustainable Energy Reviews*. 2017, pp 1205–1212. https://doi.org/10.1016/j.rser.2016.02.021.

(40) Alivisatos, P.; Buchanan, M. *Basic Research Needs for Carbon Capture: Beyond 2020*; 2010.

(41) Wijmans, J. G.; Baker, R. W. The Solution-Diffusion Model: A Review. *J. Memb. Sci.* **1995**, *107* (1–2), 1–21. https://doi.org/10.1016/0376-7388(95)00102-I.

(42) Lin, H.; Freeman, B. D. 7.6 Permeation and Diffusion. In *Springer Handbook of Materials Measurement Methods*; Czichos, H., Saito, T., Smith, L., Eds.; Springer Berlin Heidelberg: Berlin, Heidelberg, 2006. https://doi.org/10.1007/978-3-540-30300-8.

(43) Minelli, M.; Sarti, G. C. 110th Anniversary: Gas and Vapor Sorption in Glassy Polymeric Membranes—Critical Review of Different Physical and Mathematical Models. *Ind. Eng. Chem. Res.* **2020**, *59* (1), 341–365. https://doi.org/10.1021/acs.iecr.9b05453.

(44) Doghieri, F.; Sarti, G. C. Nonequilibrium Lattice Fluids: A Predictive Model for the

Solubility in Glassy Polymers. *Macromolecules* **1996**, *29* (24), 7885–7896. https://doi.org/10.1021/ma951366c.

(45) Koros, W. J. Model for Sorption of Mixed Gases in Glassy Polymers. *J. Polym. Sci. Polym. Phys. Ed.* **1980**, *18* (5), 981–992. https://doi.org/10.1002/pol.1980.180180506.

(46) Robeson, L. M. Correlation of Separation Factor versus Permeability for Polymeric Membranes. *J. Memb. Sci.* **1991**, *62* (2), 165–185. https://doi.org/10.1016/0376-7388(91)80060-J.

(47) Robeson, L. M. The Upper Bound Revisited. *J. Memb. Sci.* **2008**, *320* (1–2), 390–400. https://doi.org/10.1016/j.memsci.2008.04.030.

(48) Freeman, B. D. Basis of Permeability/Selectivity Tradeoff Relations in Polymeric Gas Separation Membranes. *Macromolecules* **1999**, *32* (2), 375–380. https://doi.org/10.1021/ma9814548.

(49) Comesaña-Gándara, B.; Chen, J.; Bezzu, C. G.; Carta, M.; Rose, I.; Ferrari, M.-C.; Esposito, E.; Fuoco, A.; Jansen, J. C.; McKeown, N. B. Redefining the Robeson Upper Bounds for CO_2/CH_4 and CO_2/N_2 Separations Using a Series of Ultrapermeable Benzotriptycene-Based Polymers of Intrinsic Microporosity. *Energy Environ. Sci.* **2019**, *12* (9), 2733–2740. https://doi.org/10.1039/C9EE01384A.

(50) Wu, A. X.; Drayton, J. A.; Smith, Z. P. The Perfluoropolymer Upper Bound. *AIChE J.* **2019**, *65* (12), e16700. https://doi.org/10.1002/aic.16700.

(51) Burns, R. L.; Koros, W. J. Defining the Challenges for C_3H_6/C_3H_8 Separation Using Polymeric Membranes. *J. Memb. Sci.* **2003**, *211* (2), 299–309. https://doi.org/10.1016/S0376-7388(02)00430-1.

(52) Wang, Y.; Ma, X.; Ghanem, B. S.; Alghunaimi, F.; Pinnau, I.; Han, Y. Polymers of Intrinsic Microporosity for Energy-Intensive Membrane-Based Gas Separations. *Mater. Today Nano* **2018**, *3* (2018), 69–95. https://doi.org/10.1016/j.mtnano.2018.11.003.

(53) Lin, H.; Yavari, M. Upper Bound of Polymeric Membranes for Mixed-Gas CO_2/CH_4 Separations. *J. Memb. Sci.* **2015**, *475*, 101–109. https://doi.org/10.1016/j.memsci.2014.10.007.

(54) Pixton, M. R.; Paul, D. R. Relationships Between Structure and Transport Properties for Polymers with Aromatic Backbones. In *Polymeric Gas Separation Membranes*; Paul, D. R., Yampolskii, Y. P., Eds.; CRC Press: Boca Raton, 1994; pp 83–154.

(55) Petropoulos, J. H. Mechanisms and Theories for Sorption and Diffusion of Gases in Polymers. In *Polymeric Gas Separation Membranes*; Paul, D. R., Yampolskii, Y. P., Eds.; CRC Press: Boca Raton, 1994; pp 17–82.

(56) Horn, N. R.; Paul, D. R. Carbon Dioxide Plasticization and Conditioning Effects in Thick vs . Thin Glassy Polymer Films. *Polymer* **2011**, *52* (7), 1619–1627. https://doi.org/10.1016/j.polymer.2011.02.007.

(57) Bos, A.; Pünt, I. G. M.; Wessling, M.; Strathmann, H. CO_2-Induced Plasticization Phenomena in Glassy Polymers. *J. Memb. Sci.* **1999**, *155* (1), 67–78.

https://doi.org/10.1016/S0376-7388(98)00299-3.

(58) Genduso, G.; Pinnau, I. Quantification of Sorption, Diffusion, and Plasticization Properties of Cellulose Triacetate Films under Mixed-Gas CO_2/CH_4 Environment. *J. Memb. Sci.* **2020**, 118269. https://doi.org/10.1016/j.memsci.2020.118269.

(59) Wessling, M.; Schoeman, S.; van der Boomgaard, T.; Smolders, C. A. Plasticization of Gas Separation Membranes. *Gas Sep. Purif.* **1991**, *5* (4), 222–228. https://doi.org/10.1016/0950-4214(91)80028-4.

(60) Swaidan, R.; Ghanem, B.; Litwiller, E.; Pinnau, I. Effects of Hydroxyl-Functionalization and Sub-Tg Thermal Annealing on High Pressure Pure- and Mixed-Gas CO_2/CH_4 Separation by Polyimide Membranes Based on 6FDA and Triptycene-Containing Dianhydrides. *J. Memb. Sci.* **2015**, *475*, 571–581. https://doi.org/10.1016/j.memsci.2014.10.046.

(61) Abdulhamid, M. A.; Genduso, G.; Wang, Y.; Ma, X.; Pinnau, I. Plasticization-Resistant Carboxyl-Functionalized 6FDA-Polyimide of Intrinsic Microporosity (PIM-PI) for Membrane-Based Gas Separation. *Ind. Eng. Chem. Res.* **2020**, *59* (12), 5247–5256. https://doi.org/10.1021/acs.iecr.9b04994.

(62) Wang, Y.; Ghanem, B. S.; Han, Y.; Pinnau, I. Facile Synthesis and Gas Transport Properties of Hünlich's Base-Derived Intrinsically Microporous Polyimides. *Polymer* **2020**, *201*, 122619. https://doi.org/10.1016/j.polymer.2020.122619.

(63) Alaslai, N.; Ghanem, B.; Alghunaimi, F.; Pinnau, I. High-Performance Intrinsically Microporous Dihydroxyl-Functionalized Triptycene-Based Polyimide for Natural Gas Separation. *Polymer* **2016**, *91*, 128–135. https://doi.org/10.1016/j.polymer.2016.03.063.

(64) Alghunaimi, F.; Ghanem, B.; Alaslai, N.; Mukaddam, M.; Pinnau, I. Triptycene Dimethyl-Bridgehead Dianhydride-Based Intrinsically Microporous Hydroxyl-Functionalized Polyimide for Natural Gas Upgrading. *J. Memb. Sci.* **2016**, *520*, 240–246. https://doi.org/10.1016/j.memsci.2016.07.058.

(65) Swaidan, R.; Ghanem, B. S.; Litwiller, E.; Pinnau, I. Pure- and Mixed-Gas CO_2/CH_4 Separation Properties of PIM-1 and an Amidoxime-Functionalized PIM-1. *J. Memb. Sci.* **2014**, *457*, 95–102. https://doi.org/10.1016/j.memsci.2014.01.055.

(66) Struik, L. C. E. Physical Aging in Plastics and Other Glassy Materials. *Polym. Eng. Sci.* **1977**, *17* (3), 165–173. https://doi.org/10.1002/pen.760170305.

(67) Low, Z. X.; Budd, P. M.; McKeown, N. B.; Patterson, D. A. Gas Permeation Properties, Physical Aging, and Its Mitigation in High Free Volume Glassy Polymers. *Chemical Reviews*. 2018, pp 5871–5911. https://doi.org/10.1021/acs.chemrev.7b00629.

(68) Rowe, B. W.; Freeman, B. D.; Paul, D. R. Influence of Previous History on Physical Aging in Thin Glassy Polymer Films as Gas Separation Membranes. *Polymer* **2010**, *51* (16), 3784–3792. https://doi.org/10.1016/j.polymer.2010.06.004.

(69) Rowe, B. W.; Freeman, B. D.; Paul, D. R. Physical Aging of Ultrathin Glassy Polymer Films Tracked by Gas Permeability. *Polymer* **2009**, *50* (23), 5565–5575. https://doi.org/10.1016/j.polymer.2009.09.037.

(70) Murphy, T. M.; Langhe, D. S.; Ponting, M.; Baer, E.; Freeman, B. D.; Paul, D. R. Physical Aging of Layered Glassy Polymer Films via Gas Permeability Tracking. *Polymer* **2011**, *52* (26), 6117–6125. https://doi.org/10.1016/j.polymer.2011.10.061.

(71) Bondi, A. Van Der Waals Volumes and Radii. *J. Phys. Chem.* **1964**, *68* (3), 441–451. https://doi.org/10.1021/j100785a001.

(72) Park, J. Y.; Paul, D. R. Correlation and Prediction of Gas Permeability in Glassy Polymer Membrane Materials via a Modified Free Volume Based Group Contribution Method. *J. Memb. Sci.* **1997**, *125* (1), 23–39. https://doi.org/10.1016/S0376-7388(96)00061-0.

(73) van Krevelen, D. W.; Te Nijenhuis, K. *Properties of Polymers*; Elsevier, 2009. https://doi.org/10.1016/B978-0-08-054819-7.X0001-5.

(74) Wu, A. X.; Lin, S.; Mizrahi Rodriguez, K.; Benedetti, F. M.; Joo, T.; Grosz, A. F.; Storme, K. R.; Roy, N.; Syar, D.; Smith, Z. P. Revisiting Group Contribution Theory for Estimating Fractional Free Volume of Microporous Polymer Membranes. *J. Memb. Sci.* **2021**, *636*, 119526. https://doi.org/10.1016/j.memsci.2021.119526.

(75) Hill, A. J. Positron Annihilation Lifetime Spectroscopy. In *Polymer Characterization Techniques and Their Application to Blends*; Simon, G. P., Ed.; ACS, 2003; pp 401–435.

(76) Jean, Y. C.; Mallon, P. E.; Schrader, D. M. *Principles and Applications of Positron & Positronium Chemistry*; World Scientific: Singapore, 2003.

(77) Fong, C.; Dong, A. W.; Hill, A. J.; Boyd, B. J.; Drummond, C. J. Positron Annihilation Lifetime Spectroscopy (PALS): A Probe for Molecular Organisation in Self-Assembled Biomimetic Systems. *Physical Chemistry Chemical Physics*. Royal Society of Chemistry 2015, pp 17527–17540. https://doi.org/10.1039/c5cp01921d.

(78) Tao, S. J. Positronium Annihilation in Molecular Substances. *J. Chem. Phys.* **1972**, *56* (11), 5499–5510. https://doi.org/10.1063/1.1677067.

(79) Eldrup, M.; Lightbody, D.; Sherwood, J. N. The Temperature Dependence of Positron Lifetimes in Solid Pivalic Acid. *Chem. Phys.* **1981**, *63* (1–2), 51–58. https://doi.org/10.1016/0301-0104(81)80307-2.

(80) Shantarovich, V. P.; Suzuki, T.; He, C.; Gustov, V. W. Inhibition of Positronium Formation by Polar Groups in Polymers - Relation with TSL Experiments. *Radiat. Phys. Chem.* **2003**, *67* (1), 15–23. https://doi.org/10.1016/S0969-806X(02)00481-4.

(81) Kirkegaard, P.; Eldrup, M.; Mogensen, O. E.; Pedersen, N. J. Program System for Analysing Positron Lifetime Spectra and Angular Correlation Curves. *Comput. Phys. Commun.* **1981**, *23*, 307–335.

(82) Pascual-Izarra, C.; Dong, A. W.; Pas, S. J.; Hill, A. J.; Boyd, B. J.; Drummond, C. J. Advanced Fitting Algorithms for Analysing Positron Annihilation Lifetime Spectra. *Nucl. Instruments Methods Phys. Res. Sect. A Accel. Spectrometers, Detect. Assoc. Equip.* **2009**, *603* (3), 456–466. https://doi.org/10.1016/j.nima.2009.01.205.

(83) Shuk, A.; Peter, M.; Hoffmann, L. Analysis of Positron Lifetime Spectra Using Quantified Maximum Entropy and a General Linear Filter. *Nucl. Instruments Methods m Phys. Res. A*

1993, *335*, 310–317. https://doi.org/10.1016/0168-9002(93)90286-Q.

(84) Consolati, G.; Genco, I.; Pegoraro, M.; Zanderighi, L. Positron Annihilation Lifetime (PAL) in Poly[1-(Trimethylsilyl)Propine] (PTMSP): Free Volume Determination and Time Dependence of Permeability. *J. Polym. Sci. Part B Polym. Phys.* **1996**, *34* (2), 357–367. https://doi.org/10.1002/(SICI)1099-0488(19960130)34:2<357::AID-POLB17>3.0.CO;2-I.

(85) Shantarovich, V. P.; Novikov, Y. A.; Suptel, Z. K.; Kevdina, I. B.; Masuda, T.; Khotimskii, V. S.; Yampolskii, Y. P. Influence of Deformation and Chemical Structure on Elementary Free Volumes in Glassy Polymers. *Radiat. Phys. Chem.* **2000**, *58* (5–6), 513–520. https://doi.org/10.1016/S0969-806X(00)00209-7.

(86) Budd, P. M.; Ghanem, B. S.; Makhseed, S.; McKeown, N. B.; Msayib, K. J.; Tattershall, C. E. Polymers of Intrinsic Microporosity (PIMs): Robust, Solution-Processable, Organic Nanoporous Materials. *Chem. Commun.* **2004**, *4* (2), 230. https://doi.org/10.1039/b311764b.

(87) McKeown, N. B. The Synthesis of Polymers of Intrinsic Microporosity (PIMs). *Science China Chemistry* **2017**, *60*, 1023–1032. https://doi.org/10.1007/s11426-017-9058-x.

(88) Rose, I.; Bezzu, C. G.; Carta, M.; Comesaña-Gándara, B.; Lasseuguette, E.; Ferrari, M. C.; Bernardo, P.; Clarizia, G.; Fuoco, A.; Jansen, J. C.; et al. Polymer Ultrapermeability from the Inefficient Packing of 2D Chains. *Nat. Mater.* **2017**, *16* (9), 932–937. https://doi.org/10.1038/nmat4939.

(89) Thomas, S.; Pinnau, I.; Du, N.; Guiver, M. D. Pure- and Mixed-Gas Permeation Properties of a Microporous Spirobisindane-Based Ladder Polymer (PIM-1). *J. Memb. Sci.* **2009**, *333* (1–2), 125–131. https://doi.org/10.1016/j.memsci.2009.02.003.

(90) Scholes, C. A.; Kanehashi, S. Polymeric Membrane Gas Separation Performance Improvements through Supercritical CO_2 Treatment. *J. Memb. Sci.* **2018**, *566*, 239–248. https://doi.org/10.1016/j.memsci.2018.09.014.

(91) Kim, H.-J.; Hong, S.-I. The Sorption and Permeation of CO_2 and CH_4 for Dimethylated Polysulfone Membrane. *Korean J. Chem. Eng.* **1997**, *14* (3), 168–174. https://doi.org/10.1007/BF02706090.

(92) Guiver, M. D.; Robertson, G. P.; Dai, Y.; Bilodeau, F.; Kang, Y. S.; Lee, K. J.; Jho, J. Y.; Won, J. Structural Characterization and Gas-Transport Properties of Brominated Matrimid Polyimide. *J. Polym. Sci. Part A Polym. Chem.* **2002**, *40* (23), 4193–4204. https://doi.org/10.1002/pola.10516.

(93) Budd, P. M.; Elabas, E. S.; Ghanem, B. S.; Makhseed, S.; McKeown, N. B.; Msayib, K. J.; Tattershall, C. E.; Wang, D. Solution-Processed, Organophilic Membrane Derived from a Polymer of Intrinsic Microporosity. *Adv. Mater.* **2004**, *16* (5), 456–459. https://doi.org/10.1002/adma.200306053.

(94) Carta, M.; Croad, M.; Malpass-Evans, R.; Jansen, J. C.; Bernardo, P.; Clarizia, G.; Friess, K.; Lanč, M.; McKeown, N. B. Triptycene Induced Enhancement of Membrane Gas Selectivity for Microporous Tröger's Base Polymers. *Adv. Mater.* **2014**, *26* (21), 3526–

3531. https://doi.org/10.1002/adma.201305783.

(95) Wiegand, J. R.; Smith, Z. P.; Liu, Q.; Patterson, C. T.; Freeman, B. D.; Guo, R. Synthesis and Characterization of Triptycene-Based Polyimides with Tunable High Fractional Free Volume for Gas Separation Membranes. *J. Mater. Chem. A* **2014**, *2* (33), 13309–13320. https://doi.org/10.1039/c4ta02303j.

(96) Carta, M.; Malpass-Evans, R.; Croad, M.; Rogan, Y.; Jansen, J. C.; Bernardo, P.; Bazzarelli, F.; McKeown, N. B. An Efficient Polymer Molecular Sieve for Membrane Gas Separations. *Science* **2013**, *339* (6117), 303–307. https://doi.org/10.1126/science.1228032.

(97) Park, H. B.; Jung, C. H.; Lee, Y. M.; Hill, A. J.; Pas, S. J.; Mudie, S. T.; Van Wagner, E.; Freeman, B. D.; Cookson, D. J. Polymers with Cavities Tuned for Fast Selective Transport of Small Molecules and Ions. *Science* **2007**, *318* (5848), 254–258. https://doi.org/10.1126/science.1146744.

(98) Smith, Z. P.; Hernández, G.; Gleason, K. L.; Anand, A.; Doherty, C. M.; Konstas, K.; Alvarez, C.; Hill, A. J.; Lozano, A. E.; Paul, D. R.; et al. Effect of Polymer Structure on Gas Transport Properties of Selected Aromatic Polyimides, Polyamides and TR Polymers. *J. Memb. Sci.* **2015**, *493*, 766–781. https://doi.org/10.1016/j.memsci.2015.06.032.

(99) Han, S. H.; Misdan, N.; Kim, S.; Doherty, C. M.; Hill, A. J.; Lee, Y. M. Thermally Rearranged (TR) Polybenzoxazole: Effects of Diverse Imidization Routes on Physical Properties and Gas Transport Behaviors. *Macromolecules* **2010**, *43* (18), 7657–7667. https://doi.org/10.1021/ma101549z.

(100) MacDonald, S. A.; Willson, C. G.; Fréchet, J. M. J. Chemical Amplification in High-Resolution Imaging Systems. *Acc. Chem. Res.* **1994**, *27* (6), 151–158. https://doi.org/10.1021/ar00042a001.

(101) Omote, T.; Koseki, K.; Yamaoka, T. Fluorine-Containing Photoreactive Polyimides. 6. Synthesis and Properties of a Novel Photoreactive Polyimide Based on Photoinduced Acidolysis and the Kinetics for Its Acidolysis. *Macromolecules* **1990**, *23* (22), 4788–4795. https://doi.org/10.1021/ma00224a007.

(102) Fukumaru, T.; Fujigaya, T.; Nakashima, N. Design and Preparation of Porous Polybenzoxazole Films Using the Tert-Butoxycarbonyl Group as a Pore Generator and Their Application for Patternable Low-k Materials. *Polym. Chem.* **2012**, *3* (2), 369–376. https://doi.org/10.1039/c1py00470k.

(103) Merlet, S.; Marestin, C.; Romeyer, O.; Mercier, R. “Self-Foaming” Poly(Phenylquinoxaline)s for the Designing of Macro and Nanoporous Materials. *Macromolecules* **2008**, *41* (12), 4205–4215. https://doi.org/10.1021/ma800228u.

(104) Merlet, S.; Marestin, C.; Schiets, F.; Romeyer, O.; Mercier, R. Preparation and Characterization of Nanocellular Poly(Phenylquinoxaline) Foams. A New Approach to Nanoporous High-Performance Polymers. *Macromolecules* **2007**, *40* (6), 2070–2078. https://doi.org/10.1021/ma062259t.

(105) Xiao, Y.; Chung, T. S. Grafting Thermally Labile Molecules on Cross-Linkable Polyimide to Design Membrane Materials for Natural Gas Purification and CO_2 Capture. *Energy*

Environ. Sci. **2011**, *4* (1), 201–208. https://doi.org/10.1039/c0ee00278j.

(106) Askari, M.; Chua, M. L.; Chung, T. S. Permeability, Solubility, Diffusivity, and PALS Data of Cross-Linkable 6FDA-Based Copolyimides. *Ind. Eng. Chem. Res.* **2014**, *53* (6), 2449–2460. https://doi.org/10.1021/ie403505u.

(107) Askari, M.; Xiao, Y.; Li, P.; Chung, T. S. Natural Gas Purification and Olefin/Paraffin Separation Using Cross-Linkable 6FDA-Durene/DABA Co-Polyimides Grafted with α, β, and γ-Cyclodextrin. *J. Memb. Sci.* **2012**, *390–391*, 141–151. https://doi.org/10.1016/j.memsci.2011.11.030.

(108) Chua, M. L.; Xiao, Y. C.; Chung, T. S. Effects of Thermally Labile Saccharide Units on the Gas Separation Performance of Highly Permeable Polyimide Membranes. *J. Memb. Sci.* **2012**, *415–416*, 375–382. https://doi.org/10.1016/j.memsci.2012.05.022.

(109) Islam, M. N.; Zhou, W.; Honda, T.; Tanaka, K.; Kita, H.; Okamoto, K. I. Preparation and Gas Separation Performance of Flexible Pyrolytic Membranes by Low-Temperature Pyrolysis of Sulfonated Polyimides. *J. Memb. Sci.* **2005**, *261* (1–2), 17–26. https://doi.org/10.1016/j.memsci.2005.02.019.

(110) Zhou, W.; Watari, T.; Kita, H.; Okamoto, K. I. Gas Permeation Properties of Flexible Pyrolytic Membranes from Sulfonated Polyimides. *Chem. Lett.* **2002**, No. 5, 534–535. https://doi.org/10.1246/cl.2002.534.

(111) Maya, E. M.; Tena, A.; de Abajo, J.; de la Campa, J. G.; Lozano, A. E. Partially Pyrolyzed Membranes (PPMs) Derived from Copolyimides Having Carboxylic Acid Groups. Preparation and Gas Transport Properties. *J. Memb. Sci.* **2010**, *349* (1–2), 385–392. https://doi.org/10.1016/j.memsci.2009.12.001.

(112) Martínez-Mercado, E.; Ruiz-Treviño, F. A.; Cruz-Rosado, A.; Zolotukhin, M. G.; González-Montiel, A.; Cárdenas, J.; Gaviño-Ramírez, R. L. Tuning Gas Permeability and Selectivity Properties by Thermal Modification of the Side Groups of Poly(Oxindolebiphenylylene)s Membranes. *Ind. Eng. Chem. Res.* **2014**, *53* (40), 15755–15762. https://doi.org/10.1021/ie5028765.

(113) Zheng, S.; Robeson, L. M.; Murphy, M. K.; Quay, J. R. Polymers, Polymer Membranes and Methods of Producing the Same, US Patent 8926733B2, 2015.

(114) Sánchez-García, S.; Ruiz-Treviño, F. A.; Aguilar-Vega, M. J.; Zolotukhin, M. G. Gas Permeability and Selectivity in Thermally Modified Poly(Oxyindole Biphenylylene) Membranes Bearing a Tert-Butyl Carbonate Group. *Ind. Eng. Chem. Res.* **2016**, *55* (25), 7012–7020. https://doi.org/10.1021/acs.iecr.6b01304.

(115) Hernández-Martínez, H.; Ruiz-Treviño, F. A.; Ortiz-Espinoza, J.; Aguilar-Vega, M. J.; Zolotukhin, M. G.; Marcial-Hernandez, R.; Olvera, L. I. Simultaneous Thermal Cross-Linking and Decomposition of Side Groups to Mitigate Physical Aging in Poly(Oxyindole Biphenylylene) Gas Separation Membranes. *Ind. Eng. Chem. Res.* **2018**, *57* (13), 4640–4650. https://doi.org/10.1021/acs.iecr.8b00529.

(116) Ho, C. H.; Vu-Khanh, T. Effects of Time and Temperature on Physical Aging of Polycarbonate. *Theor. Appl. Fract. Mech.* **2003**, *39* (2), 107–116.

https://doi.org/10.1016/S0167-8442(02)00151-9.

(117) Huang, Y.; Paul, D. R. Physical Aging of Thin Glassy Polymer Films Monitored by Gas Permeability. *Polymer* **2004**, *45* (25), 8377–8393. https://doi.org/10.1016/j.polymer.2004.10.019.

(118) Huang, Y.; Paul, D. R. Effect of Temperature on Physical Aging of Thin Glassy Polymer Films. *Macromolecules* **2005**, *38* (24), 10148–10154. https://doi.org/10.1021/ma051284g.

(119) Gray, L. A. G.; Yoon, S. W.; Pahner, W. A.; Davidheiser, J. E.; Roth, C. B. Importance of Quench Conditions on the Subsequent Physical Aging Rate of Glassy Polymer Films. *Macromolecules* **2012**, *45* (3), 1701–1709. https://doi.org/10.1021/ma202493n.

(120) Wang, H.; Chung, T. S.; Paul, D. R. Physical Aging and Plasticization of Thick and Thin Films of the Thermally Rearranged Ortho-Functional Polyimide 6FDA-HAB. *J. Memb. Sci.* **2014**, *458*, 27–35. https://doi.org/10.1016/j.memsci.2014.01.066.

(121) Ansaloni, L.; Minelli, M.; Baschetti, M. G.; Sarti, G. C. Effects of Thermal Treatment and Physical Aging on the Gas Transport Properties in Matrimid®. *Oil Gas Sci. Technol.* **2015**, *70* (2), 367–379. https://doi.org/10.2516/ogst/2013188.

(122) Tanaka, K.; Kita, H.; Okano, M.; Okamoto, K. Permeability and Permselectivity of Gases in Fluorinated Polyimides. *Polymer* **1992**, *33* (3), 585–592. https://doi.org/10.2115/fiber.46.12_541.

(123) Stern, S. A.; Mi, Y.; Yamamoto, H.; Clair, A. K. S. Structure/Permeability Relationships of Polyimide Membranes. Applications to the Separation of Gas Mixtures. *J. Polym. Sci. Part B Polym. Phys.* **1989**, *27* (9), 1887–1909. https://doi.org/10.1002/polb.1989.090270908.

(124) Kim, T. H.; Koros, W. J.; Husk, G. R.; O'Brien, K. C. Relationship between Gas Separation Properties and Chemical Structure in a Series of Aromatic Polyimides. *J. Memb. Sci.* **1988**, *37* (1), 45–62. https://doi.org/10.1016/S0376-7388(00)85068-1.

(125) Qiu, W.; Xu, L.; Chen, C. C.; Paul, D. R.; Koros, W. J. Gas Separation Performance of 6FDA-Based Polyimides with Different Chemical Structures. *Polymer* **2013**, *54* (22), 6226–6235. https://doi.org/10.1016/j.polymer.2013.09.007.

(126) Smith, Z. P.; Sanders, D. F.; Ribeiro, C. P.; Guo, R.; Freeman, B. D.; Paul, D. R.; McGrath, J. E.; Swinnea, S. Gas Sorption and Characterization of Thermally Rearranged Polyimides Based on 3,3'-Dihydroxy-4,4'-Diamino-Biphenyl (HAB) and 2,2'-Bis-(3,4-Dicarboxyphenyl) Hexafluoropropane Dianhydride (6FDA). *J. Memb. Sci.* **2012**, *415–416*, 558–567. https://doi.org/10.1016/j.memsci.2012.05.050.

(127) Sanders, D. F.; Smith, Z. P.; Ribeiro, C. P.; Guo, R.; McGrath, J. E.; Paul, D. R.; Freeman, B. D. Gas Permeability, Diffusivity, and Free Volume of Thermally Rearranged Polymers Based on 3,3'-Dihydroxy-4,4'-Diamino-Biphenyl (HAB) and 2,2'-Bis-(3,4-Dicarboxyphenyl) Hexafluoropropane Dianhydride (6FDA). *J. Memb. Sci.* **2012**, *409–410*, 232–241. https://doi.org/10.1016/j.memsci.2012.03.060.

(128) Guo, R.; Sanders, D. F.; Smith, Z. P.; Freeman, B. D.; Paul, D. R.; McGrath, J. E. Synthesis and Characterization of Thermally Rearranged (TR) Polymers: Influence of

Ortho-Positioned Functional Groups of Polyimide Precursors on TR Process and Gas Transport Properties. *J. Mater. Chem. A* **2013**, *1* (2), 262–272. https://doi.org/10.1039/c2ta00799a.

(129) Sanders, D. F.; Guo, R.; Smith, Z. P.; Liu, Q.; Stevens, K. A.; McGrath, J. E.; Paul, D. R.; Freeman, B. D. Influence of Polyimide Precursor Synthesis Route and Ortho-Position Functional Group on Thermally Rearranged (TR) Polymer Properties: Conversion and Free Volume. *Polymer* **2014**, *55* (7), 1636–1647. https://doi.org/10.1016/j.polymer.2014.02.001.

(130) Weidman, J. R.; Luo, S.; Doherty, C. M.; Hill, A. J.; Gao, P.; Guo, R. Analysis of Governing Factors Controlling Gas Transport through Fresh and Aged Triptycene-Based Polyimide Films. *J. Memb. Sci.* **2017**, *522*, 12–22. https://doi.org/10.1016/j.memsci.2016.09.013.

(131) Pethrick, R. A. Positron Annihilation—A Probe for Nanoscale Voids and Free Volume? *Prog. Polym. Sci.* **1997**, *22* (1), 1–47. https://doi.org/10.1016/S0079-6700(96)00023-8.

(132) Siegel, R. W. Positron Annihilation Spectroscopy. *Annu. Rev. Mater. Sci.* **1980**, *10* (1), 393–425. https://doi.org/10.1146/annurev.ms.10.080180.002141.

(133) Kansy, J. Microcomputer Program for Analysis of Positron Annihilation Lifetime Spectra. *Nucl. Instruments Methods Phys. Res. Sect. A Accel. Spectrometers, Detect. Assoc. Equip.* **1996**, *374* (2), 235–244.

(134) Frisch, H. L. The Time Lag in Diffusion. *J. Phys. Chem.* **1957**, *61* (1), 93–95. https://doi.org/10.1021/j150547a018.

(135) Bevington, P. R.; Robinson, D. K.; Blair, J. M.; Mallinckrodt, A. J.; McKay, S. Data Reduction and Error Analysis for the Physical Sciences. *Comput. Phys.* **1993**, *7* (4), 415. https://doi.org/10.1063/1.4823194.

(136) Luo, S.; Zhang, Q.; Bear, T. K.; Curtis, T. E.; Roeder, R. K.; Doherty, C. M.; Hill, A. J.; Guo, R. Triptycene-Containing Poly(Benzoxazole-Co-Imide) Membranes with Enhanced Mechanical Strength for High-Performance Gas Separation. *J. Memb. Sci.* **2018**, *551*, 305–314. https://doi.org/10.1016/j.memsci.2018.01.052.

(137) Lee, C. Development and Advanced Characterization of Novel Chemically Amplified Resists for Next Generation Lithography, PhD Dissertation, Georgia Institute of Technology, **2008**.

(138) Horn, N. R. A Critical Review of Free Volume and Occupied Volume Calculation Methods. *J. Memb. Sci.* **2016**, *518*, 289–294. https://doi.org/10.1016/j.memsci.2016.07.014.

(139) Budd, P. M.; McKeown, N. B.; Ghanem, B. S.; Msayib, K. J.; Fritsch, D.; Starannikova, L.; Belov, N.; Sanfirova, O.; Yampolskii, Y.; Shantarovich, V. Gas Permeation Parameters and Other Physicochemical Properties of a Polymer of Intrinsic Microporosity: Polybenzodioxane PIM-1. *J. Memb. Sci.* **2008**, *325* (2), 851–860. https://doi.org/10.1016/j.memsci.2008.09.010.

(140) Staiger, C. L.; Pas, S. J.; Hill, A. J.; Cornelius, C. J. Gas Separation, Free Volume

Distribution, and Physical Aging of a Highly Microporous Spirobisindane Polymer. *Chem. Mater.* **2008**, *20* (8), 2606–2608. https://doi.org/10.1021/cm071722t.

(141) Luo, S.; Wiegand, J. R.; Kazanowska, B.; Doherty, C. M.; Konstas, K.; Hill, A. J.; Guo, R. Finely Tuning the Free Volume Architecture in Iptycene-Containing Polyimides for Highly Selective and Fast Hydrogen Transport. *Macromolecules* **2016**, *49* (9), 3395–3405. https://doi.org/10.1021/acs.macromol.6b00485.

(142) Li, P.; Chung, T. S.; Paul, D. R. Gas Sorption and Permeation in PIM-1. *J. Memb. Sci.* **2013**, *432*, 50–57. https://doi.org/10.1016/j.memsci.2013.01.009.

(143) Perrin, C. L.; Nielson, J. B. "Strong" Hydrogen Bonds in Chemistry and Biology. *Annu. Rev. Phys. Chem.* **1997**, *48* (1), 511–544. https://doi.org/10.1146/annurev.physchem.48.1.511.

(144) Comer, A. C.; Ribeiro, C. P.; Freeman, B. D.; Kalakkunnath, S.; Kalika, D. S. Dynamic Relaxation Characteristics of Thermally Rearranged Aromatic Polyimides. *Polymer* **2013**, *54* (2), 891–900. https://doi.org/10.1016/j.polymer.2012.12.022.

(145) Matteucci, S.; Yampolskii, Y.; Freeman, B. D.; Pinnau, I. Transport of Gases and Vapors in Glassy and Rubbery Polymers. In *Materials Science of Membranes for Gas and Vapor Separation*; John Wiley & Sons, Ltd: Chichester, UK, 2006; pp 1–47. https://doi.org/10.1002/047002903X.ch1.

(146) Jiang, X.; He, S.; Li, S.; Bai, Y.; Shao, L. Penetrating Chains Mimicking Plant Root Branching to Build Mechanically Robust, Ultra-Stable CO_2-Philic Membranes for Superior Carbon Capture. *J. Mater. Chem. A* **2019**, *7* (28), 16704–16711. https://doi.org/10.1039/c9ta03416a.

(147) Cohen, M. H.; Turnbull, D. Molecular Transport in Liquids and Glasses. *J. Chem. Phys.* **1959**, *31* (5), 1164–1169. https://doi.org/10.1063/1.1730566.

(148) Japip, S.; Lee, G. R.; Chung, T. S. The Role of Fluorinated Aryl Ether Moiety in Polyimide- Co-Etherimide on Gas Transport Properties. *Ind. Eng. Chem. Res.* **2020**, *59* (12), 5315–5323. https://doi.org/10.1021/acs.iecr.9b04713.

(149) Nagel, C.; Günther-Schade, K.; Fritsch, D.; Strunskus, T.; Faupel, F. Free Volume and Transport Properties in Highly Selective Polymer Membranes. *Macromolecules* **2002**, *35* (6), 2071–2077. https://doi.org/10.1021/ma011028d.

(150) Thran, A.; Kroll, C.; Faupel, F. Correlation between Fractional Free Volume and Diffusivity of Gas Molecules in Glassy Polymers. *J. Polym. Sci. Part B Polym. Phys.* **1999**, *37* (23), 3344–3358. https://doi.org/10.1002/(SICI)1099-0488(19991201)37:23<3344::AID-POLB10>3.0.CO;2-A.

(151) Koros, W. J. Simplified Analysis of Gas/Polymer Selective Solubility Behavior. *Am. Inst. Chem. Eng. Natl. Meet.* **1984**, *23*, 1611–1628.

(152) Ghosal, K.; Chern, R. T.; Freeman, B. D.; Daly, W. H.; Negulescu, I. I. Effect of Basic Substituents on Gas Sorption and Permeation in Polysulfone. *Macromolecules* **1996**, *29* (12), 4360–4369. https://doi.org/10.1021/ma951310i.

(153) Mason, C. R.; Maynard-Atem, L.; Heard, K. W. J.; Satilmis, B.; Budd, P. M.; Friess, K.; Lancì, M.; Bernardo, P.; Clarizia, G.; Jansen, J. C. Enhancement of CO_2 Affinity in a Polymer of Intrinsic Microporosity by Amine Modification. *Macromolecules* **2014**, *47* (3), 1021–1029. https://doi.org/10.1021/ma401869p.

(154) Robeson, L. M.; Smith, Z. P.; Freeman, B. D.; Paul, D. R. Contributions of Diffusion and Solubility Selectivity to the Upper Bound Analysis for Glassy Gas Separation Membranes. *J. Memb. Sci.* **2014**, *453*, 71–83. https://doi.org/10.1016/j.memsci.2013.10.066.

(155) Yampolskii, Y. Polymeric Gas Separation Membranes. *Macromolecules* **2012**, *45* (8), 3298–3311. https://doi.org/10.1021/ma300213b.

(156) Bezzu, C. G.; Carta, M.; Tonkins, A.; Jansen, J. C.; Bernardo, P.; Bazzarelli, F.; Mckeown, N. B. A Spirobifluorene-Based Polymer of Intrinsic Microporosity with Improved Performance for Gas Separation. *Adv. Mater.* **2012**, *24* (44), 5930–5933. https://doi.org/10.1002/adma.201202393.

(157) Wang, S.; Li, X.; Wu, H.; Tian, Z.; Xin, Q.; He, G.; Peng, D.; Chen, S.; Yin, Y.; Jiang, Z.; et al. Advances in High Permeability Polymer-Based Membrane Materials for CO_2 Separations. *Energy and Environmental Science*. Royal Society of Chemistry 2016, pp 1863–1890. https://doi.org/10.1039/c6ee00811a.

(158) McKeown, N. B.; Budd, P. M. Polymers of Intrinsic Microporosity (PIMs): Organic Materials for Membrane Separations, Heterogeneous Catalysis and Hydrogen Storage. *Chem. Soc. Rev.* **2006**, *35* (8), 675–683. https://doi.org/10.1039/b600349d.

(159) Long, T. M.; Swager, T. M. Molecular Design of Free Volume as a Route to Low-κ Dielectric Materials. *J. Am. Chem. Soc.* **2003**, *125* (46), 14113–14119. https://doi.org/10.1021/ja0360945.

(160) Liu, S.; Jin, Z.; Teo, Y. C.; Xia, Y. Efficient Synthesis of Rigid Ladder Polymers via Palladium Catalyzed Annulation. *J. Am. Chem. Soc.* **2014**, *136* (50), 17434–17437. https://doi.org/10.1021/ja5110415.

(161) Zhao, Y.; He, Y.; Swager, T. M. Porous Organic Polymers via Ring Opening Metathesis Polymerization. *ACS Macro Lett.* **2018**, *7* (3), 300–304. https://doi.org/10.1021/acsmacrolett.8b00041.

(162) Swaidan, R.; Ghanem, B.; Al-Saeedi, M.; Litwiller, E.; Pinnau, I. Role of Intrachain Rigidity in the Plasticization of Intrinsically Microporous Triptycene-Based Polyimide Membranes in Mixed-Gas CO_2/CH_4 Separations. *Macromolecules* **2014**, *47* (21), 7453–7462. https://doi.org/10.1021/ma501798v.

(163) Du, N.; Park, H. B.; Robertson, G. P.; Dal-Cin, M. M.; Visser, T.; Scoles, L.; Guiver, M. D. Polymer Nanosieve Membranes for CO_2-Capture Applications. *Nat. Mater.* **2011**, *10* (5), 372–375. https://doi.org/10.1038/nmat2989.

(164) Dhara, M. G.; Banerjee, S. Fluorinated High-Performance Polymers: Poly(Arylene Ether)s and Aromatic Polyimides Containing Trifluoromethyl Groups. *Prog. Polym. Sci.* **2010**, *35* (8),1022–1077. https://doi.org/10.1016/j.progpolymsci.2010.04.003.

(165) Alexander Stern, S. Polymers for Gas Separations: The next Decade. *J. Memb. Sci*. **1994**,

95 (1), 1–65. https://doi.org/10.1016/0376-7388(94)00141-3.

(166) Mason, C. R.; Maynard-Atem, L.; Al-Harbi, N. M.; Budd, P. M.; Bernardo, P.; Bazzarelli, F.; Clarizia, G.; Jansen, J. C. Polymer of Intrinsic Microporosity Incorporating Thioamide Functionality: Preparation and Gas Transport Properties. *Macromolecules* **2011**, *44* (16), 6471–6479. https://doi.org/10.1021/ma200918h.

(167) Costa Gomes, M. F.; Pádua, A. A. H. Interactions of Carbon Dioxide with Liquid Fluorocarbons. *J. Phys. Chem. B* **2003**, *107* (50), 14020–14024. https://doi.org/10.1021/jp0356564.

(168) Hellums, M. W.; Koros, W. J.; Husk, G. R.; Paul, D. R. Fluorinated Polycarbonates for Gas Separation Applications. *J. Memb. Sci.* **1989**, *46* (1), 93–112. https://doi.org/10.1016/S0376-7388(00)81173-4.

(169) Adewole, J. K.; Ahmad, A. L.; Ismail, S.; Leo, C. P. Current Challenges in Membrane Separation of CO_2 from Natural Gas: A Review. *Int. J. Greenh. Gas Control* **2013**, *17*, 46–65. https://doi.org/10.1016/j.ijggc.2013.04.012.

(170) Du, N.; Dal-Cin, M. M.; Robertson, G. P.; Guiver, M. D. Decarboxylation-Induced Cross-Linking of Polymers of Intrinsic Microporosity (PIMs) for Membrane Gas Separation. *Macromolecules* **2012**, *45* (12), 5134–5139. https://doi.org/10.1021/ma300751s.

(171) Qiu, W.; Chen, C.-C.; Xu, L.; Cui, L.; Paul, D. R.; Koros, W. J. Sub-T_g Cross-Linking of a Polyimide Membrane for Enhanced CO_2 Plasticization Resistance for Natural Gas Separation. *Macromolecules* **2011**, *44* (15), 6046–6056. https://doi.org/10.1021/ma201033j.

(172) Kratochvil, A. M.; Koros, W. J. Decarboxylation-Induced Cross-Linking of a Polyimide for Enhanced CO_2 Plasticization Resistance. *Macromolecules* **2008**, *41* (21), 7920–7927. https://doi.org/10.1021/ma801586f.

(173) Swaidan, R.; Ghanem, B.; Litwiller, E.; Pinnau, I. Physical Aging, Plasticization and Their Effects on Gas Permeation in “Rigid” Polymers of Intrinsic Microporosity. *Macromolecules* **2015**, *48* (18), 6553–6561. https://doi.org/10.1021/acs.macromol.5b01581.

(174) Bernardo, P.; Bazzarelli, F.; Tasselli, F.; Clarizia, G.; Mason, C. R.; Maynard-Atem, L.; Budd, P. M.; Lanč, M.; Pilnáček, K.; Vopička, O.; et al. Effect of Physical Aging on the Gas Transport and Sorption in PIM-1 Membranes. *Polymer* **2017**, *113*, 283–294. https://doi.org/10.1016/j.polymer.2016.10.040.

(175) Kim, J. H.; Koros, W. J.; Paul, D. R. Physical Aging of Thin 6FDA-Based Polyimide Membranes Containing Carboxyl Acid Groups. Part II. Optical Properties. *Polymer* **2006**, *47* (9), 3104–3111. https://doi.org/10.1016/j.polymer.2006.02.079.

(176) Lin, H. Integrated Membrane Material and Process Development for Gas Separation. *Curr. Opin. Chem. Eng.* **2014**, *4*, 54–61. https://doi.org/10.1016/j.coche.2014.01.010.

(177) Koros, W. J.; Zhang, C. Materials for Next-Generation Molecularly Selective Synthetic Membranes. *Nat. Mater.* **2017**, *16* (3), 289–297. https://doi.org/10.1038/nmat4805.

(178) Budd, P. M.; Makhseed, S. M.; Ghanem, B. S.; Msayib, K. J.; Tattershall, C. E.; McKeown, N. B. Microporous Polymeric Materials. *Mater. Today* **2004**, *7* (4), 40–46. https://doi.org/10.1016/S1369-7021(04)00188-9.

(179) Luo, S.; Liu, Q.; Zhang, B.; Wiegand, J. R.; Freeman, B. D.; Guo, R. Pentiptycene-Based Polyimides with Hierarchically Controlled Molecular Cavity Architecture for Efficient Membrane Gas Separation. *J. Memb. Sci.* **2015**, *480*, 20–30. https://doi.org/10.1016/j.memsci.2015.01.043.

(180) He, Y.; Benedetti, F. M.; Lin, S.; Liu, C.; Zhao, Y.; Ye, H. Z.; Van Voorhis, T.; De Angelis, M. G.; Swager, T. M.; Smith, Z. P. Polymers with Side Chain Porosity for Ultrapermeable and Plasticization Resistant Materials for Gas Separations. *Adv. Mater.* **2019**, *31*, 1807871. https://doi.org/10.1002/adma.201807871.

(181) Mitra, T.; Bhavsar, R. S.; Adams, D. J.; Budd, P. M.; Cooper, A. I. PIM-1 Mixed Matrix Membranes for Gas Separations Using Cost-Effective Hypercrosslinked Nanoparticle Fillers. *Chem. Commun.* **2016**, *52* (32), 5581–5584. https://doi.org/10.1039/c6cc00261g.

(182) Bhavsar, R. S.; Mitra, T.; Adams, D. J.; Cooper, A. I.; Budd, P. M. Ultrahigh-Permeance PIM-1 Based Thin Film Nanocomposite Membranes on PAN Supports for CO_2 Separation. *J. Memb. Sci.* **2018**, *564*, 878–886. https://doi.org/10.1016/j.memsci.2018.07.089.

(183) Bushell, A. F.; Attfield, M. P.; Mason, C. R.; Budd, P. M.; Yampolskii, Y.; Starannikova, L.; Rebrov, A.; Bazzarelli, F.; Bernardo, P.; Carolus Jansen, J.; et al. Gas Permeation Parameters of Mixed Matrix Membranes Based on the Polymer of Intrinsic Microporosity PIM-1 and the Zeolitic Imidazolate Framework ZIF-8. *J. Memb. Sci.* **2013**, *427*, 48–62. https://doi.org/10.1016/j.memsci.2012.09.035.

(184) Starannikova, L. E.; Alentiev, A. Y.; Nikiforov, R. Y.; Ponomarev, I. I.; Blagodatskikh, I. V.; Nikolaev, A. Y.; Shantarovich, V. P.; Yampolskii, Y. P. Effects of Different Treatments of Films of PIM-1 on Its Gas Permeation Parameters and Free Volume. *Polymer* **2021**, *212*, 123271. https://doi.org/10.1016/j.polymer.2020.123271.

(185) Brandt, W. W. Model Calculation of the Temperature Dependence of Small Molecule Diffusion in High Polymers. *J. Phys. Chem.* **1959**, *63* (7), 1080–1085. https://doi.org/10.1021/j150577a012.

(186) Alaslai, N.; Ghanem, B.; Alghunaimi, F.; Litwiller, E.; Pinnau, I. Pure- and Mixed-Gas Permeation Properties of Highly Selective and Plasticization Resistant Hydroxyl-Diamine-Based 6FDA Polyimides for CO_2/CH_4 Separation. *J. Memb. Sci.* **2016**, *505*, 100–107. https://doi.org/10.1016/j.memsci.2015.12.053.

(187) Wessling, M.; Huisman, I.; Boomgaard, T. v. d.; Smolders, C. A. Time-Dependent Permeation of Carbon Dioxide through a Polyimide Membrane above the Plasticization Pressure. *J. Appl. Polym. Sci.* **1995**, *58* (11), 1959–1966. https://doi.org/10.1002/app.1995.070581105.

(188) Staudt-Bickel, C.; J. Koros, W. Improvement of CO_2/CH_4 Separation Characteristics of Polyimides by Chemical Crosslinking. *J. Memb. Sci.* **1999**, *155* (1), 145–154. https://doi.org/10.1016/S0376-7388(98)00306-8.

(189) Kim, J. H.; Koros, W. J.; Paul, D. R. Effects of CO_2 Exposure and Physical Aging on the Gas Permeability of Thin 6FDA-Based Polyimide Membranes. Part 2. with Crosslinking. *J. Memb. Sci.* **2006**, *282* (1–2), 32–43. https://doi.org/10.1016/j.memsci.2006.05.003.

(190) Song, Q.; Cao, S.; Pritchard, R. H.; Ghalei, B.; Al-Muhtaseb, S. A.; Terentjev, E. M.; Cheetham, A. K.; Sivaniah, E. Controlled Thermal Oxidative Crosslinking of Polymers of Intrinsic Microporosity towards Tunable Molecular Sieve Membranes. *Nat. Commun.* **2014**, *5*. https://doi.org/10.1038/ncomms5813.

(191) Bos, A.; Pünt, I. G. M.; Wessling, M.; Strathmann, H. Plasticization-Resistant Glassy Polyimide Membranes for CO_2/CO_4 Separations. *Sep. Purif. Technol.* **1998**, *14* (1–3), 27–39. https://doi.org/10.1016/S1383-5866(98)00057-4.

(192) Vaughn, J.; Koros, W. J. Effect of the Amide Bond Diamine Structure on the CO_2, H_2S, and CH_4 Transport Properties of a Series of Novel 6FDA-Based Polyamide–Imides for Natural Gas Purification. *Macromolecules* **2012**, *45* (17), 7036–7049. https://doi.org/10.1021/ma301249x.

(193) Vaughn, J. T.; Koros, W. J.; Johnson, J. R.; Karvan, O. Effect of Thermal Annealing on a Novel Polyamide-Imide Polymer Membrane for Aggressive Acid Gas Separations. *J. Memb. Sci.* **2012**, *401–402*, 163–174. https://doi.org/10.1016/j.memsci.2012.01.047.

(194) Duthie, X.; Kentish, S.; Pas, S. J.; Hill, A. J.; Powell, C.; Nagai, K.; Stevens, G.; Qiao, G. Thermal Treatment of Dense Polyimide Membranes. *J. Polym. Sci. Part B Polym. Phys.* **2008**, *46* (18), 1879–1890. https://doi.org/10.1002/polb.21521.

(195) Alaslai, N.; Ma, X.; Ghanem, B.; Wang, Y.; Alghunaimi, F.; Pinnau, I. Synthesis and Characterization of a Novel Microporous Dihydroxyl-Functionalized Triptycene-Diamine-Based Polyimide for Natural Gas Membrane Separation. *Macromol. Rapid Commun.* **2017**, *38* (18), 1–5. https://doi.org/10.1002/marc.201700303.

(196) Ma, X.; Swaidan, R.; Belmabkhout, Y.; Zhu, Y.; Litwiller, E.; Jouiad, M.; Pinnau, I.; Han, Y. Synthesis and Gas Transport Properties of Hydroxyl-Functionalized Polyimides with Intrinsic Microporosity. *Macromolecules* **2012**, *45* (9), 3841–3849. https://doi.org/10.1021/ma300549m.

(197) Li, F.; Zhang, C.; Weng, Y. Preparation and Gas Separation Properties of Triptycene-Based Microporous Polyimide. *Macromol. Chem. Phys.* **2019**, *220* (10), 1–7. https://doi.org/10.1002/macp.201900047.

(198) Williams, R.; Burt, L. A.; Esposito, E.; Jansen, J. C.; Tocci, E.; Rizzuto, C.; Lanč, M.; Carta, M.; McKeown, N. B. A Highly Rigid and Gas Selective Methanopentacene-Based Polymer of Intrinsic Microporosity Derived from Tröger's Base Polymerization. *J. Mater. Chem. A* **2018**, *6* (14), 5661–5667. https://doi.org/10.1039/C8TA00509E.

(199) Lasseuguette, E.; Malpass-Evans, R.; Carta, M.; McKeown, N. B.; Ferrari, M. C. Temperature and Pressure Dependence of Gas Permeation in a Microporous Tröger's Base Polymer. *Membranes* **2018**, *8* (4), 1–11. https://doi.org/10.3390/membranes8040132.

(200) Ma, X.; Pinnau, I. Effect of Film Thickness and Physical Aging on Intrinsic Gas Permeation Properties of Microporous Ethanoanthracene-Based Polyimides.

Macromolecules **2018**, *51* (3), 1069–1076. https://doi.org/10.1021/acs.macromol.7b02556.

(201) Benedetti, F. M.; Wu, Y.-C.; Lin, S.; He, Y.; Flear, E.; Liu, C.; Zhao, Y.; Swager, T. M.; Smith, Z. P. Elucidating the Role of Side-Chain Length and Dispersity in ROMP Polymers with Pore-Generating Side Chains for Gas Separations. *In preparation.*

(202) Sanders, E. S. Penetrant-Induced Plasticization and Gas Permeation in Glassy Polymers. *J. Memb. Sci.* **1988**, *37* (1), 63–80. https://doi.org/10.1016/S0376-7388(00)85069-3.

(203) Wind, J. D.; Sirard, S. M.; Paul, D. R.; Green, P. F.; Johnston, K. P.; Koros, W. J. Relaxation Dynamics of CO_2 Diffusion, Sorption, and Polymer Swelling for Plasticized Polyimide Membranes. *Macromolecules* **2003**, *36* (17), 6442–6448. https://doi.org/10.1021/ma034359u.

(204) Gleason, K. L.; Smith, Z. P.; Liu, Q.; Paul, D. R.; Freeman, B. D. Pure- and Mixed-Gas Permeation of CO_2 and CH_4 in Thermally Rearranged Polymers Based on 3,3'-Dihydroxy-4,4'-Diamino-Biphenyl (HAB) and 2,2'-Bis-(3,4-Dicarboxyphenyl) Hexafluoropropane Dianhydride (6FDA). *J. Memb. Sci.* **2015**, *475*, 204–214. https://doi.org/10.1016/j.memsci.2014.10.014.

(205) Swaidan, R.; Ma, X.; Litwiller, E.; Pinnau, I. High Pressure Pure- and Mixed-Gas Separation of CO_2/CH_4 by Thermally-Rearranged and Carbon Molecular Sieve Membranes Derived from a Polyimide of Intrinsic Microporosity. *J. Memb. Sci.* **2013**, *447*, 387–394. https://doi.org/10.1016/j.memsci.2013.07.057.

(206) Visser, T.; Wessling, M. When Do Sorption-Induced Relaxations in Glassy Polymers Set In? *Macromolecules* **2007**, *40* (14), 4992–5000. https://doi.org/10.1021/ma070202g.

(207) *Virial Coefficients of Pure Gases*; Frenkel, M., Marsh, K. N., Eds.; Landolt-Börnstein - Group IV Physical Chemistry; Springer-Verlag: Berlin/Heidelberg, 2002; Vol. 21A. https://doi.org/10.1007/b71692.

(208) Stevens, K. A.; Smith, Z. P.; Gleason, K. L.; Galizia, M.; Paul, D. R.; Freeman, B. D. Influence of Temperature on Gas Solubility in Thermally Rearranged (TR) Polymers. *J. Memb. Sci.* **2017**, *533*, 75–83. https://doi.org/10.1016/j.memsci.2017.03.005.

(209) Wu, A. X.; Drayton, J. A.; Mizrahi Rodriguez, K.; Benedetti, F. M.; Qian, Q.; Lin, S.; Smith, Z. P. Elucidating the Role of Fluorine Content on Gas Sorption Properties of Fluorinated Polyimides. *Macromolecules* **2021**, *54* (1), 22–34. https://doi.org/10.1021/acs.macromol.0c01746.

(210) Jansen, J. C.; Macchione, M.; Tocci, E.; De Lorenzo, L.; Yampolskii, Y. P.; Sanfirova, O.; Shantarovich, V. P.; Heuchel, M.; Hofmann, D.; Drioli, E. Comparative Study of Different Probing Techniques for the Analysis of the Free Volume Distribution in Amorphous Glassy Perfluoropolymers. *Macromolecules* **2009**, *42* (19), 7589–7604. https://doi.org/10.1021/ma901244d.

(211) Mizrahi Rodriguez, K.; Wu, A. X.; Qian, Q.; Han, G.; Lin, S.; Benedetti, F. M.; Lee, H.; Chi, W. S.; Doherty, C. M.; Smith, Z. P. Facile and Time-Efficient Carboxylic Acid Functionalization of PIM-1: Effect on Molecular Packing and Gas Separation

Performance. *Macromolecules* **2020**, *53* (15), 6220–6234. https://doi.org/10.1021/acs.macromol.0c00933.

(212) Raaijmakers, M. J. T.; Ogieglo, W.; Wiese, M.; Wessling, M.; Nijmeijer, A.; Benes, N. E. Sorption Behavior of Compressed CO_2 and CH_4 on Ultrathin Hybrid Poly(POSS-Imide) Layers. *ACS Appl. Mater. Interfaces* **2015**, *7* (48), 26977–26988. https://doi.org/10.1021/acsami.5b08286.

(213) Simons, K.; Nijmeijer, K.; Sala, J. G.; van der Werf, H.; Benes, N. E.; Dingemans, T. J.; Wessling, M. CO_2 Sorption and Transport Behavior of ODPA-Based Polyetherimide Polymer Films. *Polymer* **2010**, *51* (17), 3907–3917. https://doi.org/10.1016/j.polymer.2010.06.031.

(214) Swaidan, R. J.; Ghanem, B.; Swaidan, R.; Litwiller, E.; Pinnau, I. Pure- and Mixed-Gas Propylene/Propane Permeation Properties of Spiro- and Triptycene-Based Microporous Polyimides. *J. Memb. Sci.* **2015**, *492*, 116–122. https://doi.org/10.1016/j.memsci.2015.05.044.

(215) Kanehashi, S.; Nagai, K. Analysis of Dual-Mode Model Parameters for Gas Sorption in Glassy Polymers. *J. Memb. Sci.* **2005**, *253* (1–2), 117–138. https://doi.org/10.1016/j.memsci.2005.01.003.

(216) Koros, W. J.; Paul, D. R.; Huvard, G. S. Energetics of Gas Sorption in Glassy Polymers. *Polymer* **1979**, *20* (8), 956–960. https://doi.org/10.1016/0032-3861(79)90192-7.

(217) Ricci, E.; De Angelis, M. G. Modelling Mixed-Gas Sorption in Glassy Polymers for CO_2 Removal: A Sensitivity Analysis of the Dual Mode Sorption Model. *Membranes* **2019**, *9* (1), 8. https://doi.org/10.3390/membranes9010008.

(218) Wu, A. X.; Drayton, J. A.; Ren, X.; Mizahi Rodriguez, Rodriguez, K.; Grosz, A. F.; Lee, J.-W.; Smith, Z. P. Non-Equilibrium Lattice Fluid Modeling of Gas Sorption for Fluorinated Poly(Ether Imide)s. *Macromolecules* **2021**. https://doi.org/10.1021/acs.macromol.1c00950.

(219) Park, J. S.; Gleason, K. L.; Gaines, K. E.; Mecham, S. J.; McGrath, J. E.; Freeman, B. D. Effect of UV Crosslinking on Transport Properties of CO_2 and N_2 Through Poly(Imide-Siloxane) Segmented Copolymer. *Energy Procedia* **2014**, *63*, 210–216. https://doi.org/10.1016/j.egypro.2014.11.022.

(220) Lin, A. A.; Sastri, V. R.; Tesoro, G.; Reiser, A.; Eachus, R. On the Crosslinking Mechanism of Benzophenone-Containing Polyimides. *Macromolecules* **1988**, *21* (4), 1165–1169. https://doi.org/10.1021/ma00182a052.

(221) Kita, H.; Inada, T.; Tanaka, K.; Okamoto, K. ichi. Effect of Photocrosslinking on Permeability and Permselectivity of Gases through Benzophenone- Containing Polyimide. *J. Memb. Sci.* **1994**, *87* (1–2), 139–147. https://doi.org/10.1016/0376-7388(93)E0098-X.

(222) Shin, G. J.; Jung, J. C.; Chi, J. H.; Oh, T. H.; Kim, J. B. Synthesis and Micropatterning Properties of a Novel Base-Soluble, Positive-Working, Photosensitive Polyimide Having Ano-Nitrobenzyl Ether Group. *J. Polym. Sci. Part A Polym. Chem.* **2007**, *45* (5), 776–788. https://doi.org/10.1002/pola.21833.

(223) Fukukawa, K.; Ueda, M. Recent Progress of Photosensitive Polyimides. *Polym. J.* **2008**, *40* (4), 281–296. https://doi.org/10.1295/polymj.PJ2007178.

(224) Mizrahi Rodriguez, K.; Lin, S.; Wu, A. X.; Han, G.; Teesdale, J. J.; Doherty, C. M.; Smith, Z. P. Leveraging Free Volume Manipulation to Improve the Membrane Separation Performance of Amine-Functionalized PIM-1. *Angew. Chemie Int. Ed.* **2021**, *60* (12), 6593–6599. https://doi.org/10.1002/anie.202012441.

(225) Satilmis, B.; Lanč, M.; Fuoco, A.; Rizzuto, C.; Tocci, E.; Bernardo, P.; Clarizia, G.; Esposito, E.; Monteleone, M.; Dendisová, M.; et al. Temperature and Pressure Dependence of Gas Permeation in Amine-Modified PIM-1. *J. Memb. Sci.* **2018**, *555*, 483–496. https://doi.org/10.1016/j.memsci.2018.03.039.

(226) Yanaranop, P.; Santoso, B.; Etzion, R.; Jin, J. Facile Conversion of Nitrile to Amide on Polymers of Intrinsic Microporosity (PIM-1). *Polymer* **2016**, *98*, 244–251. https://doi.org/10.1016/j.polymer.2016.06.041.

(227) Jeon, J. W.; Kim, D. G.; Sohn, E. H.; Yoo, Y.; Kim, Y. S.; Kim, B. G.; Lee, J. C. Highly Carboxylate-Functionalized Polymers of Intrinsic Microporosity for CO_2-Selective Polymer Membranes. *Macromolecules* **2017**, *50* (20), 8019–8027. https://doi.org/10.1021/acs.macromol.7b01332.

(228) Du, N.; Robertson, G. P.; Song, J.; Pinnau, I.; Guiver, M. D. High-Performance Carboxylated Polymers of Intrinsic Microporosity (PIMs) with Tunable Gas Transport Properties. *Macromolecules* **2009**, *42* (16), 6038–6043. https://doi.org/10.1021/ma9009017.

(229) Liu, Y.; Liu, Z.; Liu, G.; Qiu, W.; Bhuwania, N.; Chinn, D.; Koros, W. J. Surprising Plasticization Benefits in Natural Gas Upgrading Using Polyimide Membranes. *J. Memb. Sci.* **2020**, *593*, 117430. https://doi.org/10.1016/j.memsci.2019.117430.

(230) Yi, S.; Ma, X.; Pinnau, I.; Koros, W. J. A High-Performance Hydroxyl-Functionalized Polymer of Intrinsic Microporosity for an Environmentally Attractive Membrane-Based Approach to Decontamination of Sour Natural Gas. *J. Mater. Chem. A* **2015**, *3* (45), 22794–22806. https://doi.org/10.1039/c5ta05928c.

(231) Doris, S. E.; Ward, A. L.; Frischmann, P. D.; Li, L.; Helms, B. A. Understanding and Controlling the Chemical Evolution and Polysulfide-Blocking Ability of Lithium-Sulfur Battery Membranes Cast from Polymers of Intrinsic Microporosity. *J. Mater. Chem. A* **2016**, *4* (43), 16946–16952. https://doi.org/10.1039/c6ta06401a.

(232) Li, C.; Ward, A. L.; Doris, S. E.; Pascal, T. A.; Prendergast, D.; Helms, B. A. Polysulfide-Blocking Microporous Polymer Membrane Tailored for Hybrid Li-Sulfur Flow Batteries. *Nano Lett.* **2015**, *15* (9), 5724–5729. https://doi.org/10.1021/acs.nanolett.5b02078.

(233) Brunauer, S.; Emmett, P. H.; Teller, E. Adsorption of Gases in Multimolecular Layers. *J. Am. Chem. Soc.* **1938**, *60* (2), 309–319. https://doi.org/10.1021/ja01269a023.

(234) Halgren, T. A. Merck Molecular Force Field. I. Basis, Form, Scope, Parameterization, and Performance of MMFF94. *J. Comput. Chem.* **1996**, *17* (5–6), 490–519. https://doi.org/10.1002/(SICI)1096-987X(199604)17:5/6<490::AID-JCC1>3.0.CO;2-P.

(235) Halgren, T. A. Merck Molecular Force Field. II. MMFF94 van Der Waals and Electrostatic Parameters for Intermolecular Interactions. *J. Comput. Chem.* **1996**, *17* (5–6), 520–552. https://doi.org/10.1002/(SICI)1096-987X(199604)17:5/6<520::AID-JCC2>3.0.CO;2-W.

(236) Halgren, T. A. Merck Molecular Force Field. III. Molecular Geometries and Vibrational Frequencies for MMFF94. *J. Comput. Chem.* **1996**, *17* (5–6), 553–586. https://doi.org/10.1002/(SICI)1096-987X(199604)17:5/6<553::AID-JCC3>3.0.CO;2-T.

(237) Hanwell, M. D.; Curtis, D. E.; Lonie, D. C.; Vandermeersch, T.; Zurek, E.; Hutchison, G. R. Avogadro: An Advanced Semantic Chemical Editor, Visualization, and Analysis Platform. *J. Cheminform.* **2012**, *4* (1), 17. https://doi.org/10.1186/1758-2946-4-17.

(238) Rogan, Y.; Starannikova, L.; Ryzhikh, V.; Yampolskii, Y.; Bernardo, P.; Bazzarelli, F.; Jansen, C.; Mckeown, N. B. Synthesis and Gas Permeation Properties of Novel Spirobisindane-Based Polyimides of Intrinsic Microporosity. *Polym. Chem.* **2013**, *4*, 3813–3820. https://doi.org/10.1039/c3py00451a.

(239) Robeson, L. M.; Dose, M. E.; Freeman, B. D.; Paul, D. R. Analysis of the Transport Properties of Thermally Rearranged (TR) Polymers and Polymers of Intrinsic Microporosity (PIM) Relative to Upper Bound Performance. *J. Memb. Sci.* **2017**, *525*, 18–24. https://doi.org/10.1016/j.memsci.2016.11.085.

(240) Hill, A. J.; Pas, S. J.; Bastow, T. J.; Burgar, M. I.; Nagai, K.; Toy, L. G.; Freeman, B. D. Influence of Methanol Conditioning and Physical Aging on Carbon Spin-Lattice Relaxation Times of Poly(1-Trimethylsilyl-1-Propyne). *J. Memb. Sci.* **2004**, *243*, 37–44. https://doi.org/10.1016/j.memsci.2004.06.007.

(241) Chiou, J. S.; Barlow, J. W.; Paul, D. R. Plasticization of Glassy Polymers by CO_2. *J. Appl. Polym. Sci.* **1985**, *30*, 2633–2642.

(242) Wind, J. D.; Staudt-Bickel, C.; Paul, D. R.; Koros, W. J. The Effects of Crosslinking Chemistry on CO_2 Plasticization of Polyimide Gas Separation Membranes. *Ind. Eng. Chem. Res.* **2002**, *41* (24), 6139–6148. https://doi.org/10.1021/ie0204639.

(243) Horn, N. R.; Paul, D. R. Carbon Dioxide Plasticization of Thin Glassy Polymer Films. *Polymer* **2011**, *52* (24), 5587–5594. https://doi.org/10.1016/j.polymer.2011.10.004.

(244) Jordan, S. M.; Fleming, G. K.; Koros, W. J. Permeability of Carbon Dioxide at Elevated Pressures in Substituted Polycarbonates. *J. Polym. Sci. Part B Polym. Phys.* **1990**, *28*, 2305–2327.

(245) Coleman, M. R.; Koros, W. J. Conditioning of Fluorine-Containing Polyimides. 2. Effect of Conditioning Protocol at 8% Volume Dilation on Gas-Transport Properties. *Macromolecules* **1999**, *32* (9), 3106–3113. https://doi.org/10.1021/ma981376o.

(246) Tiwari, R. R.; Smith, Z. P.; Lin, H.; Freeman, B. D.; Paul, D. R. Gas Permeation in Thin Films of "High Free-Volume" Glassy Perfluoropolymers: Part II. CO_2 Plasticization and Sorption. *Polymer* **2015**, *61*, 1–14. https://doi.org/10.1016/j.polymer.2014.12.008.

(247) Zhang, C.; Fu, L.; Tian, Z.; Cao, B.; Li, P. Post-Crosslinking of Triptycene-Based Tröger's Base Polymers with Enhanced Natural Gas Separation Performance. *J. Memb.*

Sci. **2018**, *556*, 277–284. https://doi.org/10.1016/j.memsci.2018.04.013.

(248) Tiwari, R. R.; Jin, J.; Freeman, B. D.; Paul, D. R. Physical Aging, CO_2 Sorption and Plasticization in Thin Films of Polymer with Intrinsic Microporosity (PIM-1). *J. Memb. Sci.* **2017**, *537*, 362–371. https://doi.org/10.1016/j.memsci.2017.04.069.

(249) Chiou, J. S.; Paul, D. R. Sorption and Transport of Inert Gases in PVF_2/PMMA Blends. *J. Appl. Polym. Sci.* **1986**, *32* (5), 4793–4814. https://doi.org/10.1002/app.1986.070320503.

(250) Srinivasan, R.; Auvil, S. R.; Burban, P. M. Elucidating the Mechanism(s) of Gas Transport in Poly[1-(Trimethylsilyl)-1-Propyne] (PTMSP) Membranes. *J. Memb. Sci.* **1994**, *86* (1–2), 67–86. https://doi.org/10.1016/0376-7388(93)E0128-7.

(251) Peng, D. Y.; Robinson, D. B. A New Two-Constant Equation of State. *Ind. Eng. Chem. Fundam.* **1976**, *15* (1), 59–64. https://doi.org/10.1021/i160057a011.

(252) Merkel, T. C.; Gupta, R. P.; Turk, B. S.; Freeman, B. D. Mixed-Gas Permeation of Syngas Components in Poly(Dimethylsiloxane) and Poly(1-Trimethylsilyl-1-Propyne) at Elevated Temperatures. *J. Memb. Sci.* **2001**, *191* (1–2), 85–94. https://doi.org/10.1016/S0376-7388(01)00452-5.

(253) Vopička, O.; De Angelis, M. G.; Du, N.; Li, N.; Guiver, M. D.; Sarti, G. C. Mixed Gas Sorption in Glassy Polymeric Membranes: II. CO_2/CH_4 Mixtures in a Polymer of Intrinsic Microporosity (PIM-1). *J. Memb. Sci.* **2014**, *459*, 264–276. https://doi.org/10.1016/j.memsci.2014.02.003.

(254) Fraga, S. C.; Monteleone, M.; Lanč, M.; Esposito, E.; Fuoco, A.; Giorno, L.; Pilnáček, K.; Friess, K.; Carta, M.; McKeown, N. B.; et al. A Novel Time Lag Method for the Analysis of Mixed Gas Diffusion in Polymeric Membranes by On-Line Mass Spectrometry: Method Development and Validation. *J. Memb. Sci.* **2018**, *561*, 39–58. https://doi.org/10.1016/j.memsci.2018.04.029.

(255) Garrido, L.; García, C.; López-González, M.; Comesaña-Gándara, B.; Lozano, Á. E.; Guzmán, J. Determination of Gas Transport Coefficients of Mixed Gases in 6FDA-TMPDA Polyimide by NMR Spectroscopy. *Macromolecules* **2017**, *50* (9), 3590–3597. https://doi.org/10.1021/acs.macromol.7b00384.

(256) Lin, S.; Joo, T.; Benedetti, F. M.; Chen, L. C.; Wu, A. X.; Mizrahi Rodriguez, K.; Qian, Q.; Doherty, C. M.; Smith, Z. P. Free Volume Manipulation of a 6FDA-HAB Polyimide Using a Solid-State Protection/Deprotection Strategy. *Polymer* **2021**, *212*, 123121. https://doi.org/10.1016/j.polymer.2020.123121.

(257) Matsui, S.; Nakagawa, T. Effect of Ultraviolet Light Irradiation on Gas Permeability in Polyimide Membranes. II. Irradiation of Membranes with High-Pressure Mercury Lamp. *J. Appl. Polym. Sci.* **1998**, *67* (1), 49–60. https://doi.org/10.1002/(SICI)1097-4628(19980103)67:1<49::AID-APP6>3.0.CO;2-O.

(258) Liu, Y.; Pan, C.; Ding, M.; Xu, J. Gas Permeability and Permselectivity of Photochemically Crosslinked Copolyimides. *J. Appl. Polym. Sci.* **1999**, *73* (4), 521–526. https://doi.org/10.1002/(SICI)1097-4628(19990725)73:4<521::AID-APP8>3.0.CO;2-P.

(259) Ulery, V. L.; Smith, T. J.; Grubb, T. L.; Tullos, G. L.; Mathias, L. J.; Langsam, M. Highly

Soluble Polyimides from Sterically Hindered Diamines. *Am. Chem. Soc. Polym. Prepr. Div. Polym. Chem.* **1997**, *38* (1), 182–183.